Cardiff University

School of Engineering

Ph.D. Thesis

entitled

Application of Artificial Intelligence and Optimisation Techniques for Fault Detection and Classification in Power Transformers

Presented by: Ehsan Mohamed Altayef

Student ID:1871595

Supervisor: Dr. Fatih Anayi

Co-supervisor: Dr. Michael Packianather

Cardiff 2023

Declaration

This work has not been submitted in substance for any other degree or award at this or any other university of learning. It is not being submitted concurrently in candidature for any degree or other awarded.

Signed (candidate)

Date

Statement 1

This thesis is being submitted in partial fulfilment of the requirements for the degree of Ph.D.

Signed (candidate)

Date

Statement 2

This thesis is the result of my own work, except where otherwise stated. Other sources are acknowledged by footnote giving explicit reference. A bibliography is appended.

Signed (candidate)

Date

Statement 3

I hereby give consent for my thesis, if accepted, to be available for photocopying and for inter-library loan and for the title and summary to be made available to an outside organisation.

Signed (candidate)

Date

Acknowledgments

The research presented in this thesis has been carried out at the Magnetics Materials Group, Cardiff School of Engineering, Cardiff University. And financially supported by The Libyan Ministry of Education under the supervision of Dr. Fatih Anayi. I wish to express my deepest gratitude to them for the guidance, encouragement, patience, and support they have given me in the past few years and for providing the financial support, opportunity, and resources required in my study and completing this project.

First and foremost, I thank ALLAH for helping me to complete this thesis.

I appreciate the excellent guidance, dedication, and exemplary academic standards of my supervisor, Doctor Fatih Anayi. I appreciate his vast knowledge and skills in many areas, and his advice during my study, in writing papers and this thesis.

I would like to express my deepest gratitude to my co-supervisor: Dr. Michael Packianather, for his guidance, encouragement, and caring and for providing me with an excellent atmosphere during this project. And I would also like to thank Dr. Turgut Meydan (deceased) for the time and effort he spent on many theoretical discussions and for the outstanding moral support, his smile, and the family atmosphere he created.

Big thanks are due to many members of staff at Cardiff University for taking time out of their busy schedules to help and support my project during my study at Cardiff University.

My most fantastic thanks are reserved for my family. Especially my mother and father, for their Doa, and unconditional love, support, and encouragement throughout the whole of my life. I will never forget their heart-warming support to me in tracking my progress and encouraging me continuously to reach my goals.

I would like to show my gratitude to Shawqi, Shaima, and Aminah, who stood by me every step of the way with encouragement and support.

Abstract

The thesis reviews the core lamination faults in power transformers and the testing and condition monitoring methods to confirm that artificial intelligence has not yet been applied to diagnose the edge burr faults and the degradation of the lamination insulation fault in the power transformer core. Experimental tests are conducted on the transformer core to observe the effects of faults. A clamping system is designed to apply artificial burrs in a repeatable manner in the range of 0.5T to 1.8T, while insulation faults are created by removing insulation material, short-circuits of 2, 6, 8, and 12 laminations were considered for flux densities of 0.5, 1.0, 1.5, 1.7, and 1.8 T. The faults were generated at different locations on the transformer core, and a total of 5 sites were selected. Artificial intelligence techniques are applied to investigate the impact of edge burr faults and insulation degradation on the total power loss in a 15 kVA three-phase transformer core. Features are extracted from current signals and thermal images and used as input vectors for training and testing using KNN, SVM, and DT classifiers. The accuracy rate obtained from the classifiers was over 90%. A new feature extraction technique called the RGB technique was presented for thermal images. A hybrid model of SVM with BOA and PSO optimization algorithms was developed to enhance the SVM classifier. The results from BOA-SVM were more appropriate for current signals data, while the results from BOA-SVM were the same for thermal image data. The results showed that for a large number of laminations affected by both faults, the overall core losses were doubled. And the results showed a satisfactory accuracy rate for fault detection and classification.

List of abbreviations and nomenclatures

Abbreviations

∇.	Divergence
∇×	Curl
2-D FEM	Two-dimension finite element modelling
3-D FEM	Three-dimension finite element modelling
AEs	Acoustic Emissions
B	Magnetic Flux Density
CGO	Conventional grain-oriented electrical steel
CIGRE	French acronym, standing for Conseil International des Grands Réseaux Electriques; this translates as Council on Large Electric Systems.
CWT	Continuous Wavelet Transform
DGA	Dissolved Gas Analysis
DRA	Dielectric Response Analysis
DT	Decision Tree
DWT	Discrete Wavelet Transform
EB	Edge Burrs
FDS	Frequency Dielectric Response
FFT	Fast Fourier Transform
G	Gauss
GO	Grain-oriented electrical steel
H	Magnetic Field
I	Current
KNN	K-Nearest Neighbour
l	Distance
LTC	Load Tab Charge
M	Magnetisation

m	Magnetic moment
N	Number of turns
NO	Non-oriented electrical steel
O_e	Oersted
P_a	Anomalous loss
P_{cu}	Copper losses
PD	Partial Discharge
PDC	Polarisation Depolarisation Current
P_e	Eddy current losses
P_h	Hysteresis losses
P_m	Magnetic Losses
P_{me}	Mechanical losses
RD	Rolling direction
RGB	Red, Green, Blue
SCI	Short Circuit Impedance
SFRA	Sweep Frequency Response Analysis
SST	Single Strip Tester
STD	Standard Deviation
SVM	Support Vector Machine
T	Tesla
TD	Transverse direction
TF	Transfer Function
THD	Total Harmonic Distortion
TTR	Transformer Turns Ration
WT	Wavelet Transforms
A	Surface area

χ	Susceptibility
p	Dipole strength
D	Electric flux
E	Electric field
J	Eddy Current density
ε_0	The permittivity of free space
μ_0	Permeability of free space
μ_r	Relative permeability of the material
ρ_v	Volume charge density
$\boldsymbol{\Phi}$	Magnetic flux

Contents

List of tables

CHAPTER 3

CHAPTER 4

CHAPTER 5

CHAPTER 6

CHAPTER 7

CHAPTER 8

List of figures

CHAPTER 2

CHAPTER 3

CHAPTER 4

CHAPTER 5

CHAPTER 6

CHAPTER 7

List of publications

[1] E. Altayef, F. Anayi, M. S. Packianather, and O. Kherif, "On the effects of lamination artificial faults in a 15 KVA three-phase transformer core," IEEE Access, vol. 10, pp. 19348–19355, 2022.

[2] E. Altayef, F. Anayi, M. Packianather, Y. Benmahamed, and O. Kherif, "Detection and classification of lamination faults in a 15 KVA three-phase transformer core using SVM, KNN and DT algorithms," *IEEE Access*, vol. 10, pp. 50925–50932, 2022.

[3] E. Altayef, F. Anayi, and M. Packianather, "Power transformer fault detection methods and effects of Edge Burrs Fault: A Review," *2022 2nd International Conference on Advance Computing and Innovative Technologies in Engineering (ICACITE)*, 2022.

[4] E. Altayef, F. Anayi, and M. Packianather, "Experimental investigation on impacts of insulation damage fault between laminations of Power Transformers," *2022 2nd International Conference on Advance Computing and Innovative Technologies in Engineering (ICACITE)*, 2022.

[5] E. Altayef, F. Anayi, and M. Packianather, "A new enhancement of the K-NN algorithm by using an optimization technique," *2022 2nd International Conference on Advance Computing and Innovative Technologies in Engineering (ICACITE)*, 2022.

CHAPTER 1: Introduction

This chapter deals with some generalities in the field of power transformers, presenting the major and common types of faults. Particular interest has been carried in the lamination's faults, namely edge burrs and insulation lamination degradation.

1.1 Introduction

Due to increased electricity consumption, and competition in the electricity market, the need for delivery with reliability and high quality is inevitable. In this regard, power transformers are considered the most critical and expensive equipment in terms of their crucial role in supplying power [1][2]. Power transformers play an essential role in a power network. They are expensive, and once damaged, their repairs are time-consuming. Thus, their successful operation is foremost for continuous operation and stability of the overall system.

This equipment can sometimes be damaged for environmental reasons. Creating a defect in transformers reduces the reliability and power quality of the network and causes fundamental problems in the power system. Therefore, early detection of transformer faults should be an integral part of the power grid monitoring system [3].

Transformer-protective relays are often tested for their dependability, stability, and operation speed under different operating conditions. The protective relays should operate in cases of faults and avoid tripping the circuit breakers when there is no fault [4]. Researchers have proposed various techniques to improve transformer differential protection. Several studies have addressed the issue of accurate discrimination of different internal faults in transformers using intelligent systems.

1.2 Power losses in power transformers cores

Electrical machines, i.e., motors, generators, and transformers, are integral and vital parts of industry and power systems. In the design and analysis of electric machines, power loss plays an important role which is usually divided into three major categories: copper losses P_{cu}, mechanical losses P_{me} and magnetic losses P_c. The copper loss takes place in the electrical windings of the machine. Failure in mechanical systems can result from the rotation of rotating components or the movement of sliding components in linear machines. Eddy current loss and hysteresis loss are the two main causes of magnetic energy loss in transformers and other magnetic devices [5][6].

Magnetic cores are one of the main parts of electrical machines and other magnetic devices. The central role of the magnetic core is to concentrate the magnetic field to make the maximum possible magnetic coupling between the primary and secondary windings of a transformer or stator and the rotor of a rotating machine [7].

Magnetic materials are widely used in power electronic equipment, especially power transformers PT. The PT operates at a high frequency, typically in the kilohertz range, to minimize size, resulting in a significant core loss [8]. Traditionally, three approaches, including hysteresis models, core loss separation method, and Steinmetz equation (SE) practice, are mainly adopted to calculate the core loss for sinusoidal excitations, among which the SE is widely used for its simplicity and practicality [9].

Total power losses of the distribution transformers are about 2-3 % of the total electric power production. The total power losses in the distribution transformers can be estimated as 30 % copper losses P_{CU} or load losses P_L that depend on the transformer load; and 70 % core losses P_C or no-load losses $P_{N\text{-}L,}$ also called magnetic losses P_m which depends on the voltage applied to the transformer [10][11].

1.3 Inter-laminar short circuit faults

The manufacturing process of electrical machines, which includes punching/cutting, core assembly, and welding, induces mechanical and thermal stresses to the electrical steel sheet. The induced stresses cause degradation of the magnetic properties of the laminated steel sheet around the cutting edge and the welded region [12]-[16], which directly impacts the core losses of the final manufactured electrical machine. Furthermore, the mechanical stress during the punching process inevitably causes a burr on the cut edge of the steel. When the sheets are stacked and welded together to form the machine core, it can lead to the formation of an inter-laminar short circuit fault between laminations. Since the core is subjected to a time-varying magnetic field during operation, circulating eddy currents are induced around the short circuit region. These currents create an additional localized power loss around the short circuit region, and if this electrical shorting covers several laminations, high currents can circulate, leading to a significant increase in power loss and excessive localized heating. In the absence of adequate cooling, this phenomenon might lead to an insulation breakdown of the machine laminations. Thus, it causes the potential of a complete machine failure [17]. Inter-laminar faults (ILFs) have major impacts on the overall performance of electrical machines and power transformers, among which extra power loss and hence lower efficiency could be highlighted [18].

1.4 Aim and objectives of the project

Thesis's Aim:

This thesis addresses the need for a comprehensive review of the core lamination faults and the testing and condition monitoring methods to demonstrate that artificial intelligence has not been applied yet to detect the Edge Burrs and the degradation of the lamination insulation faults. And to experimentally analyse these faults in a 15 kVA three-phase power transformer and diagnose these faults using AI by extracting features from current signals and thermal images.

Thesis's objectives

1- Experimentally simulate and analyze the Edge Burrs fault and the degradation of lamination insulation fault in a 15 kVA three-phase power transformer and investigate their effects.

2- Use artificial intelligence to diagnose the faults in the power transformer core by extracting features from current signals and using KNN, SVM, and DT classifiers.

3- Apply the RGB technique to extract features from thermal images and diagnose faults in the power transformer core.

4- Enhance the performance of the SVM algorithm by combining it with BOA and PSO optimization algorithms to develop a hybrid model of classification.

1.5 Contributions

1- Application of artificial intelligence for diagnosing Edge Burrs and lamination insulation faults in a 15 kVA three-phase power transformer using current signals and thermal images. This particular application has utilised three classification algorithms (KNN, SVM, and DT).

2- Development of a new method for thermal image feature extraction using the RGB technique.

3- Improvement of the performance of the SVM algorithm through the application of BOA and PSO optimization algorithms.

To the best of the author's knowledge, the above three points have never been touched by other researchers on these particular faults.

1.6 Research Problem

Confirming that the artificial intelligent has not been applied to detect these faults. And The investigation of the effect of edge burr faults and insulation degradation on the total power loss in a 15 kVA three-phase transformer core. It also explores the potential impact of artificial

intelligence in diagnosing these faults. And to find a non-destructive, effective and efficient method to detect these faults and analyze their impact on the power loss of the transformer.

1.7 Research Methodology

The research methodology used in this thesis includes the following steps:

Comprehensive Review: A comprehensive review of the literature is conducted to cover the up-to-date knowledge of core lamination faults and the methods for testing and condition monitoring for fault analysis and detection in power transformers.

Simulation of Edge Burrs and Insulation Faults: A clamping system is designed for the application of artificial burrs in a wholly repeatable and reversible manner. The impact of these faults is investigated through the application of artificial faults and the utilization of analytical techniques and experimental work.

Data Collection: The equipment for conducting the experimental tests is described, as well as the description of the specific faults and data acquisition.

Fault Detection and Classification using AI: Features are extracted from current signals and used as input vectors for the training and testing process using KNN, SVM, and DT classifiers.

Fault Detection using Thermal Imaging: A new feature extraction technique, the RGB technique, is used to diagnose faults in the power transformer core using thermal images.

Optimization of SVM Algorithm: The performance of the SVM algorithm is improved by applying the particle swarm optimization (PSO) and the genetic optimization algorithm (BOA) to develop a hybrid model of classification.

1.8 Thesis Structure

1- Introduction

- Background and context of the problem
- Statement of the research question

2- Literature Review

- Overview of the current state of the research in core laminations faults

3- Methodology

- Design of the experimental setup
- Data collection methods
- Data analysis techniques

3- Results and Discussion

- Analysis of the experimental results

- Comparison of different classifiers
- Comparison of results with optimization method

4- Conclusion

- Summary of the findings
- Implications for future research

1.9 Reference

[1] Z. Liang and A. Parlikad, "A Markovian model for power transformer maintenance," Int. J. Electr. Power Energy Syst., vol. 99, no. December 2017, pp. 175–182, 2018.

[2] R. Murugan and R. Ramasamy, "Failure analysis of power transformer for effective maintenance planning in electric utilities," Eng. Fail. Anal., vol. 55, pp. 182–192, 2015.

[3] A. Moradzadeh and K. Pourhossein, "Early Detection of Turn-to-Turn Faults in Power Transformer Winding: An Experimental Study," Proc. 2019 Int. Aegean Conf. Electr. Mach. Power Electron. ACEMP 2019 2019 Int. Conf. Optim. Electr. Electron. Equipment, OPTIM 2019, pp. 199–204, 2019.

[4] R. Hamilton, "Analysis of transformer inrush current and comparison of harmonic restraint methods in transformer protection," Rec. Conf. Pap. - Annu. Pet. Chem. Ind. Conf., vol. 49, no. 4, pp. 1890–1899, 2012.

[5] R . S. Bhide, M. S. S. Srinivas, A. Banerjee, and R. Somakumar, "Analysis of winding inter-turn fault in transformer: A review and transformer models," 2010 IEEE Int. Conf. Sustain. Energy Technol. ICSET 2010, 2010.

[6] Y. Zhang, M.C. Cheng, and P. Pillay, "A Novel Hysteresis Core Loss Model for Magnetic Laminations," IEEE Trans. Energy Convers., vol. 26, no. 4, pp. 993–999, Dec. 2011.

[7] Y. Chen and P. Pillay, "An Improved Formula for Lamination Core Loss Calculations in Machines Operating with High Frequency and High Flux Density Excitation," IEEE 37th IAS Annual Meeting, vol. 2, 13-18 Oct 2002, pp. 759–766.

[8] B. S Guru, H R Hiziroglu, "Electric Machinery and Transformers", Third edition, Oxford university press, 2001

[9] I. Villar, U. Viscarret, I. Etxeberria-Otadui and A. Rufer, "Global loss evaluation methods for nonsinusoidally fed medium-frequency power transformers", IEEE Trans. Ind. Electron., vol. 56, no. 10, pp. 4132-4140, Oct. 2009.

[10] D Maheswaran, K K Jembu Kailas, "Energy Efficiency in Electrical Systems ", Proceeding of IEEE International Conference on Power Electronics, Drives and Energy Systems, Dec, Bengaluru, India 2012

[11] S. Yurekten, A. Kara, K. Mardikyan, "Energy Efficient Green Transformer Manufacturing with Amorphous Cores ", Proceeding of International Conference on Renewable Energy Research and Applications, Madrid, Spain 201

[12] Harstick, H.M.S.; Ritter, M.; Riehemann, W. Influence of Punching and ToolWear on the Magnetic Properties of Nonoriented Electrical Steel. IEEE Trans. Magn. 2014, 50, 1–4.

[13] Siebert, R.; Schneider, J.; Beyer, E. Laser Cutting and Mechanical Cutting of Electrical Steels and its Effect on the Magnetic Properties. IEEE Trans. Magn. 2014, 50, 1–4.

[14] Kuo, S.; Lee, W.; Lin, S.; Lu, C. The Influence of Cutting-Edge Deformations on Magnetic Performance Degradation of Electrical Steel. IEEE Trans. Ind. Appl. 2015, 51, 4357–4363.

[15] Schoppa, A.; chneider, J.; Wuppermann, C.D. Influence of the manufacturing process on the magnetic properties of non-oriented electrical steels. J. Magn. Magn. Mater. 2000, 215–216, 74–78.

[16] Dems, M.; Komeza, K.; Kubiak, W.; Szulakowski, J. Impact of Core Sheet Cutting Method on Parameters of Induction Motors. Energies 2020, 13, 1960, doi:10.3390/en13081960.

[17] O.Osemwinyen, A. Hemeida, F. Martin, A. Belahcen, and A. Arkkio, "Parameter estimation of inter-laminar fault-region in laminated sheets through inverse approach," Energies, vol. 13, no. 12, pp. 1–10, 2020.

[18] H.Hamzehbahmani, "Inter-laminar fault analysis of magnetic cores with grain-oriented electrical steels under harmonic distortion magnetisations," IET Sci. Meas. Technol., vol. 14, no. 1, pp. 26–31, 2020.

CHAPTER 2: Power transformer fault detection methods and effects of laminations fault

This chapter covers the methods for analysing and detecting faults in power transformers and reviews laminations faults, in addition to how these faults are identified and confirmed. It investigates the benefits and challenges of established and novel approaches to detecting emerging faults, considering advanced methods' range of measurement' accuracy' and reliability. It identifies which approach to detecting edge burr faults is most suitable for different instances of faults. The study provides valuable information for understanding and detecting edge burr faults by applying varied detection approaches.

2.1 Introduction

Power transformers form a central component of a power network, and when a transformer fails, this causes unexpected disruptions to operations and repair work which is costly. Transformers can be affected by various faults, among which is the laminations' fault. These faults have been found to increase power transformer losses, as well as lead to greater eddy current losses within magnetic circuits. For a larger transformer core, short-circuit current may rise to a level where the core is damaged.

In general, power transformer cores are constructed using thinly laminated electrical steel, which decreases losses in eddy current and allows for highly efficient operations [1]. The laminations have an inorganic coat of between 1, and 3μm thickness applied to each side, and this protects one lamination from directly coming into electrical contact with the next. As the electrical steel is punched and cut, this mechanically stresses the lamination, causing it to deform and degrading its magnetic characteristics [2]. The core of an electrical machine undergoes various processes, and these can directly affect the properties of that core. Cores can be mechanically damaged as they are assembled or as they are rewound or re-wedged, foreign bodies may be introduced during construction, and they can be affected by vibrations, heat exposure, arcing, and deterioration of the insulation, which separates the laminations [3][4]. As the steel is cut, burrs can develop on the cut edge due to mechanical shear deformation [5]. These faults can cause the degrading of the insulation separating each sheet, leading to the inter-lamination of electrical shorts. Where such shorting occurs across a number of laminations, this can lead to a high circulating current, significantly increasing power losses and causing the core to overheat locally. This can then burn or melt sheets, with a risk that the machine will then fail completely [6][7]. The authors in [7] ran simulated computer models of a core to predict effects

from edge burrs, with burrs of varying size and location manufactured in the core for each model. More recent works have considered edge burr effects on laminated sheets in the core.

For example, a study in [8] investigated the impact of connected edges for losses in a ring core sample, demonstrating that eddy current power losses rise significantly where edges in the core connect. The phenomenon of additional shorting between laminations occurs due to minor damage in the insulation at the surface of the lamination within the central region of the core. On the other hand, there is an extremely low stochastic probability that this type of fault will emerge [9]. Burrs are generated when the laminar sheets are punched, and this leads to both cut-edge shorting and shorting between layers. Burrs form due to the shear exerted when the sheet is cut using the 2-blade guillotine. When the blade in motion comes into contact with the metal, and it begins to turn over, the load is increased, causing the sheet to undergo fracture shear stress [10][11]. From here, the load is increased, creating cracking which yields a sudden breakthrough via ductile fracture, and burrs form [12]. The shear effect exerted alters during the cutting process and can be seen at the cut edge of the sheet. As the metal is the first subject to the force of the blade/punch, the tool clearance permits plastic deformation of the metal to occur, and the edge rolls over, while the more profound impact of the tool into the sheet, shear creates a burnished area to appear vertically across the sheet. In the last stage of the process, angled fracturing occurs, creating a minor burring to the cut edge. The different zones of the cut may be smaller or larger depending on factors such as toll clearance and sharpness. The results of the cutting procedure are shown in figure 2-1.

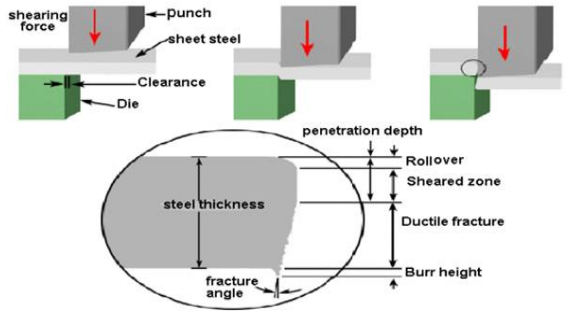

Figure 2-1: Cutting procedure for lamination, with a generation of edge burr [78].

It is essential to have a monitoring plan in place for diagnosing faults in power transformers which reflects their significance, to ensure that they perform reliably and effectively over their lifespan [13].

In certain instances, when gradual degradation of insulation occurs, this can lead to short-circuiting faults based on outside factors as described below [14]:

- Mechanically induced damage from assembling, rewinding, or re-wedging core
- Foreign bodies present since assemblage
- Vibrations, heating, arcs
- Inter-laminar insulation deteriorates

Where one lamination comes into contact with another, circulation of local currents is induced in the short circuit volume, increasing machine losses [6]. Moreover, flows of currents on the lamination surface are chiefly due to burrs that arise in the process of cutting the lamination. Often, the burr faults lead to localised contacts at the machines outside edges, offering a flow pathway to the eddy current induced [15].

2.2 Data on transformer failures

Transformer insulation degrades in strength mechanically and dielectrically throughout its service life. Therefore, over time it becomes more likely to fail, and its remaining lifespan is reduced. The industry standard sets an average operational lifespan of around four decades for power transformers, after which there is an expectation of a high risk of catastrophic failures. Various internal and external mechanisms have an impact on the expected remaining life and rate of failure for transformers. Statistical information regarding factors responsible for transformer failures is given in figure 2- 2 [16]-[18].

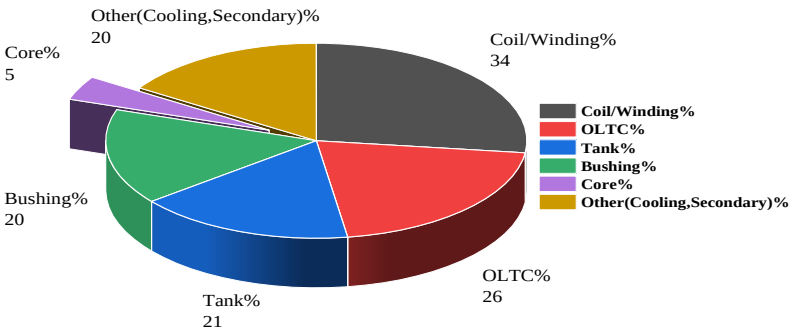

Figure 2-2: Transformer failures by location

2.3 Diagnostic testing and condition monitoring for power transformers

Unusually for industrial equipment, the transformer contains many parts whose condition cannot practically be visually assessed due to being placed in an oil tank. Due to this limitation, various methods have been developed to indirectly evaluate transformer status via measuring multiple variables.

Once a power transformer has been commissioned and installed, it is expected that it will be in constant operation across its operational lifespan, with routine maintenance kept to a minimal level. Unplanned outage events and functions costs (the costs associated with unplanned outage events) are minimised by performing various types of testing, both regular and diagnostic, for the assessment of insulation and the mechanical condition of transformers. Different routine and diagnostic testing methods are described below, covering widely used and more complex approaches, with Figure 3 taxonomically representing significant diagnostic approaches to assessing transformer conditions.

2.3.1 Dissolved gas analysis

The longstanding technique known as dissolved gas analysis (DGA) is frequently applied to monitor power transformers [19]-[21]. However, while DGA is adequate for fault detection and classification, it is not generally able to locate the position of faults. Therefore, in operation, additional findings must be obtained to support DGA diagnosis using different approaches. The different DGA approaches are reviewed below.

• Key gas analysis (KGA) makes fault diagnosis by measuring combustible gas proportions [22].

• Roger's Ratios method (RRM) depends on gas concentration ratios in detecting and categorising transformer faults [22].

• Gas patterns method, this approach mainly uses ethylene (C_2H_4) and methane (CH_4) measurements to diagnose reduced conductor-conductor connections [23].

• The Doernenburg method uses four ratios of gas between 5 main gaseous substances, namely H_2, CH_4, C_2H_2, C_2H_4, and C_2H_6. This technique is used in transformer fault detection and PD activity [24].

• The Duval Triangle Method (DTM) uses a triple-axis graph in which an axis represents CH_4, one C_2H_4, and one C_2H_2 percentage between 0 and 100% [24]-[32].

2.3.2 Oil quality test

This test of the quality of the insulating oil is frequently applied to assess transformer condition while it is operational [33]-[36].

2.3.3 Infrared thermograph test

Rapid imaging without destructive processes can be achieved through infrared thermography to visualise outer surface temperatures for a transformer while it is in service [37][38].

2.3.4 Excitation current test

The excitation current test is applied for the identification of ground faults, short-circuited turns, shorted core laminations, core de-laminations, load tap changer (LTC) issues and poor electrical connections [39].

2.3.5 Power factor/dielectric dissipation factor test

Applications of the dielectric dissipation factor (tan δ) test include verifying insulation conditions in transformer windings, oil tanks, and bushings [40].

2.3.6 Polarisation index measure

The polarisation index (PI) is frequently used to identify how clean and dry the solid insulation of windings is, depending on insulation categories A, B and C, as well as windings parts [41][42].

2.3.7 Capacitance measure

Through measuring capacitance, bushings condition can be assessed, and gross windings movement identified. The transformer's bushings are analogous in electrical terms to several series capacitors [43].

2.3.8 Measure of transfer function

Transfer function (TF) measurement has widespread acceptance as a technique for predicting the moisture levels of solid insulation as well as for identifying mechanical defects such as deformed or displaced windings caused by short-circuit currents, being transported and switching impulse [44]-[46].

2.3.9 Tap changer condition

A transformer's load tap changer (LTC) controls voltage irrespective of load variation. Various insulation materials are applied for tap changers, including fiberglass, oil, proxy resin, and cardboard [43][47].

2.3.10 Cellulose paper insulation tests

Transformers' internal solid paper insulation contains approximately 90% cellulose, 6–7% hemicelluloses, and 3–4% lignin with long glucose ring chains [48][40].

• CO_2:CO ratio Measuring the proportion of CO_2 to CO assists in assessing paper insulation's integrity [43].

• The Furan analysis method assesses cellulose paper status within a transformer and is an operationally non-disruptive, post-diagnosis, non-periodic and integral approach [40][43].

• Degree of Polymerisation measurement (DP) offers reliable assessment for paper insulation conditions [49][50].

2.3.11 Dielectric response analysis

Moisture levels in transformers' oil/paper insulation materials can be assessed through dielectric response analysis (DRA) [51][52].

• The recovery voltage measurement (RVM) tool provides dielectric responses in the time domain for the identification of moisture levels within transformer insulation [53][54].

• Analysing polarisation and depolarisation current: Recently, measuring polarisation and depolarisation current (PDC) has emerged as a non-destructive technique for the measurement of moisture level and oil conductivity for composites and homogenous materials in transformer insulation [55][56].

• Frequency dielectric response (FDS) is frequently applied in the diagnosis of moisture levels and aging conditions for oil–paper transformer insulation [57][58].

• Time–frequency domain dielectric response is a technologically-advanced approach that draws on both the benefits of FDS and PDC to evaluate transformer insulation health [59].

2.3.12 Partial discharge analysis

This involves analysing partial discharge (PD), which refers to dielectric discharges over part of a system of electrical insulation under intense electrical fields [60][61].

• Chemical detection is a fundamental approach to PD detection, which identifies chemical alterations to insulation materials [62].

• Electrical detection identifies high-frequency electrical pulses which are generated in voids based on significant electrical stresses over those voids [63][64].

• Detecting acoustic emissions, Measurement of acoustic emissions (AEs) encompasses measuring attenuation, amplitude, and phase delays in PD-generated acoustic signals and is used in identifying and locating PD [64][65].

• Detecting ultrahigh frequencies, Ultrahigh-frequency (UHF) methods are used routinely and consistently to monitor power transformer processes [62][66].

• Optical detection is an advanced and recently introduced method for identifying and locating transformer PD [67][68].

• Installing a high-frequency current transformer, High-frequency current transformers (HFCTs), or other sensors based on inductive coupling are applied to find online PD for power transformers [69][70].

• Transfer function measure, The high-frequency transfer function (TF) of the transformer's windings is applied for the assessment and location of PD sources originating in windings [71][72].

2.3.13 Leakage reactance/short-circuit impedance measure

Measuring short-circuit impedance (SCI) involves an assessment based on the frequency and is long-established in the detection of deformed windings or a displaced transformer core [73][74].

2.3.14 Turns ratio test

The transformer turns ratio (TTR) test can identify short/open circuits between turns in a single winding [75].

2.3.15 Winding resistance test

Winding resistance tests are applied in detecting loosened connections, stand breakages, or faulty contacts within LTC. Measurement of resistance is to be carried out for each tap for LTC contact verification [43][76].

2.3.16 Core-to-ground resistance test

Most newer transformers have an intentional connection between the core and one ground point via a small bushing. This is to prevent circulating current as well as to identify multiple grounds. Grounding systems can be damaged or loosened during transport.

2.3.17 Sweep frequency response analysis

Sweep frequency response analysis (SFRA) is applied in detecting mechanical deformations and transformer core/windings displacement and offers accuracy, sensitivity, cost-effectiveness, and a non-destructive approach [77].

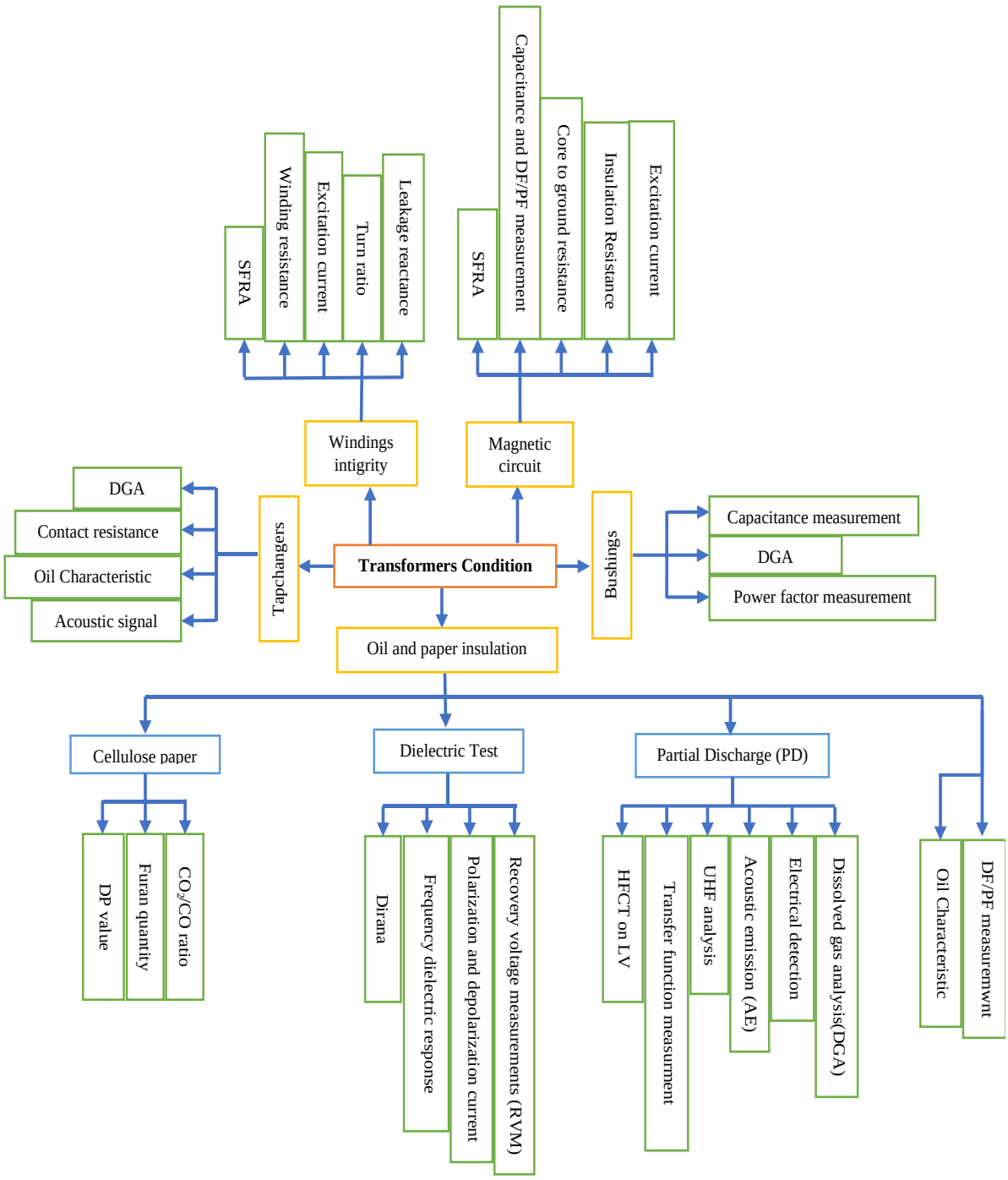

Figure 2- 3: Condition monitoring and methods of diagnosis

While for 70% of the most frequent fault types, diagnosis through DGA is adequate, further tests are necessary to demonstrate the occurrence of a mechanical fault. In order to detect edge burr faults, the optimal test types are for current alteration and the use of thermal imaging to test temperatures.

2.4 Review of works on edge burr faults

Where an edge burr is poorly situated within the transformer core stack, short-circuiting occurs from one lamination to the next, causing an eddy current that adds to core loss [78]. This happens where burrs on opposing sides of the stack create closed pathways, which permit further circulating eddy currents. Although the burrs might be too minor to damage the core, the transformer's operation can become less efficient: especially when high flux densities are used [79].

Edge burring can arise because of a range of issues, as shown below:

- Lamination fabrication flaws are termed burrs.
- When electrical steel is cut and punched, edge burring can be caused, leading to interlaminar short-circuiting.
- Stack sides can be mechanically damaged when they are assembled, during winding, or when inspected.
- When stacks are assembled, wound, or inspected, unintended components can be left inside them, e.g., broken laminations, nuts, or bolts.
- Chemicals, heat, or mechanical pressure may occur when the winding is stripped and rewound.
- Rubbing of the core can occur during construction or in service.
- Vibrations from unsecured laminations or windings.
- Failure of the windings leads to arcing.

Edge burr faults, causing interlaminar fault currents, represent a central potential issue for those producing and purchasing electrical steel.

Moses and Aimonitois (1989) investigated the effects of edge burr faults on overall power losses in a single-phase transformer core by placing artificially induced burrs on the core's edge figure 2-4, with a core constructed using 3% silicon iron. Measurements of power losses were performed at 1.3, 1.5, and 1.7 T with a 50 Hz magnetising frequency.

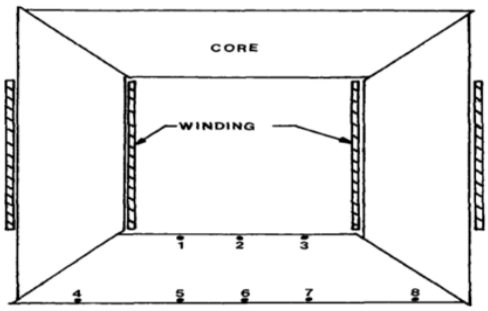

Figure 2- 4: Schematic diagram illustrating eight artificially induced burrs located within a single-phase core [79]

For the artificial production of edge burring, holes of 0.3 mm diameter were drilled through the laminations close to their edge, and the insertion of a rod or pin made of steel to the necessary lamination layer for the specific test. Figure 2-5 shows pins located in a sample limb.

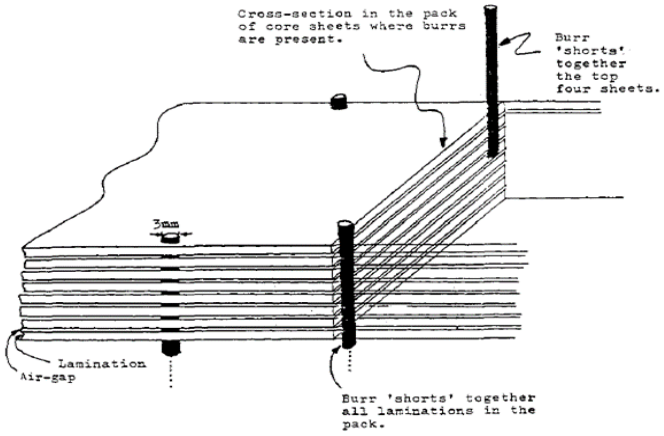

Figure 2-5: Method of producing artificial burrs [79]

Before measuring total power losses, power was applied to transformer cores with various artificially induced burr configurations. The findings were then examined in comparison to a core without burring. Measurement was carried out for localised losses across 32 locations on specified laminations by applying the initial rate of rising temperature approach. A specifically developed thermocouple bridge controlled by a microprocessor was used in scanning a 32-thermistor array to assess losses, with thermistors located on laminations of the core for measurement of power losses. The findings reveal significant rises in power losses in relation to the number of laminations short-circuited together, with this trend increasing with the number of laminations involved. The reason for this is the closed pathway linking the burrs, which leads to extremely elevated localised losses near burrs [80][81].

Aimoniotis and Moses (1993) applied finite element software to assess induced linear steady - state eddy currents within cores [82]. This work used an equation derived from Maxwell's equations to describe time-varied electromagnetic fields (1)

$$\nabla \frac{X1}{\mu} \nabla x \bar{A} = -\sigma \frac{\partial \bar{A}}{\partial t} + \bar{J} \qquad (2\text{-}1)$$

where:

∇ is the del operator, a vector differential operator used to calculate the gradient of a scalar field or the curl of a vector field. *X*1/μ is the impedance of free space (1/μ), where μ is the permeability of free space. A¯is the magnetic vector potential. σ is the electrical conductivity of the material. ∂A¯/∂t is the time derivative of the magnetic vector potential, representing the rate of change of A¯over time. And j¯is the current density, representing the flow of electric charge in a material."

Shorting each side of laminations was conducted, with current density variations being a lengthy line extending slightly under the surface of lamination three within the core, running parallel with the surface. The findings suggest that extremely high eddy current levels were present where each burr was located and in that immediate area, falling at a distance of 2.5 mm from the burr. Eddy currents grew in strength with higher numbers of laminations being shorted. Additional findings from the model show that edge burr effects arise solely in cases where the core has burrs on each side, and where a single side only is shorted, total power losses are unaffected.

Schulz et al investigated the effects of short-circuiting two magnetic sheets in a simple study by applying insulation faults to opposing sides of the sheets. Application of the fault to a single side did not influence total power losses in figure 2- 6 due to the failure of the single fault to create a closed pathway for current induced at right angles to vector B as a flux density component [83].

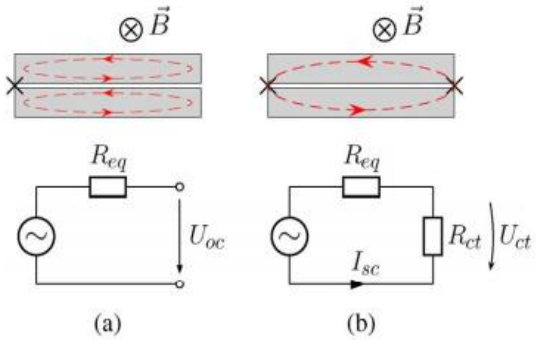

Figure 2- 6: a Single-sided insulation fault, and b, faults on opposing sheet [81]

Mazurek et al.'s study consisted of experiments to assess effects from an inter-laminar fault in a 3-phase, 350 kVA transformer, in which burrs were artificially created using a clamping instrument in lengths of 10, 15, and 20 mm to short out respective numbers of laminations of 33, 50 and 66. Simulation of edge burrs was conducted by pressing copper tape of 8μm thickness to the lamination stack sides using a wooden block before applying a firm clamp pressure from a torque meter clamp, thus applying burrs to a limb of the core figure 2- 7[82].

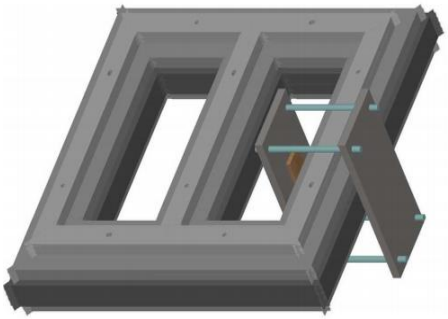

Figure 2- 7:Three-phase transformer core with clamp devise [82]

The experiment utilised copper tape, which was similar in thickness to the size of the edge burring found in practice. It was found that use of the clamp had no influence on total power losses, which were measured via a power analyser. In contrast, localised loss in the presence and absence of burrs was calculated using an initial rate of rising temperature [82].

Mazurek et *al*. conducted a study to address challenges in quantifying increased loss from burr faults at the cut edges of electrical steel laminations within transformer cores by applying artificially induced burrs in a 3-phase, 350 kVA, 5-packet transformer core figure 2-8.

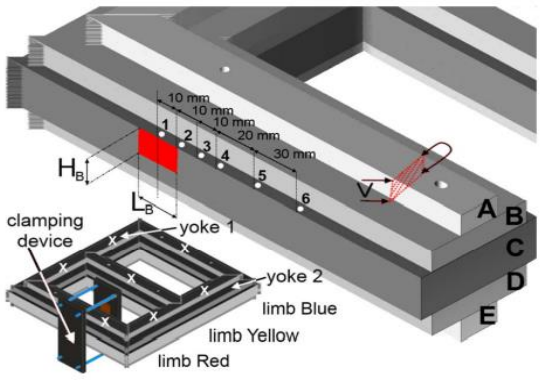

Figure 2- 8: : Experimental 350 kVA transformer core with clamp device for application of artificially induced burrs, thermocouples, and locations of measurement by needle probe [84]

Measurements were taken for overall losses of the core, distributed flux density, and localised losses close to burr positions. The burrs' impact on total and localised loss was calculated using

a modified classical equation for eddy current based on the assumption that there is a non-negligible thickness in the burred laminated sheets compared with width [84].

$$\boldsymbol{P_{eddy} = \frac{\pi^2 f^2 d^2 B^2}{6_\rho}} \quad (2\text{-}2)$$

The equation represents the formula for the power loss due to eddy currents in a conductor where:

P_eddy is the power loss due to eddy currents.

π is the mathematical constant pi.

f is the frequency of the alternating magnetic field.

d is the thickness of the conductor.

B is the magnetic flux density.

ρ is the electrical resistivity of the conductor.

6 is a constant factor."

$$\boldsymbol{P_y = \frac{4\pi^2 f^2 B_{max}^2}{\rho}\ (\frac{1}{3}((\frac{b}{2} + d_b)^3 - \frac{b^3}{8}))} \quad (2\text{-}3)$$

"The equation represents the formula for the power loss due to hysteresis in a magnetic material, where:

P_Y is the power loss due to hysteresis.

4π^2 is a constant factor.

f is the frequency of the alternating magnetic field.

B_max is the maximum magnetic flux density.

ρ is the electrical resistivity of the magnetic material.

b is the width of the magnetic material.

d_b is the depth of the magnetic material.

The term (1/3((b/2+d_b)^3-b^3/8)) represents the volume of the magnetic material."

The study shows that edge burr impacts are mainly seen in proportion to the number of laminations with burring: for the 66-lamination burrs, there was a 13% and 100% rise in power losses at 1.5 T and 1.8 T, respectively. In addition, edge burrs led to more significant temperature increases with greater local losses. Localised power losses were seen to occur up to 70 mm away from the boundary of the burred area. Burrs were induced across part of a lamination stack on a single limb, reducing uniformity in flux distribution across the whole core.

There was a significant rise in localised losses in the core with the largest burr region covering 66 laminations, the specific total loss increases by 13% at 1.5 T and by 100% at 1.8 T. The effect of increasing the number of burred laminations on the local loss in the centre of the burred region at core flux densities from 1.5 T to 1.8 T. Between 1.5 T and 1.7 T a square relationship exists between the loss and the number of laminations, but this breaks down at higher flux density [84].

It has been shown here that burr faults can lead to flux distortions for cruciform stacked cores, in addition to causing raised temperatures locally inside and around the area with a burr. Significant decreases in flux density are also seen in burred areas compared with densities for experimental core limbs, with other regions showing a corresponding increase in flux. There was little correlation linking measurements and calculations for burr impacts. This difference is likely caused by oversimplifying the model for the eddy current. However, issues with measuring thermal loss may also be a contributing factor because heat is transferred rapidly close to the burr. At the same time, the artificially induced burrs investigated show significantly more significant adverse impacts compared to burrs occurring in practice.

Hamzehbahmani et al. (2013) proposed a measurement system for localised power losses in electrical steel lamination using the initial temperature rise rate technique. Unique design and development of the software and hardware elements aimed for accuracy in measurements., before running 3 experiments for systems calibration and quantification across a broad range of measures. The system's applications were shown for two instances of localised power loss: close to lamination bolt holes and to artificially induced lamination edge burring for 300 kVA, 3-phase transformer cores [85].

The experiment's findings demonstrate the system's ability to measure localised power losses across a broad spectrum, giving <2% uncertainty in measurement. However, care in interpretation is needed for areas where significant loss variation is found within a region measuring only a few cm. The suitability of the measurement system was shown for measuring localised loss surrounding lamination bolt holes and close-to-edge burrs with nonuniform loss distributions across a spectrum of a loss of approximately 0.4 W/kg, for which the greatest uncertainty level was under 2% [85].

The experimental findings showed the application of the measurement system for broad-ranging localised power losses with under 2% measurement uncertainty. At the same time,

lower flux densities gave lower signal-to-noise ratios because of the small temperature increase. An improved adiabatic box, such as a vacuum chamber, would be preferable in such cases.

Hamzehbahmani et al. (2014) find that edge burring can occur when electrical steel is cut and punched, subsequently causing short-circuiting inter-lamination. An analysis approach was designed based on equivalent electric circuits for eddy current paths, which could estimate the core's current power loss due to this fault across broad flux density and magnetising frequency ranges. The work considers skin effect, nonuniform flux density distribution, non-linear B-H relations, and complex relative permeability as significant variables not extensively addressed in other works. Foundational principles related to interlaminar faults and the issues they cause were examined, considering their impacts on magnetic core configurations, and verification was conducted through finite-element approaches, with the application of a 2-D FEM model see figure 2-9 for equivalent configuration verification as well as visualisation of the pathways of eddy current traveling along the thickness of the laminations [86].

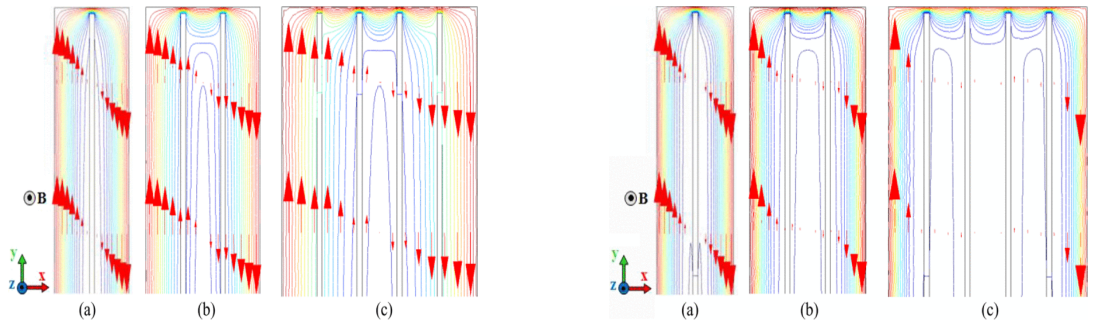

Figure 2- 9: (A) and (B)2D FEM model for distribution of eddy currents within magnetic laminations impacted by burrs using a 50 and 100 Hz frequency respectively of magnetisation for: (a) 2, (b) 3, and (c) 5 laminar sheets. [86].

From the FEM models and findings from analysis, the skin effect is identified as central to investigating eddy current power losses in magnetic cores across both higher and lower frequencies, in which edge burrs impact the core [86].

Hamzehbahmani et al., in the second of a 2-part paper (2014), generated a model of analysis for estimation of power losses from eddy current for magnetic cores displaying interlaminar faults using an analogous core configuration and eddy current circuit paths across a broad magnetising frequency spectrum. Artificial shorting of stacks containing 2, 3 and 4 Epstein-size laminar layers was performed, and the additional power losses due to interlaminar faults were measured, supporting the analytical model see figure 2-10. Significant factors frequently ignored in previous studies are addressed, including skin effect, complex relative permeability, non-uniform flux density distribution, and nonlinear B-H relations.

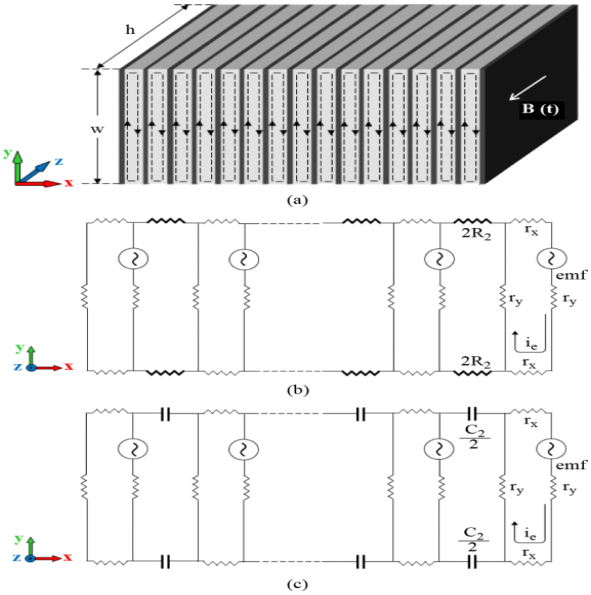

Figure 2- 10: (a) Magnetic lamination stack. (b) Equivalent of pure resistive circuit. (c) Equivalent of RC equivalent circuit [87].

The findings show that where the magnetic core had an interlaminar fault, the skin effect was definitive in determining high and low-frequency magnetic properties [87].

Eldieb et al. (2015) investigated the impacts of edge burrs for machine laminations across varied magnetising frequencies and setpoints. This experimental work was performed via a strip tester. The findings suggest that edge burr faults significantly impact the core's magnetic characteristics and that the location of the edge burr and the number of laminations shorted are the main determinants of the eddy current induced. In addition, it was found, based on power loss separation, that loss from eddy currents increased significantly as the number of laminar layers shorted rose [15].

Laminated toroidal core materials are becoming more widespread across various application areas, with varied magnetising frequencies and power ratings figure 2- 11.

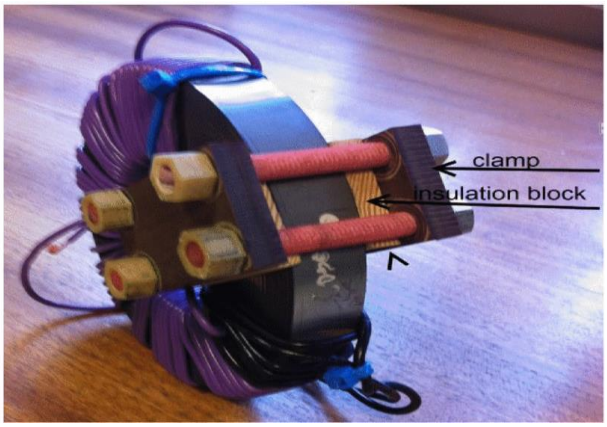

Figure 2- 11:: Test sample in clamp [88].

The lamination cutting procedure is a factor within increased power loss arising from interlayer short-circuiting through edge burrs, based on measuring specific power loss of electrical steel measured in 2 toroidal core specimens with different parameters. Measurement was taken at 1.5 T across a spectrum of magnetising frequencies. In addition, the study took into account the effects of inter-laminar short circuits, simulating the impacts of this fault on overall power losses across various frequencies using artificially induced burrs. Surface flux distribution was also examined using the COMSOL Multi-Physics modeling program [88].

The findings related to specific power losses for grain-oriented electrical steel were found through measurements carried out for two differently sized cores to examine the effects of size parameters on overall power loss measurements see figure 2-12.

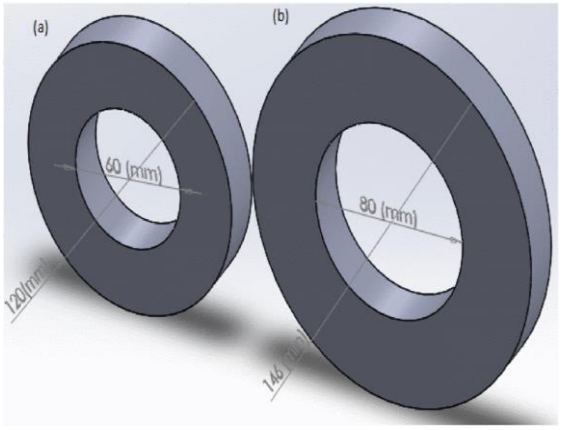

Figure 2- 12: Dimensions for 2 toroid cores: (a) 60 *120*20 mm and toroid (b) 80*146*20 mm [88].

Concentrations of magnetic flux were examined for the surface of the two toroids via COMSOL, supporting the findings achieved. The study investigated impacts from inter-lamination short-circuiting or edge burr faults. The findings show that the higher the number of laminations shorted, the greater the power losses[88].

Poveda-Lerma et al. (2016) examined the impacts of the magnetic core laminations for an EI transformer, validated using an experiment see figure 2-13 as well as 3D FEM modeling, and comparison to a conventional 2D model [89].

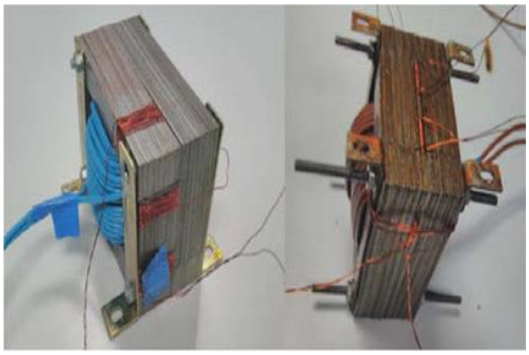

Figure 2- 13:Prototype cores applied to verify experimental findings alongside the relevant exploratory coils. Left: 2-block magnetic core with a single E I. Right: magnetic core constructed with a number of E I sheet transpositions [89].

Based on the findings, lamination is a central factor in inter-laminar magnetic flux flows. It is necessary to examine this impact when designing a novel magnetic core to minimise saturation and loss in specific areas and minimize the use of materials [89].

Shah et al. (2017) identified equivalent conductivity (the electrical conductivity of a material that would have the same magnetic properties as the actual core material) for the EI core in the presence or absence of interlaminar contact via 3D FEM calculations and measures in figure 2-14.

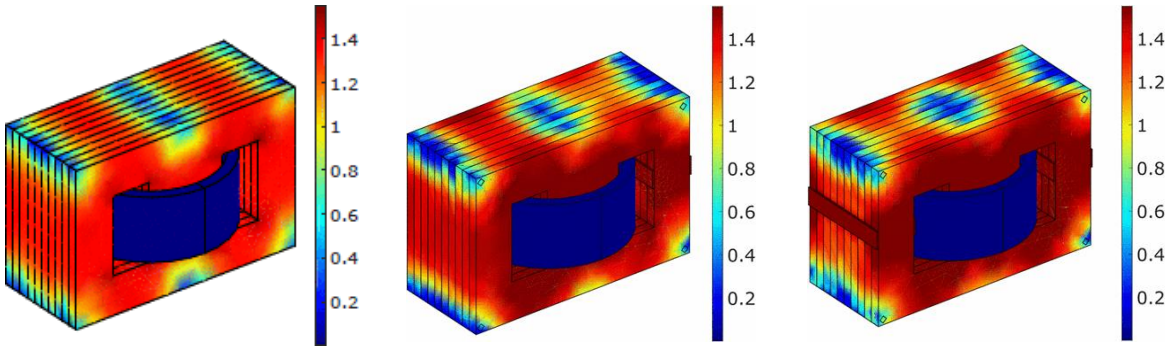

(A) (B) (C)

Figure 2- 14: (A) Magnetic flux density (T) for 50 Hz (healthy condition). (B) Magnetic flux density (T) for 50 Hz (single-limb fault). (C) Magnetic flux density (T) for 50 Hz (2-limb fault) [90].

An investigation was carried out on the impact of contact between laminations upon the core's equivalent conductivities. When this fault was present in a single limb, a 2% rise in the eddy current loss coefficient was seen, while 2-limb interlaminar faults caused a 2.7% rise in the eddy current loss coefficient compared to the normal condition [90].

Hamzehbahmani conducted a detailed (2020) analytical study of energy loss and its components for stacked grain-oriented electrical steel laminations with various faults induced

across laminations using non-sinusoidal and sinusoidal induction figure 2-15. The study proposed a practical approach for monitoring magnetic core quality based on dynamic/static hysteresis loop measurements.

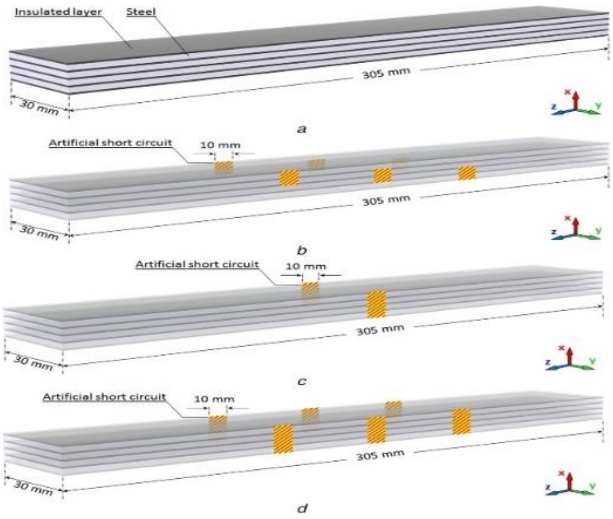

Figure 2- 15: Stacked laminations seen in perspective: (a) no interlaminar fault (Pack#1); with interlaminar faults, (b) Across 3 step-like points (Pack#2), (c) With 1 set-point (Pack#3), (d) With 3 set-points (Pack#4) [91].

Based on the findings, interlaminar faults significantly affect core dynamic energy losses and performance, with minimal effect in terms of hysteresis losses. In addition, such faults cause greater damage with non-sinusoidal induction, meaning that in non-sinusoidal uses, there is a greater need to monitor magnetic cores [91].

Secic et al. (2019) state that each diagnostic process should lead to knowledge about the physical events occurring inside and surrounding a specimen. Effective diagnostics, including signal analysis and extracting and classifying features, should indicate the reasons for an event occurring at a particular time point and the potential causes of these events. Considering this, modelling through simulations that are descriptive of the physical process is very useful. A range of software can be used for simulation of this type, with continual development in this area, and is extremely helpful. Evolving approaches to signal-to-process can be seen within the acoustic signal analysis to evaluate the condition of transformers. This has allowed the characteristics of strongly non-stationary signals to be extracted, for example, and further approaches to classifying and recognising patterns will continue to be developed. However, currently, there is a dearth of fingerprints related to various transformers. Now used and future approaches to diagnosis could be made more reliable by creating a database of acoustic signatures for research and industry use. This would allow the performance of the various

approaches to be compared and those with the greatest reliability to be adopted but would require these groups to co-operate to achieve this [92].

2.5 impacts of insulation damage fault

Electrical machine cores generally consist of laminated steel in these layers, as this design reduces eddy current loss to allow highly efficient operation. The layers are coated with an inorganic substance on each side, this thin layer is usually between 1 and 3μm in thickness, and this stops the layers from direct electrical interaction with each other. Degradation of the inter-laminar insulation in the transformer core can occur from several sources, such as:

- Aging of lamination coating.
- Mechanical damage from external objects.
- Overheating of laminations in the region of a winding failure [93][94].

Insulation degradation occurs due to displaced core steel and time factors. When the insulation separating laminations of power transformers breaks down, this can cause severe failures in large transformers and causes accidental outage, which can be costly to remedy and leads to financial loss. Moreover, the insulation quality in terms of materials and production, as well as the transformer motion and short-circuiting, can be factors in the lamination insulation becoming mechanically damaged [95][96][97][98].

When electrical steel coatings are damaged in an extensive area, the laminations can touch, and eddy currents flow over the volume. This can be simulated, as figure 2-16 shows, displaying eddy currents which can occur when laminations are short-circuited [99]. It is possible to ignore the current where the shift occurs across double the sheet width, as it is under 10% of the maximal magnitude [100]. In general, vibration, arcing, and heating lead to insulation degradation between the sheets. These actions may result in an electrical shorting between the stacked laminations. Several works have been carried out to study these faults experimentally [84][101][102].

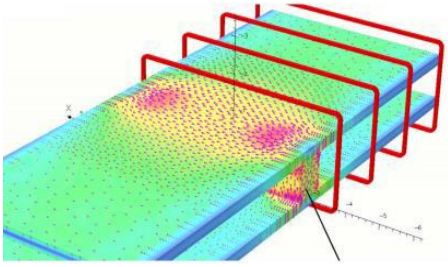

Figure 2- 16: 3-D numerically simulated for a basic short-circuit [7]

2.6 Fault detection based on machine learning.

Machine learning was used to detect and classify transformer faults. A probabilistic Neural Network (PNN) was used to differentiate various operating conditions in a transformer in reference [103]. Artificial Neural Networks (ANN) trained with Genetic Algorithm was used by Balaga et al. to detect and classify faults [104]. A support Vector Machine (SVM) was used for the identification of different transformer winding faults (mechanical and short circuits) [105]. Reference [106] proposed Relevance Vector Machine (RVM) to detect and classify the faults and argued that RVM offers better performance than PNN and SVM. Shin et al. used a fuzzy-based method to overcome mal-operations and enhance conventional differential relays' fault detection sensitivities. Segatto et al. [107] [108] proposed two different subroutines for transformer protection based on ANN. Shah et al. [109] used Discrete Wavelet Transforms (DWT) and SVM based differential protection. Barbosa et al. used Clarke's transformation and Fuzzy logic-based technique to generate a trip signal in case of an internal fault [110]. RF classifier was used to discriminate internal faults and inrush [111]. DWT and ANN were used to detect and classify internal faults in a power transformer [112]. Wavelet-based protection and fault classification in a Phase Shift transformer (PST), a special transformer, was used in [113][114]. Ensemble-based learning was used to classify 40 internal faults in the PST, and the performance was compared with ANN and SVM [115]. In [116] DT based algorithms were used to discriminate the internal faults and other transient disturbances in an interconnected system with PSTs and power transformers. The applicability of seven machine learning algorithms with different sets of features as inputs for the detection and localization of faults was investigated in [117].

2.7 Summary

This up-to-date (2022 published works) comprehensive review of all diagnostic testing and condition monitoring confirmed that artificial intelligence was not yet applied to diagnose the transformer core lamination faults.

Each reviewed study investigated simulation methods of transformer core burr faults designed to permit the measurement of artificially induced burrs repeatably and reversibly. These burr approaches use methods that do not impact the core's performance: e.g., clamping systems. From a range of approaches and materials investigated, it was found that copper foil performs most reliably and repeatably in the simulation of artificial burrs, which is based both on its

reversibility and increased control of experimental variables, as well as being flexible enough to be applied across a wide range of configurations.

This review confirms the effects of edge burr faults on power transformer core performance based on previously published work. While a significant alteration in the way flux density is distributed in a limb is seen where edge burring occurs within a limb/yoke in the transformer core, there is an additional and significant effect on this distribution across the entire core structure. It seems probable that impacts from rising overall losses linked with edge burring become more effective at densities of over 1.5T in the transformer core modelled based on the skin effect and redistributed flux density in the core's cross-section where burrs occur. Moreover, edge burring of laminations leads to losses in the locality of the fault, which are over 600 times greater than usual core losses, with the models' findings showing strong agreement with the measured values in the studies. Moreover, when localised losses are measured, it is found that the area impacted by such losses correlates with the central location of a burr fault.

This work has reviewed diagnostic testing, and condition monitoring applied to substation transformers. Covering studies over an extensive period seek to determine causal factors and potential solutions to the problems involved in this area and to determine which factors most significantly affect the active lifespan and performance of power transformers.

The review concludes that condition monitoring, diagnostics, and maintenance for transformers are essential, decreasing the cost of maintaining the machines and reducing the risk of serious adverse events. Such activities allow power transformers to remain operational for a longer lifespan. The studies reviewed clearly demonstrate the significant role being taken by developing technology in this field, including intelligent software for developing new approaches to diagnosis and maintenance which provide high reliability in the data produced and allow assessment of the equipment in use in the power network.

Degradation of the inter-laminar insulation in the transformer core significantly affects the cores' magnetic properties. As shorted lamination numbers increase, the temperatures and the power loss increase significantly.

2.8 References

[1] S. Bin Lee, G. B. Kliman, M. R. Shah, W. T. Mall, N. K. Nair, and R. M. Lusted, "An advanced technique for detecting inter-laminar stator core faults in large electric machines," IEEE Trans. Ind. Appl., vol. 41, no. 5, pp. 1185–1193, 2005.

[2] A. Kedous-Lebouc, B. Cornut, J. C. Perrier, P. Manfé, and T. Chevalier, "Punching influence on magnetic properties of the stator teeth of an induction motor," J. Magn. Magn. Mater., vol. 254–255, pp. 124–126, 2003.

[3] R. M. Tallam et al., "A survey of methods for detection of stator related faults in induction machines," IEEE Int. Symp. Diagnostics Electr. Mach. Power Electron. Drives, SDEMPED 2003 - Proc., vol. 43, no. 4, pp. 35–46, 2003.

[4] C. R. 1, "Electrical machine core imperfection detection," IET Digit. Libr., vol. 133, no. 3, pp. 190–195, 1986.

[5] P. Handgruber, A. Stermecki, O. Biro, and G. Ofnery, "Evaluation of interlaminar eddy currents in induction machines," IECON Proc. (Industrial Electron. Conf., pp. 2792–2797, 2013.

[6] P. Beckley, Electrical Steels for Rotating Machines, Illustrate. IET, 2014.

[7] M. B. Aimoniotis and A. J. Moses, "Evaluation of induced eddy currents in transformer sheets due to edge-burrs, employing computer aided design programs," Jt. Int. Power Conf. " Athens Power Tech" Planning, Oper. Control Today''s Electr. Power Syst. APT 1993 - Proc., vol. 2, pp. 847–850, 1993.

[8] E. Lamprecht and R. Gräf, "Fundamental investigations of eddy current losses in laminated stator cores created through the impact of manufacturing processes," 1st Int. Electr. Drives Prod. Conf. 2011, EDPC-2011 - Proc., pp. 29–35, 2011.

[9] M. C. Marion-Pera, A. Kedous-Lebouc, T. Waeckerle, and B. Cornut, "Characterization of SiFe Sheet Insulation," IEEE Trans. Magn., vol. 31, no. 4, pp. 2408–2415, 1995.

[10] X. Wu, L. Li, and N. He, "Investigation on the burr formation mechanism in micro cutting," Precis. Eng., vol. 47, pp. 191–196, 2017.

[11] S. L. Ko and D. A. Dornfeld, "A study on burr formation mechanism," J. Eng. Mater. Technol. Trans. ASME, vol. 113, no. 1, pp. 75–87, 1991.

[12] P. Baudouin, M. De Wulf, L. Kestens, and Y. Houbaert, "The effect of the guillotine clearance on the magnetic properties of electrical steels," J. Magn. Magn. Mater., vol. 256, no. 1–3, pp. 32–40, 2003.

[13] H. De Faria, J. G. S. Costa, and J. L. M. Olivas, "A review of monitoring methods for predictive maintenance of electric power transformers based on dissolved gas analysis," Renew. Sustain. Energy Rev., vol. 46, pp. 201–209, 2015.

[14] R. M. Tallam et al., "A survey of methods for detection of stator related faults in induction machines," IEEE Int. Symp. Diagnostics Electr. Mach. Power Electron. Drives, SDEMPED 2003 - Proc., vol. 43, no. 4, pp. 35–46, 2003.

[15] A. Eldieb, F. Anayi, and A. Fahmy, "Investigation of short-circuit fault effects on non-oriented steel at different range of magnetisations," Proc. Univ. Power Eng. Conf., vol. 2015–Novem, pp. 1–6, 2015.

[16] M. M. Islam, G. Lee, and S. N. Hettiwatte, "A review of condition monitoring techniques

and diagnostic tests for lifetime estimation of power transformers," Electr. Eng., vol. 100, no. 2, pp. 581–605, 2018.

[17] A. N. Jahromi, R. Piercy, S. Cress, J. R. R. Service, and W. Fan, "An approach to power transformer asset management using health index," IEEE Electr. Insul. Mag., vol. 25, no. 2, pp. 20–34, 2009.

[18] M. M. Islam, "Development of a quantitative health index and diagnostic method for efficient asset management of power transformers," no. August 2017.

[19] A. D. Ashkezari, T. K. Saha, C. Ekanayake, and H. Ma, "Evaluating the accuracy of different DGA techniques for improving the transformer oil quality interpretation," 2011 21st Australas. Univ. Power Eng. Conf. AUPEC 2011, pp. 1–6, 2011.

[20] V. G. Arakelian, "Effective diagnostics for oil-filled equipment," IEEE Electr. Insul. Mag., vol. 18, no. 6, pp. 26–38, 2002.

[21] M. Wang, A. J. Vandermaar, and K. D. Srivastava, "Review of condition assessment of power transformers in service," IEEE Electr. Insul. Mag., vol. 18, no. 6, pp. 12–25, 2002.

[22] E. A. Mackenzie, J. Crossey, A. Depablo, and W. Ferguson, "On-line monitoring and diagnostics for power transformers: Application to on-load tap-changers," Conf. Rec. IEEE Int. Symp. Electr. Insul., pp. 1–5, 2010.

[23] S. Tenbohlen and F. Figel, "On-line condition monitoring of power transformers," 2000 IEEE Power Eng. Soc. Conf. Proc., vol. 3, no. c, pp. 2211–2216, 2000.

[24] N. Bakar, A. Abu-Siada, and S. Islam, "A review of dissolved gas analysis measurement and interpretation techniques," IEEE Electr. Insul. Mag., vol. 30, no. 3, pp. 39–49, 2014.

[25] A. Akbari, A. Setayeshmehr, H. Borsi, and E. Gockenbach, "A software implementation of the Duval triangle method," Conf. Rec. IEEE Int. Symp. Electr. Insul., pp. 124–127, 2008.

[26] Standard for Safety Requirements for Electrical Equipment for Measurement, Control, and Laboratory Use - Part 1 [ISO_354] International Organization for Standardization (ISO). "International Standard ISO 354." 61010-1 © IEC 2001, vol. 2003, p. 13, 2003.

[27] S. N. Hettiwatte and H. A. Fonseka, "Analysis and interpretation of dissolved gases in transformer oil: A case study," Proc. 2012 IEEE Int. Conf. Cond. Monit. Diagnosis, C. 2012, no. September, pp. 35–38, 2012.

[28] M. M. Islam, G. Lee, and S. N. Hettiwatte, "A nearest neighbour clustering approach for incipient fault diagnosis of power transformers," Electr. Eng., vol. 99, no. 3, pp. 1109–1119, 2017.

[29] A. E. B. Abu-Elanien, M. M. A. Salama, and M. Ibrahim, "Determination of transformer health condition using artificial neural networks," INISTA 2011 - 2011 Int. Symp. Innov. Intell. Syst. Appl., pp. 1–5, 2011.

[30] M. Pal and G. M. Foody, "Feature selection for classification of hyperspectral data by SVM," IEEE Trans. Geosci. Remote Sens., vol. 48, no. 5, pp. 2297–2307, 2010.

[31] A. E. B. Abu-Elanien, M. M. A. Salama, and M. Ibrahim, "Calculation of a health index for oil-immersed transformers rated under 69 kV using fuzzy logic," IEEE Trans. Power Deliv., vol. 27, no. 4, pp. 2029–2036, 2012.

[32] M. M. Islam, G. Lee, and S. N. Hettiwatte, "Incipient fault diagnosis in power

transformers by clustering and adapted KNN," Proc. 2016 Australas. Univ. Power Eng. Conf. AUPEC 2016, pp. 0–4, 2016.

[33] F. Vahidi, M. Jovalekic, S. Tenbohlen, M. Rosner, C. Perrier, and H. Fink, "Electrical conductivity measurement and determination of ion mobility in insulating oil," 2013 IEEE Electr. Insul. Conf. EIC 2013, no. June, pp. 313–317, 2013.

[34] A. D. Ashkezari, H. Ma, T. Saha, and C. Ekanayake, "Application of fuzzy support vector machine for determining the health index of the insulation system of in-service power transformers," IEEE Trans. Dielectr. Electr. Insul., vol. 20, no. 3, pp. 965–973, 2013.

[35] N. A. Bakar, A. Abu-Siada, S. Islam, and M. F. El-Naggar, "A new technique to measure interfacial tension of transformer oil using UV-Vis's spectroscopy," IEEE Trans. Dielectr. Electr. Insul., vol. 22, no. 2, pp. 1275–1282, 2015.

[36] L. Yang, J. Dai, M. Dong, and L. Wang, "Molecular dynamics simulation of temperature impact on the viscosity of transformer oil-based nanofluids," C. 2016 - Int. Conf. Cond. Monit. Diagnosis, no. 2, pp. 376–379, 2016.

[37] N. Y. Utami, Y. Tamsir, A. Pharmatrisanti, H. Gumilang, B. Cahyono, and R. Siregar, "Evaluation condition of transformer based on infrared thermography results," Proc. IEEE Int. Conf. Prop. Appl. Dielectr. Mater., pp. 1055–1058, 2009.

[38] T. K. Saha and P. Purkait, "Understanding the impacts of moisture and thermal ageing on transformer's insulation by dielectric response and molecular weight measurements," IEEE Trans. Dielectr. Electr. Insul., vol. 15, no. 2, pp. 568–582, 2008.

[39] M. Zaman, "IEEE C57.12.90-2006 - IEEE Standard Test Code for Liquid-Immersed Distribution, Power, and Regulating Transformers," IEEE Power and Energy Society, 2007. [Online]. Available: https://standards.ieee.org/standard/C57_12_90-2006.html. [Accessed: 04-May-2021].

[40] H. Malik, A. Azeem, and R. K. Jarial, "Application research based on modern-technology for transformer Health Index estimation," Int. Multi-Conference Syst. Signals Devices, SSD 2012 - Summ. Proc., pp. 18–21, 2012.

[41] H. Torkaman and F. Karimi, "Measurement variations of insulation resistance/polarization index during utilizing time in HV electrical machines - A survey," Meas. J. Int. Meas. Confed., vol. 59, pp. 21–29, 2015.

[42] L. Xiao, L. Ruijin, L. Maochang, Y. Lijun, Y. Junkun, and Q. Chaoliang, "Influence of aging degree on polarization and depolarization currents of oil-paper insulation," Annu. Rep. - Conf. Electr. Insul. Dielectr. Phenomena, CEIDP, vol. 1, no. 1, pp. 612–616, 2013.

[43] X. Zhang and E. Gockenbach, "Asset-management of transformers based on condition monitoring and standard diagnosis," IEEE Electr. Insul. Mag., vol. 24, no. 4, pp. 26–40, 2008.

[44] A. Baral and S. Chakravorti, "Condition assessment of cellulosic part in power transformer insulation using transfer function zero of modified debye model," IEEE Trans. Dielectr. Electr. Insul., vol. 21, no. 5, pp. 2028–2036, 2014.

[45] M. Florkowski and J. Furgal, "Detection of transformer winding deformations based on the transfer function - Measurements and simulations," Meas. Sci. Technol., vol. 14, no. 11, pp. 1986–1992, 2003.

[46] M. Bigdeli, M. Vakilian, and E. Rahimpour, "A new method for detection and evaluation

of winding mechanical faults in transformer through transfer function measurements," Adv. Electr. Comput. Eng., vol. 11, no. 2, pp. 23–30, 2011.

[47] F. Jakob, K. Jakob, and S. Jones, "Use of Gas Concentration Ratios to Interpret LTC & OCB Dissolved Gas Data," Electr. Insul. Conf. Electr. Manuf. Coil Wind. Conf. Exhib., pp. 301–304, 2003.

[48] E. Gockenbach and H. Borsi, "Condition monitoring and diagnosis of power transformers," Proc. Int. Symp. Electr. Insul. Mater., pp. 16–19, 2008.

[49] W. McDermid and D. H. Grant, "Use of furan-in-oil analysis to determine the condition of oil filled power transformers," Proc. 2008 Int. Conf. Cond. Monit. Diagnosis, C. 2008, pp. 479–481, 2008.

[50] A. B. Norazhar, A. Abu-Siada, and S. Islam, "A review on chemical diagnosis techniques for transformer paper insulation degradation," 2013 Australas. Univ. Power Eng. Conf. AUPEC 2013, pp. 2–6, 2013.

[51] Y. Cui, H. Ma, T. Saha, and C. Ekanayake, "Understanding Moisture Dynamics and Its Effect on the Dielectric Response of Transformer Insulation," IEEE Trans. Power Deliv., vol. 30, no. 5, pp. 2195–2204, 2015.

[52] D. Martin, C. Perkasa, and N. Lelekakis, "Measuring paper water content of transformers: A new approach using cellulose isotherms in nonequilibrium conditions," IEEE Trans. Power Deliv., vol. 28, no. 3, pp. 1433–1439, 2013.

[53] M. A. Talib et al., "Diagnosis of transformer insulation condition using recovery voltage measurements," Natl. Power Eng. Conf. PECon 2003 - Proc., pp. 329–332, 2003.

[54] T. K. Saha and P. Purkait, "Investigation of an expert system for the condition assessment of transformer insulation based on dielectric response measurements," IEEE Trans. Power Deliv., vol. 19, no. 3, pp. 1127–1134, 2004.

[55] T. K. Saha and P. Purkait, "Investigation of Polarization and Depolarization Current Measurements for the Assessment of Oil-paper Insulation of Aged Transformers," IEEE Trans. Dielectr. Electr. Insul., vol. 11, no. 1, pp. 144–154, 2004.

[56] U. Gafvert, L. Adeen, M. Tapper, P. Ghasemi, and B. Jonsson, "Dielectric spectroscopy in time and frequency domain applied to diagnostics of power transformers," Proc. IEEE Int. Conf. Prop. Appl. Dielectr. Mater., vol. 2, pp. 825–830, 2000.

[57] M. Jaya, T. Leibfried, and M. Koch, "Information within the dielectric response of power transformers for wide frequency ranges," Conf. Rec. IEEE Int. Symp. Electr. Insul., pp. 2–6, 2010.

[58] R. Liao et al., "Extraction of frequency domain dielectric characteristic parameter of oil-paper insulation for transformer condition assessment," Electr. Power Components Syst., vol. 43, no. 5, pp. 578–587, 2015.

[59] J. Liu, R. Liao, Y. Zhang, C. Gong, C. Wang, and J. Gao, "Condition evaluation for aging state of transformer oil-paper insulation based on time-frequency domain dielectric characteristics," Electr. Power Components Syst., vol. 43, no. 7, pp. 759–769, 2015.

[60] H. Wang, C. Li, and H. He, "Influence of temperature to developing processes of surface discharges in oil-paper insulation," Conf. Rec. IEEE Int. Symp. Electr. Insul., pp. 25–28, 2010.

[61] H. Wang, C. R. Li, K. Sheng, and Y. Miao, "Experimental study on the evolution of

surface discharge for oil-paper insulation in transformers," Annu. Rep. - Conf. Electr. Insul. Dielectr. Phenomena, CEIDP, pp. 405–408, 2009.

[62] M. M. Yaacob, M. A. Alsaedi, J. R. Rashed, A. M. Dakhil, and S. F. Atyah, "Review on partial discharge detection techniques related to high voltage power equipment using different sensors," Photonic Sensors, vol. 4, no. 4, pp. 325–337, 2014.

[63] S. A. Boggs and U. Systems, "Partial Dischar e: Overview and ignal Generation 8," vol. 6, no. 4, 1990.

[64] P. Janus, "Acoustic Emission Properties of Partial Discharges in the time-domain and their applications," 2012.

[65] A. Akbari, P. Werle, H. Borsi, and E. Gockenbach, "Transfer function-based partial discharge localization in power transformers: A feasibility study," IEEE Electr. Insul. Mag., vol. 18, no. 5, pp. 22–32, 2002.

[66] I. Fofana and Y. Hadjadj, "Electrical-Based Diagnostic Techniques for Assessing Insulation Condition in Aged Transformers," Energies, vol. 9, no. 9, p. 679, 2016.

[67] R. Schwarz, M. Muhr, and S. Pack, "Partial discharge detection in oil with optical methods," 2005 IEEE Int. Conf. Dielectr. Liq. ICDL 2005, pp. 245–248, 2005.

[68] S. Karmakar, N. K. Roy, and P. Kumbhakar, "Monitoring of high voltage power transformer using direct optical partial discharge detection technique," J. Opt., vol. 38, no. 4, pp. 207–215, 2009.

[69] I. K. S. and o. Y. w. G. Ariastina", I. A. D. Giriantari', "Condition Monitoring of Power Transformer: A Field Experience," Transm. Distrib. Expo. Conf. 2008 IEEE PES Powering Towar. Futur. PIMS 2008, pp. 1051–1054, 2009.

[70] T. R. Blackburn, B. T. Phung, Z. Liu, and R. E. James, "ON-LINE PARTIAL DISCHARGE MEASUREMENT ON INSTRUMENT TRANSFORMERS," pp. 497–500, 1998.

[71] M. R. Hussain, S. S. Refaat, and H. Abu-Rub, "Overview and Partial Discharge Analysis of Power Transformers: A Literature Review," IEEE Access, vol. 9, pp. 64587–64605, 2021.

[72] S. Seifi, P. Werle, A. A. Shayegani Akmal, H. Mohseni, and H. Borsi, "A feasibility study on estimating induced charge of partial discharges in transformer windings adjacent to its origin," Int. J. Electr. Power Energy Syst., vol. 129, no. March, p. 106899, 2021.

[73] C. AJ, M. A. Salam, Q. M. Rahman, F. Wen, S. P. Ang, and W. Voon, "Causes of transformer failures and diagnostic methods – A review," Renew. Sustain. Energy Rev., vol. 82, no. July 2017, pp. 1442–1456, 2018.

[74] B. chul Kim and J. seok Oh, "The novel short circuit withstand test configuration for ITER VS1 power transformer," Fusion Eng. Des., vol. 147, no. January, p. 111239, 2019.

[75] O. W. Iwanusiw, "The Art and Science of Transformer Ratio Measurement," 2018 IEEE Electr. Insul. Conf. EIC 2018, no. June, pp. 390–394, 2018.

[76] K. Niyomsatian, J. J. C. Gyselinck, and R. V. Sabariego, "Experimental Extraction of Winding Resistance in Litz-Wire Transformers - Influence of Winding Mutual Resistance," IEEE Trans. Power Electron., vol. 34, no. 7, pp. 6736–6746, 2019.

[77] Z. Li, Y. Zhang, B. Zhu, Y. Luo, T. Zhang, and Z. Zhang, "Survey of frequency response

analysis on winding deformation of transformers," 2019 4th Int. Conf. Intell. Green Build. Smart Grid, IGBSG 2019, no. 51707103, pp. 567–571, 2019.

[78] A. S. A. Eldieb, "Evaluation of loss generated by edge- burrs in electrical steel," Cardiff University, 2016.

[79] A. J. Moses and M. Aimoniotis, "Effects of artificial edge burrs on the properties of a model transformer core," Phys. Scr., vol. 39, no. 3, pp. 391–393, 1989.

[80] M. B. Aimoniotis, A. J. Moses, and N. Rtj, "Evaluation op induced eddy curren?'s in tkansformer sheets due to edge-burrs, employing computer," 1993.

[81] C. A. Schulz, D. Roger, S. Duchesne, and J. N. Vincent, "Experimental characterization of interlamination shorts in transformer cores," IEEE Trans. Magn., vol. 46, no. 2, pp. 614–617, 2010.

[82] R. Mazurek, P. Marketos, A. Moses, and J. N. Vincent, "Effect of artificial burrs on the total power loss of a three-phase transformer core," IEEE Trans. Magn., vol. 46, no. 2, pp. 638–641, 2010.

[83] D. Jiles, Introduction to Magnetism and Magnetic Materials, Third edit. CRC press, 2016.

[84] R. Mazurek, H. Hamzehbahmani, A. J. Moses, P. I. Anderson, F. J. Anayi, and T. Belgrand, "Effect of artificial burrs on local power loss in a three-phase transformer core," IEEE Trans. Magn., vol. 48, no. 4, pp. 1653–1656, 2012.

[85] H. Hamzehbahmani, A. J. Moses, and F. J. Anayi, "Opportunities and precautions in measurement of power loss in electrical steel laminations using the initial rate of rise of temperature method," IEEE Trans. Magn., vol. 49, no. 3, pp. 1264–1273, 2013.

[86] H. Hamzehbahmani, P. Anderson, J. Hall, and D. Fox, "Eddy current loss estimation of edge burr-affected magnetic laminations based on equivalent electrical network - Part I: Fundamental concepts and FEM modeling," IEEE Trans. Power Deliv., vol. 29, no. 2, pp. 642–650, 2014.

[87] D. F. Hamed Hamzehbahmani, Philip Anderson, Jeremy Hall, "Eddy Current Loss Estimation of Edge Burr-Affected Magnetic Laminations Based on Equivalent Electrical Network—Part II: Analytical Modeling and Experimental Results," IEEE Int. Symp. Diagnostics Electr. Mach. Power Electron. Drives, SDEMPED 2003 - Proc., vol. 29., no. no2, p. 9, 2014.

[88] A. Eldieb, F. Anayi, and A. Fahmy, "Experimental investigation on effect of edge burr's fault on toroidal magnetic cores laminations at different range of magnetisations," Proc. Univ. Power Eng. Conf., vol. 2015–Novem, pp. 1–5, 2015.

[89] G. S.-C. A. Poveda-Lerma and R. P. M. Riera-Guasp, M. Pineda-Sanchez, "3D Simulation of a power transformer considering lamination effects," 2017 18th Int. Symp. Electromagn. Fields Mechatronics, Electr. Electron. Eng. B. Abstr., vol. 116, no. 17318541, pp. 3–4, 2016.

[90] S. B. Shah, P. Rasilo, A. Belahcen, and A. Arkkio, "Experimental and theoretical study of interlaminar eddy current loss in laminated cores," 2017 20th Int. Conf. Electr. Mach. Syst. ICEMS 2017, 2017.

[91] H. Hamzehbahmani, "Inter-laminar fault analysis of magnetic cores with grain-oriented electrical steels under harmonic distortion magnetisations," IET Sci. Meas. Technol., vol. 14, no. 1, pp. 26–31, 2020.

[92] A. Secic, M. Krpan, and I. Kuzle, “Vibro-Acoustic Methods in the Condition Assessment of Power Transformers: A Survey,” IEEE Access, vol. 7, pp. 83915–83931, 2019.

[93] S. Bin Lee, G. B. Kliman, M. R. Shah, W. T. Mall, N. K. Nair, and R. M. Lusted, “An advanced technique for detecting inter-laminar stator core faults in large electric machines,” IEEE Trans. Ind. Appl., vol. 41, no. 5, pp. 1185–1193, 2005, doi: 10.1109/TIA.2005.853383.

[94] E. Altayef, F. Anayi, M. S. Packianather, and O. Kherif, ``On the effects of lamination arti_cial faults in a 15 kVA three-phase transformer core," *IEEE Access*, vol. 10, pp.19348_19355, 2022, doi:10.1109/ACCESS.2022.3151367.

[95] V. Anand, A. Jain, D. More, and S. Mohaney, “Experimental Failure Analysis and Investigation of causes for 200 kVA, 11kV/415V Distribution Transformers,” SSRN Electron. J., pp. 1–6, 2021, Doi: 10.2139/ssrn.3808988.

[96] E. C. Sakshaug, S. Member, and G. Electric, “Influence of Rate of Rise on Distribution ArresterProtective Characteristic,” vol. 75, no. 2, pp.519–526, 2020.

[97] O. F. D. Systems, “RESEARCH INTO LIGHTNING PROTECTION OF SYSTEMS Departmei at of Electrical Engineering,” no. 4, pp. 673–682, 1984.

[98] T. K. Saha, M. Darveniza, D. J. T. Hill, and T. T. Le, “Electrical and insulation-part A : Aged transformer samples,” IEEE Trans. Power Deliv., vol. 12, no. 4, pp.1547–1554, 1997, doi: 10.1109/61.634174.

[99] J. P. Bielawski, S. Duchesne, D. Roger, C. Demian, and T. Belgrand, “Contribution to the study of losses generated by interlaminar shortcircuits,” IEEE Trans. Magn., vol.48, no. 4, pp. 1397–1400, 2012, Doi: 10.1109/TMAG.2011.2173472.

[100] C. Schulz, D. Roger, S. Duchesne, and J. N. Vincent, “Experimental characterization of interlamination shorts in transformer cores,” IEEE Trans. Magn., vol. 46, no. 2, pp. 614–617, 2010, Doi: 10.1109/TMAG.2009.2032834.

[101] I. Reva, O. Bialobrzheskyi, and O. Usatiuk, ``Investigation of distribution a harmonic power in three phase transformers at idling mode," in Proc. IEEE 7th Int. Conf. Energy Smart Syst. (ESS), May 2020, pp. 273-276.

[102] A. Patel, N. K. Sharma, A. Banshwar, B. B. Sharma, and M. Pathak, ``An evaluation of different health assessment methods on 50 MVA power transformer: A case study," in Proc. IEEE Students Conf. Eng. Syst. (SCES), Jul. 2020, pp. 1-5.

[103] M. Tripathy, R. P. Maheshwari, and H. K. Verma, “Neuro-fuzzy technique for power transformer protection,” Electr. Power Components Syst., vol. 36, no. 3, pp. 299–316, 2008.

[104] H. Balaga, N. Gupta, and D. N. Vishwakarma, “GA trained parallel hidden layered ANN based differential protection of three phase power transformer,” Int. J. Electr. Power Energy Syst., vol. 67, pp. 286–297, 2015.

[105] M. Bigdeli, M. Vakilian, and E. Rahimpour, “Transformer winding faults classification based on transfer function analysis by support vector machine,” IET Electr. Power Appl., vol. 6, no. 5, pp. 268–276, 2012.

[106] M. Raichura, N. Chothani, and D. Patel, “Review of methodologies used for detection of magnetising inrush and fault conditions in power transformer,” IET Energy Syst. Integr., vol. 3, no. 2, pp. 109–129, 2021.

[107] M. C. Shin, C. W. Park, and J. H. Kim, “Fuzzy logic-based relaying for large power transformer protection,” IEEE Trans. Power Deliv., vol. 18, no. 3, pp. 718–724, 2003.

[108] Ê. C. Segatto and D. V. Coury, "A differential relay for power transformers using intelligent tools," IEEE Trans. Power Syst., vol. 21, no. 3, pp. 1154–1162, 2006.
[109] A. M. Shah and Bhalja, "Discrimination between internal faults and other disturbances in transformer using the support vector machine-based protection scheme," IEEE Trans. Power Deliv., vol. 28, no. 3, pp. 1508–1515, 2013.
[110] D. Barbosa, U. C. Netto, D. V. Coury, and M. Oleskovicz, "Power transformer differential protection based on Clarke's transform and fuzzy systems," IEEE Trans. Power Deliv., vol. 26, no. 2, pp. 1212–1220, 2011.
[111] A. M. S. 1 and B. R. Bhalja, "Fault discrimination scheme for power transformer using random forest technique," IET, vol. 10, no. 6, 21 April 2016, pp. 1431 – 1439, 2016.
[112] A. Ngaopitakkul and A. Kunakorn, "Internal fault classification in transformer windings using combination of discrete wavelet transforms and back-propagation neural networks," Int. J. Control. Autom. Syst., vol. 4, no. 3, pp. 365–371, 2006.
[113] S. K. Bhasker, P. K. Bera, V. Kumar, and M. Tripathy, "Differential protection of indirect symmetrical phase shift transformer using wavelet transform," 12th IEEE Int Conf. Electron. Energy, Environ. Commun. Comput. Control (E3-C3), INDICON 2015, pp. 1–6, 2016.
[114] S. K. Bhasker, P. K. Bera, V. Kumar, and M. Tripathy, ""Differential protection of indirect symmetrical phase shift transformer and internal faults classification using wavelet and ann," 12th IEEE Int. Conf. Electron. Energy, Environ. Commun. Comput. Control (E3-C3), INDICON 2015, pp. 3–8, 2016.
[115] P.K. Bera, R. Kumar, and C. Isik, "Identification of internal faults in indirect symmetrical phase shift transformers using ensemble learning," 2018 IEEE Int. Symp. Signal Process. Inf. Technol. ISSPIT 2018, vol. 2019–Janua, 2018.
[116] P. K. Bera, C. Isik, and V. Kumar, "Discrimination of Internal Faults and Other Transients in an Interconnected System with Power Transformers and Phase Angle Regulators," IEEE Syst. J., pp. 1–12, 2020.
[117] P. K. Bera and C. Isik, "A Data Mining Based Protection and Classification of Transients for Two-Core Symmetric Phase Angle Regulators," IEEE Access, vol. 9, pp. 72937–72948, 2021.

CHAPTER 3: Lamination faults in power transformer: experimental setup and data acquisition

This chapter describes all the pieces of equipment that have been used in this research to carry out the experimental tests. The different types of faults, specific faults, the test rig and the data acquisition, have also been described. Furthermore, the data collection procedure has been explained. It also presents the healthy and faulty signals of the power transformer to be used to detect the power transformer faults using the current signals and thermal images.

3.1 Introduction:

Power transformers are electric power systems' most expensive and strategic components [1]. It plays an essential role by interconnecting in every stage of the power transmission and distribution system[2]. The failure of a power transformer directly affects the reliability of the whole network[3]. Failures in transformers may cause disturbances to operating systems, resulting in unprepared outages and power delivery problems also can be costly [4]. Several works of literature have reported many power transformer failures in various electric utilities across the world CIGRÉ A2.37 working group[5].

Statistics show that 70–80% of the power transformers' damages arise from internal faults. It is begun with a slight discharge within the tank [6]. If this phenomenon is prolongs, the discharge currents can damage the transformer more, accelerating the insulation breakdown and finally completely damaging the transformers[7][8]. Internal faults can be divided into internal short circuit faults and incipient internal faults [9]. External faults occur due to external short circuits of the power system and improper utilizing conditions such as over flux, overload, and voltage [10].

The reason for these types of faults is the insulation failure and short circuits of conductors with different voltages. As a general rule, there are several reasons for the faults in transformers[11]. The percentage of faults in different parts of the power transformers is presented in [12] and [13]. On the other hand, according to CIGRÉ WG A2.37 and surveys from some locomotive maintenance departments in China the deteriorated and damaged insulation coatings of lamination layers (often caused by winding inter-turn arcing faults, manufacturing defects, and mechanical damages due to assemblage, regular maintenance, and abnormal vibration, etc.), as well as edge burrs (always produced in the processes of slitting, punching, and cutting) are the main origins of multipoint ground faults and interlaminar faults [14][15].

The cores of electrical machines are built from thin electrical steel laminations to reduce the eddy current loss [16]. Each lamination is coated on both sides with an inorganic coating. The process of punching and cutting the electrical steel causes mechanical stress, which deforms the sheet and deteriorates its magnetic properties[17]. Mechanical deformations shear causes burrs on the cut edges[18]. These burrs tend to cause insulation breakdown between the sheets resulting in electrical shorting between the stacked laminations. Thus it causes the potential for complete machine failure[19][20]. Some studies have shown a dramatic increase in the eddy current power loss when connecting core edges[21].

3.4 Sample preparation and fault generation

Faults were applied, and data were collected in multiple methods to investigate possible faults caused by the edge burrs, resulting in reduced power delivery, leading to the transformer's failure.

The transformer's failure is one problem that should get much attention because the transformer fails to function. It would cause some issues, such as unpleasant financial outcomes. That is one of the main reasons for regularly checking transformer operations to avoid failure by establishing preliminary diagnosis through artificial intelligence. Applying faults will be discussed in detail in the next chapter.

3.5 Condition monitoring scheme

The most important phase is training because it prepares the data and trains the classification algorithm (train model). In contrast, the prediction phase depends on the training phase for predicting the new incoming data (unseen data). The specified power transformer has been tested to check whether it works in a healthy or faulty condition. In case of healthy conditions, the overall signal condition should be identified by the machine learning algorithms and keep the transformer running safely. However, suppose the machine learning indicates that the power transformer has fault in any parts. In that case, maintenance action should be taken immediately, and repair or change of the transformer should be done in order to prevent catastrophic issues. Figure 3-1 illustrates the research framework and procedure followed to reach the main goal, which is classifying the PT faults accurately.

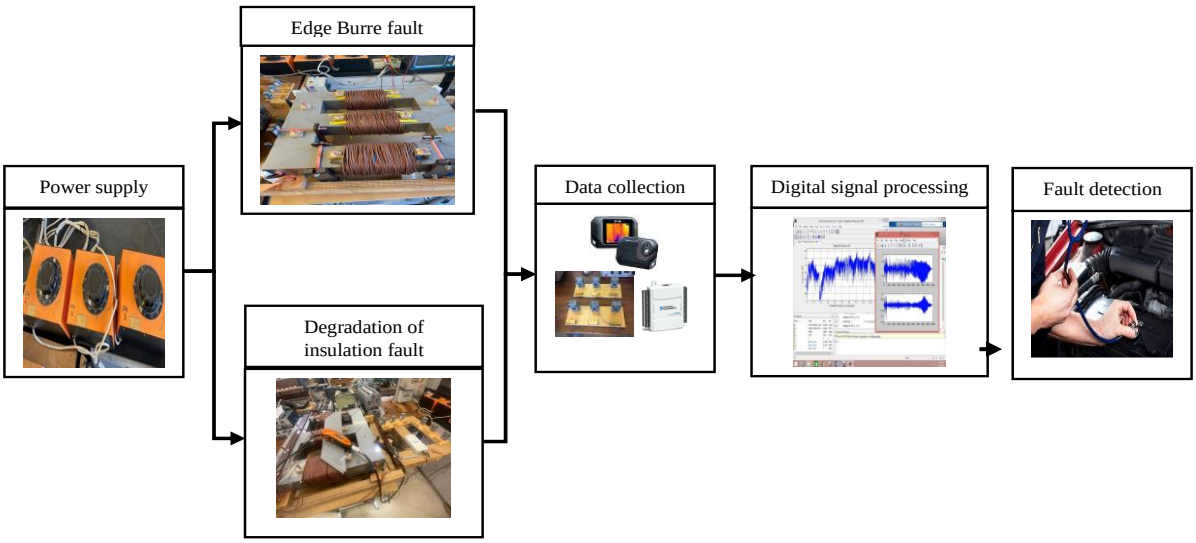

Figure 3- 1: Condition monitoring scheme

3.6 Test rig equipment and data collection

A testbed has been built and located at Cardiff University, School of Engineering, and it has been used to perform all the experimental tests for this work figure 3- 2.

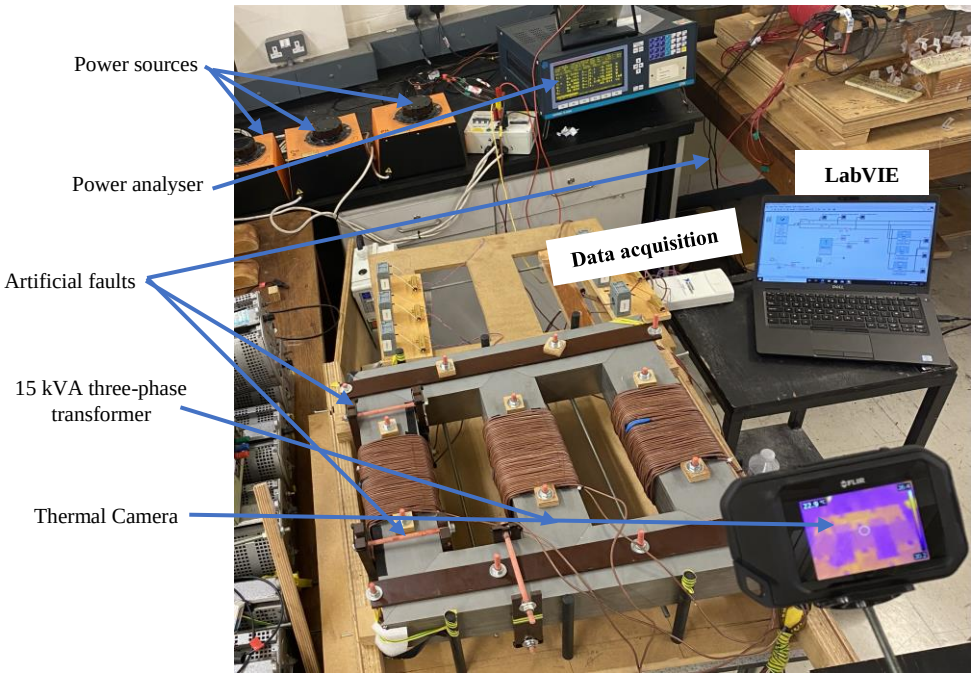

Figure 3- 2: Experimental setup

The experimental test rig in this research consists of as follows:

3.6.1 Three-phase power transformer core

This part describes the structures of transformer core models used in the data collection and investigation. And describes the procedure for the measurement of temperature and current.

Some of the transformer core models were assembled from three grades of electrical steel: conventional grain oriented (CGO), high permeability grain oriented (HGO), and laser scribed domain refined (LDR), using a similar procedure to the manufacturers with laminations 100 mm wide, 0.3 mm thick and density of 7650 kg/m3. The significant differences between these three materials are Magnetic flux density at a magnetic field of 800 A/m, 50 Hz, and core loss. They have the same texture, known as Goss texture or cube-on-edge texture [22]. Norman P Goss developed it in 1933 [23]. The HGO material has a more prominent grain size and lower core loss than the CGO. The LDR was developed to reduce core loss of the HGO through reducing the width of magnetic domains by means of laser irradiation [24].

Transformer cores are usually built up from a stack of grain-oriented electrical steel laminations. To minimise the core losses due to magnetic flux flow across the lamination grain orientation direction (rolling direction) at the joints, the ends of the lamination are cut at 45° to the rolling direction. The jointing is known as a mitred joint [25]. To stack the laminations, an overlap is needed. If the stack has only one step overlap (two different shapes of laminations), it is called a single step lap (SSL). If the stack has more than one step overlap (three or more different shapes of laminations), it is termed a multistep lap (MSL). There are two constructions of step overlap: cross step and longitudinal step as shown in Figure 3-3.

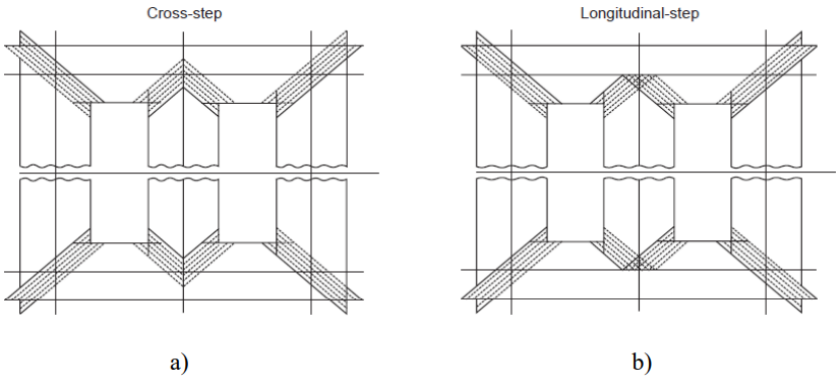

Figure 3-3:The mitred joint constructions (a) Cross-step construction (b) Longitudinal step construction [26]

Mitred joints can have single step lap or multistep lap. Each step can be assembled with one or more laminations depending on the size and cost of the cores [27]. figure 3-4 shows photographs of the multi-step lap and the single step lap configuration of corner joints

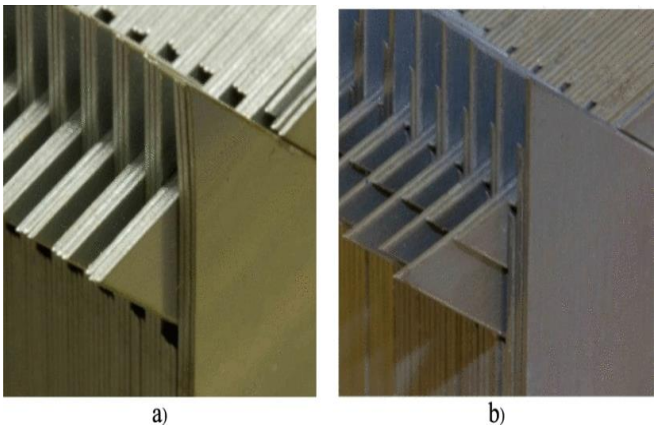

Figure 3- 4:Examples of corner joints. (a) Single step with three laminations per layer and 6 mm of length overlap shift. (b) Four-step MSL joint with one lamination per layer and 6 mm overlap length (these are not the values used in the investigation but are included for illustration) [25].

Three-phase power transformer core and its specification has been illustrated in figure 3- 5and table 3-1. The transformer core has windows 320 mm × 120 mm build up as well as the core width 540mm. And height 520mm. Primary and secondary windings were evenly wound along the limbs with 50 turns each of insulated copper wire, 1.5 mm^2. The numbers of turns were calculated from Faraday's induced voltage equation as shown in Eq.3-1.

$$\text{Number of turns} = \frac{V}{4.44.\ fBA_c}\ \text{turn} \qquad (3\text{-}1)$$

where (V) is induced voltage (*V*), (*f*) is the frequency (Hz), (A_c) core cross-sectional area (m^2), and (B) is the flux density.

The size of the conductor was calculated from the approximate apparent power per unit weight of the laminations, the core weight at a maximum magnetic flux density, and the approximate current density [26].

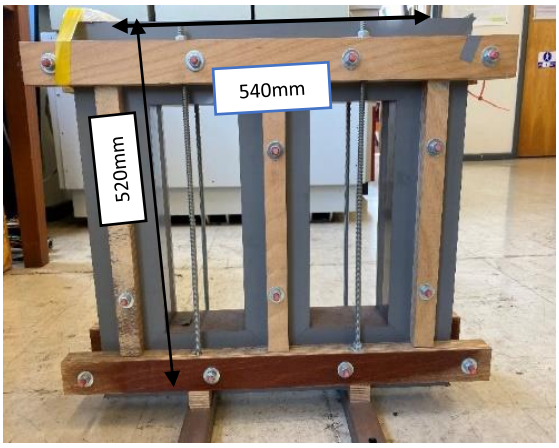

Figure 3- 5:Power transformer core used in the experimental work

Table 3- 1: Transformer specification

Core	3-ph MSL
Wight	115kg
Primary turns ration	50
Secondary turns ration	50
Frequency	50HZ
Width	540mm
Height	520mm

Figures 6, 7, and 8. show the dimensions of the yoke, outer limb, and middle limb of a three-phase, three-limb transformer core with a multistep lap configuration. Identical dimensions of the middle layer of the yoke and outer limb of the multistep lap configuration were used for the single-step lap configuration. Typical dimensions of the middle limb of the single-step lap configuration are shown in figure 3-9.

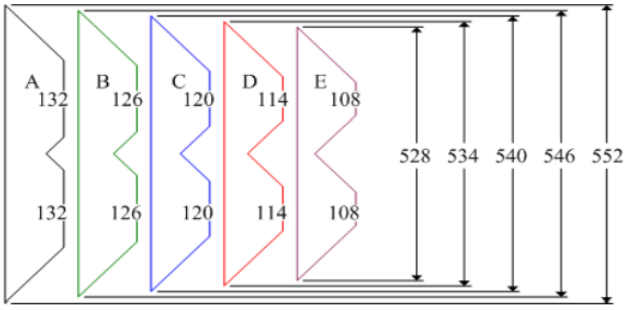

Figure 3- 6:Dimensions of the yoke of three phase three limb transformer core with multistep lap configuration [26]

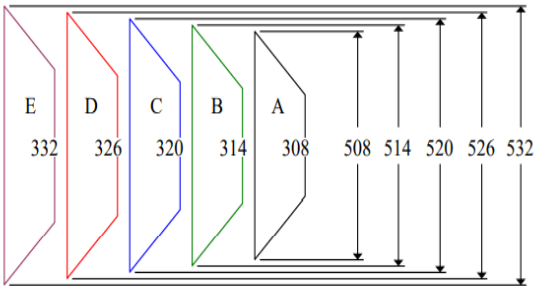

Figure 3- 7:Dimensions of the outer limb of three phase three limb transformer core with multistep lap configuration [26]

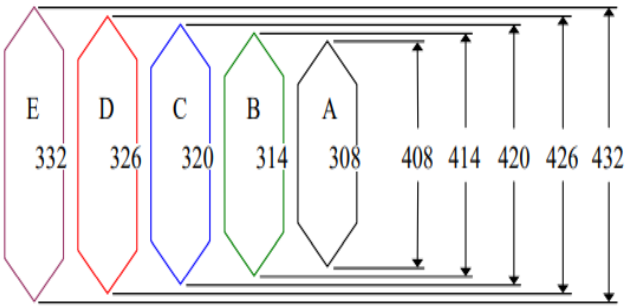

Figure 3- 8: Dimensions of the middle limb of three phase three limb transformer core with multistep lap configuration [26]

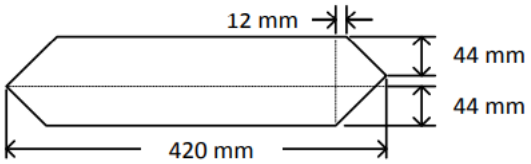

Figure 3- 9:Dimension of the middle limb of three phase three limb transformer core with single step lap configuration [26]

3.6.2 Data acquisition

The output data (signal) that are received from the current transformers will be connected to the National Instrument Data Acquisition card (NI-DAQ USB-6211, 16 AI multifunction I/O) figures 3-10.

Figure 3- 10:National Instrument Data Acquisition card (NI DAQ USB-6211 16 AI multifunction I/O)

3.6.3 LabView software

The LabView version 2019 software has been used to save the current data as “Excel” or “csv” file to be used for further processing figure 3-11.

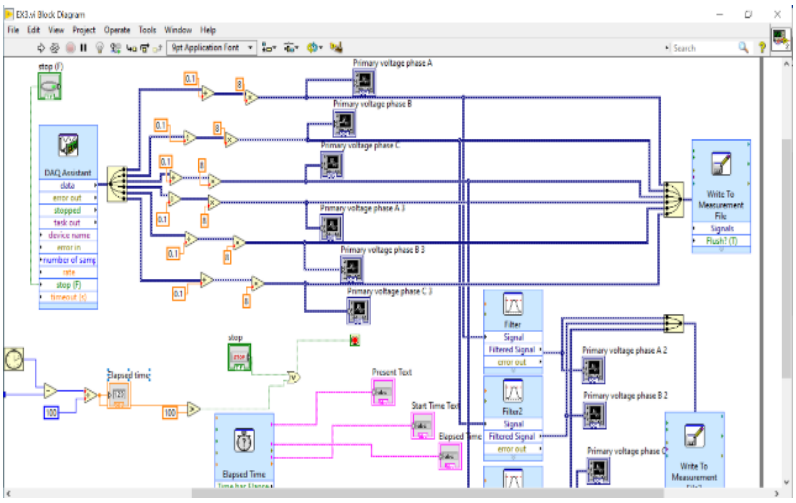

Figure 3- 11: LabView circuit for collecting the transformer current data

3.6.4 Current transformer

Figure 3-12 three current transformers have been used for core magnetising current reading (three phases); they are fitted to measure the input current. A power analyser was installed to measure the output current; the specification of the current transformer has been described in table 3-2. 50 Watts and 1Ω resistors have been inserted between current transformers and the DAQ to determine the actual individual current values by measuring voltages crossing them.

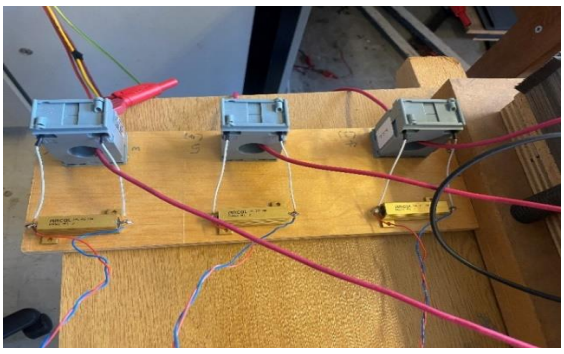

Figure 3-12: current transformers

Table 3- 2: Current transformer specification

Attribute	Value
Current Ratio	40:5
Maximum Cable Diameter	21mm
Overall, Height	65mm
Overall Width	45mm
Overall Depth	30mm
Minimum Temperature	-30°C
Maximum Temperature	+85°C

3.6.5 Power analyser

The measurement of no-load loss of the 15 kVA three phase-transformer in the project was made using a NORMA D6100 power analyser utilising the three-watt meter method, measuring all three voltages of the star-connected secondary windings, figure 3-13.

Figure 3- 13: NORMA D6100 power analyser

3.6.6 Thermal camera

FLIR C2 thermal camera has been used in this experiment in order to capture the thermal image of the healthy and faulty transformer cores. This camera has a resolution of 640× 480 pixels with an image frequency of 9Hz. The temperature within the range of − 10 to + 50 °C can be measured for an accuracy of + 2 to − 2 ℃ of reading. The Thermal camera is placed 0.8 m away from the transformer core. Six images for each scenario during the whole day and with a resolution of (80 × 60) are taken during the time intervals of 15 min for each flux density value. The specification of this camera has been illustrated in figure 3-14 below, and its specification in table 3-3.

Figure 3- 14: Thermal camera

Table 3- 3: Thermal camera specifications

1	Focal length	1.54 mm
2	Size (L*W*H)	124.46*78.74*12.44 mm
3	IR sensor	80*60 (4,800 measurement pixel)
4	Operating temperature range	-10°C to +50°C
5	Storage temperature range	-40°C to +70°C
6	Digital camera	640*480 pixel
7	Image frequency	9 Hz
8	Accuracy	±2°C
9	Thermal sensitivity	< 0.10°C

3.6.7 The clamp device

A clamping device shown in figure 3-15 was designed to fit the experimental core described in this section. It consists of two wooden plates that do not affect the magnetic field, secured by two bolts that enable a known pressure to be applied to the copper foil on both sides of a stack of laminations.

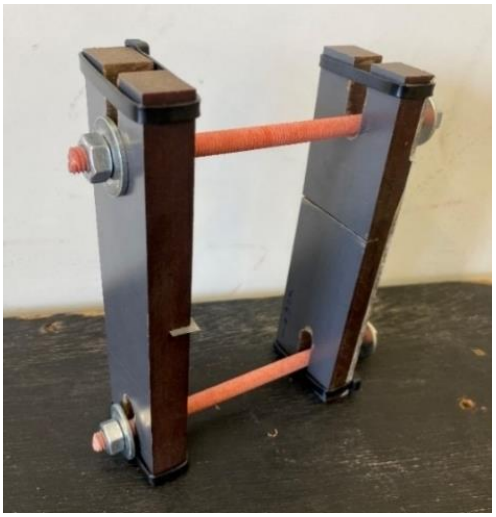

Figure 3-15: clamping device

The effect of the clamps without artificial burrs applied on the total specific power loss of the core was nearly no effect at 1.7 and 1.8T, as shown in figure 3-16[28].

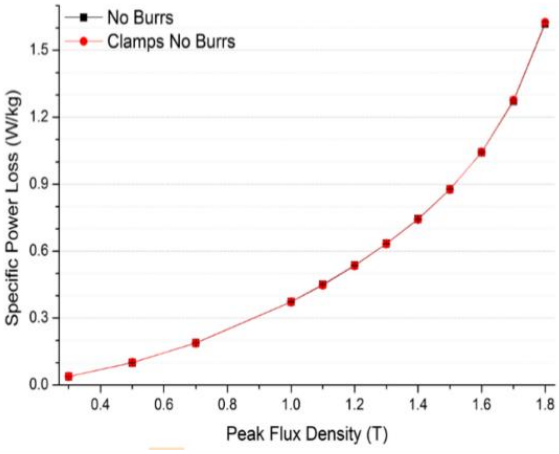

Figure 3-16: Effect of the clamping device on the total specific core losses of the three-phase transformer [28]

Grooves are drilled on the surface of the wooden block from the inner side opposite the iron core of the transformer in order to fix the conductive foil. The wooden blocks were later located on both sides of the stack and gradually tightened each of the four bolts in turn to ensure even pressure distribution. A torque value of 20 Nm on each bolt was chosen to ensure repeatable experimental results. A photo of the components of a single artificial burr application is shown in figure 3-17. The edge of the limb of the experimental transformer is shown on the left.

Figure 3-17: Artificial burr setup

The clamping device allows burrs between just two or three limitations to the experimental Core. A schematic of the application location is shown in figure 3-18. A burr of height H_B and length L_B is applied here to stack C of one of the transformer core limbs.

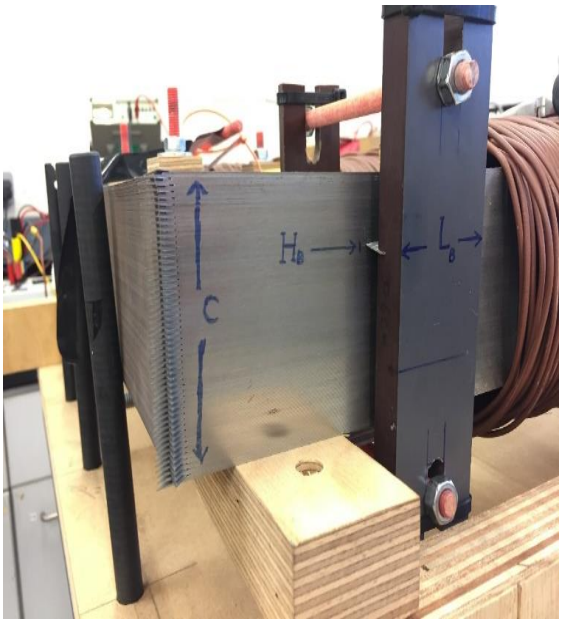

Figure 3- 18: Artificial burr placement and dimension labels

The clamping device allows for the application of artificial burrs in different configurations on the core layout. Two clamping devices can be placed on the same limb enabling the application of the short circuits not opposite each other but in a shifted configuration. The possible short-circuit placement is shown in figure 3-19, marked with red circles.

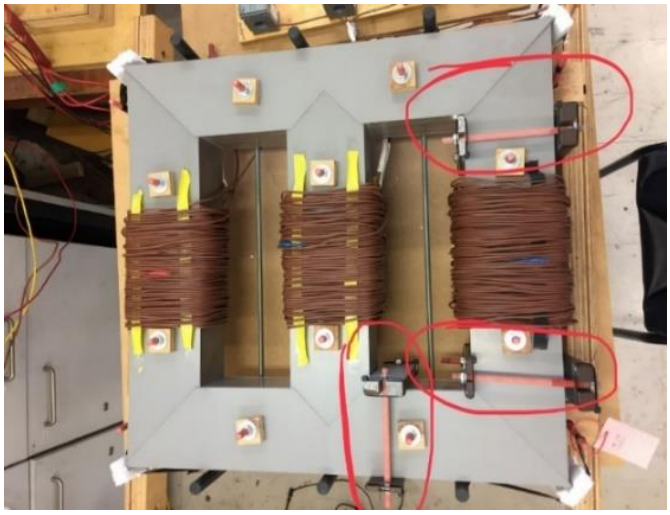

Figure 3- 19: Sketch of example artificial burr clamping placement configurations

3.6.8 Multi-functional rotary tool

A 135W Rotary Tool has been used for removing around 400mm^2 insulation material of the power transformer core laminations for the second fault for this thesis figure 20.

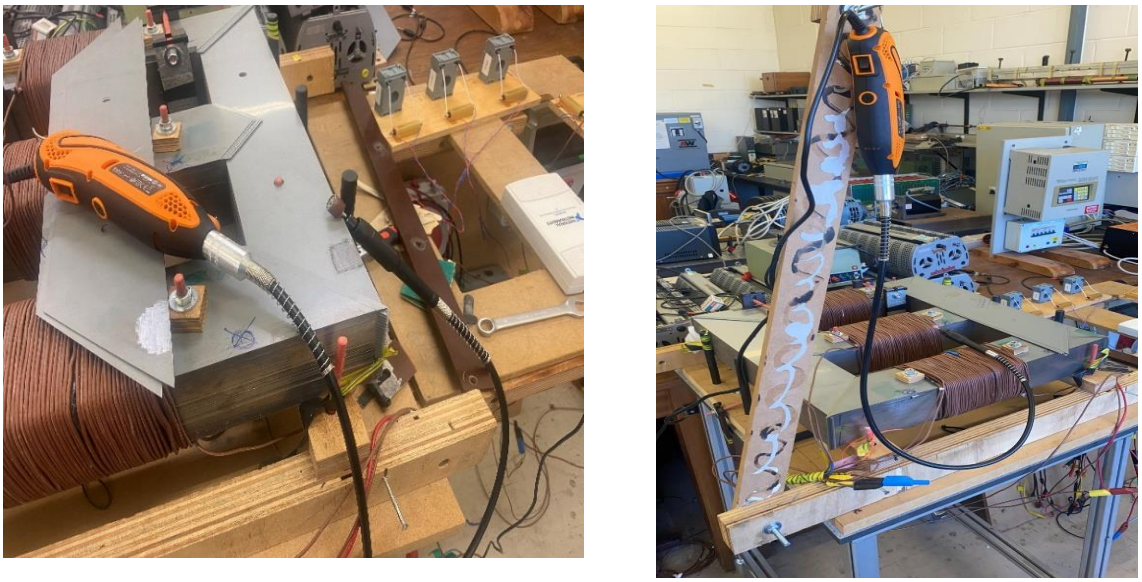

Figure 3- 20: Rotary Tool for laminations insulation removal

The data collection, analytical procedure, and results obtained from the power transformer faults are described in the next chapter.

3.7 Summary

In this chapter, the proposed experimental setup of power transformer core data collection has been described and explained in detail. This fault-test system has been developed in the Wolfson Centre for Magnetics for such testing. This system helps measure different electromagnetic parameters and properties (i.e., voltage, current, flux density, etc.). The next chapter will describe the proposed feature extraction methods from the current signal and thermal image using LabView–MATLAB software.

3.8 References

[1] R. Monošík, M. Streďanský, and E. Šturdík, "Failures, monitoring, and new trends of power transformers," vol. 5, no. 1, pp. 109–120, 2012.

[2] N. U. A. Wardani, A. P. Purnomoadi, H. I. Septiani, I. Arifianto, and B. Cahyono, "Condition assessment of 500/150 kV power transformer based on condition-based maintenance," *Proc. 2011 Int. Conf. Electr. Eng. Informatics, ICEEI 2011*, no. July, pp. 14–17, 2011.

[3] M. Abdelfatah, M. El-Shimy, and H. M. Ismail, "Outage data analysis of utility power transformers based on outage reports during 2002-2009," *Int. J. Electr. Power Energy Syst.*, vol. 47, no. 1, pp. 41–51, 2013.

[4] V. Mijailovic, "Probabilistic model for planning keeping of power transformer spare components with general repair time distribution," *Electr. Power Syst. Res.*, vol. 97, pp. 109–115, 2013.

[5] H. L. A Bossi, JE Dind, JM Frisson, U Khoudiakov, "An international survey on failures in large power transformers," *CIGRE Working Group 12.05*, 2021. [Online]. Available: https://e-cigre.org/publication/ELT_088_1-an-international-survey-on-failures-in-large-power-transformers.

[6] R. Murugan and R. Ramasamy, "Failure analysis of power transformer for effective maintenance planning in electric utilities," *Eng. Fail. Anal.*, vol. 55, pp. 182–192, 2015.

[7] O. Ozgonenel, E. Kilic, D. Thomas, and A. E. Ozdemir, "Identification of transformer internal faults by using an RBF network based on dynamical principal component analysis," *POWERENG 2007 - Int. Conf. Power Eng. - Energy Electr. Drives Proc.*, pp. 719–724, 2007.

[8] G. D. González, J. G. A. Fernández, and P. A. Arboleya, "Diagnosis of a turn-to-turn short circuit in power transformers by means of zero sequence current analysis," *Electr. Power Syst. Res.*, vol. 69, no. 2–3, pp. 321–329, 2004.

[9] C. Ciulavu and E. Helerea, "Power transformer incipient faults monitoring," *Ann Univ Craiova-Electr Eng Ser*, vol. 32, no. 32, pp. 72–77, 2008.

[10] J. Faiz and R. Heydarabadi, "Diagnosing power transformers faults," *Russ. Electr. Eng.*, vol. 85, no. 12, pp. 785–793, 2014.

[11] Y. Hong, W. Q. Meeker, and J. D. McCalley, "Prediction of remaining life of power transformers based on left truncated and right censored lifetime data," *Ann. Appl. Stat.*, vol. 3, no. 2, pp. 857–879, 2009.

[12] M. Koch and M. Kruger, "A new method for on-line monitoring of bushings and partial discharges of power transformers," *Proc. 2012 IEEE Int. Conf. Cond. Monit. Diagnosis, C. 2012*, no. July 2014, pp. 1205–1208, 2012.

[13] R. Monošík, M. Streďanský, and E. Šturdík, "Failures, Monitoring and New Trends of Power Transformers," *IEEE*, vol. 5, no. 1, pp. 109–120, 2012.

[14] S. Tenbohlen, J. Jagers, and F. Vahidi, "Standardized survey of transformer reliability: On behalf of CIGRE WG A2.37," *Proc. Int. Symp. Electr. Insul. Mater.*, vol. 2, no. December, pp. 593–596, 2017.

[15] Q. Fu, J. Zhu, Z. H. Mao, G. Zhang, and T. Chen, "Online Condition Monitoring of Onboard Traction Transformer Core Based on Core-Loss Calculation Model," *IEEE Trans. Ind. Electron.*, vol. 65, no. 4, pp. 3499–3508, 2018.

[16] S. Bin Lee, G. B. Kliman, M. R. Shah, W. T. Mall, N. K. Nair, and R. M. Lusted, "An advanced technique for detecting inter-laminar stator core faults in large electric machines," *IEEE Trans. Ind. Appl.*, vol. 41, no. 5, pp. 1185–1193, 2005.

[17] A. Kedous-Lebouc, B. Cornut, J. C. Perrier, P. Manfé, and T. Chevalier, "Punching influence on magnetic properties of the stator teeth of an induction motor," *J. Magn. Magn. Mater.*, vol. 254–255, pp. 124–126, 2003.

[18] P. Handgruber, A. Stermecki, O. Biro, and G. Ofnery, "Evaluation of interlaminar eddy currents in induction machines," *IECON Proc. (Industrial Electron. Conf.*, pp. 2792–2797, 2013.

[19] A. S. A. Eldieb, "Evaluation of loss generated by edge- burrs in electrical steelNo Title," cardiff university, 2016.

[20] M. Bigdeli, M. Vakilian, and E. Rahimpour, "Transformer winding faults classification based on transfer function analysis by support vector machine," *IET Electr. Power Appl.*, vol. 6, no. 5, pp. 268–276, 2012.

[21] R. Mazurek, H. Hamzehbahmani, A. J. Moses, P. I. Anderson, F. J. Anayi, and T. Belgrand, "Effect of artificial burrs on local power loss in a three-phase transformer core," *IEEE Trans. Magn.*, vol. 48, no. 4, pp. 1653–1656, 2012.

[22] S. Tabrizi, "study of effective methods of characterisation of magnetostriction and its fundamental effect on transformer core noise shervin tabrizi," no. December 2013.

[23] C. D. G. B. D. Cullity, *Introduction to Magnetic Materials*, 2nd ed. NEW JERSEY: SIMULTANEOUSLY IN CANADA, 2011.

[24] M. Bereznicki, "The influence of skin effect on the accuracy of eddy current energy loss calculation in electrical steel sheets," *2015 Sel. Probl. Electr. Eng. Electron. WZEE 2015*, no. 2, pp. 2–5, 2016.

[25] A. J. Moses, P. I. Anderson, and T. Phophongviwat, "Localized Surface Vibration and Acoustic Noise Emitted from Laboratory-Scale Transformer Cores Assembled from Grain-Oriented Electrical Steel," *IEEE Trans. Magn.*, vol. 52, no. 10, pp. 1–15, 2016.

[26] T. Phophongviwat, "Investigation of the Influence of Magnetostriction and Magnetic Forces on Transformer Core Noise and Vibration," no. August 2013.

[27] H. Ahmadi, B. Vahidi, and A. Foroughi Nematollahi, "A simple method to detect internal and external short-circuit faults, classify and locate different internal faults in transformers," *Electr. Eng.*, 2020.

[28] R. Mazurek, "Effects of burrs on a three-phase transformer core including local loss, total loss and flux distribution," no. October 2012.

CHAPTER 4: Lamination faults in power transformer: results interpretation using signal processing techniques applied to current signal.

The chapter reports on collected data for a faulty power transformer core. The data is analyzed to detect, diagnose, and assess the severity of seeded faults. The experiment uses a 15 kVA three-phase power transformer and considers different scenarios, such as the affected region and number of short-circuited laminations. The results show that the transformer current increases with the number of short-circuits for both faults (edge burr and lamination insulation faults), which is related to the flux density and can indicate the severity of the faults.

4.1 Introduction

Edge burrs from cutting and punching steel and degraded lamination insulation can cause interlaminar short circuits in power transformer cores. Analysing these faults improves understanding of their impact on the transformer's reliability and performance. Power transformers are key components in electrical energy transmission and distribution systems. [1], [2].

Regarding their importance in the energy systems, reliable and safe operation of the transformers is of great significance to guarantee a long lifetime [3]. Power transformers have a significant impact on the cost of power transmission and distribution, and they should last several decades. Monitoring their condition is important. [4]– [6]. Health conditions can be assessed through the state of its insulation systems, such as the insulating oil [7] and that between windings or inter-laminations [8]. Quality control tests are necessary for testing filled transformers and reliable monitoring and diagnostic techniques are required to detect faults and avoid catastrophic failures, improving equipment reliability through an efficient predictive maintenance program [9], [10]. The operation status of a transformer has a direct impact on the safety of the power system due to its significant influence [11].

Power transformers can be affected by numerous issues authors in [12] analysed data on 343 power transformer failures occurring in the voltage range of 33–400 kV. As reported in their work, insulation problems were the most common cause of failure, covering 36.74% of failures in power transformers. Among many other failures, winding, bushings, on-load tap changer, and core failures are the most pertinent. The core failure can be identified as a primary failure regarding the laminations and interlaminations issues [13].

Transformer cores are made of many thin electrical steel laminations to minimize eddy current losses and increase efficiency. The core laminations may be affected during the processes of building the core [14]– [16]. For instance, the process of punching and cutting the electrical steel can deform the sheet shape and deteriorate its magnetic properties [16]. several works have been carried out to study these faults experimentally (e.g., [17]– [19]). Other authors tried to study the impact of edge burrs and interlaminar short-circuits by computer simulations (e.g, [20]– [22]). Such as FEM models [15]. Iron loss models have also been proposed to help develop a more accurate design of high-speed motors, including the punching effects (e.g., [23]).

In this thesis, experiments have been conducted to show the impact of short circuits in transformer laminations from edge burrs and insulation degradation. A fault-testing system has been developed using a 15 kVA three-phase power transformer. Different fault scenarios, such as affected region area and short-circuited laminations, were considered. The current at no-load was recorded for various flux densities (0.5 to 1.8 T).

The following section explains the experiment setup used to study the impact of lamination faults in power transformers. It describes the data collection system and process. Section 4.3 shows the process used to create edge burrs and insulation degradation faults. Results for each type of fault are presented and discussed in Section 4.5. A comparison between both faults is given and conclusions are summarized in the last section.

4.2 Experimental setup and sample preparation

This section explains the data collection system and process used to investigate the impact of lamination faults in power transformers. A fault-test system has been developed in the Cardiff School of Engineering for such type of testing. This system helps measure different electromagnetic parameters and properties (i.e., voltage, current, flux density, etc.). Figures 4-1a and 4-1b show a photo of the experimental setup and a schematic diagram of the measurement system, respectively.

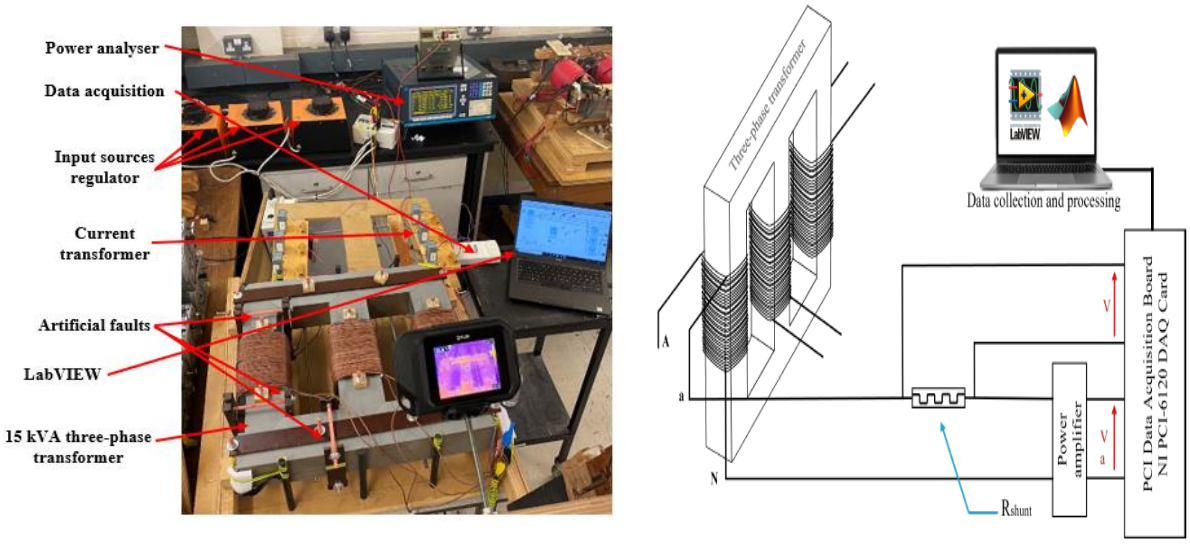

(a) Experimental setup (b) Per phase schematic diagram

Figure 4- 1: Experimental setup and a schematic diagram for the laminations faults analysis

In fact, the test rig consists of several components, including a three-phase power transformer of 15 kVA, current transformers (with shunt-resistance), and a data acquisition system connected to a laptop for data analyses and signal processing in LabView–MATLAB software environment. Clamps are designed to be used for fixation during the application of faults and a Rotary Tool used for removing around 400mm^2 insulation material of the power transformer core laminations for the second fault for this work. Flux densities are calculated from the measured voltages and currents using the power analyser connected to the power transformer. It should be noted that a thermal camera is used in the experimental test, but its results are not within the scope of this chapter.

It is well known that the transformer's total loss is composed of ohmic loss, iron loss and additional loss. According to [24], the core-loss component is usually much larger in magnitude than the other two components in transformers with a magnetic core. Indeed, this investigation mainly considers iron loss since both types of faults are directly applied to the transformer core (laminations). The magnitude of the iron loss is basically independent of the magnitude of the load, which means that the no-load loss is equal to the iron loss at the load, but it is the case at the nominal voltage. The no-load current measurements can express no-load loss or iron loss. For this reason, a transformer no-load test has been carried out by applying the nominal voltage (220 V) of the primary set of transformer coils when the secondary coils are open.

As shown in this figure, the clamping device consists of two wooden plates secured by two plastic bolts, enabling good pressure on the copper foil on both sides of a stack of laminations, The pressure required for the clamping device is approximately 20 N/m. Both wood and plastic

are transparent to electromagnetic waves. Thus, their effects on the experimental results can be neglected. In fact, several works have neglected the effect of the clamping device (e.g., [17]).

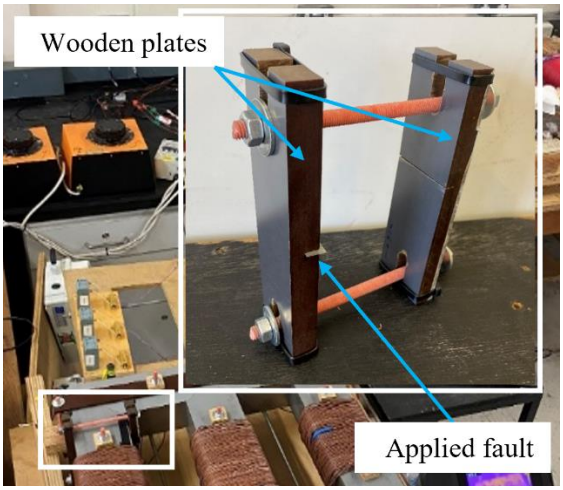

Figure 4-2: Clamping device used for the laminations fault fixation

4.3 Artificial lamination faults

Mechanical deformations shear causes burrs on the cut edges, usually followed by the process of punching and cutting the electrical steel, as represented in figure 4-3. These deformations may affect the performance of the transformer and cause power losses. In this investigation, two types of faults have been considered in the transformer core. These faults are the edge burrs and insulation deterioration between laminations, which are the most commonly appeared faults in transformers. The forthcoming parts explain each fault individually.

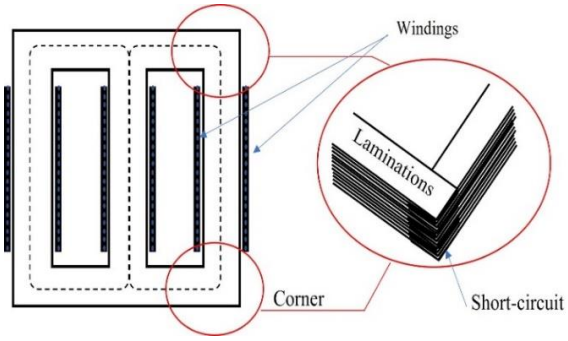

Figure 4- 3: Representation of edge burrs faults in three-phase power transformer - laminations short-circuit

In order to study the impact of the edge burr fault, the healthy operation mode is firstly investigated. In this mode, voltage and current in the three phases have been recorded for different flux densities to guarantee satisfactory results. Flux densities of 0.5, 0.8, 1.0, 1.5, 1.7 and 1.8 T have been considered. The measured results are re-examined three times to ensure

reliable and feasible quality. For instance, a whole day is allotted to take the data of each fault separately in order to leave the transformer core enough time to cool down.

4.3.1 Edge burr fault

To simulate the edge burr fault, a short-circuit has been created between laminations of the transformer core. According to the number of sheets in short-circuit (affected area), four scenarios have been selected for this type of fault. Figure 4-4 shows the four considered faults (From scenarios 1 to 4) and indicates the affected area of the transformer core. In the first scenario of the edge burr fault shown in figure4-4(a), a metal chip has been inserted to create a short circuit between two adjacent laminations out of 520 in the transformer core. The coverage area of the short circuit is 45 mm in length and 0.5 mm in thickness (i.e., 22.5 mm^2), which is guaranteed two laminations be short-circuited at a certain location and then increase the number of places.

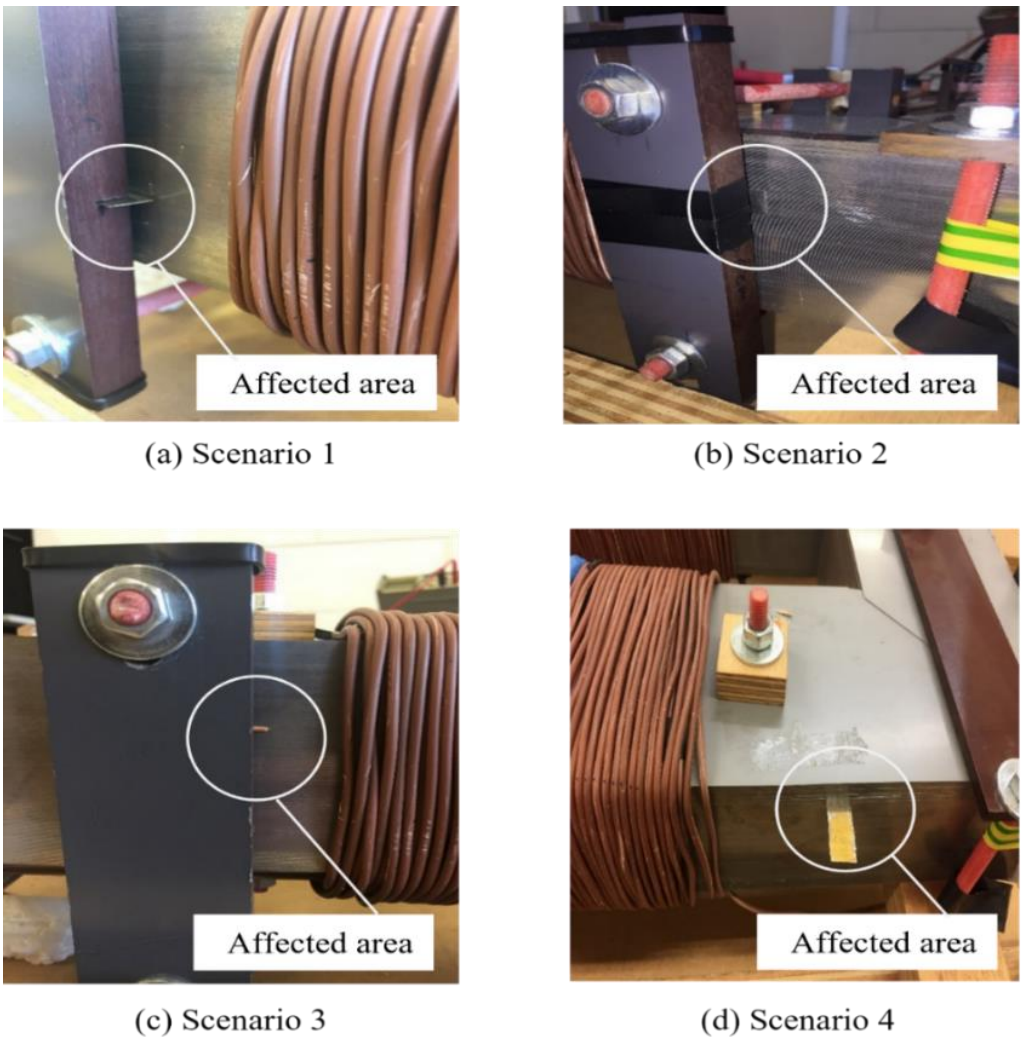

(a) Scenario 1 (b) Scenario 2

(c) Scenario 3 (d) Scenario 4

Figure 4-4: Artificial edge burr lamination faults (a) scenario 1, (b) scenario 2, (c) scenario 3 and (d) scenario 4

In addition, a 9.7 mm chip is also used to increase the number of short-circuits between laminations up to 33. As demonstrated in figure 4-4(b), the coverage area in this scenario is 45 mm in length and 10 mm in thickness (i.e., 450 mm^2). In figure 4-4(c), 1.3 mm copper wire has been used to create a short-circuit between 4 laminations, covering an area of 58 mm^2: 45 mm length and 1.3 mm thickness. The fourth scenario of faults is shown in Figure 4(d). In this scenario, a short-circuit between 2 laminations has been created, which covers an area of 135 mm^2 (9 mm*15 mm).

For the edge burrs fault, the stage of collecting data was without applying any faults (Healthy) when the flux density was 0.5 T, -1.8 T to guarantee satisfactory results. Afterward, the faults were introduced by implementing faults in two and three places with different scenarios in many positions across the transformer core see figure 4-5. It will be explained in detail in the next chapter. The clamping device allows for securing burrs of various sizes to the experimental core. A schematic of the application location as well as the clamping device allows for the application of artificial burrs in several different configurations on the core layout. The possible short circuit placement and the locations of the faults are marked with blue circles and crosses to avoid any similarities in locations, as it's expected that the behaviour of the flux on those locations are the same.

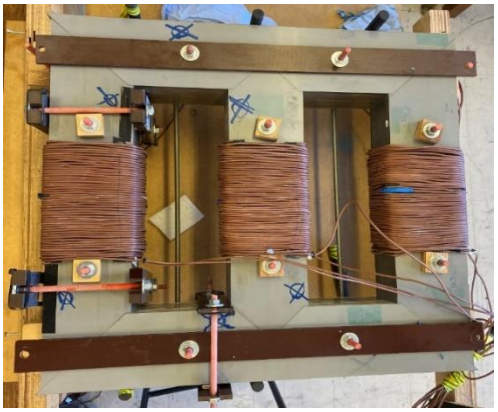

Figure 4-5: Locations of the Edge Burrs faults

4.3.2 Lamination insulation fault

Thin electrical steel laminations form the cores of electrical machines to reduce the eddy current loss for high-efficiency operation. Each lamination is coated on both sides with an inorganic coating. This thin layer is usually 1 to 3 µm in thickness, used to prevent any direct electrical contact between laminations. Degradation of the inter-laminar insulation in the transformer core can occur from a number of sources, such as the aging of lamination coating, mechanical

damage from external objects, and/or overheating of laminations in the region of a winding failure. In order to study the impact of such types of lamination faults, the experiment involved applying these faults and then gathering data to examine the transformer state in faults from insulation breakdowns see figure 4-6.

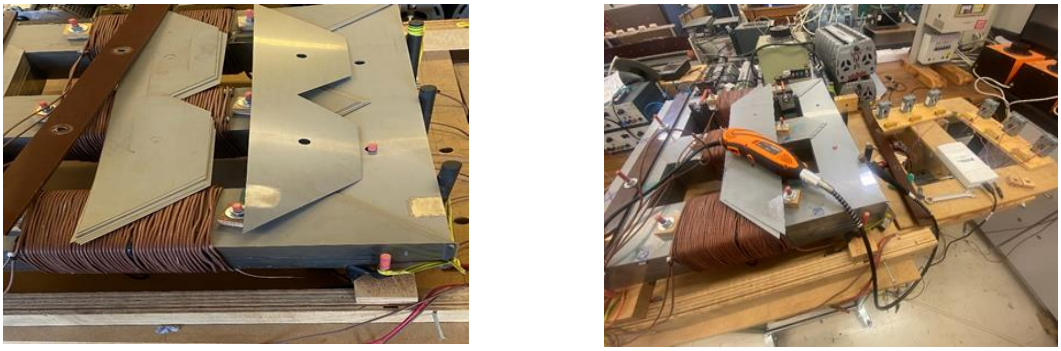

Figure 4-6: Experimental setup used for the laminations fault analysis

Insulation faults have been prepared by removing the insulation on the corresponding laminations and putting a copper chip between them to maintain connectivity figure 4-6. Damaged insulation faults are created on the two opposing sides of a selected number of transformer core laminations. Short-circuit of 2, 6, 8, and 12 core laminations are considered for flux density of 0.5, 1.0, 1.5, 1.7, and 1.8 T. Damage has been generated by removing around 40 mm^2 of the insulation material by applying rotary equipment. It is worth noting that the faults are produced at different locations in the transformer core. Figure 4-7 shows a total of 5 sites on the core of the transformer have been selected as described below:

- The central area of the middle limb
- Joint connecting the right-hand most limb to the yoke
- Joint connecting the central limb to the central yoke
- Upper or lower yoke
- Middle area of the limb on the left or right.

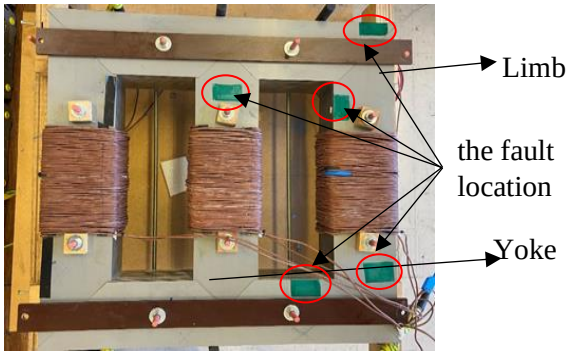

Figure 4-7: faults applied to sites

4.4 Data analysis (current signals)

Digital signal processing has been applied to extract the signal information, as the signal is not helpful for recognizing the fault.

"In this section, popular signal processing techniques are used to extract important features from the signal for fault classification. Not all feature extraction techniques will be utilized, only the one that gives the best results will be applied". Figure 4-8 shows the Data analysis diagram.

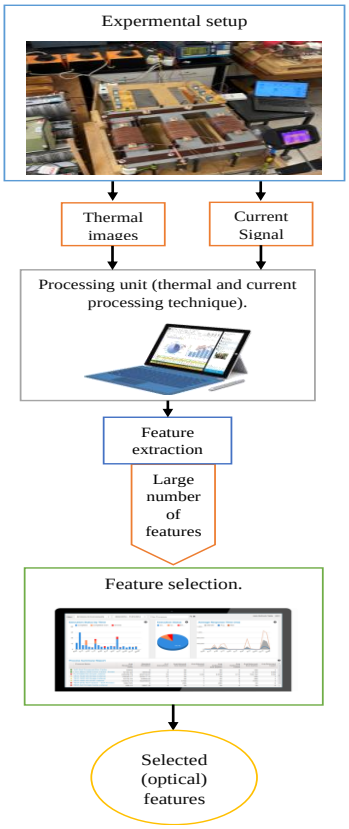

Figure 4- 8: Data analysis diagram

4.4.1 Data machine learning

Machine learning heavily relies on data, using correct terminology is crucial. In ML, data is viewed from two perspectives: statistical and computer science. The statistical perspective views data as a function (f) that the algorithm tries to learn, relating input variables to the predicted output. In computer science, a row of data represents an entity or observation about it, with columns referred to as attributes and the row referred to as an instance [25].

4.4.2 Feature extraction

The differential currents used to extract the features are time-series signals which can be differentiated in many ways. The resemblance between time-series data points can be established with commonly used Euclidean distance measure or with Dynamic Time Warping in the case of time-series of variable length [26]. The differential currents from a distinct fault type can also be differentiated from the rest using first and second-order features of mean, standard deviation, and Skewness-Kurtosis [27]. Global characteristics of time-series described by classical and statistical features like trend, seasonality, periodicity, autocorrelation, skewness, kurtosis, nonlinearity, chaos, and self-similarity were used in [28]. Wirth et al. [29] further extended this approach to multivariate time-series signals. Kumar et *al*. [30][31] used a variety of time and frequency domain features to distinguish binary classes. A number of feature extraction techniques for current signal and thermal images have been used in this project.

4.4.3 Extraction using the FFT technique

The Fast Fourier Transform (FFT) Analyzer app allows you to perform Fourier analysis of simulation data and provides access to all the simulation data that are defined as structure-with-time variables in the workspace. The app displays the spectrum as a bar graph or as a list in percentages relative to a base value or to the DC component of the signal[32].

This section extracts features from the differential currents of the 3-phases, covering some basic and some complex time series features like minimal, maximal, median, quantile, and average values. The FFT technique was applied to the measured current for healthy and faulty operation modes. The strongly related to the type of transformer fault features are fundamental, average, computed total harmonic distortion (THD) of signals extracted by the FFT technique. Figure 4-9 shows the frequency spectrum of the current waveform in the frequency band of 0-500Hz. This figure is for the power transformer core faulty details. The coefficients for two and three place faulty transformer cores for only one scenario with the no-load condition. (Edge burrs current signals at 1.7T as an example). For full example see appendix 2.

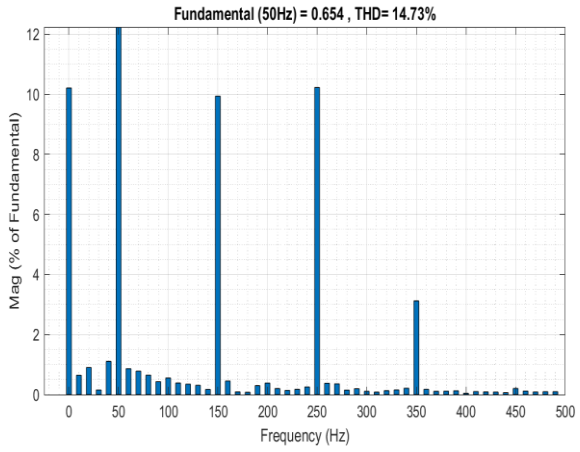

Faulty 2 places

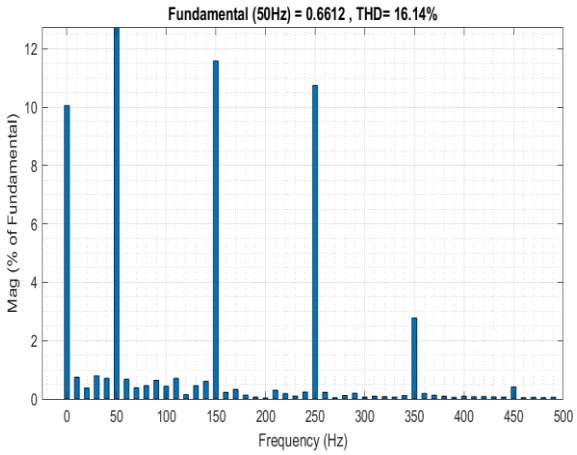

Faulty 3 places

Figure 4- 9: the frequency spectrum of the current waveform in the frequency band of 0-500Hz by the FFT technique

4.4.4 Wavelet transforms analysis

Wavelet transforms mathematical tools for analyzing data where features vary over different scales. For signals, features can be frequencies varying over time, transients, or slowly varying trends of signals. For images, features include edges and textures. Wavelet transforms were primarily created to address the limitations of the Fourier transform[33][34]. Table 4-1 illustrates a brief comparison between the performance of continuous wavelet transform (CWT) and Discrete wavelets transform (DWT).

Table 4-1: Comparison of the performance of CWT and DWT [35]

No	CWT	DWT
1	It uses exponential scales with a base smaller than 2	It uses exponential scales with the base equal to 2.
2	Large computational resources are required to compute the CWT.	Less computational resources are required to compute the DWT
3	It is a shift-invariant	It is not shift-invariant.
4	It is highly redundant transform.	It is also redundant but less than the CWT.
5	It is an orthonormal transform.	It is an orthonormal vector.
6	The outputs are not down sample but not better than DWT.	The outputs are down-sampled but better than CWT.
7	The inverse of CWT could be implemented, but usually, the signal reconstruction is not perfect.	It provides perfect signal reconstruction upon inversion, which means that the DWT of signal coefficients could be used to synthesise and exact the reproduction of the signal with numerical precision.

4.4.5 Plot the results of CWT (continuous wavelet transform)

The CWT is analysed into two parameters; scaled and translated. The formula represents one function below (mw x, y (s)) and mother wavelet mw(s)

$$mw_{x,w} = \frac{1}{\sqrt{|x|}}\, mw\left(\frac{s-y}{x}\right) \quad (4\text{-}1)$$

This equation appears to be a simplified form of the continuous wavelet transform (CWT) equation.

The variable "x" is the translation variable, and "w" is the scale variable. These two variables determine the position and size of the wavelet function used in the CWT. The term "mw" likely represents the mother wavelet function, which is a basic waveform that is used to generate the wavelet functions used in the CWT. The mother wavelet function is scaled and translated by the variables x and w, respectively. The term "|x|" represents the absolute value of x, meaning it removes any negative sign and provides the magnitude only. The term "(S-Y)/x" could represent the ratio of the difference between two signal values (S and Y) and the translation variable x. This term could be used to determine the local variation in the signal being analyzed.

$$mw_{x,w} = \frac{1}{\sqrt{|2^j|}}\, mw\left(2^{-j}s - k\right) \quad (4\text{-}2)$$

The variable "x" is the translation variable, and "w" is the scale variable. These two variables determine the position and size of the wavelet function used in the CWT. The term "mw" represents the mother wavelet function, which is a basic waveform that is used to generate the wavelet functions used in the CWT. The mother wavelet function is scaled and translated by the variables x and w, respectively. The term "|2^j |" represents the absolute value of 2 raised to the power of j, meaning it removes any negative sign and provides the magnitude only. The term "2^(-j) s-k" represent the ratio of the difference between the scale factor 2 raised to the power of negative j and a constant k, with the signal value "s". This term could be used to determine the local variation in the signal being analyzed.

The same as the Fourier Transform (FT), which obtains the correlation coefficients between the analysed and sinusoidal one. The WT obtains the correlation coefficients between the signal and an orthonormal function, which is called a “wavelet function”. The CWT allows the signals to be analysed through the correlation coefficients of that signals instead of using the whole signal information. The mathematical formula for determining CWT is shown below:

$$W_x(a,b;\psi) = a^{-\frac{1}{2}} \int x(t)\bar{\psi} * \left(\frac{t-b}{a}\right) dt \quad (4\text{-}3)$$

Where a is the scale parameter b is the time parameter $\psi(t)$is an analysing wavelet, And $\bar{\psi}$ is the complex conjugate of ψ [34]

CWT is one of the best tools available to detect signal singularity, carried out with the local maxima lines[31]. It has been applied for diagnosing the notched rotor [37], the CWT coefficient has been used as input into the Artificial Neural Network (ANN), and it has been investigated to show that their system has been able to detect combined faults, shaft cracks, and unbalance [38]. The use of CWT for diagnosis of the fault in the rotating machinery is still relatively rare; this is since the visual interpretation of wavelet results is often difficult. Thus, more efforts have been made to extract the best signal features for analysing the residual wavelet scalogram[39].

Figure 4-10 shows the results obtained using the continuous wavelet transforms (CWT) to analyse modulated signals. The signal's frequency is approximately 50 Hz the flux 1.7T as an example. The time-frequency analysis gives new information which cannot be inferred from the original time series. It can be seen that the minimum magnitude pole point of the magnitude scalogram is around 0.55 for some faults and increases significantly to about 0.8, while in the healthy stage is 0.65.

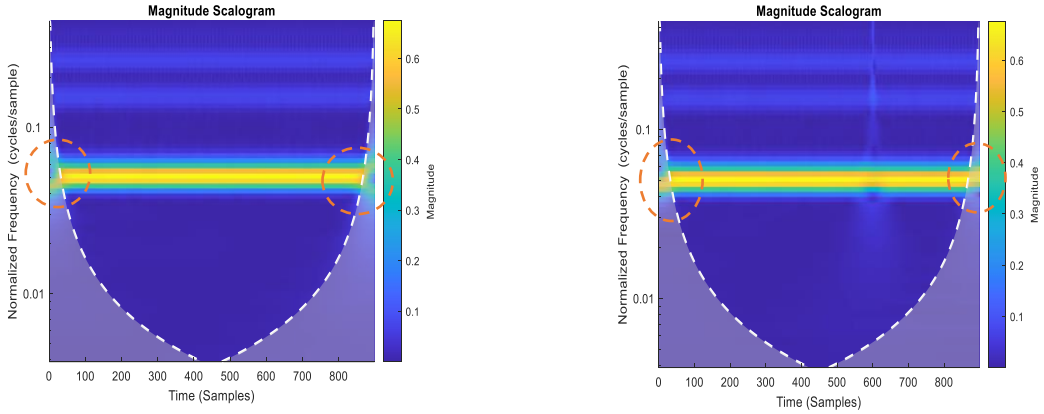

F3.3places F3.2places

Figure 4- 10: The continuous wavelet transforms (CWT) results

4.4.6 Discrete wavelets transform (DWT)

The DWT has been widely used for analysing the machine's signal (thermal image, current, and vibration signals) due to its excellent decorrelation property. It has been used as a transform stage in many modern image and video compression systems[40][41].

In this work, the DWT technique has been adopted for extracting the best features from the power transformer current signal among the various DWT techniques.

The wavelet toolbox in MATLAB software (version R2021a) has been used for analysing the current signature signal. After preparing and selecting the DWT parameters, the DWT is now ready for analysing the power transformer core current signal for extracting the information to discriminate between the transformer faults.

A one-dimensional discreet wavelet analysis tool has been used for analysing the current signal. The procedure for analysing these signals is as follows:

- Import the current signals.
- Apply the DWT to extract the signal features.
- Save the extracted features for further processing.
- Repeat the process for all faulty signals.

Figure 4-11 illustrates the power transformer core faculty details coefficients based on db7 at five levels. It demonstrates the d_1, d_2, and d_5 for two and three places faulty transformer core for only one scenario with no load condition (Edge Burrs) current signals at 1.7T as an example. By looking at this figure, the difference between the two and three places of faulty signals is obvious, and the behaviour of the current signal is completely different in the shape and range of the signal. Thus, the coefficients will be very strong for the classification system to distinguish between the power transformer core faults. The complete figures and description are available in appendix 4.

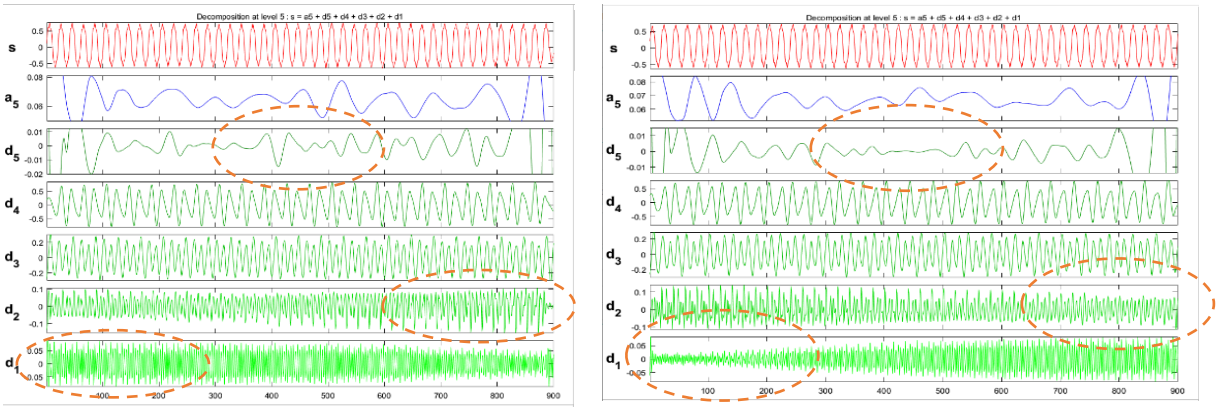

Faulty 2 places Faulty 3 places

Figure 4- 11: Wavelet analysis for the faulty current signal at 1.7T

Discrete wavelet transform is widely used in the feature extraction step because it efficiently works in this field, as confirmed by the results of previous studies. The most important part of DWT is that it uses discrete data as a scale parameter. In the DWT, the scale and the time, as described in the last equation above, are discretized as follows [40][42]

$$a = a_0^m, b = na_0^m b_0 \quad (4\text{-}4)$$

Where m and n are integers, thus the CWT function $\psi_{a,b}(t)$ in the equation above converted to the DWT by the following formula:

$$\psi_{m,n}(t) = a_0^{\frac{-m}{2}} \psi(a_0^{-m}t - nb_0) \quad (4\text{-}5)$$

The discretisation of the scale parameter and time parameter leads to the discrete wavelet transform, which is defined as:

$$w_x(m,n;\psi) = a_0^{\frac{-m}{2}} \int x = (t)\psi * (a_0^{-m}t - nb_0)dt \quad (4\text{-}6)$$

The DWT has two important approaches to discrete the signal at different scales and positions (resolution levels and different frequencies), which are decomposing the signal into approximations (A) and details (D). The approximation information could be obtained from a low pass filter, while the detail information could be obtained from a high pass filter, as explained in figure 4-12.

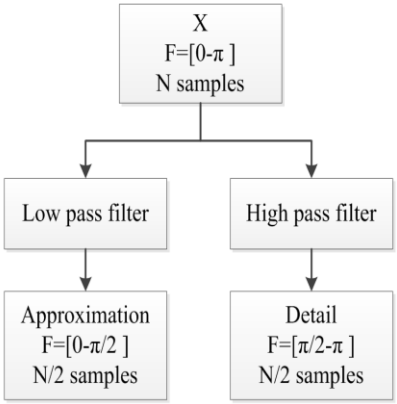

Figure 4- 12: DWT decomposition signal to approximation and detail using filters [42]

Figure 4-13 shows how to analyses and synthesise the signal. The input signal goes through two one-dimensional filters, one for a high-pass filter (H_0) and one for a low-pass filter (H_1). These filters have filtering operations and are followed by subsampling by a factor of 2. Then, the signal will be reconstructed by first-up sampling. After that, filtering and summing the sub-bands will be followed[43]

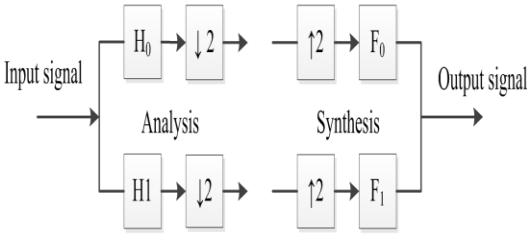

Figure 4- 13: DWT two-channel filters [40]

The synthesis filters F_0 and F_1 must be adapted for analysing the H_0 and H_1 filters in order to achieve perfect reconstruction. It is very easy to obtain the satisfying relationship between the 2-channel filters by considering the Z-transform function. After analysis, the two sub-bands will be as follows[47][45]:

$$\frac{1}{2}\left[H_0\left(Z^{\frac{1}{2}}\right)X\left(Z^{\frac{1}{2}}\right)+H_0\left(-Z^{\frac{1}{2}}\right)X\left(-Z^{\frac{1}{2}}\right)\right] \quad (4\text{-}7)$$

$$\frac{1}{2}\left[H_1\left(Z^{\frac{1}{2}}\right)X\left(Z^{\frac{1}{2}}\right)+H_1\left(-Z^{\frac{1}{2}}\right)X\left(-Z^{\frac{1}{2}}\right)\right] \quad (4\text{-}8)$$

The combination of these filters is:

$$\hat{X}(z)=\frac{1}{2}[F_0(z)H_0(z)+F_1(z)H_1(z)]X(z)+\frac{1}{2}[F_0(z)H_0(-z)+F_1(z)H_1(z-)]X(-z). \quad (4\text{-}9)$$

To overcome the problem of aliasing and distortion, the following conditions should be considered[24][26]:

$$F_0(z)=H_1(-z) \text{ and } F_1(z)=-H_0(-Z) \quad (4\text{-}10)$$

The multiscale pyramid decomposition and reconstruction of an image or signal with high and low pass filters have been illustrated in figures 4-14 and 4-15 below.

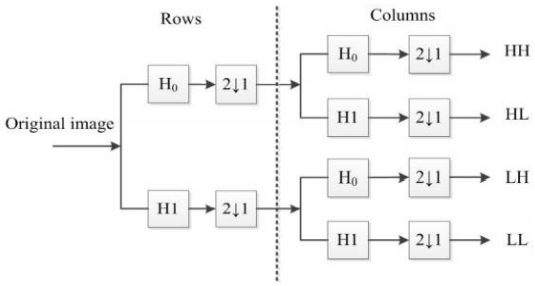

Figure 4- 14: Filter bank structure of the DWT analysis [39]

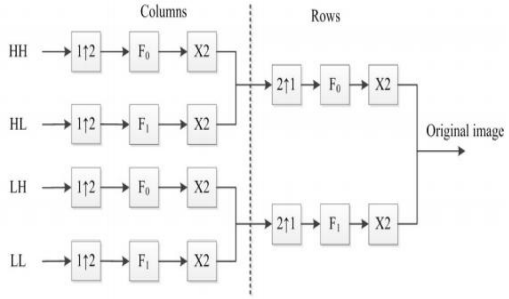

Figure 4- 15: Filter bank structure of the reverse DWT synthesis [39]

4.4.7 Standard deviation (STD)

For a random variable vector, A, made up of N scalar observations, the standard deviation is defined as:

$$S = \sqrt{\frac{1}{N-1}\sum_{i=1}^{N}|A_i - \mu|^2} \quad (4\text{-}11)$$

where μ is the mean of A:

$$\mu = \frac{1}{N}\sum_{i=1}^{n} A_i \quad (4\text{-}12)$$

The standard deviation is the square root of the variance. Some definitions of standard deviation use a normalization factor of N instead of N-1, which you can specify by setting w to 1.

4.4.8 Shannon entropy

The Shannon entropy can measure the uncertainty of a random process. Rolling element machinery without failure generates a more random signal, and the machine with failure usually tends to have a more deterministic signal, i.e., the Shannon entropy will be different. To extract the periodicity in the signal. The Shannon entropy formula is as follows:

$$H = -\frac{1}{\log N}\sum_i p_i \log p_i \quad (4\text{-}13)$$

where *N* is the total number of observed events, and *pi* is the probability of the *i* event [45].

4.5. Results and discussions

After applying several feature extraction techniques, FFT and STD techniques were selected to use in this work because they gave better results..

This section gives certain selected results of the experimental work. These results consist of the current waveform in the transformer, measured for various flux density values. Since the current signal obtained for 0.5 T is lower than that obtained for 1.8 T, the results are separated into four subfigures for better visualisation. Firstly, figure 4-16 shows the current waveforms for normal conditions before applying any faults to understand these faults' impact better.

For healthy conditions of the transformer core, one can see that the flux density has an important effect on the magnitude and the current waveform in a no-loaded power transformer. For low flux density in figure 4-16a, the current is of very low magnitude in the order of 0.1 A. In the same flux density range, the current waveform is approximately similar to a noise signal with a periodical signal of lower amplitude.

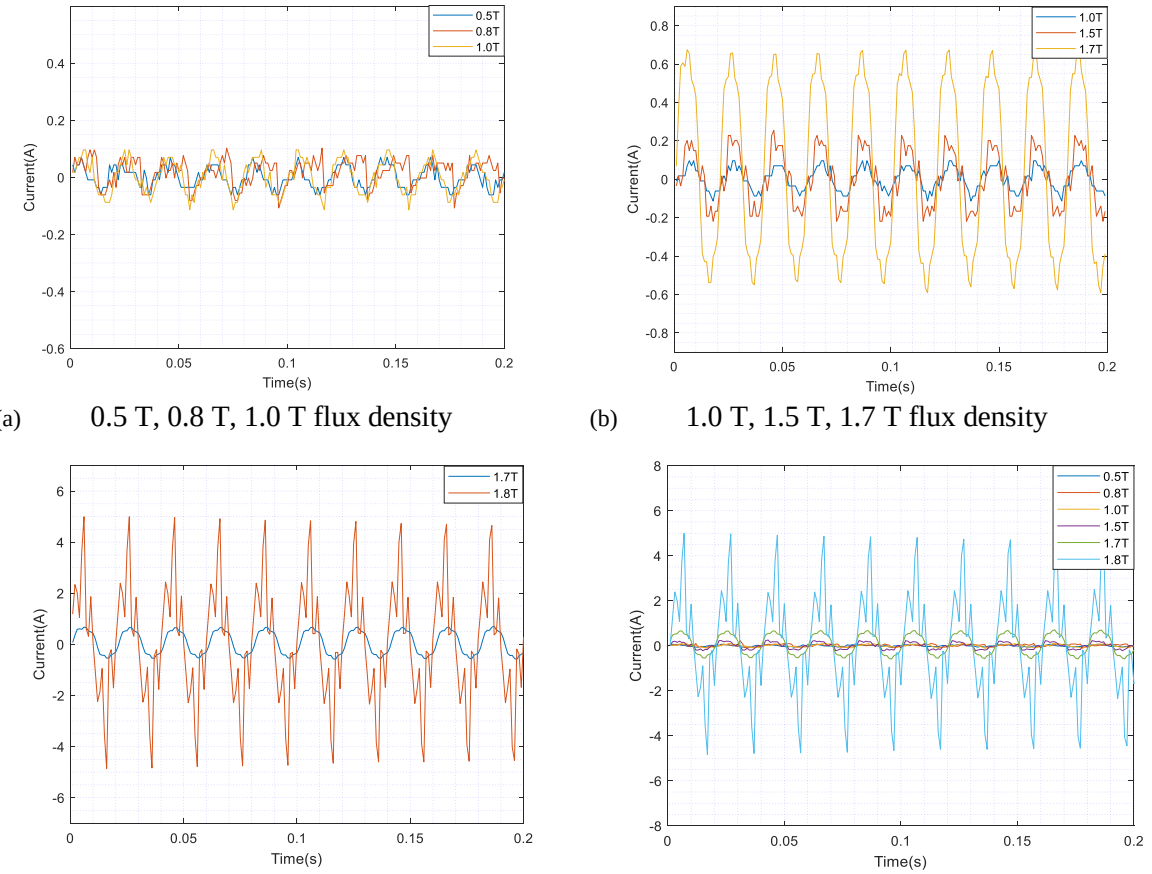

(a) 0.5 T, 0.8 T, 1.0 T flux density

(b) 1.0 T, 1.5 T, 1.7 T flux density

(c) 1.7 T, 1.8 T flux density

(d) 0.5 T, 0.8 T, 1.0 T, 1.5 T, 1.7 T, 1.8 T flux density

Figure 4- 16: Current waveforms under healthy conditions

After applying several feature extraction techniques, the FFT and STD have been selected as parameters. They are now ready to analyse the power transformer current signal for extracting the information to discriminate between the transformer faults. Using Fourier analysis FFT, figure 4-17 illustrates an example of the frequency spectrum of the current signal for 1.7 T flux density as an example with multi scenarios obtained under healthy and faulty conditions. For full figures see appendix 2.

From this figure, it was found that the healthy state is characterised by a low magnitude of the current fundamental, which is around 0.6 A. This operation state is also characterised by the appearance of harmonics of the order 3, 5, and 7. Other odd harmonics of higher order cannot be seen for lower flux densities, but a very low magnitude of the harmonic of order 9 is noticed for 1.7 T flux density.

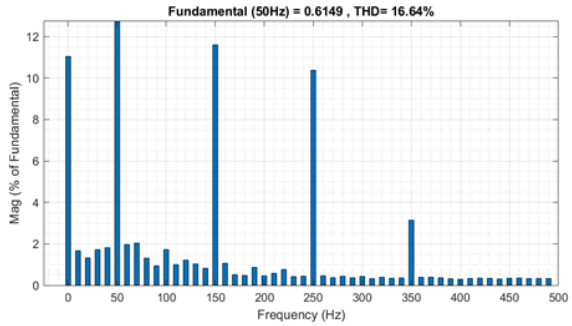

(a) Healthy

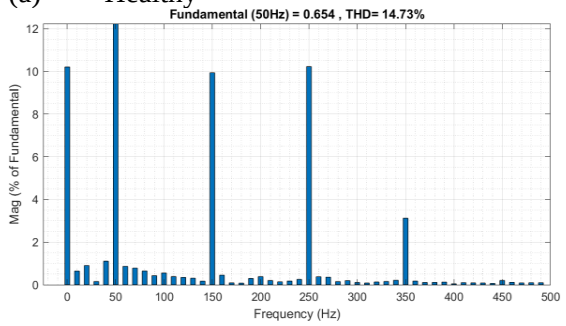

(b) Scenario 1, 2 places

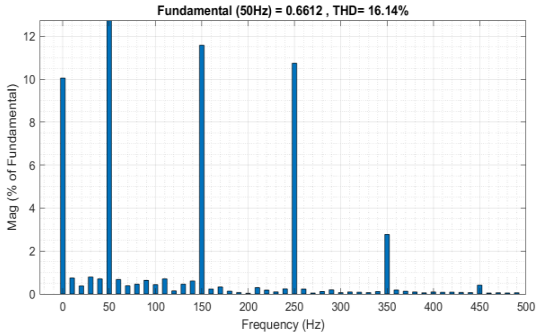

(c) Scenario 1, 3 places

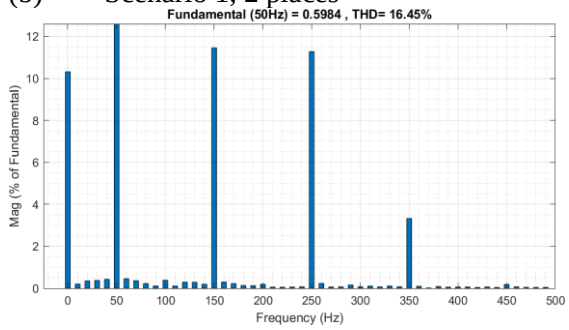

(d) Scenario 2, 2 places

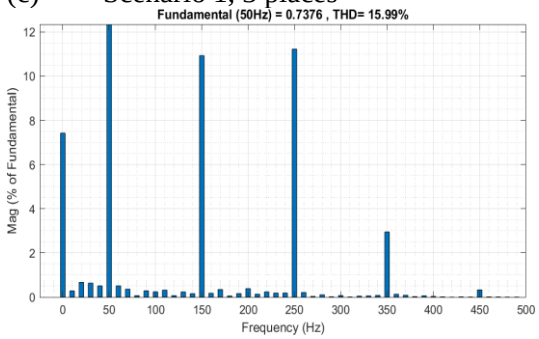

(e) Scenario 2, 3 places

Figure 4- 17: Frequency spectrum of the current signal in normal and faulty mode with 1.7 T flux density

4.5.1 Edge burrs results

The results of the first selected type of faults (i.e., edge burrs faults) have been presented in this part. The same type of fault has been applied in two and three different places within the transformer core. Figure 4-18 shows the current waveforms for the considered cases. Selected flux densities (i.e., 0.8 T, 1.7 T, and 1.8 T) have been shown in this figure to highlight the effect of the flux density on the current waveform of the transformer under edge burr faults.

This figure shows that different shapes characterise the current waveforms obtained during edge burr faults compared to those obtained in the healthy operation mode. This means that edge burrs faults considerably affect the transformer currents, thus, the performance of the transformer.

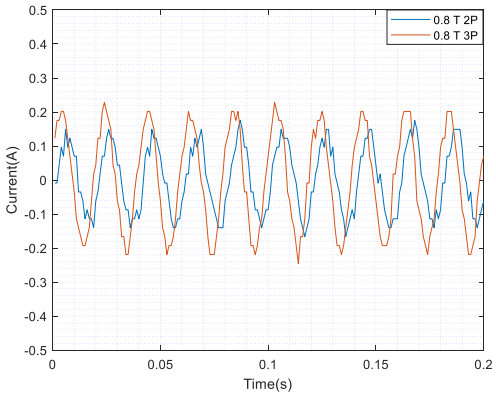

(a) 0.8 T flux density

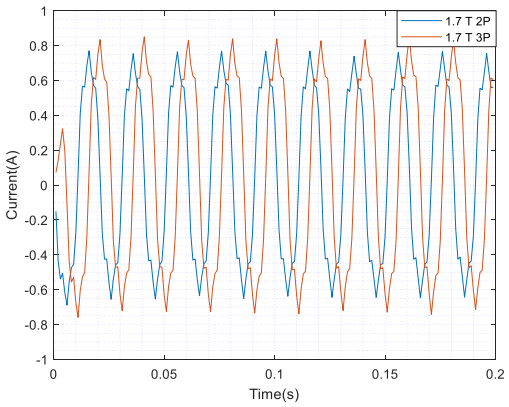

(b) 1.7 T flux density

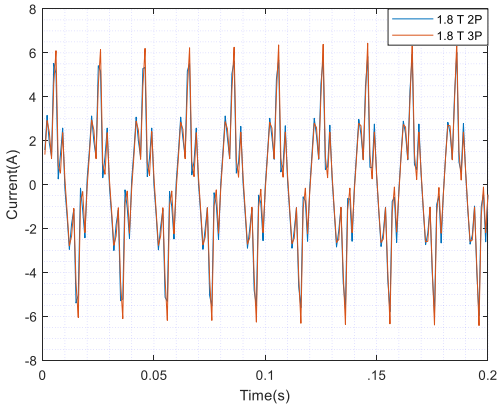

(c) 1.8 T flux density

Figure 4- 18: Current waveform in transformer primary windings for edge burr faults applied in two and three different places

Indeed, the current magnitude increases and harmonics become pertinent. For instance, the magnitude increased approximately from 0.1 to 0.2 A for a flux density of 0.5 T, corresponding to a rate of 100%. This rate of increase becomes more important with the increment of the flux density and the number of affected places within the transformer core, as shown in figure 4-19. This figure illustrates the magnitude of the current signals as a function of the flux density obtained for normal and faulty operation modes. The current has a large magnitude for all considered flux densities compared to the other studied cases.

In this figure, the obtained results show a non-linear variation of the current magnitude with respect to the flux density. For full example see appendix 6.

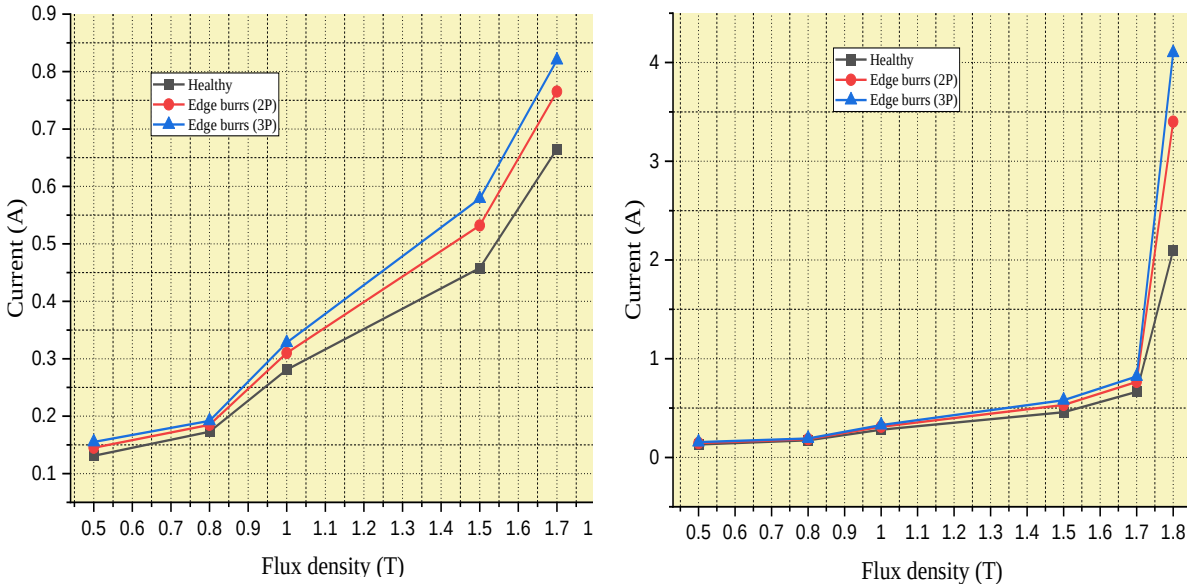

(a) Scenario (1) 0.5 T-1.7 T flux density (b) Scenario (1) 0.5 T-1.8 T flux density

Figure 4- 19: Magnitude of the current waveform in transformer primary windings with and without edge burrs faults

Slight augmentation has been observed in the current magnitude for low flux density. The dramatic increase is recorded for higher values of the flux density. The highest magnitude of edge burr faults in three locations is typically between 0.15 and 0.82 A, while healthy conditions show lower values between 0.4 and 0.65 A. table 4-2 gives a brief comparison between the results measured with and without edge burr faults in the transformer core. The table shows some parameters obtained using Fourier Analysis, such as THD, average, fundamental, and the magnitude of the first four harmonics.

As shown in this table 1, the edge burr faults affect the transformer currents. A remarkable increase of magnitude in the current fundamental as well as the first-order harmonics. Overall, the increase is 150 mA for the fundamental, and up to 22 mA in the harmonics shown. However, the THD shows a slight decrease when the faults are applied. This decrease might be justified by the increase of the overall magnitude of the transformer current. It should be noted that such a problem may be considerable. The consequences can be significant, especially if the studied faults happen in an oil-immersed power transformer of high capacity. For instance, the edge burrs faults result in an increase of the transformer current, which, in its round, can increase the temperature inside the transformer. This rise in temperature might affect the properties of the insulating oil and/or insulating paper, thus, reducing the performance of the transformer. For this reason, it would be better to examine the effect of such faults in high-capacity transformers.

Table 4- 2: Fourier Analysis parameters for an edge burr fault applied to the transformer core at 1.7 T Scenario 4

			average, fundamental, and first harmonics in (A)					
		THD (%)	average	Fundamental	3	5	7	9
healthy		16.64	0.0682	0.6149	0.0719	0.0664	0.0196	0.0024
edge burrs faults	2 places	16.12	0.0677	0.684	0.0786	0.0759	0.0198	0.0020
	3 places	16.10	0.0596	0.765	0.0895	0.0887	0.0244	0.0015

4.5.2 Results of lamination insulation faults

As described in the previous Section, artificial short circuits, as the second type of fault, have been applied between transformer core laminations by removing the insulation covering the laminations. Figure 4-20 shows the measured current waveforms in the transformer's primary windings. The results correspond to faults between 2, 6, 8, and 12 laminations for 0.5 T, 0.8 T, 1.7 T,1.8 T flux densities as an example, as indicated in figures 4-20a: 4-20d, respectively.for full figures see appendix 6. It should be noted that the impact of the position of the short circuit applied between laminations has been investigated previously in [20]. For this reason, the same position of the applied faults has been considered in this investigation.

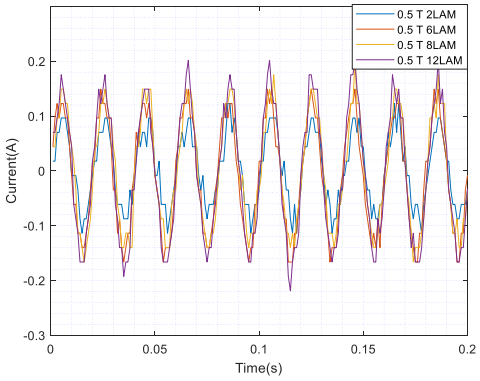

(a) 0.5 T flux density

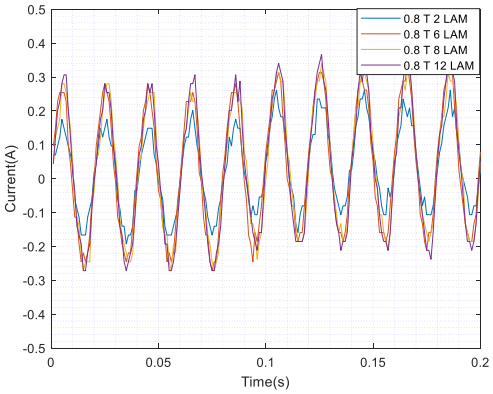

(b) 0.8 T flux density

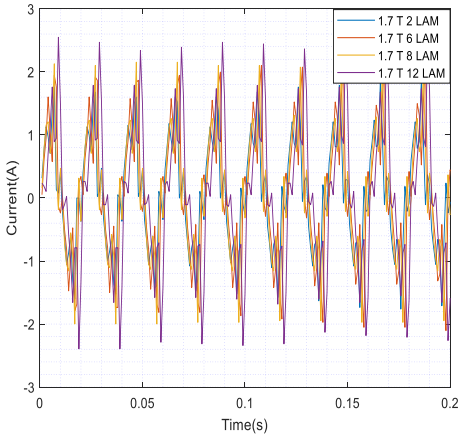

(c) 1.7 T flux density

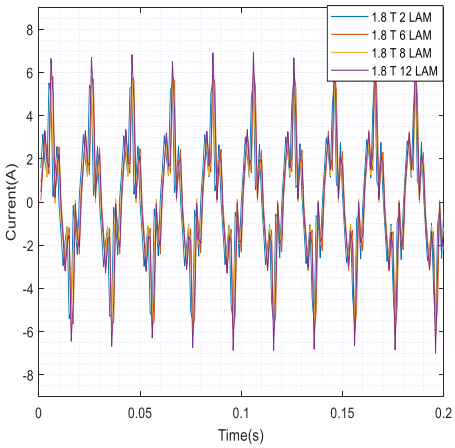

(d) 1.8 T flux density

Figure 4- 20: Current waveform in transformer primary windings for insulation degradation faults

From this figure, it is clear that the faults' size (number of affected laminations) has an important effect on the current within the transformer windings. The results show that the short circuit current is approximately a linear function of the number of affected laminations, as can be seen in figure 4-21. This figure shows the current magnitude as a function of the number of the affected laminations at flux density between 0.5 and 1.8 T.

This figure shows that the current caused by the insulation damage fault is related to the number of laminations in the short circuit and the flux density. and, the current magnitude follows a non-linear function with respect to the flux density. It was found for two, six, eight and twelve shorted laminations that the current magnitude is extremely high at flux density of 1.8 T.

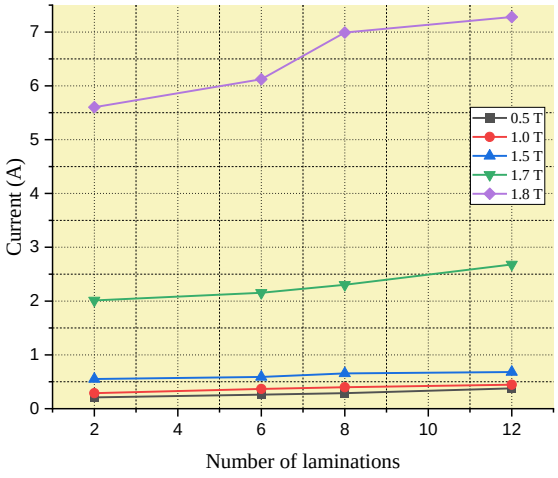

Figure 4- 21: Magnitude of the current waveform in transformer primary windings with insulation degradation faults applied between 2, 6, 8 and 12 laminations

Table 4-3 gives the THD, average, fundamental, and magnitude of the first four harmonics of the current signal for lamination insulation faults in the transformer core. When applying lamination insulation faults, the results show a considerable increase in the THD as well as the magnitude of fundamental and harmonics compared to the healthy conditions. For instance, the THD rises from 16.64% with 0.6 A fundamental to 50.14% THD with a fundamental of 1.11A for insulation faults between two laminations. This is equivalent to a 66.81% increase in the THD value and 45.95% in the fundamental magnitude. These rates generally increase with the number of affected laminations, as given in Table 4-3. In addition, the obtained results are considerably affected by the flux density, as shown in figure 4-21. Overall, the results demonstrate that the healthy operation mode can be distinguished from the faulty one in most proposed cases. In addition, the results associated with this type of fault are also different to those obtained when applying edge burrs faults. This means that fault detection and

classification technique can be considered in these types of faults using the current waveforms as information support.

Table 4-3: Fourier Analysis parameters for lamination insulation faults applied to the transformer core at 1.7 T

		THD (%)	average, fundamental (fd), and first harmonics in (A)					
			average	fd	3	5	7	9
Lamination insulation faults	2 lamentations.	50.14	0.0612	1.113	0.0790	0.4618	0.2771	0.5676
	6 laminations.	57.85	0.0612	1.303	0.2149	0.6254	0.3531	0.0325
	8 laminations.	56.94	0.0587	1.175	0.0834	0.5499	0.3630	0.0916
	12 laminations.	54.77	0.0612	1.459	0.2626	0.6653	0.3487	0.0729

4.6 Summary

This investigation studied the impact of edge burrs and damaged insulation systems between laminations on the performance of power transformers. An experimental methodology was presented to simulate both laminations' faults. A three-phase transformer was used where different scenarios of the faults were applied, and several flux densities were considered. Overall, the obtained results demonstrated that Edge burrs and insulation degradation both could cause flux distortion regarding the recorded current signals, which considerably affects the reliability of the transformer operation.

Edge burrs and/or insulation degradation affecting the transformer core can increase the transformer currents. These later become important with the increase of the flux density and the number of short-circuited laminations. Therefore, a high current loss might be developed for the transformer core under faulty conditions. This can cause flux distortion in cruciform stacked cores and high localised heating within and outside of the affected region.

The current change caused by the insulation damage fault is related to the number of laminations in the short circuit as well as to the flux density. It was found for two, six, eight, and twelve shorted laminations that the current magnitude is extremely high at a flux density of 1.8 T, increased with the number of the affected laminations. This significant increase in current may lead to an increase in power losses, hence, the transformer efficiency or engendering thermal power transformer failure.

Such findings indicate the severity of short circuits in the transformer core, and manufacturers should take precautions to eliminate burrs as far as practicable, especially for transformers of high capacity where the consequences might be more significant. Moreover, it is noticed that the transformer currents are affected in different ways according to the applied faults. This implies that the detection and classification of faults can be achieved using these currents.

4.7 References

[1] A. Santisteban, F. Delgado, A. Ortiz, I. Fernandez, C. J. Renedo, and F. Ortiz, “Numerical analysis of the hot-spot temperature of a power trans- former with alternative dielectric liquids,” IEEE Trans. Dielectr. Electr. Insul., vol. 24, no. 5, pp. 3226–3235, 2017.

[2] F. Bedell, “History o A -C wave Form, ts Determination and Standardiza- tion,” IEEE Trans. Dielectr. Electr. Insul., vol. 61, no. 12, Dec 1942, pp. 864–868, 1942.

[3] C. Gu et al., “A Transformer Vibration Signal Separation Method Based on BP Neural Network,” 2018 IEEE Int. Power Modul. High Volt. Conf. IPMHVC 2018, no. 080037, pp. 312–316, 2018.

[4] W. Lai, W. Li, H. Meng, R. Ding, Y. Wang, and S. Fang, “Research on the Relation between Load Coefficient and Hot Spot Temperature of Oil-immersed Power Transformer,” 2019 IEEE Int. Conf. Power, Intell. Comput. Syst. ICPICS 2019, pp. 393–396, 2019.

[5] S. Bustamante, M. Manana, A. Arroyo, R. Martinez, A. Gonzalez, and J. I. Rodriguez, “Case Study-Calculation of DGA Limit Values and Sampling Interval in Power Transformers,” ARWtr 2019 - Proc. 2019 6th Adv. Res. Work. Transform., no. October, pp. 64–68, 2019.

[6] Y. Benmahamed, O. Kherif, M. Teguar, A. Boubakeur, and S. S. M. Ghoneim, “Accuracy Improvement of Transformer Faults Diagnostic Based on DGA Data Using SVM-BA Classifier,” Energies, vol. 14, no. 10, p. 2970, May 2021.

[7] O. Kherif, Y. Benmahamed, M. Teguar, A. Boubakeur and S. S. M. Ghoneim, "Accuracy Improvement of Power Transformer Faults Diagnos- tic Using KNN Classifier with Decision Tree Principle," in IEEE Access, vol. 9, pp. 81693-81701, 2021, doi: 10.1109/ACCESS.2021.3086135.

[8] M. F. Al Hamdani, R. Azis Prasojo, Suwarno, and A. Abu-Siada, “Power Transformer Degradation Condition and Insulation Index Estimation Based on Historical Oil Dat,” Proc. 2nd Int. Conf. High Volt. Eng. Power Syst. Towar. Sustain. Reliab. Power Deliv. ICHVEPS 2019, pp. 1–5, 2019.

[9] N. Abu Bakar and A. Abu-Siada, “A novel method of measuring trans- former oil interfacial tension using UV-Vis’s spectroscopy,” IEEE Electr. Insul. Mag., vol. 32, no. 1, pp. 7–13, 2016.

[10] H. Huang, Y. Liu, Y. Yuan, P. Li, Y. Yang, and Y. Wang, “Research of a transformer fault diagnose method using multi-source recording waves,” China Int. Conf. Electr. Distrib. CICED, vol. 2014–December, no. Ciced, pp. 873–878, 2014.

[11] A. J. Moses and M. Aimoniotis, “Effects of artificial edge burrs on the properties of a model transformer core,” Phys. Scr., vol. 39, no. 3, pp. 391–393, 1989.

[12] R. Murugana and R. Ramasamy, "Understanding the power transformer component failures for health index-based maintenance planning in elec- tric utilities", Engineering Failure Analysis, vol. 96, pp. 274-288, Feb. 2019.

[13] H. Hamzehbahmani, P. Anderson and K. Jenkins, "Interlaminar Insulation Faults Detection and Quality Assessment of Magnetic Cores Using Flux Injection Probe," in IEEE Transactions on Power Delivery, vol. 30, no. 5, pp. 2205-2214, Oct. 2015.

[14] A. Eldieb, F. Anayi, and A. Fahmy, “Experimental investigation on effect of edge burr’s fault on toroidal magnetic cores laminations at different range of magnetisations,” Proc. Univ. Power Eng. Conf., vol. 2015–Novem, pp. 1–5, 2015.

[15] H. Hamzehbahmani, P. Anderson, J. Hall, and D. Fox, “Eddy current loss estimation of edge burr-affected magnetic laminations based on equivalent electrical network - Part I: Fundamental concepts and FEM modeling,” IEEE Trans. Power Deliv., vol. 29, no. 2, pp. 642–650, 2014.

[16] A. Eldieb and F. Anayi, "Evaluation of Loss Generated by Edge Burrs in Electrical Steels," in IEEE Transactions on Magnetics, vol. 52, no. 5, pp. 1-4, May 2016, Art no. 2001404, doi: 10.1109/TMAG.2016.2527361.

[17] R. Mazurek, H. Hamzehbahmani, A. J. Moses, P. I. Anderson, F. J. Anayi, and T. Belgrand, “Effect of artificial burrs on local power loss in a three-phase transformer core,” IEEE Trans. Magn., vol. 48, no. 4, pp. 1653–1656, 2012.

[18] I. Reva, O. Bialobrzheskyi, and O. Usatiuk, “Investigation of distribution a harmonic power in three phase transformers at idling mode,” 2020 IEEE 7th Int. Conf. Energy Smart Syst. ESS 2020 - Proc., pp. 273–276, 2020.

[19] A. Patel, N.K. Sharma, A. Banshwar, B.B. Sharma, and M. Pathak, “An evaluation of different health assessment methods on 50 MVA power transformer: A case study,” 2020 IEEE Students’ Conf. Eng. Syst. SCES 2020, pp. 1–5, 2020.

[20] M.B. Aimoniotis and A.J. Moses, “Evaluation of induced eddy currents in transformer sheets due to edge-burrs, employing computer aided design programs,” in Proc. Athens Power Tech, vol. 2. Sep. 1993, pp. 847–850.

[21] E. Lamprecht and R. Graf, “Fundamental investigations of eddy current losses in laminated stator cores created through the impact of manufactur- ing processes,” in Proc. 1st Int. Electr. Drives Prod. Conf. (EDPC), Sep. 2011, pp. 29–35.

[22] J. Bielawski, S. Duchesne, D. Roger, C. Demian and T. Belgrand, "Contri- bution to the Study of Losses Generated by Interlaminar Short-Circuits," in IEEE Transactions on Magnetics, vol. 48, no. 4, pp. 1397-1400, April 2012, doi: 10.1109/TMAG.2011.2173472.

[23] L. Bi, U. Schäfer and Y. Hu, "A New High-Frequency Iron Loss Model Including Additional Iron Losses due to Punching and Burrs’ Connection," in IEEE Transactions on Magnetics, vol. 56, no. 10, pp. 1-9, Oct. 2020, Art no. 6300209, doi: 10.1109/TMAG.2020.3015685.

[24] IEEE Standard, "IEEE Recommended Practice for Testing Transform- ers and Inductors for Electronics Applications," in IEEE Std 389-2020 (Revision of IEEE Std 389-1996), vol., no., pp.1-97, 1 May 2020, doi: 10.1109/IEEESTD.2020.9084213.

[25] J. Brownlee, Machine Learning Mastery. Vermont Victoria/ Australia: © 2019 Machine Learning Mastery Pty. Ltd. All Rights Reserved, 2019.

[26] S. Salvador and P. Chan, “Toward accurate dynamic time warping in linear time and space,” Intell. Data Anal., vol. 11, no. 5, pp. 561–580, 2007.

[27] A. Nanopoulos, R. O. B. Alcock, and Y. Manolopoulos, “Feature-based Classi cation of Time-series Data,” no. February 2016.

[28] X. Wang, K. Smith, and R. Hyndman, “Characteristic-based clustering for time series data,” Data Min. Knowl. Discov., vol. 13, no. 3, pp. 335–364, 2006.

[29] X. Wang, A. Wirth, and L. Wang, "Structure-based statistical features and multivariate time series clustering," Proc. - IEEE Int. Conf. Data Mining, ICDM, pp. 351–360, 2007.

[30] A. Primo, V. V. Phoha, R. Kumar, and A. Serwadda, "Context-aware active authentication using smartphone accelerometer measurements," IEEE Comput. Soc. Conf. Comput. Vis. Pattern Recognit. Work., pp. 98–105, 2014.

[31] S. R. Pani, P. K. Bera, and V. Kumar, "Detection and classification of internal faults in power transformers using tree-based classifiers," 9th IEEE Int. Conf. Power Electron. Drives Energy Syst. PEDES 2020, no. Lv, 2020.

[32] MathWorks."MathWorks."MathWorks,2022.[Online].Available: https://www.mathworks.com/help/physmod/sps/powersys/ref/fftanalyzer-app.html. [Accessed: March 11, 2022].

[33] MathWorks."MATLAB."MathWorks,2022.[Online].Available: https://www.mathworks.com/discovery/waveletransforms.html.[Accessed:March10,2022]

[34] A. al-Qerem, F. Kharbat, S. Nashwan, S. Ashraf, and khairi blaou, "General model for best feature extraction of EEG using discrete wavelet transform wavelet family and differential evolution," Int. J. Distrib. Sens. Networks, vol. 16, no. 3, 2020.

[35] P. E. T. Jorgensen and M. S. Song, "Comparison of discrete and continuous wavelet transforms," Comput. Complex. Theory, Tech. Appl., vol. 9781461418, pp. 513–526, 2012.

[36] Z. K. Peng and F. L. Chu, "Application of the wavelet transform in machine condition monitoring and fault diagnostics: A review with bibliography," Mech. Syst. Signal Process., vol. 18, no. 2, pp. 199–221, 2004.

[37] J. J. Sinou, "An experimental investigation of condition monitoring for notched rotors through transient signals and wavelet transform," Exp. Mech., vol. 49, no. 5, pp. 683–695, 2009.

[38] H. K. Srinivas, K. S. Srinivasan, and K. N. Umesh, "Role of an artificial neural network and a wavelet transform for condition monitoring of the combined faults of unbalance and cracked rotors," Int. J. Acoust. Vib., vol. 15, no. 3, pp. 121–127, 2010.

[39] S. F. M.B.A. Asmael*, Roslee Ahmad, Ali Ourdjini, "analysis of residual wavelet scalogram for machinery fault diagnosis," Adv. Mater. Res., vol. 845, pp. 118–122, 2013.

[40] Al-Musawi, A.K.I. "The development of new artificial intelligence based hybrid techniques combining bees' algorithm, data mining and genetic algorithm for detection, classification and prediction of faults in induction motors." Cardiff University, 2019.

[41] J. M. Shapiro, "An embedded hierarchical image coder using zerotrees of wavelet coefficients," Data Compression Conf. Proc., pp. 214–223, 1993.

[42] A. Boggess et al., "Review Reviewed Work (s): Ripples in Mathematics: The Discrete Wavelet Transform by Arne Jensen and Anders la Cour-Harbo: A First Course in Wavelets with Fourier Analysis by Published by: Taylor & Francis, Ltd. on behalf of the Mathematical Associate," 2003.

[43] L. Cristaldi, M. Lazzaroni, A. Monti, and F. Ponci, "Diagnostic and model validation of a faulty induction motor drive via wavelet decomposition," Conf. Rec. - IEEE Instrum. Meas. Technol. Conf., vol. 2, no. 6, pp. 1460–1464, 2007.

[44] K. C. D. Kompella, V. G. R. Mannam, and S. R. Rayapudi, "DWT based bearing fault detection in induction motor using noise cancellation," J. Electr. Syst. Inf. Technol., vol. 3, no. 3, pp. 411–427, 2016.

[45] D. Galar and U. Kumar, Preprocessing and Features. ScienceDirect Topics 2017.

CHAPTER 5: Detection and classification of lamination faults in a 15 kVA three-phase transformer core using SVM, KNN and DT algorithms.

This chapter deals with detecting and classifying two types of lamination faults (i.e., edge burr and lamination insulation faults) in a three-phase transformer core. Previous experimental results are exploited, which are obtained by employing a 15 kVA transformer under healthy and faulty conditions. Different test conditions were considered, such as the flux density, number of affected laminations, and fault location. Indeed, the current signals were used where four features (Average, Fundamental, Total Harmonic Distortion (THD), and Standard Deviation (STD)) were extracted. Elaborating a total of 328 samples, these features are utilized as input vectors to train and test classification models based on support vector machine (SVM), k-nearest neighbours (KNN), and decision tree (DT) algorithms. Based on the selected features, the results confirmed that the transformer current could be used to detect and classify lamination faults. An accuracy rate of more than 84% was obtained using three different classifiers. Such findings provided a promising step toward fault detection and classification in electrical transformers, helping to prevent the system and avoid other related issues such as increased power loss and temperature.

5.1 Introduction

Transformers are critical components in the power network and ensuring their safety and reliability is crucial for uninterrupted utility services. Researchers have analyzed the impact of faults in transformers to improve understanding and provide protection techniques. The studies aim to provide early detection of faults through consistent monitoring and diagnostic techniques, improving equipment reliability and operation duration. [1], [2].

In literature, numerous studies were carried out to investigate the impact of faults in electrical machines, including the power transformers, e.g., [3–6]. Other researchers focused on developing and improving solution techniques to prevent such faults or to increase the performance of the transformers, e.g., [7–10]. A couple of works aimed to detect and classify faults in transformers, e.g., [11–13]. For these reasons, the techniques developed help to better exploit electrical transformers and avoid material losses resulting from possible malfunctions.

A study in [8] found that an insulation problem caused 37% of power transformer failures. The core failure can be identified as a primary failure regarding the laminations and interlaminations issues [14].

In previous work [15], The authors investigated the effects of two types of transformer core faults: edge burrs and lamination insulation faults. They simulated and analyzed both faults using a 15 kVA three-phase power transformer, considering different scenarios such as the size of affected regions and number of short-circuited laminations. The study used flux densities ranging from 0.5 to 1.8 T. The results provide insight into the severity of short circuits in relation to their position in the transformer core and can be used to discuss power losses in the transformer core.

Based on the results presented in [15], This chapter focuses on detecting and identifying lamination faults in the core of a 15 kVA electrical transformer. Under normal and faulty conditions, various scenarios are analyzed, including flux density, number of affected laminations, and number/location of faults. The measured current signals are used to extract features as input vectors for training and testing with SVM, KNN, and DT classifiers. The study used 328 samples and selected four features.

The chapter is organized as follows: Section 5.2 details the experimental results and the signal processing process. Examples of the dataset is also presented and discussed. Section 5.4 starts with a brief description of the used classifiers, followed by the obtained results from different scenarios. The obtained results are presented and discussed, where a detailed example is given for the results of the DT algorithm.

5.2 Pre-processing methodology and results

This section provides the feature extraction process for detecting and classifying lamination faults in the transformer core. Features have been extracted using signal processing techniques - Fourier Analysis applied to the current signals. The obtained dataset is then treated to reduce the number of features, selecting those most contributing to the overall accuracy. Examples of the obtained results are presented and discussed in this chapter since the full details are the core of other work that has studied the effect of these faults in the previous chapter and [15].

5.2.1 Current signals

Mechanical shear causes burrs on the cut edges, usually followed by the process of punching and cutting the electrical steel. Edge burrs and insulation deterioration between laminations are the most common faults in this type of transformer. These deformations in the core laminations affect the performance of the transformer and electrical machines, causing power losses as experimentally verified in many studies, e.g., [15–17]. Figure 5-1 illustrates two examples of the measured current signals under normal and faulty conditions. Full figures are available in appendix 6.

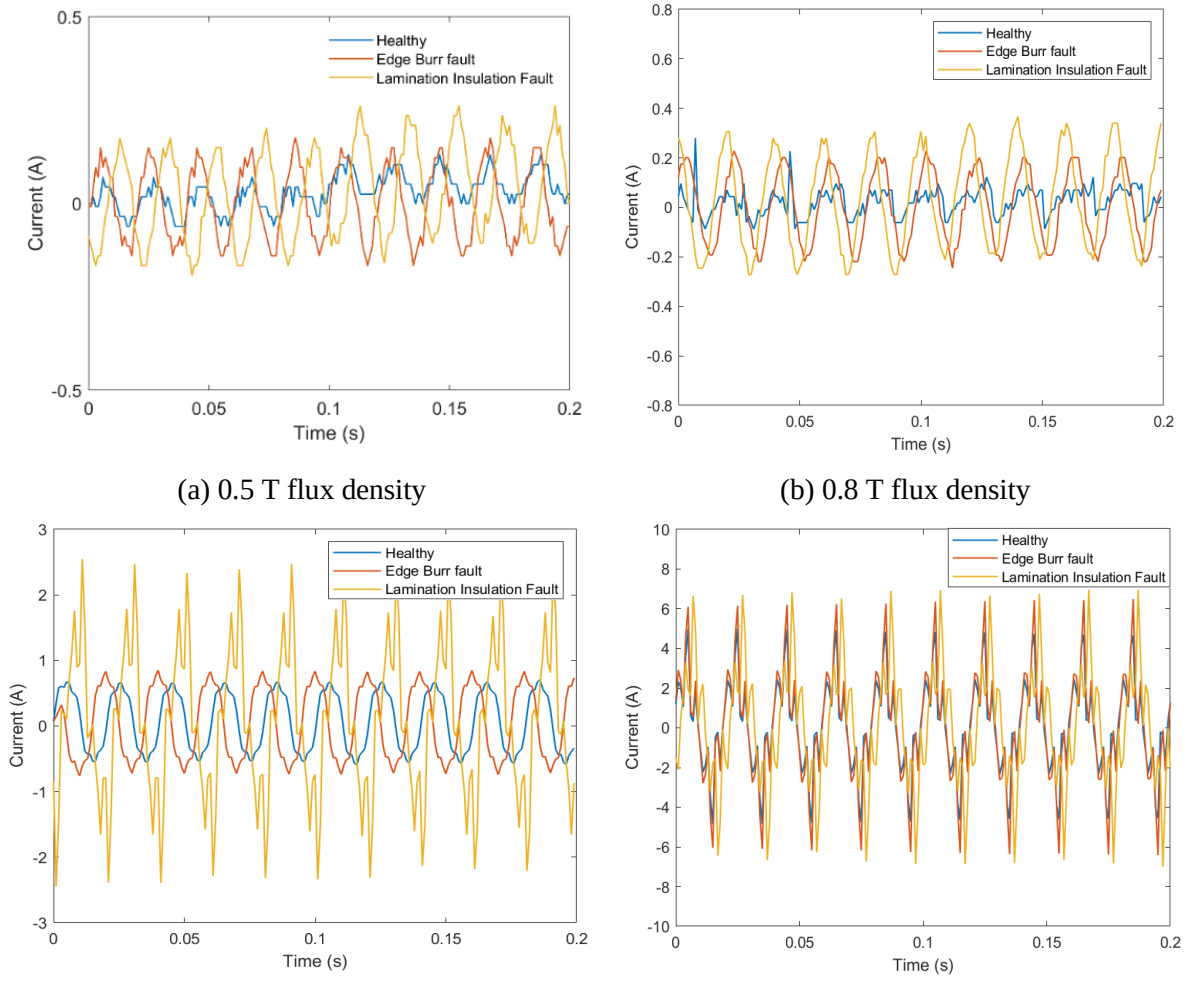

(a) 0.5 T flux density

(b) 0.8 T flux density

(c) 1.7 T flux density

(d) 1.8 T flux density

Figure 5- 1: illustrates examples of the measured current signals under normal and faulty conditions

With regard to flux density, a detailed discussion on the effect of each type of fault on the current waveforms can be found in the previous chapter and [15] and [18]. For a healthy mode, one can see that the flux density has an important effect on the magnitude and waveshape of the no-load current. At low flux density, the current is of incredibly low magnitude in the order

of 0.2 A. In the same range of flux density, the current waveform is like a noise signal accompanied by a periodical signal of low amplitude.

From the current waveform, one can obviously distinguish between each operation mode of the transformer. The current magnitude increases with both faults of laminations. However, the waveforms of the current are practically similar. This waveform approach may affect the classification or detection of transformer faults. Quantifying the current signals is a common technique to help detect and classify faults in electrical transformers or other electrical systems [19], [20]. For this, signal processing techniques have been applied to the current signals for the matter of detection and classification of the faults.

5.2.2 Features extraction

In order to increase the credibility of the database, several flux densities are considered, namely, 0.5, 0.8, 1.0, 1.5, 1.7, and 1.8 T. In the first stage, the data was collected without applying any faults - normal conditions (Healthy operating mode). In the second stage, two types of faults were applied to the transformer core to form the database. A full day was allotted to take the data of each error separately. This is to leave the transformer core enough time to cool down. The studied cases are summarized in table 5- 1.

Table 5- 1: Description of The Database

Mode	Quantity	Description
H	6	6 cases correspond to six selected flux densities
F1	4x2x6	4 scenarios (S1, S2, S3 and S4) of artificial edge burr fault are applied in 2 and 3 different places within the transformer core. Each fault case (a given scenario in 2 or 3 places) has been examined against 6 cases corresponding to the selected flux densities
F2	4x6	4 scenarios of artificial lamination insulation fault are considered, where each fault has been examined against 6 cases corresponding to the selected flux densities
H: healthy- F1: Edge burr fault- F2: insulation fault		

For reliable and feasible results, each test was examined many times. In order to increase the database furthermore and examine the obtained results, each scenario of table 5-1 has been repeated three times on different dates. Data collection started in November 2020 and continued for five months. It should be noted that a detailed description of the experimental results has been presented in [15].

A MATLAB code tool, “FFT_Analyzer_App,” has been used to perform Fourier analysis on the measured results. Current signals have been used, and the frequency spectrum has been determined for each case of the experimental results. The feature extraction process generally

starts by displaying the frequency spectrum over the [0–500 Hz] frequency band. Figure 5-2 shows an example of the frequency analysis obtained for 1.8 T flux density for healthy and faulty operation modes. For full example see appendix 2.

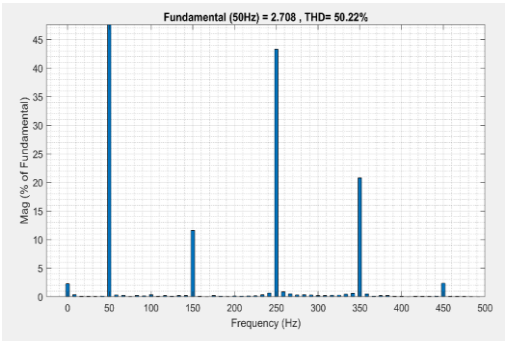

(a) Healthy conditions at 1.8 T

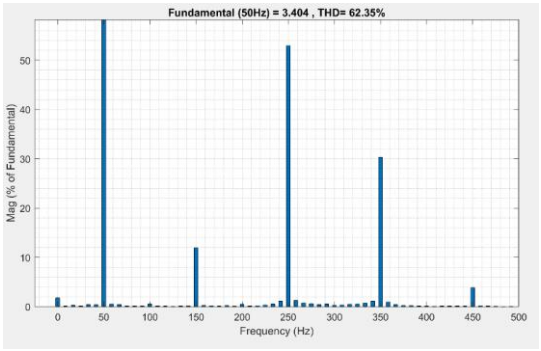

(b) Edge Burr Fault at 1.8 T

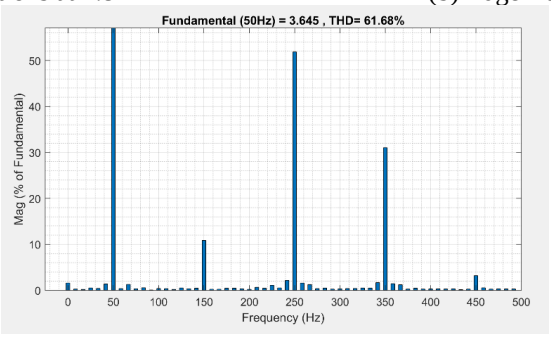

(c) Lamination Insulation Fault at 1.8 T

Figure 5- 2: Frequency spectrum of the transformer currents at 1.8 T flux density, obtained under healthy and faulty conditions

As seen from this figure, the healthy operation mode can be distinguished from the faulty one in the proposed case. This healthy mode is characterized by the appearance of harmonics of the order 3rd, 5th, and 7th. Other odd harmonics appear with neglected amplitude along the frequency spectrum of the current signals. In terms of magnitude, the healthy mode is characterized by a fundamental value of about 2.7 against 3.4 in the edge burr fault. In faulty conditions, the magnitude and number of harmonics increase compared to healthy conditions.

5.2.3 Feature selection

The feature selection step is used to minimize dimensionality by excluding irrelevant features, and Feature selection helps improve the model performance by focusing only on the important variables. This step is conducted using differential evolution. For instance, the features have been selected based on a graphical representation to distinguish the independent features from the others, which are optimized into representative features. Figure 5-3 shows an example of

fundamental values as a function of the THD of the transformer currents under 0.5 and 1.8 T flux density for healthy and faulty conditions. For full figures see appendix 5.

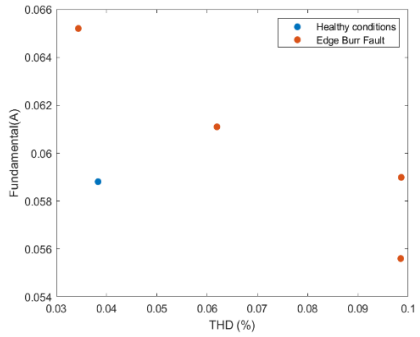

(a) Edge burr fault 0.5 T

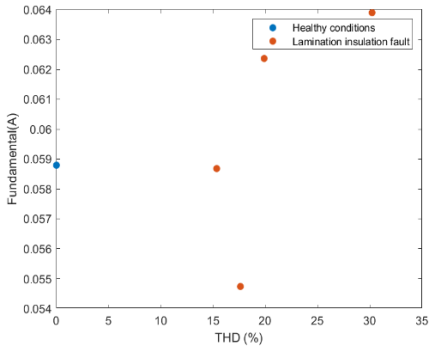

(b) Lamination insulation fault 0.5 T

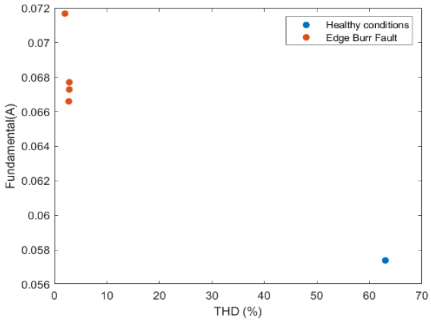

(c) Edge burr fault 1.8 T

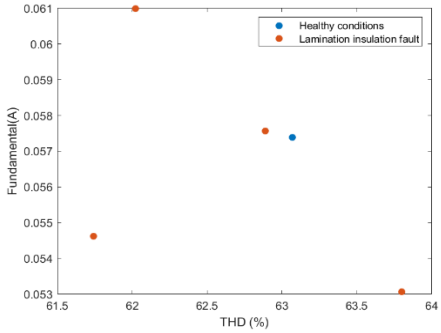

(d) Lamination insulation fault 1.8 T

Figure 5- 3: Fundamental values as a function of the THD of the transformer currents under 1.7 T flux density for both the healthy and faulty conditions

This figure clearly shows how THD and fundamental are different between healthy and faulty conditions. This means that both features can be applied to detect both types of faults of the power transformer core. For instance, in the obtained results for any couple of points located in this figure, a simple line of equation "Fundamental = α THD+β" can be used to separate between the two operation modes. We need to find the best pair alpha beta that do it properly. As shown in figure 5-4.

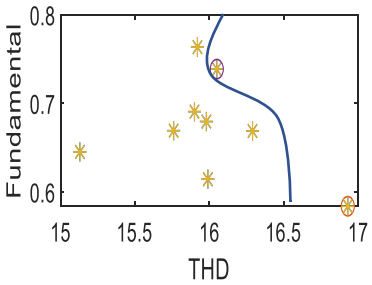

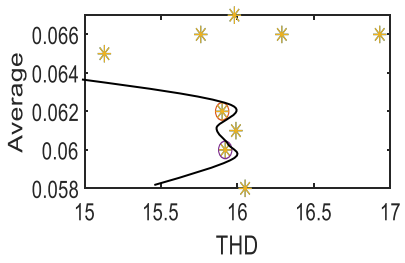

Figure 5- 4: separate the dots using the fundamental equation

Figure 5-4 shows a second example of the distribution of the STD (A) values with respect to the THD of the transformer current under healthy and faulty conditions.

The same ascertainment can be obtained from this figure. However, a graphical method is not practical in the actual situation since a large number of samples is considered. For this, four features (fundamental, average, THD, and STD) are used in this investigation. It was found that the use of such features is appropriate for detection purposes. Referring to figures 5-5, the same ascertainment has been observed with different combinations of the four selected features.

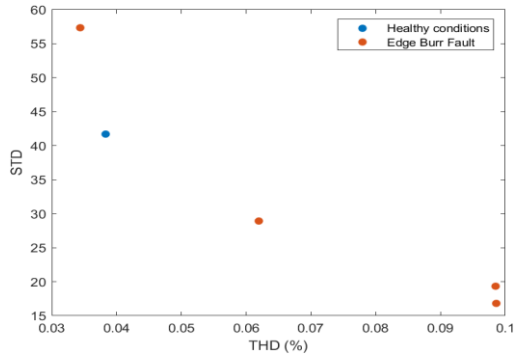

(a) Edge burr fault 0.5 T

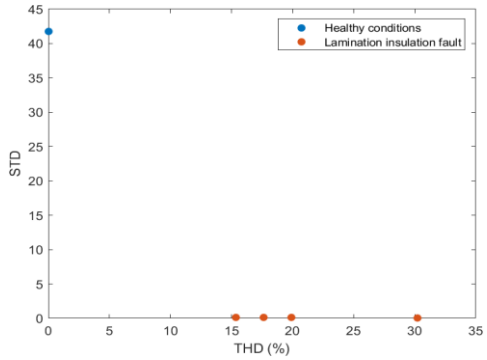

(b) Lamination insulation fault 0.5 T

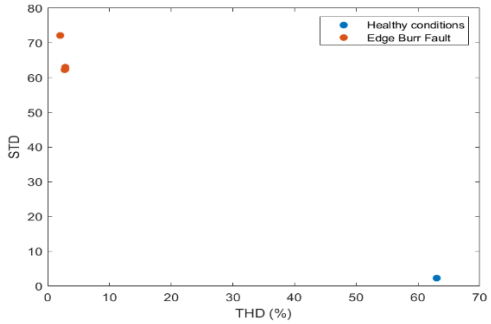

(c) Edge burr fault 1.8 T

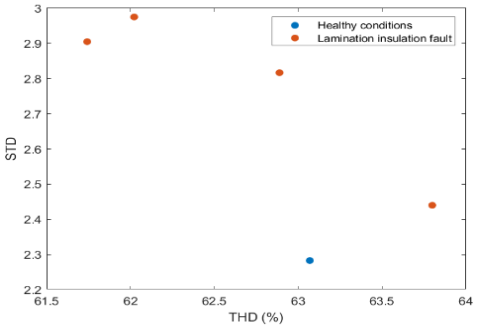

(d) Lamination insulation fault 1.8 T

Figure 5- 5: STD (A) values in as a function of the THD of the transformer currents under multi flux density for both the healthy and faulty conditions

5.3 Dataset

The FFT technique was applied to the measured current under both healthy and faulty conditions. Features are extracted from the transformer currents, and four features have been considered: the average value, the magnitude of the fundamental, total harmonic distortion (THD), and the standard deviation (STD). The average value comes from simple lone, average = the fundamental * magnitude / 100. Table 5-2 gives the selected features extracted from the current signal at 0.5 T flux density, representing a relatively low flux density.

Table 5- 2: Features in Normal and Faulty Condition at 0.5 T Flux Density

State		Selected Features			
		average (mA)	fundamental (A)	THD (%)	STD (A)
H		0.0588	0.049	41.74	0.0383
F1	S1 in 2 Places	0.0611	0.0874	28.88	0.062
	S1 in 3 Places	0.0619	0.08261	27.14	0.062
	S2 in 2 Places	0.059	0.139	16.82	0.0986
	S2 in 3 Places	0.0563	0.1342	20.33	0.0986
	S3 in 2 Places	0.0652	0.0441	57.39	0.0344
	S3 in 3 Places	0.0654	0.0404	56.64	0.0344
	S4 in 2 Places	0.0556	0.1326	19.32	0.0985
	S4 in 3 Places	0.0654	0.1369	22.84	0.0985
F2	2 places	0.0639	0.0862	30.23	0.0653
	6 places	0.0547	0.14	17.63	0.1006
	8 places	0.0623	0.1395	19.91	0.1022
	12 places	0.0586	0.1599	15.34	0.1162
H: healthy- F1: Edge burr fault- F2: insulation fault					

As shown in this table, the average values for the healthy and faulty cases are not practically different AT 0.5 T; the healthy is 0.0588 A, the highest point is 0.0654 A in fault 1, and the lowest point is 0.0556 A. These results are logical, as shown in table 5-2 due to the fact that the continuous component of the current signal can be neglected. Also, the results indicate that both types of faults do not affect the symmetry in the current signal. Furthermore, it is clear that the fundamental values are practically different for the healthy and the other faults. While the healthy value is 0.049 A, the highest point is in fault 1, which is 0.139 A, and the lowest point is 0.040 A. On the other hand, the values of the total harmonic distortion (THD) are also not that much different; they are less than the values of fundamental features and better than the values of Average features.

For a relatively high flux density of 1.7 T, table 5-3 gives the selected four features under both healthy and faulty conditions.

Table 5- 3: Features in Normal and Faulty Condition At 1.7 T Flux Density

state		Selected features			
		Average (mA)	Fundamental (A)	THD (%)	STD (A)
H		0.0682	0.6149	16.64	0.4547
F1	S1 in 2 Places	0.067	0.654	14.73	0.4666
	S1 in 3 Places	0.0667	0.661	16.14	0.4818
	S2 in 2 Places	0.0612	0.598	16.09	0.4209
	S2 in 3 Places	0.0552	0.737	15.99	0.5313
	S3 in 2 Places	0.677	0.677	16.09	0.4809
	S3 in 3 Places	0.067	0.67	15.79	0.4812
	S4 in 2 Places	0.0677	0.684	16.12	0.4945
	S4 in 3 Places	0.0596	0.765	16.10	0.5462
F2	2 places	0.0612	1.113	50.14	0.8939
	6 places	0.0612	1.303	57.85	1.0624
	8 places	0.0587	1.175	56.94	0.9495
	12 places	0.0612	1.459	54.77	1.1576
H: healthy- F1: Edge burr fault- F2: insulation fault					

Comparing between faulty and healthy conditions, the results are separated in this table compared to those obtained for relatively low flux density. In this case, the margin between the obtained results in healthy conditions differs from those measured when a fault is applied.

As shown in this table 5-3, the fundamental values for the healthy and faulty cases are practically different AT 1.7 T; the healthy is 0.614 A, the highest point is 1.459 A in fault 2, and the lowest point is 1.113 A. These results are good of fault detection.

5.4 Methods of fault detection and classification

This section describes the methods used to detect and classify faults in the transformer core. The database samples used to train and test the classifiers have been presented and discussed. The section also provides the obtained accuracy rate of each classifier for different datasets.

5.4.1 Classification algorithms

For detection and classification, three classifiers have been exploited. These include SVM, KNN, and DT techniques. SVM techniques are usually used in classification problems, prediction models, and regression [21]. For the classification problems, the principle of the SVM is to find hyperplanes of separation between two classes *yi* and *yj*. The hyperplanes should be with maximum margin. Find the hyperplane solution, which means the classification becomes an optimization problem. The optimization solution is particularly important because hyperplanes represent the decision boundaries that help to distinguish two different classes [22]. A hyperplane is a line or a plane that separates a multidimensional space into two parts. In SVM, the hyperplane is used to separate the data into different classes. The hyperplane is chosen such that it maximizes the margin, i.e., the distance between the hyperplane and the closest data points of the different classes.

The second classifier consists of the KNN algorithm. In this algorithm, the classifier's decision can be obtained from the vote of the KNN. The vote is based on calculated distances between the sampling points to the nearest neighbors of the total assigned points. Gaussian, triangular, and cosine are some of the typical distances used in this classifier. It should be noted that the KNN technique is easy to implement and apply to any problems, including complex ones such as geographic information, text, images, and sound [23], [24]. The method performance depends on the distance type, the number of neighbors, and how the neighbors' responses are combined. The results could be of inferior quality if the number of relevant attributes is low relative to the total number of characteristics. The distances on the irrelevant attributes will

drown out the proximity on the appropriate attributes. The calculations made in the classification phase can be very time-consuming if the number of data sets is too large.

A visual example of KNN Imagine you have a scatter plot with points that represent different classes, for example red dots for class A and blue dots for class B. When a new data point (represented by a green dot) is added to the plot, KNN algorithm classifies this new point based on its K nearest neighbors (in this case, K=3). So if two of the three nearest neighbors are red dots (class A) and one is a blue dot (class B), the new data point would be classified as class A.

The third classifier consists of the decision tree (DT) algorithm. This technique obtains a decision following the tree, starting from a root node down to a leaf node [25]. The leaf node comprises the classifier response.

5.4.2 Datasets for training and testing

The dataset for training and testing the model has been managed by considering different scenarios:

1. decomposition of the dataset for training and testing.

- Three types of decomposition of the database have been selected randomly. The decomposition 30-70 means that 30% of the database is reserved for the training process and 70% for testing. The second type of decomposition is 50-50 50% of the database used for training, and the remaining 50% of data is exploited for testing. The last decomposition is based on 70% for the training phase and 30% for testing.
- The K-Fold cross-validation strategy used to train the dataset for machine learning classifiers

2. managing the detection and classification form for both fault types in different scenarios in order to prove the validity of experimental results and the reliability of lamination faults detection and classification by artificial intelligence.

5.5 Results and discussion

5.5.1 Fault detection based on current signals

In this section, both types of faults have been grouped to form a separate class, representing the results of the faulty operation mode. And the dataset for training and testing was selected randomly. Therefore, a binary classification (healthy and faulty) is formulated where the aim is to detect the presence of faulty conditions. This process is based on the features extracted from the measured current. Table 5-4 gives the accuracy rate obtained using three different

classifiers, which is the ratio of the number of correct decisions over the total number of samples for each given class. As provided in the following equation.

$$\text{Accuracy rate} = \frac{\text{the number of correct decisions}}{\text{the total number of samples}} \quad (5\text{-}1)$$

Table 5- 4: Accuracy Rate for Fault Detection Execution

Scenario	**Accuracy Rate (%)**		
	SVM	KNN	DT
70-30	94.87	97.43	96.94
30-70	93.88	91.26	97.43
50-50	94.61	96.15	96.92

The obtained results show that the proposed classifiers give roughly equivalent results for the three proposed scenarios (data decomposition for training and testing). Overall, the accuracy rate is around 90%, with a maximum of 96.92%, obtained when using half of the dataset for the training with the DT classifier. And around 90%, with a maximum of more than 97%, was obtained when using 70% of the dataset for the training with the KNN classifier, which was the highest. In addition, approximately 90%, with an upper limit of more than 97%, was obtained using 30% of the dataset for training the DT classifier. This indicates that the input vectors' number and quality have an important impact on the detection results. And from the confusion matrices, one can get a general understanding of the classification process. For example, precision and recall can be defined for each of the classes in figure 5-5.

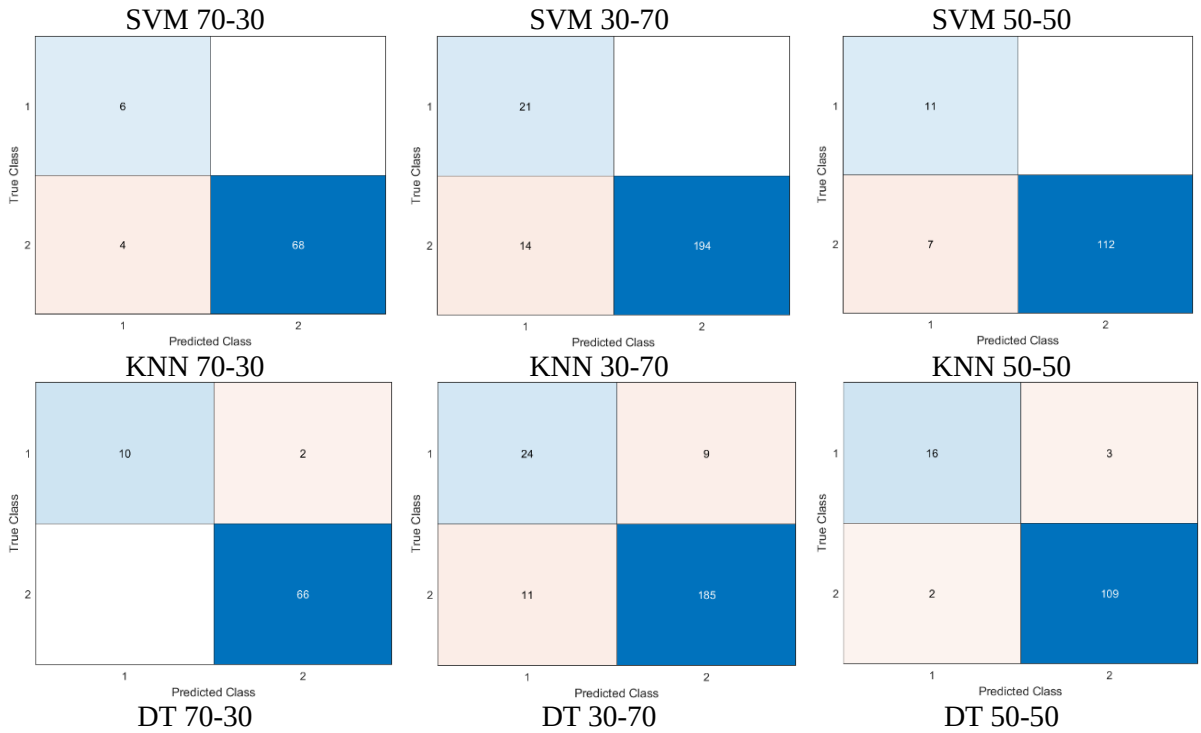

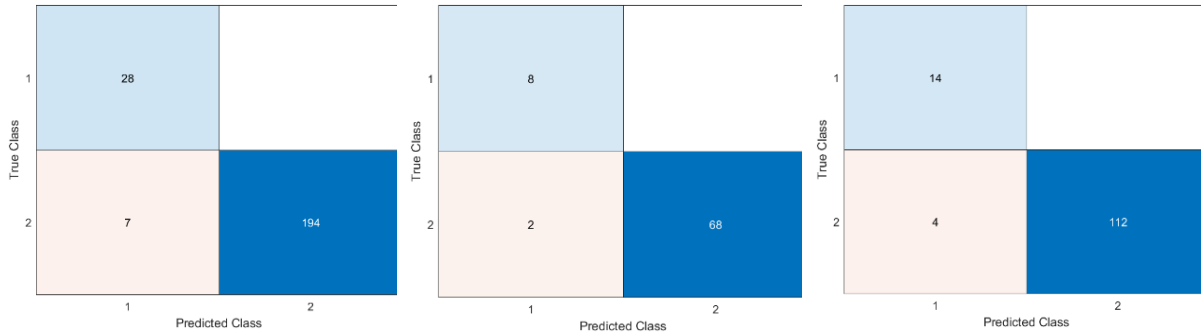

Figure 5- 6: Confusion matrix obtained using training/testing scenarios for the three classifiers of Healthy and both Faults

In general, the results indicated that fault detection was successful and accurate, especially when using 70% of the dataset for the training. The (KNN) classifier achieved the highest accuracy of detection. And the (DT) classifier achieved slightly lower accuracy. At the same time, the (SVM) classifier achieved the most insufficient accuracy. Such findings encouraged the direction of fault detection and classification of lamination faults in electrical transformers.

5.5.2 Classification between both types of laminations faults

Based on current signals, the classification between healthy and faulty conditions of both types of faults individually saved in one file has been considered. (The classes become a three-group classification). Table 5-5 provides the calculated results using the three classifiers and for three scenarios of the training and testing process. The results in this table show the accuracy rate of the three-class see eq (5-1).

Table 5- 5: Global Accuracy Rate for Fault Classification

Scenario	**Accuracy Rate (%)**		
	SVM	KNN	DT
70-30	92.30	97.43	97.43
30-70	90.82	91.26	96.94
50-50	91.53	96.15	97.69

The results of the fault classification show that the KNN classifier outperforms the DT and SVM classifiers in terms of accuracy rate. The SVM classifier's accuracy rate is influenced by the size of the training dataset, with rates of 92.30% and 91.53% for the 70/30 and 50/50 decomposition scenarios, respectively. On the other hand, the KNN classifier achieved an accuracy rate of 97% for the 70/30 training dataset and 91.26% for the 30/70 training dataset. The DT classifier performed the best, with accuracy rates of 97.43% for the 70/30 training dataset and 97.69% for the 50/50 training dataset. These results are noteworthy considering the random selection of the training dataset. The DT classifier produced the highest accuracy for

the three-class group. The confusion matrices provide valuable insights into the classification process, such as precision and recall for each class figure 6.

In conclusion, the results indicate that fault classification was successful and accurate, particularly when 50% of the dataset was used for training. The DT classifier achieved the highest accuracy, followed by the KNN classifier, while the SVM classifier showed the lowest accuracy. These findings demonstrate the potential for the effective detection and classification of lamination faults in electrical transformer cores using current signals.

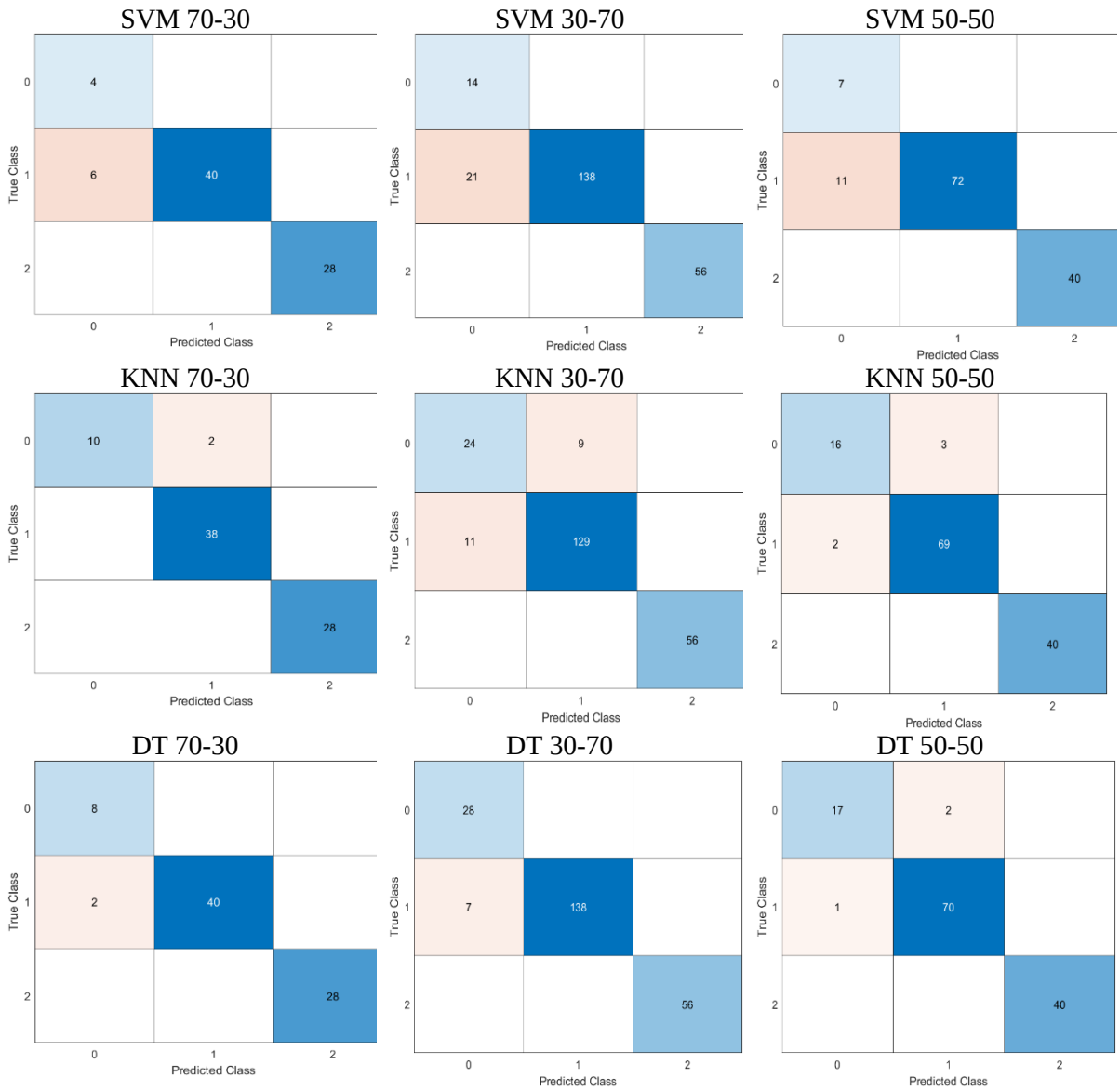

Figure 5- 7: Confusion matrix obtained using training/testing scenarios for the three classifiers of the insulation damage Fault

In general, the results indicated that the fault classification was successful and accurate, especially when using 50% of the dataset for the training. The (DT) classifier achieved the highest accuracy in faults classification. And the (KNN) classifier achieved slightly lower accuracy. In comparison, the (SVM) classifier achieved the lowest accuracy. Such findings encouraged the direction of fault detection and classification of lamination faults based on current signals in electrical transformers core.

5.5.3 Results of fault detection for each fault separately

Based on the current signals, the detection between the health and faulty conditions of each type of fault has been considered in this part. (The classes become a two-group classification for each fault). Table 5-6 provides the calculated results using the three classifiers and for three scenarios of the training and testing process. The findings in this table reflect the accuracy rate of each class for each defect, which is the ratio of the number of accurate answers to the entire number of samples for each offered class.

Table 5- 6: accuracy rate for each class of faults using different classifiers and considering three scenarios

Class	**Training - Testing Data**	**Accuracy Rate (%)**		
		SVM	KNN	DT
Fault 1	70-30	91.17	97.05	91.17
	30-70	82.35	91.17	85.29
	50-50	90.19	92.15	84.31
Fault 2	70-30	88.00	96.00	96.00
	30-70	87.86	88.43	95.95
	50-50	87.77	94.44	96.66

From this table, one can clearly see that the detection results are affected by the type of fault. For instance, the edge burr fault (Fault 1) shows a better result for fault detection. With SVM and DT classifiers, when using larger data in the training process (70% dataset for training), they obtained 91.71% and slightly lower when using 50% dataset for training. The obtained accuracy was around 97.05% when using 70% of the dataset for the training with KNN classifier, which was the highest, while the accuracy was around 92.15% obtained when using 50% of the dataset for the training with the KNN classifier. This means that the Edge Burrs fault can be easily identified from the other faults. This result is consistent with previous findings reached based on the experimental findings in Chapter 4.

In addition, the results of the second fault also show good accuracy for all the considered cases. With the KNN and DT classifiers, the accuracy obtained was around 96% when using 70% of the dataset for the training. Whereas, when 50% of the dataset for the training was used, the

accuracy rate was slightly lower, more than 88% and 95%, respectively. While for the SVM classifier accuracy obtained was 88% when using 70% of the dataset for the training and more than 87% when 50% of the dataset for the training was used. This means that the other faults can easily identify the lamination's insulation fault. This ascertainment is in accordance with the conclusion made from the experimental results in chapter 4.

Edge Burrs Fault (Fault1)

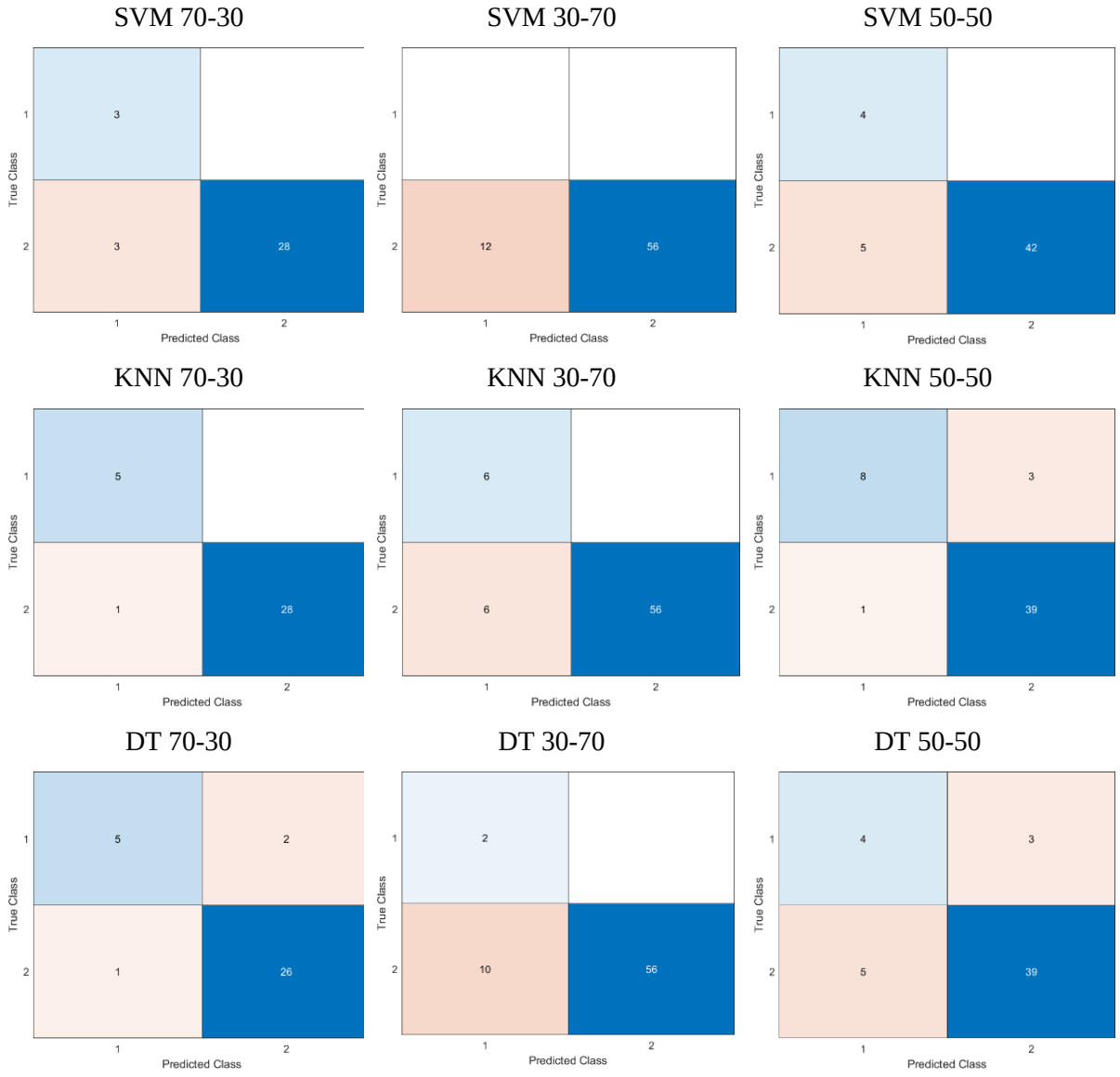

Figure 5- 8: Confusion matrix obtained using training/testing scenarios for the three classifiers of Edge Burrs Fault

Insulation Damage (Fault 2)

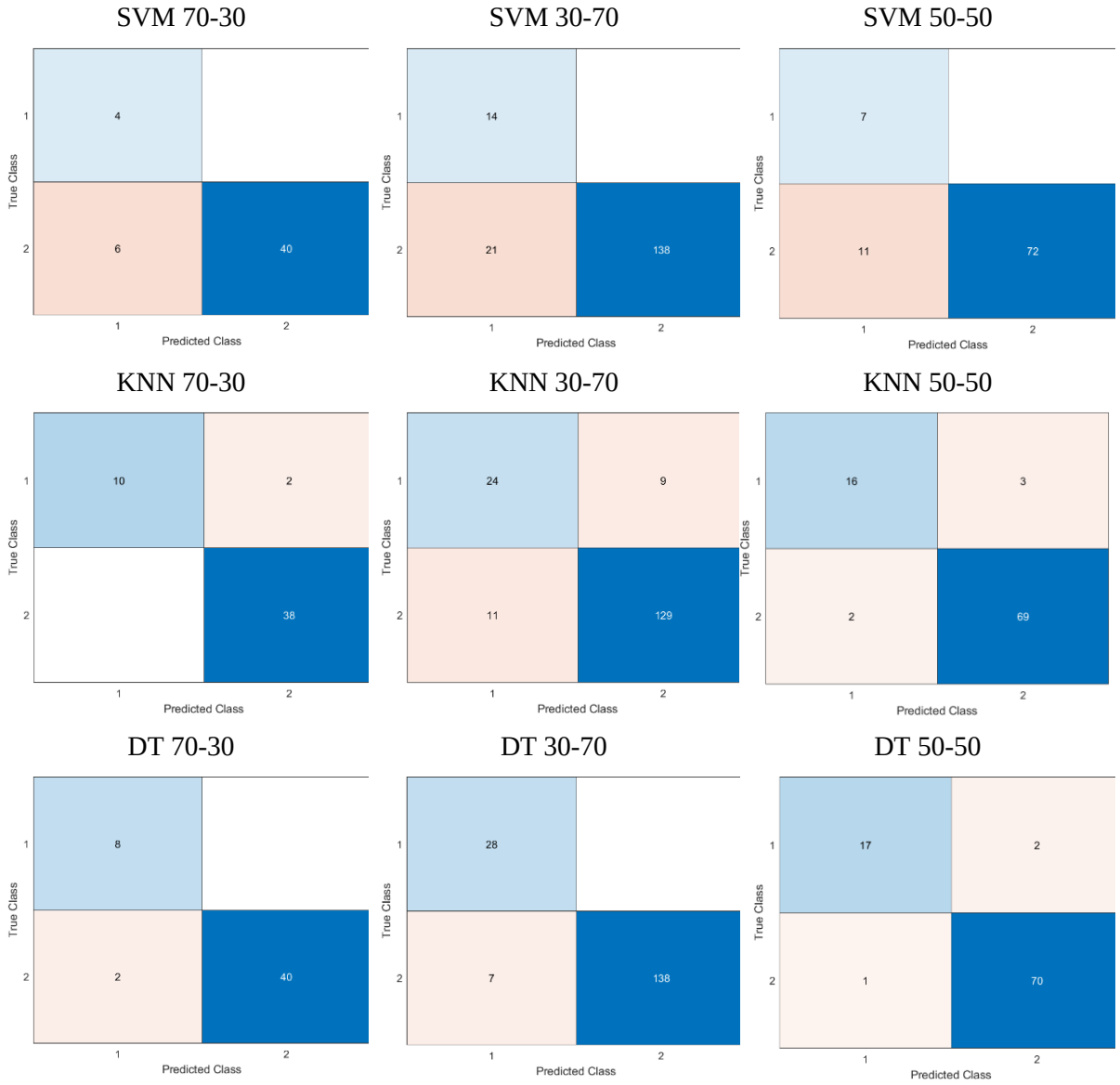

Figure 5- 9: Confusion matrix obtained using training/testing scenarios for the three classifiers of the insulation damage Fault

The results generally indicated that the fault classification was successful and somehow accurate, especially when using 70% of the dataset for the training. The (KNN) classifier achieved the highest accuracy in faults classification. And the (DT) classifier achieved slightly lower accuracy. Where the (SVM) classifier achieved the lowest accuracy. The accuracy rate for the second fault shows a slight decrease.

Moreover, the results show relatively different accuracy rates, especially when using 30% of the dataset for the training. The overall accuracy rate for fault detection of each fault is

satisfactory and presented in table 5-6. Such results present encouragement in the direction of fault identification and categorization of lamination problems in electrical transformer cores using current signals.

5.5.4 Fault Classification between healthy and different faulty scenarios using a random dataset

In this section, based on current signals the classification results between healthy and the different scenarios of each fault. Based on what was explained in the previous chapter, each fault has a set of scenarios. For example, the insulation damage fault was performed with 2, 6, 8, and 12 laminations with several specified flux density values, which were 0.5, 0.8, 1.0, 1.5, 1.7, and 1.8 T. As well as the Edge Burrs fault was investigated in several scenarios that were also explained in the same mentioned chapter to prove and confirm these mentioned target faults and their impact on the performance of the transformer core. The scenarios of each fault have been grouped to form a separate category, with multi-classification scenarios (healthy, and the scenarios of faulty 1, 2, 3, 4.) formulated where the aim is to detect and classify the presence of each scenario. After the satisfactory results obtained from the detection and classification of the two main mentioned faults, the role of detecting the fault scenarios comes in order to increase the tools of detecting such faults and to be focused in the future.

With the expected results, a relatively low accuracy rate has been obtained because of the low amount of dataset collected for this purpose due to not being focused on since it was not the main objective of the research and time limitations.

5.5.5 Edge burrs fault scenarios results

Each type of fault has been grouped to form a separate class, with multi-classification scenarios (healthy and fault scenarios 1, 2, 3, 4). designed to detect and classify the existence of each scenario. For the scenarios results of Edge Burrs fault See table 5-7. The table provides the calculated results using the SVM, KNN, and DT classifiers. For three scenarios of the training and testing process, The outcomes in this table display the accuracy rate of multi classes see eq (5-1). From the confusion matrices, one can get a general understanding of the classification process. For example, precision and recall can be defined for each class in figure 5-9.

Table 5- 7: The Scenarios of Edge Burs faults

Scenarios	**Accuracy Rate (%)**		
	SVM	KNN	DT
70-30	64.70	64.70	55.88
30-70	57.35	63.23	36.76
50-50	54.90	70.58	60.78

The findings indicate that the suggested classifiers do not produce substantially identical results for the three specified situations (data decomposition for training and testing). Overall, the accuracy rate is around 60%, with a maximum of more than 64.70%, obtained when using 70 datasets for the training with SVM and the KNN classifiers. While 60.78 % with the DT classifier when using 50% of the dataset for the training. Whereas the highest result is 70.58% when the KNN classifier is used when using half of the dataset for the training. Figure 5-9 shows the confusion matrices obtained using the three algorithms for the three scenarios.

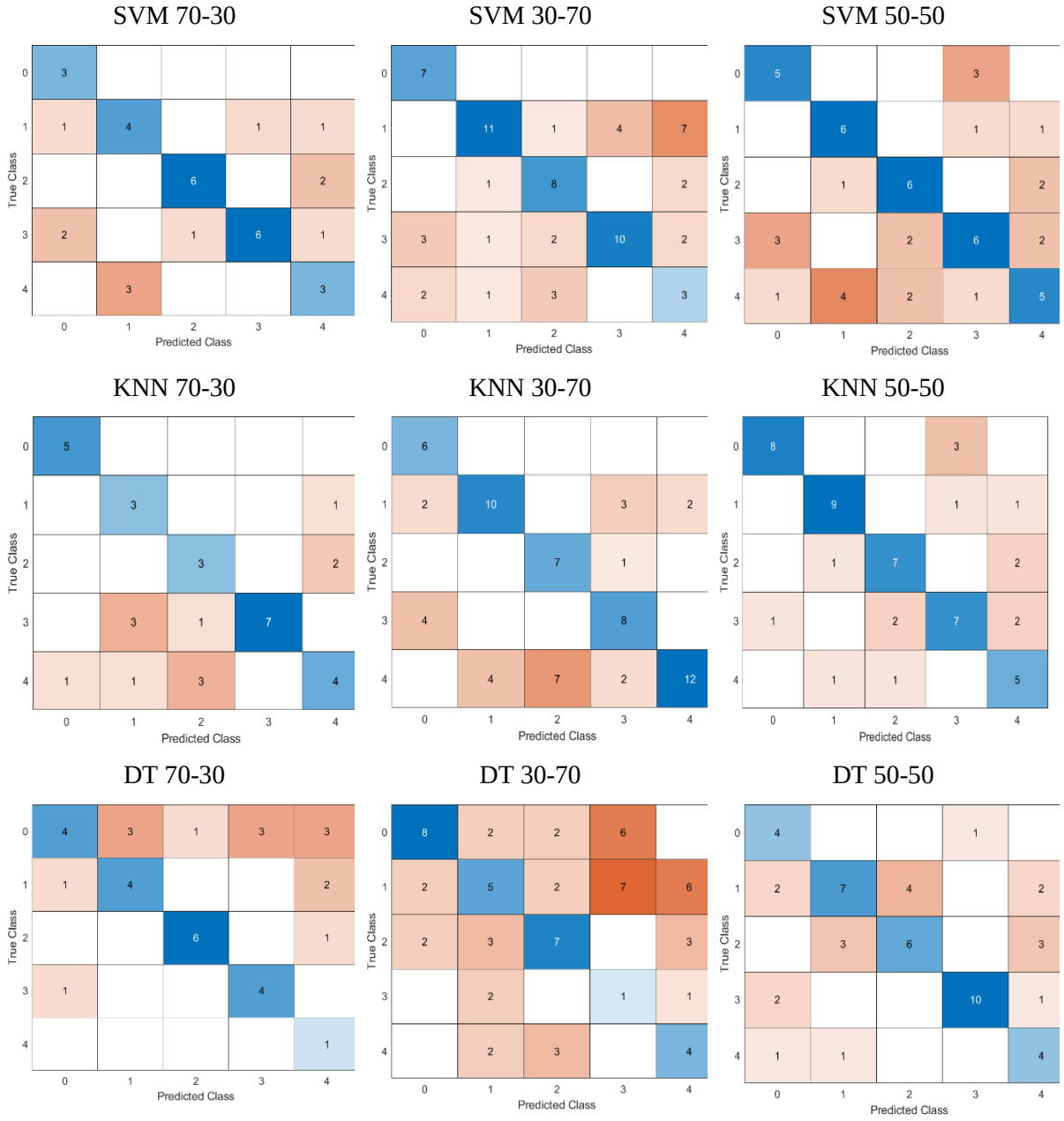

Figure 5- 10: Confusion matrix obtained using training/testing scenarios for the three classifiers of the edge burrs Fault

In general, the results indicated that the fault classification was somehow successful, especially with the KNN classifier. The KNN and SVM classifiers achieved the highest accuracy in faults classification when using 70% for dataset training. And the (DT) classifier achieved slightly lower accuracy. Such findings encouraged fault detection and classification of lamination faults based on current signals in an electrical transformer's core. In addition, this leads that the multi scenarios need more focus by increasing the number of scenarios, in data processing (feature extraction) by increasing the number of features, or in classification by choosing appropriate algorithms.

5.5.6 Insulation damage scenarios results

For the scenario results of laminations, and damage fault, see next table 5-8. The accuracy rate for many classes of this issue is shown in this table.

Table 5- 8: The scenarios of insulation damage faults

Scenarios	**Accuracy Rate (%)**		
	SVM	KNN	DT
70-30	64.00	80.00	72.00
30-70	59.53	63.58	69.36
50-50	71.11	66.66	45.55

According to the acquired results, several recommended classifiers produced fairly equal outcomes for the three offered scenarios (training and testing) when using 70% of the dataset for the training. Overall, the accuracy rate was 80% with the KNN classifier, which was the highest result and 72% obtained with the DT classifier, and 64% with the SVM when using 70% of the dataset for the training. In contrast, the accuracy rate was 71.11%, obtained when using 50% of the dataset for the training with the SVM classifier. And 66.66%, and 45.55% with the KNN and DT classifiers, respectively. This indicates that the multi-scenarios need more focus. From the confusion matrices, one can get a general understanding of the classification process. For example, precision and recall can be defined for each of the classes in figure 5-10.

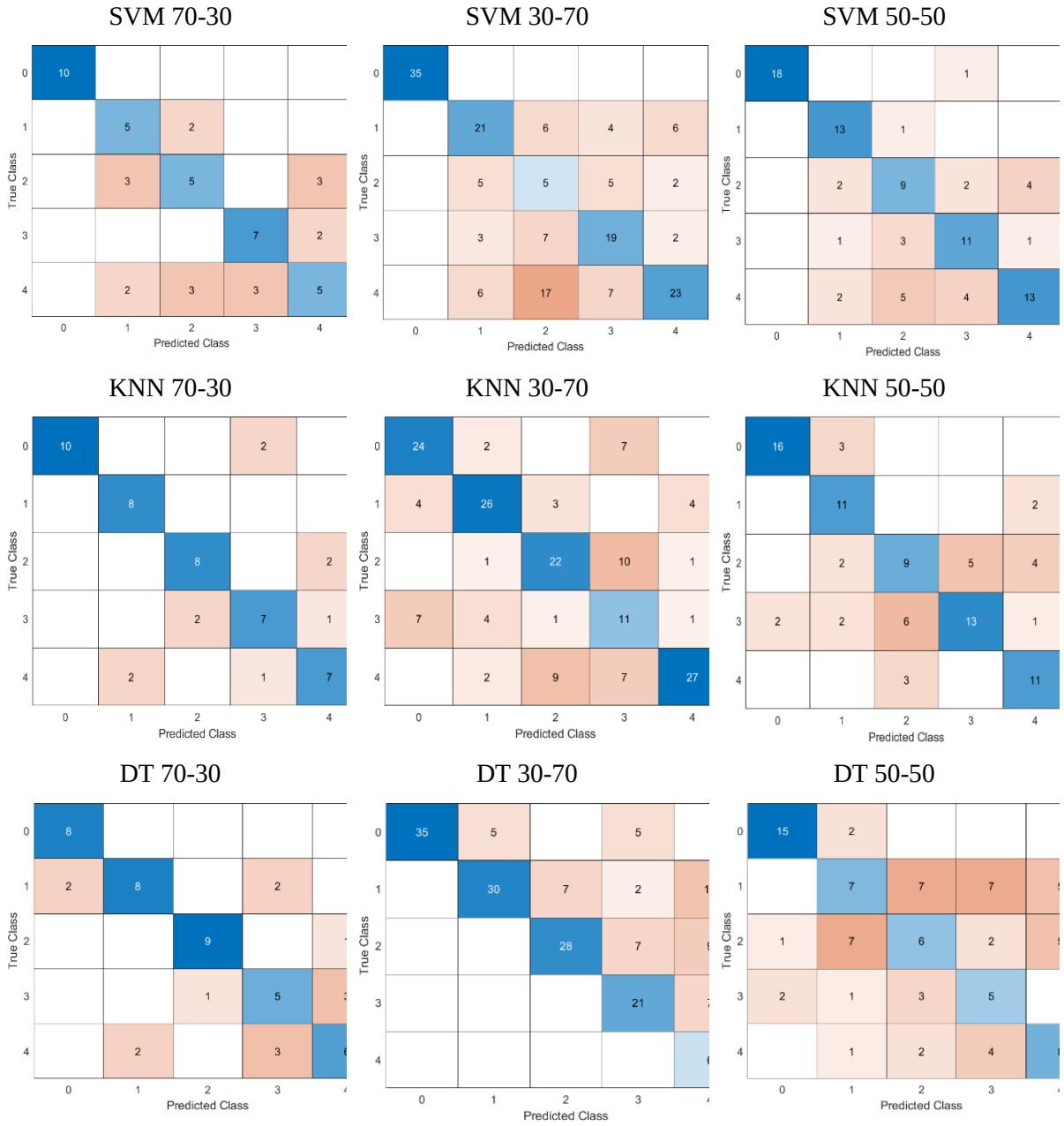

Figure 5- 11: Confusion matrix obtained using training/testing scenarios for the three classifiers of the lamination insulation Fault.

In general, the results indicated that the fault classification was successful and somehow accurate, especially when using 70% of the dataset for the training. The (KNN) classifier achieved the highest accuracy in faults classification. And the (DT) classifier achieved slightly lower accuracy. At the same time, the (SVM) classifier achieved the lowest accuracy. Such findings gave encouragement in fault classification of multi scenarios for lamination insulation fault in electrical transformers cores. However, large databases are required to reach higher

precision, and to make more accurate classifications to provide assistance in preventing the electrical system from unexpected faults.

5.6 K-fold cross-validation results

5.6.1 Definition of k-fold cross-validation

Cross-validation is a statistical method of evaluating and comparing learning algorithms by dividing data into two segments: one used to learn or train a model and the other used to validate the model. In typical cross-validation, the training and validation sets must cross over in successive rounds such that each data point has a chance of being validated against. The basic form of cross-validation is k-fold cross-validation. Other forms of cross-validation are special cases of k-fold cross-validation or involving repeated rounds of k-fold cross-validation [38]. Figure 5-11 shows how K-fold cross-validation works.

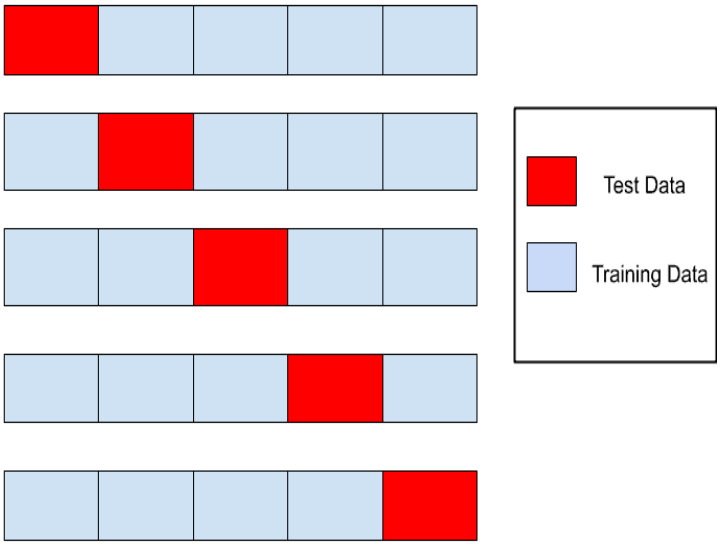

Figure 5- 12: How does K-Fold Cross-Validation Working in Machine Learning [39]

In this section, the proposed application is assessed based on the experimental data of the current signals for both faults. To verify whether the proposed model, in combination with the proposed feature selection techniques to select discriminative features, benefits the fault detection procedure, the acquired signals with the same extracted features were used as inputs to the classification algorithms. The selected optimal feature subsets were applied to three machine learning models, KNN, SVM, and DT, for classification into their respective classes. The classifiers are then trained using cross-validation. The training was repeated 3-fold, 5-fold,

and 10-fold times with cross-validation techniques to fine-tune the model and ensure consistency in the results. Each classifier's performance was evaluated using its accuracy.

5.6.2 Based on current signals fault detection results using cross-validation

In this section, both types of faults have been grouped to form one class, representing the results of the faulty operation mode. And the dataset was trained by repeated 3-fold, 5-fold, and 10-fold times with cross-validation techniques. Therefore, a binary classification (healthy and faulty) is formulated where the aim is to detect the presence of faulty conditions. This process is based on the features extracted from the measured current. Table 5-9 gives the accuracy rate obtained using three different classifiers: SVM, KNN, and DT. see eq (5-1).

Table 5-9: gives the accuracy rate obtained using three different classifiers

Fold Cross-Validation	SVM	KNN	DT
(3-fold) accuracy (%)	93.81	97.07	99.67
(5-fold) accuracy (%)	94.79	97.39	99.35
(10-fold) accuracy (%)	97.33	98.47	99.24

The Decision tree classier (DT) gained the highest classification accuracy, which was 99.67%, when the model was trained with 3-fold cross-validation by applying the current signal for fault detection. And it was 99.24% when the model was trained with 10-fold cross-validation. Furthermore, when the KNN model was trained with 3-fold cross-validation, the accuracy was 97.07%, and it was further raised to 98.47% when the model was trained with 10-fold cross-validation using the current signal. In addition, the classification accuracy using the SVM classifier was 93.81% with 3 -fold and 97.33% with 10-fold cross-validation applying the current signals. And when using 5-fold cross-validation, the accuracy obtained was 94.79% with the SVM classifier, 97.39% with the KNN classifier, and 99.35% with the DT classifier.

Overall, it can be confirmed that, as stated in table 5-9, the DT classifier achieved the highest accuracy by applying the current signal, which was 99.67%, using 3-fold cross-validation. Furthermore, when the model was trained using SVM, the lowest accuracy was achieved with the use of 10-fold cross-validation, which was 97.33% for the current signal. And from the confusion matrices, one can get a general understanding of the classification process. For example, precision and recall can be defined for each class in figure 5-12.

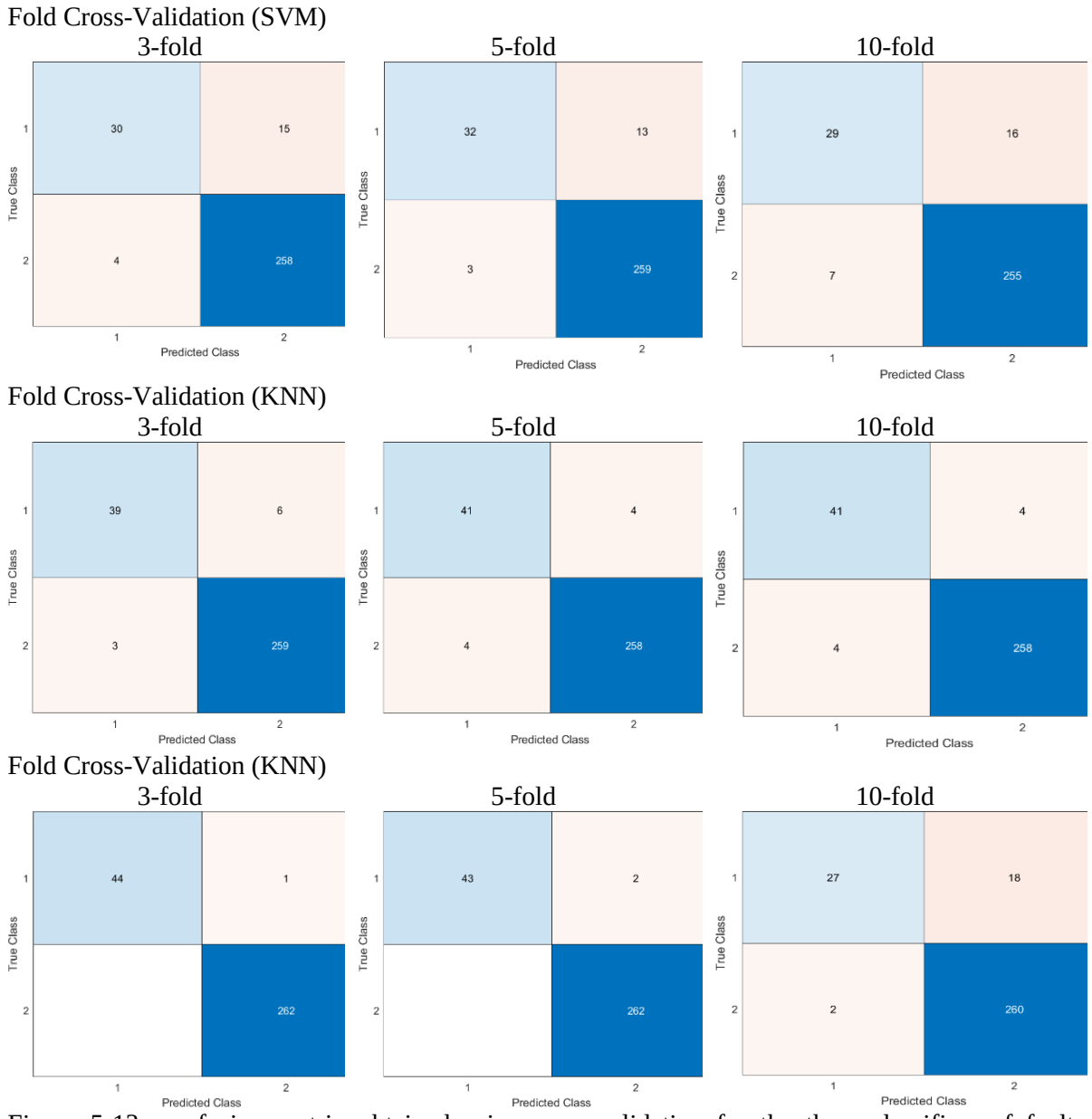

Figure 5-13: confusion matrix obtained using cross-validation for the three classifiers of fault detection

In general, the results indicated that the fault detection was successful and accurate, especially when using 10-fold cross-validation for the dataset training for most of the classifiers. The (DT) classifier achieved the highest accuracy in faults detection, and the (KNN) classifier achieved slightly lower accuracy, while the (SVM) classifier achieved the lowest accuracy. In addition, the 10-fold cross-validation of the dataset for the training gives the best results for most of the classifiers, while the 3-fold cross-validation gives fewer results accuracy for the different classifiers. This indicates that artificial intelligence can accurately detect and classify fault

detection. The study gives inspiration for identifying and categorizing lamination problems using current signals in the core of an electrical transformer.

5.6.3 Classification for both types of faults using Cross-Validation

Based on current signals, this part considers the classification between health conditions and both types of faults. Both types of faults have been separated to form two classes, and the classes become a three-group classification. Table 5-10 provides the calculated results using the three classifiers and 3,5, and 10-fold Cross-Validation for three training classes. The results in this table show the accuracy rate of the three classes together, the number of right answers multiplied by the total amount of samples for each class see eq (5-1).

Table 5-10: gives the accuracy rate obtained using three different classifiers

Fold Cross-Validation	SVM	KNN	DT
(3-fold) accuracy (%)	91.21	96.74	99.35
(5-fold) accuracy (%)	91.21	97.07	99.67
(10-fold) accuracy (%)	92.16	98.69	99.35

The DT classifier shows the best result for classification using K-fold cross-validation for the dataset training process. which was 99.67% with 5-fold cross-validation. While 99.35% with the 3, and 10-fold cross-validation. The accuracy rate for KNN shows a slight decrease. Was 96.74% with the utilization of 3-fold cross-validation. While 98.69% with the 10-fold cross-validation.

The overall accuracy rate for each case is presented in table 5-10. From this table, one can clearly see that the classification results are affected by the value of fold cross-validation. For instance, the results of the 10-fold show good accuracies for most of the considered classifiers (SVM, KNN). Moreover, the SVM shows relatively lower accuracy rates, especially when the fold value was 3 and 10 for the dataset training process, which was 91.21%. This means that each fault can be easily identified from the other. This ascertainment is in good accordance with the conclusion made from the experimental, the confusion matrices in figure 5- 13.

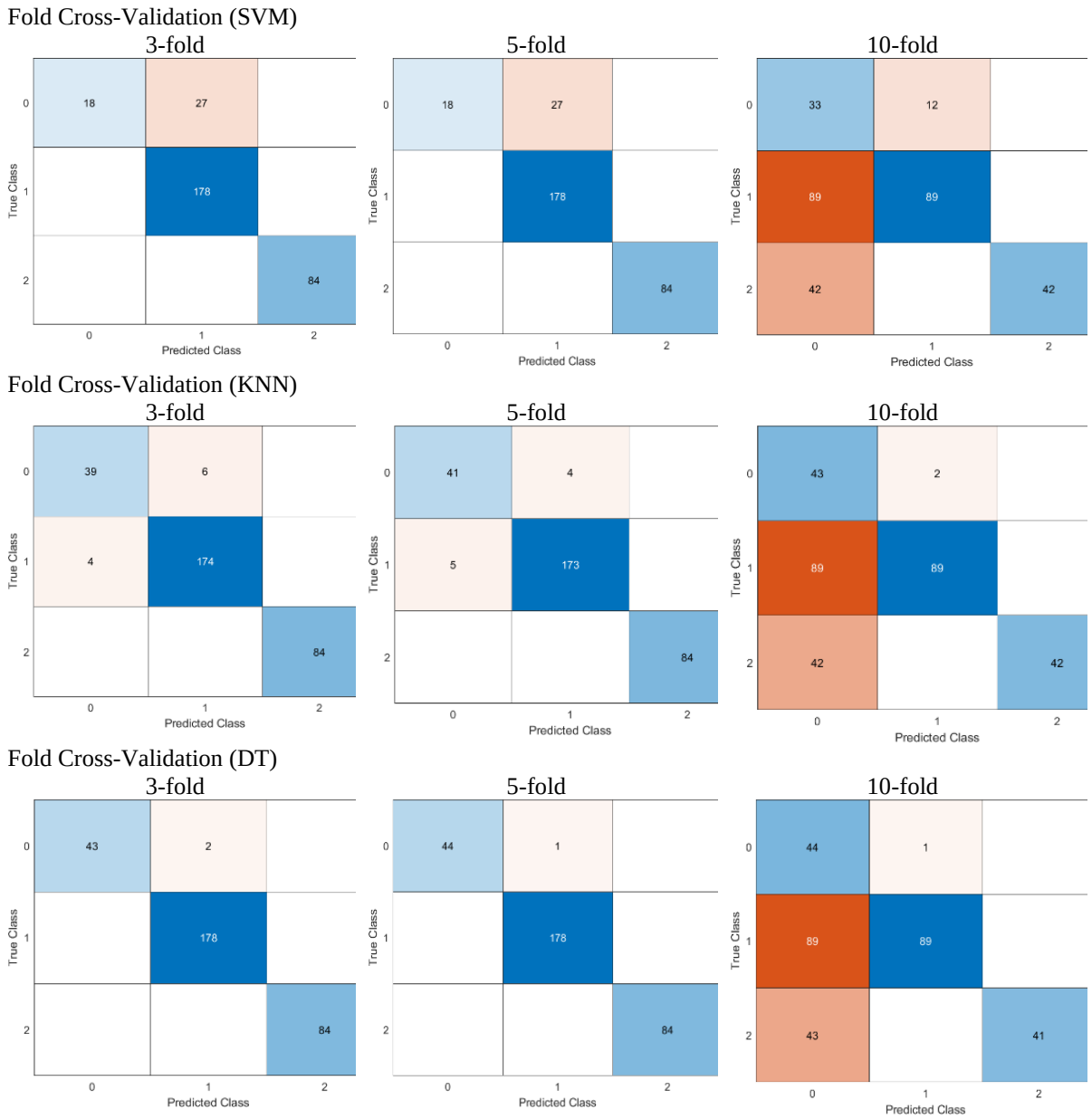

Figure 5- 14: confusion matrix obtained using cross-validation for the three classifiers of fault classification for both types.

Generally, the accuracy rate of fault classification for both types of faults using Cross-Validation is satisfactory. Again, the (DT) classifier achieved the highest accuracy in faults detection, and the (KNN) classifier achieved slightly lower accuracy, while the (SVM) classifier achieved the lowest accuracy. In addition, the 10-fold cross-validation of the dataset for the training gives the best results for most of the classifiers, while the 3-fold cross-validation gives fewer results accuracy for the same classifiers. This shows that fault classification may indeed be effectively identified and sorted using artificial intelligence. These discoveries

encouraged the categorization of lamination problems based on current signals in an electrical transformer's core.

5.6.4 Detection of each fault separately using Cross-Validation

In this section, the classification between health conditions and each type of fault separately has been considered. Every kind of fault has been separated to form one class the classes become a two-group classification. Table 5-11 provides the calculated results using the three classifiers and for three scenarios of the training and testing process. The data in this table displays the accuracy for every class individually, which is calculated as the proportion of the right selections to all samples for a certain class see eq (5-1).

Table 5- 11: accuracy rate for each class of faults using different classifiers and considering three scenarios

Class	Training - Testing Data	Accuracy Rate (%)		
		SVM	KNN	DT
Fault 1	(3-fold) accuracy (%)	82.35	95.10	84.31
	(5-fold) accuracy (%)	83.33	94.12	90.20
	(10-fold) accuracy (%)	95.24	97.62	92.86
Fault 2	(3-fold) accuracy (%)	87.89	96.41	99.10
	(5-fold) accuracy (%)	87.89	95.07	99.55
	(10-fold) accuracy (%)	90.48	97.75	99.29

From this table, one can clearly see that the classification results are affected by the type of fault and the classifiers. Each classifier is given a different result. The highest obtained accuracy for the first fault (Edge Burrs Fault) was around 90 %. With a maximum of 97.62 % with the KNN classifier when using 10-fold cross-validation for the dataset training. Whereas 92.86 % with the DT classifier and 95.24 % with the SVM classifier when using 10-fold cross-validation for the dataset training. However, the accuracy decreased relatively when using 3-fold cross-validation for the dataset training, where 82.35 % was obtained with the SVM classifier, 95.10 % with the KNN classifier, and 84.31% with the DT classifier.

In addition, the highest obtained accuracy for the second fault (insulation damage fault) was around 99 %. With a maximum of 99.55 % with the DT classifier when using 5-Fold cross-validation for the dataset training. And 99.10 % and 99.29 % when using 3, and 10-fold cross-validation for the dataset training, respectively. However, the accuracy decreased relatively with the other classifiers when using 10-fold cross-validation for the dataset training. The accuracy was 97.75 % with the KNN classifier and 90.48 % with the SVM classifier. When using 3-fold cross-validation for the dataset training, the accuracy slightly decreases where 96.41 % with the KNN classifier and 87.89 % with the SVM classifier.

Overall, the results of the second fault show better accuracies for all the considered cases, especially with the DT classifier. This means that the lamination's insulation fault can be easily identified from the other conditions. In addition, edge burr faults also show a good result for fault detection with the KNN classifier. The evidence gathered from the experimental data in the preceding chapter is well supported by this determination. And from the confusion matrices, one may gain a general idea of the categorization procedure. For each of the classes, one can define accuracy and recall, for instance, in figures 5-14 and 5-15.

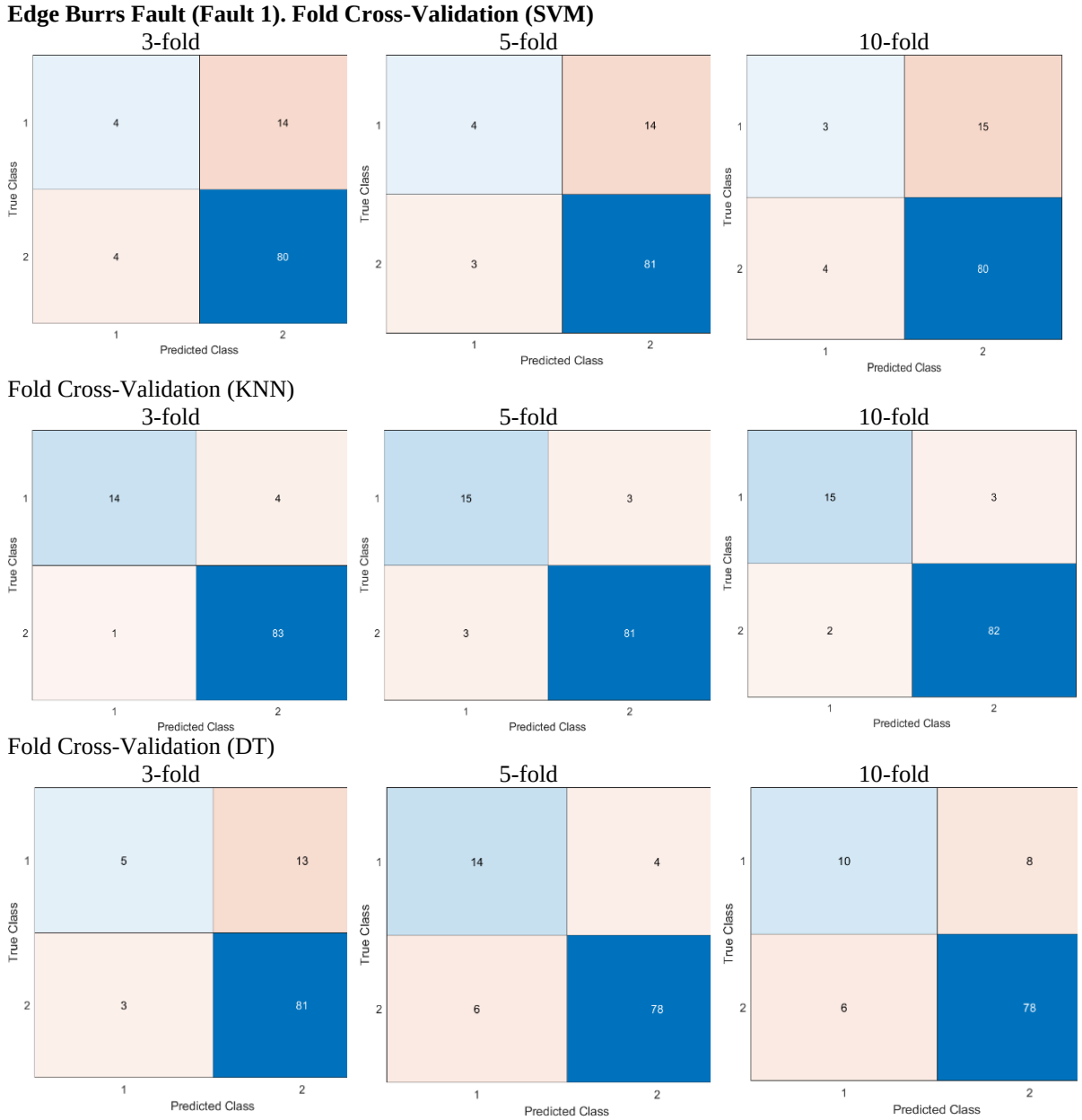

Figure 5- 15: Confusion matrix obtained using cross-validation for the three classifiers of fault classification for Edge Burrs fault (Fault 1).

Insulation Damage (Fault 2). Fold Cross-Validation (SVM)

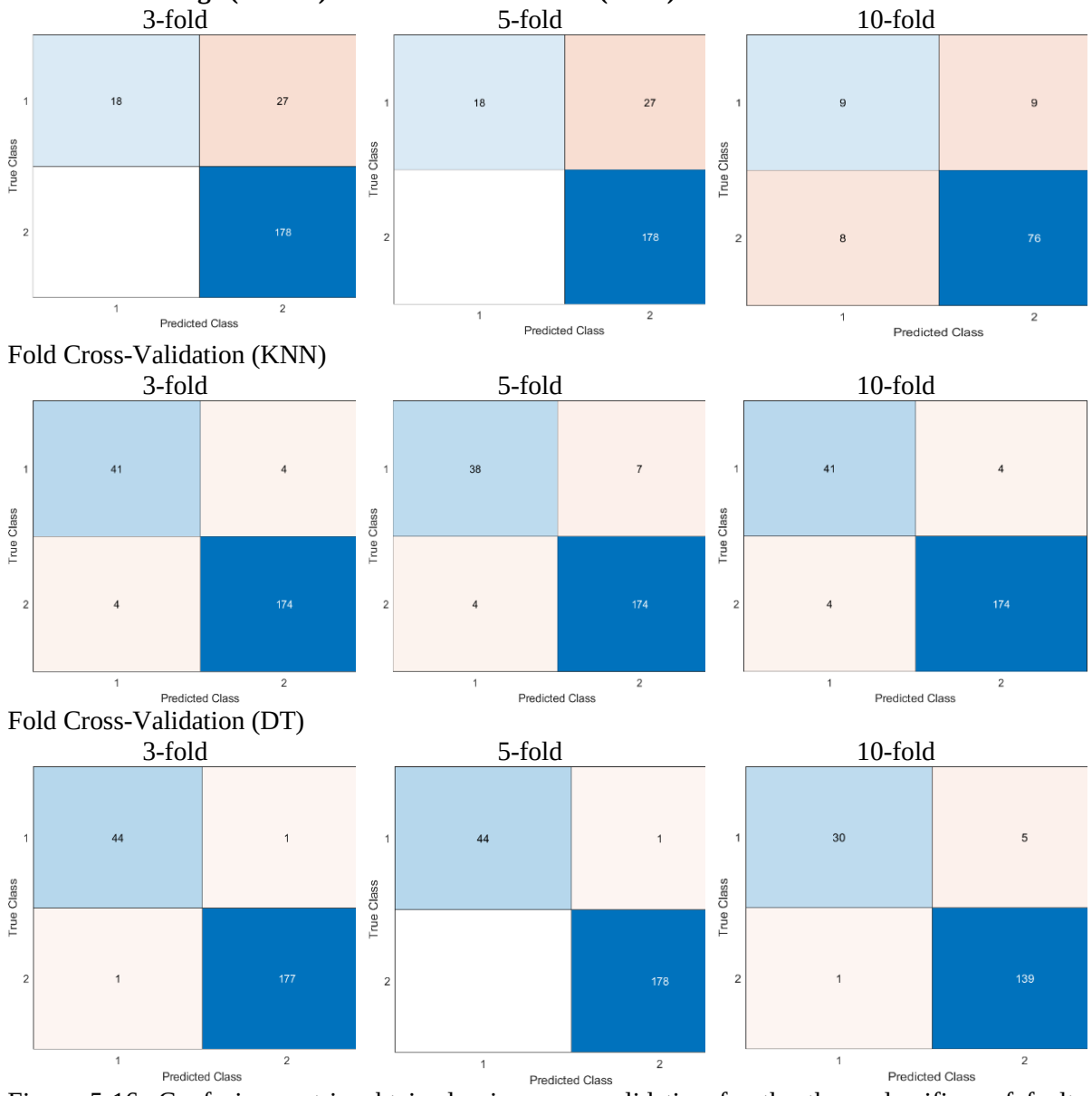

Figure 5-16: Confusion matrix obtained using cross-validation for the three classifiers of fault classification for the insulation damage Fault (Fault 2).

In general, the findings of the detection of each fault separately using Cross-Validation indicate that the proposed fault detection model can be generated using current signals and has a superior performance based on the accuracy results. The classification algorithms are essential for fault detection and classification in a detection model. The KNN classifier outperformed the DT and SVM classifiers in the first fault, especially when using 10-fold cross-validation, while the DT classifier outperformed the second fault in most cases in determining the correct class, especially when using 5-fold cross-validation. Additionally, applying a 10-fold cross-validation

strategy to train the proposed models could enhance classification accuracy with most of the classifiers.

5.6.5 Fault classification between healthy and different faulty scenarios using k-fold cross-validation

The classification accuracy results are presented between healthy and the different faulty scenarios based on the current signals of each fault. And according to what was explained in chapter 4, each fault has a set of scenarios. For example, the insulation damage fault was performed with 2, 6, 8, and 12 laminations with several specified flux density values, which were 0.5, 0.8, 1.0, 1.5, 1.7 and 1.8 T. As well as the Edge Burrs fault was investigated in several scenarios that were also explained in the same mentioned chapter in order to prove and confirm these mentioned target faults and their impact on the performance of the transformer core. After the satisfactory results obtained from the detection and classification of the two main mentioned faults, the role of detecting the scenarios comes in order to increase the tools and methods of detecting these kinds of faults and to be targeted in the future. With the expected results, a good accuracy rate has been obtained because of enough datasets collected for this purpose due to being focused on since it was the main objective of the research.

5.6.6 Edge burrs fault

Each fault's scenarios have been grouped to form a multi-class (healthy and fault scenarios1, 2, 3, 4.) formulated where the aim is to detect and classify the presence of each scenario. For the scenarios results of Edge burrs fault, see table 5-12. The table provides the calculated results using the SVM, KNN, and DT classifiers, and the training was repeated three, five, and ten times with cross-validation techniques to fine-tune the model and ensure consistency in the results for the four scenarios of the fault. The results in this table show the percentage of right answers across all samples for a specific class, which is the acquired accuracy of several classes see eq (5-1).

Table 5- 12: The Scenarios of Edge Burs faults

Fold Cross-Validation	SVM	KNN	DT
(3-fold) accuracy (%)	54.90	62.78	50.00
(5-fold) accuracy (%)	52.94	63.73	57.84
(10-fold) accuracy (%)	88.10	96.43	85.71

The obtained results show that the proposed classifiers do not give roughly equivalent results for the proposed scenarios (data decomposition for training and testing of the scenarios of edge burrs fault). Overall, when using 10-fold cross-validation of the dataset for the training, the accuracy rate is around 50 %, with a maximum of more than 88.10 % obtained with the SVM

classifier. On the other side, around 60 % was the obtained accuracy with a maximum of more than 96.43 % using the KNN classifier, which was the highest result. While it was 85.71 % with the DT classifier. However, the accuracy decreased relatively when using 3-Fold cross-validation for the dataset training, where the accuracy was 50.00 % with the DT classifier, which was the lowest result obtained. In comparison, the accuracy was 62.78 % with the KNN classifier and 54.90 % obtained with the SVM classifier. Therefore, one may gain a broad idea of the classification process from the confusion matrices. Within each of the classes, for instance, accuracy and recall can be defined in figure 5-16.

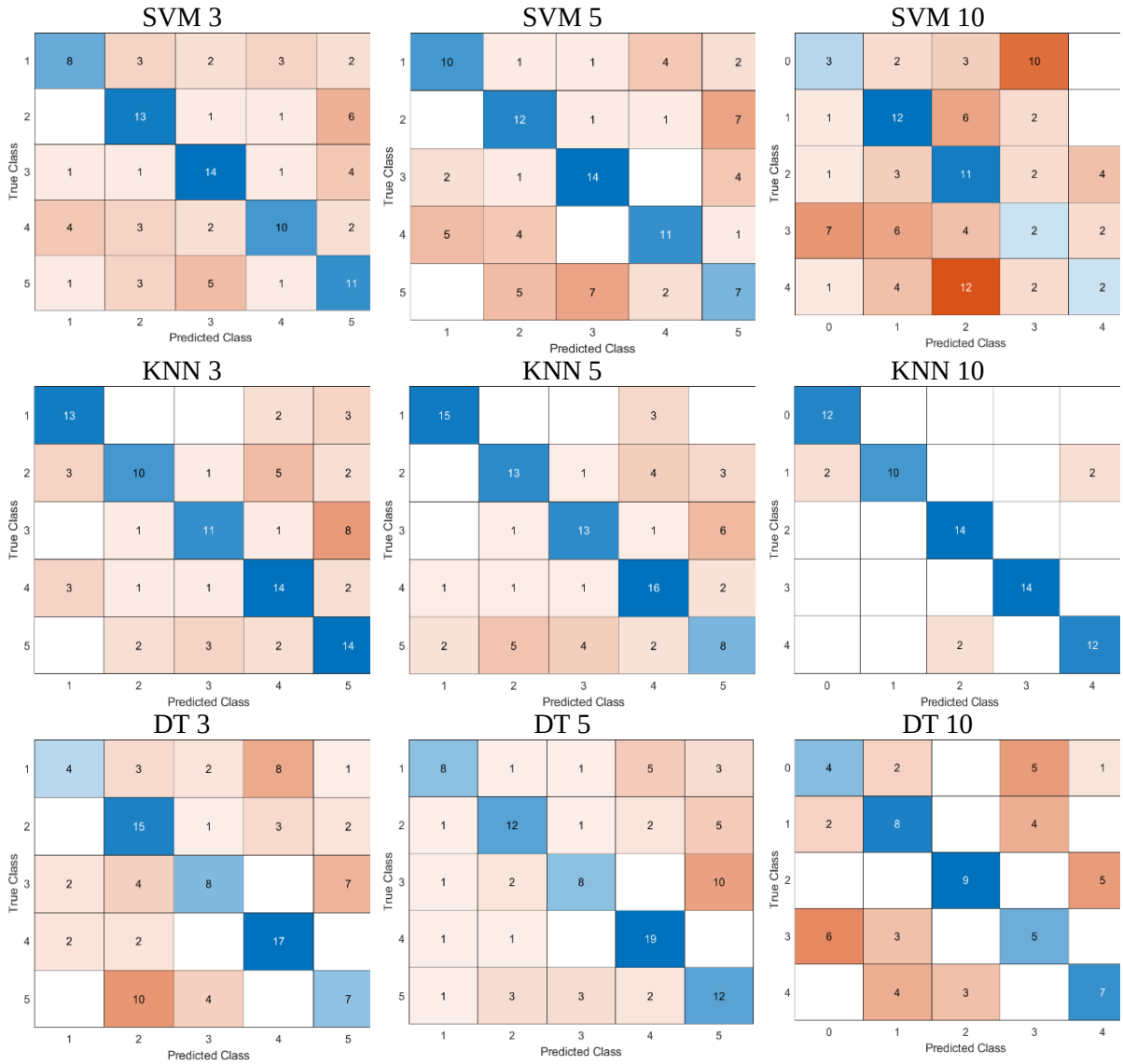

Figure 5- 17: Confusion matrix obtained using training/testing scenarios for the three classifiers of the insulation damage Fault

In general, 10-Fold cross-validation of the dataset for the training gives the best results while the 3-Fold cross-validation gets fewer results accuracy for the different classifiers. The (KNN) achieved the highest classification accuracy. This indicates that the multi scenarios of the faulty conditions need more focus, such as collecting more data and extracting more features using different feature extraction techniques.

5.6.7 Insulation damage fault results

For the results of faulty mode scenarios of laminations and damage fault, see next table 5-13. The results in this table display the accuracy rate for many classes of this issue, eq (5-1).

Table 5- 13: The scenarios of insulation damage faults

Fold Cross-Validation	SVM	KNN	DT
(3-fold) accuracy (%)	63.95	74.25	90.99
(5-fold) accuracy (%)	68.24	77.68	94.85
(10-fold) accuracy (%)	99.29	97.86	95.71

The obtained results show that some proposed classifiers gave roughly equivalent results for the proposed scenarios. Overall, 95 % is the average accuracy rate obtained using the DT classifier with a maximum of 94.85 %, obtained when using 5-fold cross-validation of the dataset for the training, which was the highest result, and 90.99% obtained with 3-fold cross-validation, which is the lowest. However, with the KNN classifier, around 70% accuracy rate was obtained with a maximum of more than 78 % using 10-fold cross-validation and 74.25% obtained with 3-fold cross-validation. On the other side, 90 % was obtained with the SVM classifier when using 10-fold cross-validation of the dataset for the training, and 63.95% was obtained with 3-fold cross-validation, which is the lowest obtained result to get a general grasp of the categorization process, see the confusion matrices in figure 5-17.

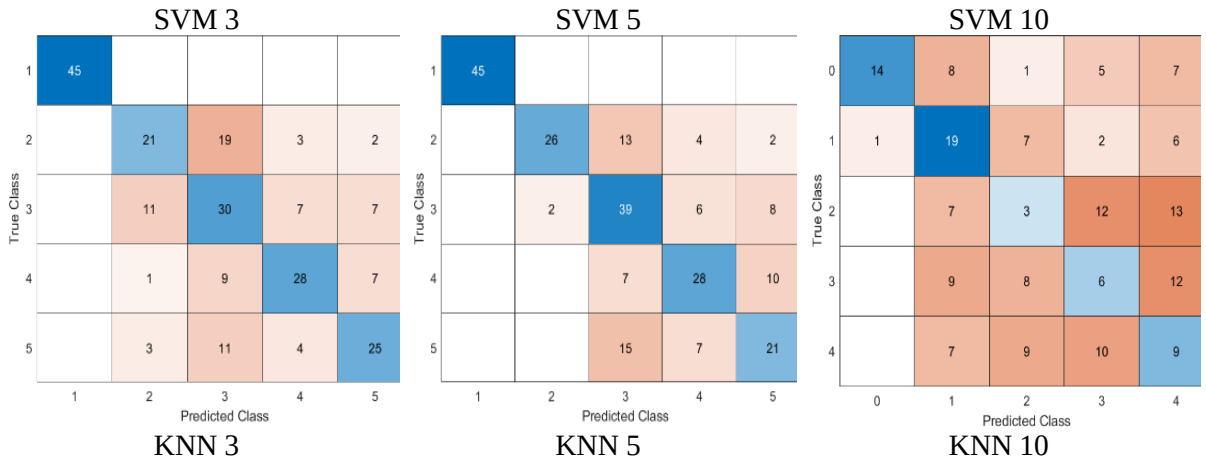

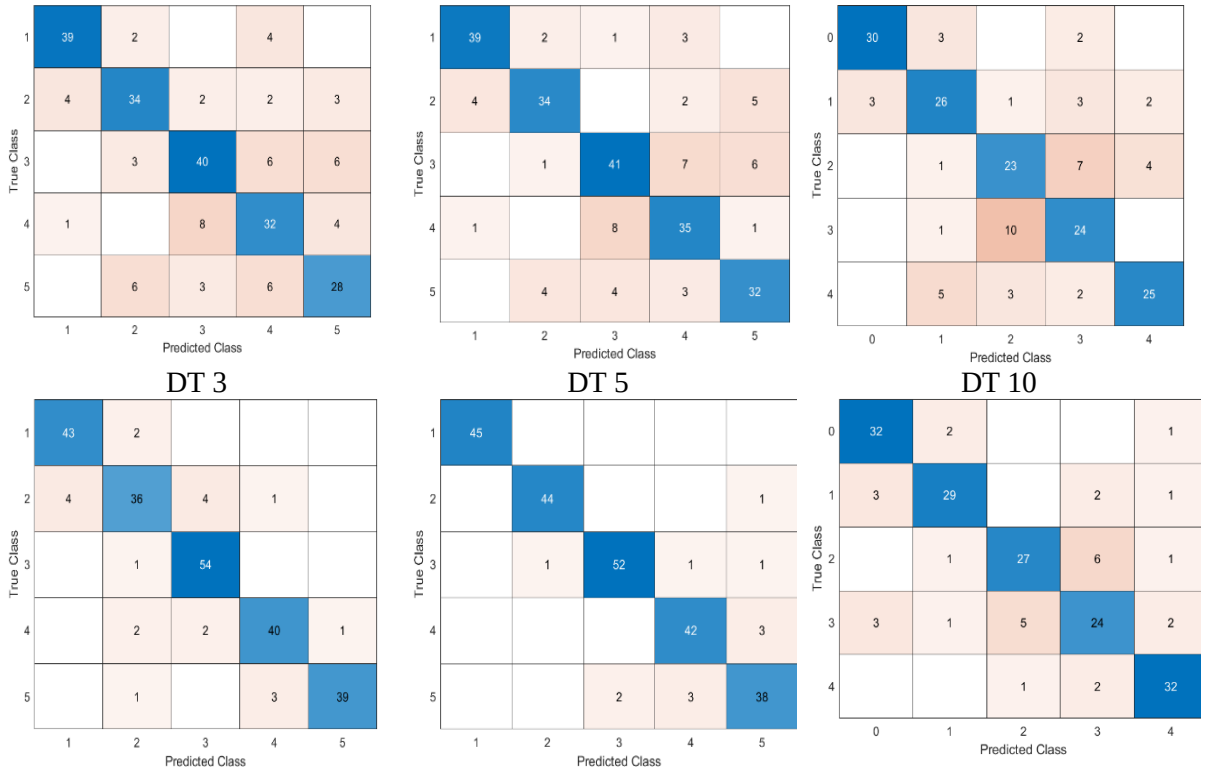

Figure 5-18: Confusion matrix obtained using training/testing scenarios for the three classifiers of the insulation damage Fault

In general, the (DT) classifier achieved the highest classification accuracy. and the (KNN) classifier achieved slightly lower accuracy, while the (SVM) classifier achieved the lowest results. And 10-fold cross-validation of the dataset for the training gives the best results, while the 3-fold cross-validation gives fewer results accuracy for the different classifiers. This indicates that the multi scenarios of lamination's insulation fault give a better result means can be easily identified and can be accurately detected and classified using artificial intelligence.

5.8 Summary

Based on current signals. This chapter studied the detection and classification of lamination faults in the power transformer core. The detection and classification of two types of lamination faults (i.e., edge burr and lamination insulation faults) in a three-phase transformer core have been studied. Using the experimental results obtained using a 15 kVA transformer were exploited. The FFT technique feature extraction for current signals has been presented, which helps diagnoses faults in the power transformer core and demonstrates its impact. Ten features were extracted, and a graphical representation was made to distinguish the independent features. Five features were selected (Average, Fundamental, Total Harmonic Distortion (THD), and Standard Deviation (STD)). Elaborating 328 samples, the dataset is utilized as input

vectors to train and test classification models based on SVM, KNN, and DT algorithms. The dataset for training and testing the model has been managed by considering different scenarios to ensure that the results of the experimental work are accurate and these faults can be identified and classified easily by artificial intelligence. Overall, the obtained results indicated that transformer thermal images are an effective tool for detecting and classifying lamination faults in the transformer core. The following conclusions are also drawn.

1. SVM, KNN, and DT have been used for fault diagnosis based on selected features. The classifiers were satisfactorily accurate when the dataset was applied randomly and with K-fold cross-validation.

2. KNN and DT classifiers gave the highest accuracy rate in the detection purpose, where two classes were considered using a random dataset. The accuracy was up to 97.43 %. The DT classifier gave the highest accuracy rate of 97.69 % in the classification purpose, where three classes were considered using a random dataset. At the same time, the KNN classifier gave the highest accuracy rate of 80 % in the classification purpose where multi classes were considered using a random dataset.

3. Using K-Fold cross-validation for the dataset training, the DT classifier has given the top accuracy rate of more than 99 % in the detection and classification purpose, where two and three classes were considered. Again, the DT classifier gives the top accuracy rate of around more than 94 % in the classification purpose where multi classes were considered using K-Fold cross-validation for the dataset training.

4. It was found that the insulation lamination fault presents a good accuracy rate compared to other classes. Higher precision and recall were obtained for this class.

5. The multi scenarios of the faulty conditions need more focus, such as collecting more data and more scenarios.

Such findings indicated that better detection and classification results might be obtained by enlarging the database or by using more accurate classification algorithms. It is also suggested to investigate the classification using other features by employing other signal processing techniques.

5.9 References

[1] N. Abu Bakar and A. Abu-Siada, "A novel method of measuring transformer oil interfacial tension using UV-Vis's spectroscopy," IEEE Electr. Insul. Mag., vol. 32, no. 1, pp. 7–13, 2016.

[2] H. Huang, Y. Liu, Y. Yuan, P. Li, Y. Yang, and Y. Wang, "Research of a transformer fault diagnose method using multi-source recording waves," China Int. Conf. Electr. Distrib. CICED, vol. 2014–December, no. Ciced, pp. 873–878, 2014.

[3] R. Murugana and R. Ramasamy, "Understanding the power transformer component failures for health index-based maintenance planning in electric utilities", Engineering Failure Analysis, vol. 96, pp. 274-288, Feb. 2019.

[4] A. Eldieb and F. Anayi, "Evaluation of Loss Generated by Edge Burrs in Electrical Steels," in IEEE Transactions on Magnetics, vol. 52, no. 5, pp. 1-4, May 2016, Art no. 2001404, doi: 10.1109/TMAG.2016.2527361.

[5] R. Mazurek, P. Marketos, A. Moses and J. Vincent, "Effect of Artificial Burrs on the Total Power Loss of a Three-Phase Transformer Core," in IEEE Transactions on Magnetics, vol. 46, no. 2, pp. 638-641, Feb. 2010, doi: 10.1109/TMAG.2009.2032094.

[6] E. Lamprecht and R. Gräf, "Fundamental investigations of eddy current losses in laminated stator cores created through the impact of manufacturing processes," 2011 1st International Electric Drives Production Conference, 2011, pp. 29-35, doi: 10.1109/EDPC.2011.6085544.

[7] A. E. Shaban, K. H. Ibrahim and T. M. Barakat, "Modeling, Simulation and Classification of Power Transformer Faults Based on FRA Test," 2019 21st International Middle East Power Systems Conference (MEPCON), 2019, pp. 908-913, doi: 10.1109/MEPCON47431.2019.9007984.

[8] M. Kezunovic and Yong Guo, "Modeling and simulation of the power transformer faults and related protective relay behavior," in IEEE Transactions on Power Delivery, vol. 15, no. 1, pp. 44-50, Jan. 2000, doi: 10.1109/61.847227.

[9] F. Marketos, D. Marnay and T. Ngnegueu, "Experimental and Numerical Investigation of Flux Density Distribution in the Individual Packets of a 100 kVA Transformer Core," in IEEE Transactions on Magnetics, vol. 48, no. 4, pp. 1677-1680, April 2012, doi: 10.1109/TMAG.2011.2173667.

[10] G. Stumberger, B. Klopcic, K. Dezelak and D. Dolinar, "Prevention of Iron Core Saturation in Multi-Winding Transformers for DC-DC Converters," in IEEE Transactions on Magnetics, vol. 46, no. 2, pp. 582-585, Feb. 2010, doi: 10.1109/TMAG.2009.2031687.

[11] O. Kherif, Y. Benmahamed, M. Teguar, A. Boubakeur and S. S. M. Ghoneim, "Accuracy Improvement of Power Transformer Faults Diagnostic Using KNN Classifier with Decision Tree Principle," in IEEE Access, vol. 9, pp. 81693-81701, 2021, doi: 10.1109/ACCESS.2021.3086135.

[12] A. Etumi and F. Anayi, "Current signal processing-based methods to discriminate internal faults from magnetizing inrush current". Electr Eng vol. 103, pp. 743–751, 2021. doi: 10.1007/s00202-020-01115-2

[13] Y. Benmahamed, O. Kherif, M. Teguar, A. Boubakeur, and S. S. M. Ghoneim, "Accuracy Improvement of Transformer Faults Diagnostic Based on DGA Data Using SVM-BA Classifier," Energies, vol. 14, no. 10, p. 2970, May 2021.

[14] H. Hamzehbahmani, P. Anderson and K. Jenkins, "Interlaminar Insulation Faults Detection and Quality Assessment of Magnetic Cores Using Flux Injection Probe," in IEEE Transactions on Power Delivery, vol. 30, no. 5, pp. 2205-2214, Oct. 2015.

[15] E. Altayef, F. Anayi, M. S. Packianather and O. Kherif, "On the Effects of Lamination Artificial Faults in a 15 kVA Three-Phase Transformer Core," in IEEE Access, vol. 10, pp. 19348-19355, 2022, doi: 10.1109/ACCESS.2022.3151367.

[16] R. Romary, C. Demian, P. Schlupp and J. Roger, "Offline and Online Methods for Stator Core Fault Detection in Large Generators," in IEEE Transactions on Industrial Electronics, vol. 60, no. 9, pp. 4084-4092, Sept. 2013, doi: 10.1109/TIE.2012.2224077.

[17] D. R. Bertenshaw, A. C. Smith, C. W. Ho, T. Chan, and M. Sasic, "Detection of stator core faults in large electrical machines," IET Elect. Power Appl., vol. 6, no. 6, pp. 295–301, Jul. 2012

[18] A. J. Moses, N. Derebasi, G. Loisos, and A. Schoppa, "Aspects of the cut-edge effect stress on the power loss and flux density distribution in electrical steel sheets," Journal of Magnetism and Magnetic Materials, vol. 215-216, pp. 690-692, 2000.

[19] O. Kherif, T. Zebbadji, Y. Gherbi, M.L. Azzouze and M. Teguar, "Simplified Diagnosis Method for CHBMIs under Open-circuit Switch or Battery Failure," ENP Engineering Science Journal, vol. 1, no. 2, December 2021, doi: 10.53907/enpesj. v1i2.23

[20] D. Maadjoudj, O. Kherif, A. Mekhaldi and M. Teguar, "Features Characterizing the Surface State of HV Insulator Glass Model under Desert Pollution," in IEEE Transactions on Dielectrics and Electrical Insulation, vol. 28, no. 6, pp. 1964-1972, December 2021, doi: 10.1109/TDEI.2021.009739.

[21] A. Mathur and G. M. Foody, "Multiclass and Binary SVM Classification: Implications for Training and Classification Users," in IEEE Geoscience and Remote Sensing Letters, vol. 5, no. 2, pp. 241-245, April 2008, doi: 10.1109/LGRS.2008.915597.

[22] Y. Benmahamed, M. Teguar and A. Boubakeur, "Application of SVM and KNN to Duval Pentagon 1 for transformer oil diagnosis," in IEEE Transactions on Dielectrics and Electrical Insulation, vol. 24, no. 6, pp. 3443-3451, Dec. 2017, doi: 10.1109/TDEI.2017.006841.

[23] J. Jia et *al.*, "Tradeoffs in the Spatial and Spectral Resolution of Airborne Hyperspectral Imaging Systems: A Crop Identification Case Study," in IEEE Transactions on Geoscience and Remote Sensing, vol. 60, pp. 1-18, 2022, Art no. 5510918, doi: 10.1109/TGRS.2021.3096999.

[24] Xiaoyu Luo," Efficient English text classification using selected Machine Learning Techniques", Alexandria Engineering Journal, Volume 60, Issue 3, 2021, Pages 3401-3409.

[25] L. Breiman, J. Friedman, C. J. Stone, and R. A. Olshen, Classification Regression Trees. Boca Raton, FL, USA: CRC Press, 1984.

[26] Refaeilzadeh P., Tang L., Liu H. (2016) Cross-Validation. In: Liu L., Özsu M. (eds) Encyclopedia of Database Systems. Springer, New York, NY. https://doi.org/10.1007/978-1-4899-7993-3_565-2.

[27] "K Fold Cross-Validation in Machine Learning? How does K Fold Work?", MLTut, 2022. [Online]. Available: https://www.mltut.com/k-fold-cross-validation-in-machine-learning-how-does-k-fold-work/. [Accessed: 21- Jul- 2022].

CHAPTER 6: Based on the Thermal Image, Detection and Classification of Lamination Faults in A 15 kVA Three-Phase Transformer Core Using SVM, KNN, And DT Algorithms

Diagnosing the transformer's failure is important to maintain its safe and stable operation. Early fault diagnosis enables to make savings related to maintenance. This chapter deals with the detection and classification of two types of lamination faults (i.e., edge burr and lamination insulation faults) in a three-phase transformer core using thermal images. In Chapter 4, the experimental results are exploited, which are obtained by employing a 15 kVA transformer under healthy and faulty conditions. Different test conditions were considered, such as the flux density, number of affected laminations, and fault location. The thermal images were used, and a new feature extraction technique for thermal images has been presented called the RGB technique, which helps diagnose faults in the power transformer core and demonstrates its impact. Eight features were extracted, and a graphical representation was made to distinguish the independent features from the others. Thus, enhanced fault detection and classification performance where four features were selected (the highest temperature value, R1, R3, and R5). Elaborating a total of 222 samples, these features are utilized as input vectors to train and test classification models based on SVM, KNN, and DT algorithms. The dataset for training and testing the model has been managed by considering different scenarios (1) decomposition of the dataset for training and testing by random selection and the K-Fold cross-validation strategy (2) managing the detection and classification form for both fault types to be in different scenarios to ensure that the results of the experimental work are accurate, and these faults can be identified and classified easily by artificial intelligence. Based on the selected features, the results confirmed that the thermal images for the power transformer core faults could be used for detection and classification. An accuracy rate of more than 98% was obtained using three different classifiers. Such findings provided a promising step toward fault detection and classification in electrical transformers, helping protect the system and avoid other related issues such as increased power loss and temperature.

6.1 Introduction

The quality of power transformer operation is directly related to the power system quality [1][2]. In addition, large power transformers constitute very expensive and vital components in electric power systems [3]. The reliability of power transformers dictates the safe and reliable performance of the entire electrical system [4]. The faults of power transformers will seriously

impact the safety of power grids [5]. It is necessary to pay attention to the higher reliability of power transformers due to possible electric system failures and their cost [6].

Generally, their unanticipated cut-out from the circuit can cause serious and sometimes irreparable damages to the system, reducing the service quality and even causing blackouts [7][8], and the failure of transformers without warning often causes catastrophic consequences on the power grid. Online monitoring of transformers has been an essential challenge for power engineers. Power engineers are devoted to intensifying the diagnosis of the transformer to discover hidden troubles timely and guarantee the normal operation of the transformer[9]. Usually, time periods, as well as the area of the diagnostics, may vary regarding every population of the transformers. It is always the decision of the owner of the fleet. Nevertheless, among all tests, there may be pointed a group of the most commonly applied measurements on the active part of the transformer that is usually mandatory according to the maintenance policy[10][11]. Recently, many detection techniques and monitoring methods have been developed for fault diagnosis of the transformer[12][13].

The single restriction for power transformers loading is the temperature of the hottest part of their lamination (so-called hot-spot HS)[14]. Heat is generated due to the losses in the transformer, and temperature increases within the core and windings. typically, the windings temperatures of the dry transformers are so much higher than ambient, it is not easy to distinguish the internal defect using thermography before it becomes serious[8].

The cores of electrical machines are normally built from thin electrical steel laminations to reduce the eddy current loss for high-efficiency operation[15]. The process of punching and cutting the electrical steel causes mechanical stress, which deforms the sheet and deteriorates its magnetic properties[16]. Mechanical deformations shear causes burrs on the cut edges[17]. Both faults tend to cause insulation breakdown between the sheets resulting in electrical shorting between the stacked laminations leading to a significant increase in power loss and local overheating, which may cause the burning or melting of the laminations. Thus it causes the potential for complete machine failure[18][19]. Studies have shown a dramatic increase in the eddy current power loss when connecting core edges[20].

Thermal images are captured by a thermo-graphic camera using infrared radiation, whereas normal images are captured by using visible light cameras. Visible light camera works in 450nm to 750nm. The infrared cameras work in as maximum as 14,000 nm, i.e., 14μm. Thermal images generally display the amount of IR energy emitted and reflected by an object [21].

6.2 Related work

Due to the different structure features, common monitoring systems, such as the oil or gas detection on the oil-immersed transformer, cannot be applied on cast-resin or Dry- type transformers. The Dry- type transformer provides the products with numerous excellent characteristics such as low no-load loss, oilless, anti-flaming, maintenance-free, good moisture and crazing resistance, etc. The Dry- type of transformer is perfectly matched to the requirement of inflammable and explosive sites such as commercial centre, high-tech factories, hospitals, underground, airports, train stations, tower buildings, industrial and mining enterprises, etc. Few pieces of literature focus on fault diagnosis for cast-resin or dry-type transformers. Sun et al. [22] proposed a sparse Bayesian temperature model for detecting the temperature warning range of a dry-type transformer based on historical operating data. Chen et al. [23] designed the rectangular sensors employed in the 11.4 kV cast-resin power transformer to detect the induction magnetic field caused by partial discharge (PD). Athikessavan et al. [24] developed low-severity inter-turn fault detection based on a core-leakage flux online technique under the operating conditions of dry-type transformers. Gockenbach et al. [25] used some fibre optic sensors fixed on the surface of the dry-type transformer to perceive online local overheating due to partial discharges. Lee et al. [26] adopted the fuzzy logic clustering (DT) method to recognize the abnormal defects pattern of PD occurring in epoxy resin insulators of high-voltage electrical equipment, etc. Some methods require operators with professional knowledge and rich experience.[27] A. Al-Musawi applies colour model identification, namely Hue, Saturation, and Value (HSV), to represent the hottest area in the thermal image to detect and correctly identify the induction motor faults and discriminate between the motor faults. In addition, many laminations short circuit fault diagnosis methods are proposed theoretically and practically, for instance, the short-circuit impedance (SCI) method based on the principle of short-circuit impedance measurement, the low-voltage impulse (LVI) method based on the principle of signal analysis, and the frequency response analysis (FRA) method, etc.[28][29].

In this thesis, experimental studies have been carried out to indicate the severity of short circuits in the transformer laminations due to edge burrs and insulation degradation faults. A fault-test system has been developed in the Magnetics Group for such testing. A 15 kVA three-phase power transformer has been used where different scenarios of faults have been considered, such

as the area of the affected regions and the number of short-circuited laminations. Of interest, the current at no-load has been recorded for various flux densities ranging from 0.5 to 1.8 T.

6.3 Experimental setup and sample preparation

This section explains the data collection system and process used to investigate the impact of lamination faults in power transformers. A fault-test system has been developed in the Magnetics Group for such testing. This system helps measure the hottest area in the transformer core by using thermal images. Figures 6-2a and 6-2b show a photo of the experimental setup and a schematic diagram of the measurement system.

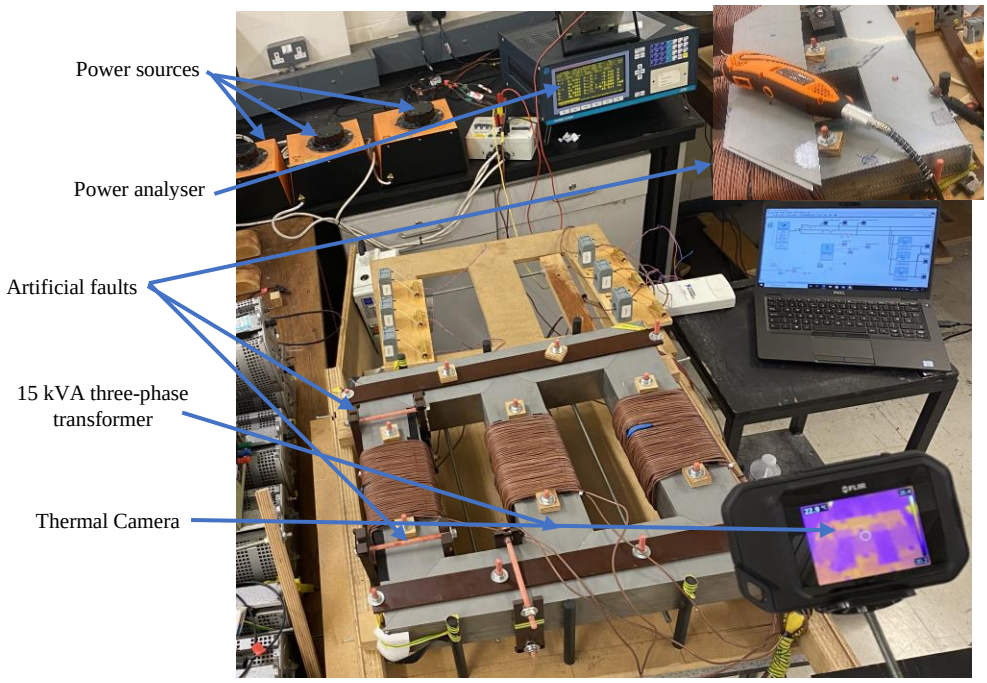

Figure 6-1:Experimental setup

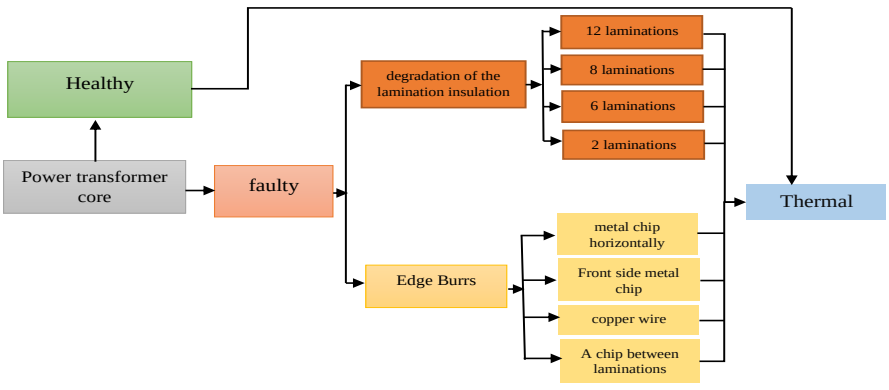

Figure 6-2: Faulty operation diagram

The test rig consists of several components, including a three-phase power transformer of 15 kVA, Clamps designed to be used for the fixation during the application of faults to apply the Edge Burrs fault, a Rotary Tool used for removing around 400mm^2 insulation material of the power transformer core laminations for the second fault for this work. Flux densities are calculated from the measured voltages and currents using the power analyser connected to the power transformer. A thermal camera was used during the experiment for the healthy and faulty transformer core was captured in order to be compared.

The transformer core is built up from a stack of grain-oriented electrical steel laminations (i.e., a total of 520 laminations); this transformer is characterised by two windows cores of 320 mm*120 mm and an outer core of 540 mm*520 mm. In addition, the primary and secondary windings are evenly wound along the limbs with 50 turns of insulated copper wire of 1.5 mm^2 cross-section.

In the initial stage of the experiments, a clamping device, shown in figure 6-3, was designed to fit the experimental core of the transformer described in this investigation. This device helps to ensure good contact of the artificial burr materials with the side of the sample stacks of laminations.

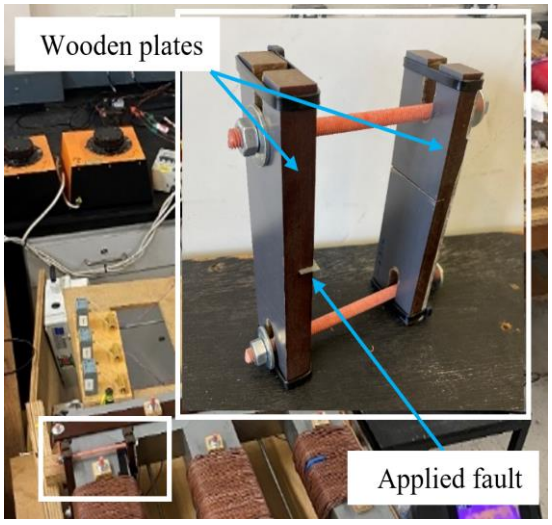

Figure 6-2: Clamping device used for the laminations fault fixation

As shown in this figure, the clamping device consists of two wooden plates secured by two plastic bolts, enabling good pressure on the copper foil on both sides of a stack of laminations. Both wood and plastic are transparent to electromagnetic waves. Thus, their effects on the experimental results can be neglected. Several works have neglected the effect of the clamping device (e.g., [17]).

6.4 Artificial lamination faults

In this investigation, two types of faults have been considered in the transformer core. These faults are the edge burrs and insulation deterioration between laminations, which are the most commonly appeared faults in transformers. The forthcoming parts explain each fault individually. The no-load current measurements can express no-load loss or iron loss. For this reason, a transformer no-load test has been carried out by applying a nominal voltage (220 V) of the primary set of transformer windings when the secondary windings are open.

In order to study the impact of both faults, the healthy operation mode is firstly investigated. In this mode, voltage and current in the three phases have been recorded for different flux densities to guarantee satisfactory results. Flux densities of 0.5, 0.8, 1.0, 1.5, 1.7 and 1.8 T have been considered. The measured results are re-examined three times to ensure reliable and feasible quality. For instance, a whole day is allotted to take the data of each fault separately to leave the transformer core enough time to cool down.

6.4.1 Edge burr fault

In order to simulate the edge burr fault, a short circuit has been created between the laminations of the transformer core. According to the number of sheets in short-circuit (affected area), four scenarios have been selected for this type of fault. See section 4.3.1.

6.4.2 Lamination insulation fault

Thin electrical steel laminations form the cores of electrical machines to reduce the eddy current loss for high-efficiency operation. Each lamination is coated on both sides with an inorganic coating. This thin layer is usually 1 to 3μm in thickness, used to prevent any direct electrical contact between laminations. Degradation of the inter-laminar insulation in the transformer core can occur from a number of sources, such as the ageing of lamination coating, mechanical damage from external objects, and/or overheating of laminations in the region of a winding failure. In order to study the impact of such types of lamination faults by using thermal imaging, the experiment involved applying these faults and then captioning the images to examine the transformer state in faults from insulation breakdowns. For full details, see section 4.3.2.

6.5 The experimental results

This section gives the results of the experimental work presented in this thesis. These results consist of the thermal images for the transformer, which have been taken for various values of flux density. FLIR C2 thermal camera is used for capturing the thermal image. Six images for

each scenario during the whole day and with a resolution of (80 × 60) are taken during the time intervals of 15 min for each flux density value. Full camera details are available in section 3.6.6.

6.5.1 Healthy operation mode

The analysis was done by capturing the thermal image of the healthy transformer core in order to be used as a reference image and later to compare it with the faulty transformer core image. For a better visualisation of the results. Firstly, figure 6-4 shows the thermal images for normal conditions before applying any faults to better understand these faults' impact. The maximum and minimum temperature clearly indicates the transformer core temperature profile for different flux densities. These values are taken as a part of the used features for the fault detection and classification section.

For healthy conditions of the transformer core, one can see that the flux density has an important effect on the core temperature in a no-loaded power transformer. For low flux density in Figure 6-4 (a), the temperature is of low degree in the order of 25.3 ℃ max and 19.1 ℃ min, while at 1.8 T in figure 6-4(f), the temperature is of high degree in the order of 30.5 ℃ max and 23.3 ℃ min.

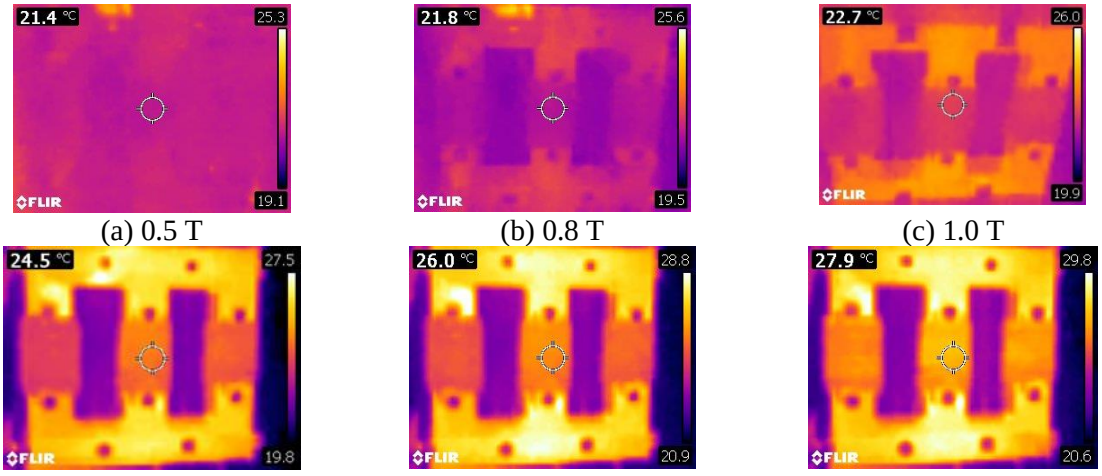

(a) 0.5 T (b) 0.8 T (c) 1.0 T

(d) 1.5 T (e) 1.7 T (f) 1.8 T

Figure 6-3: Healthy operation mode results

6.5.2 Edge burrs fault

The thermal image results of the first selected type of faults (i.e., edge burrs faults) have been viewed in this part.

The limitations are that the camera was an old version, so the images were not in high quality. Since the faults occur on the edges of the laminations, it was better to capture the images from the profiles of the transformer because those images of the faults were more precise than those caught on the surface of the transformer, as shown in figure (6-5).

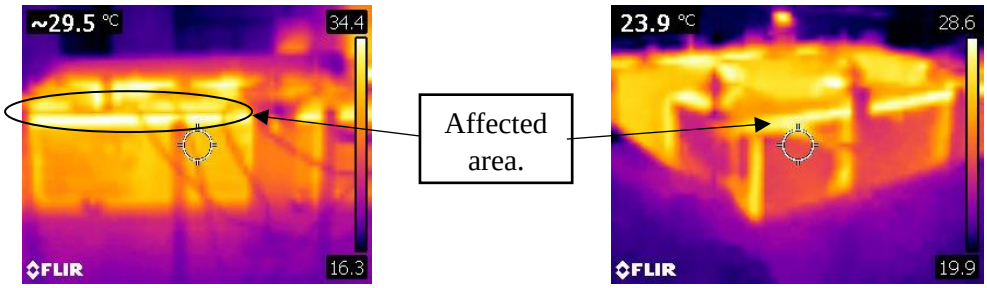

Figure 6-4: The caught image on the profiles of the transformer

This fault has been applied in different scenarios and places within the transformer core. Figures 6-6, 6-7 and b show the thermal images for the considered scenarios. The applied flux densities (i.e., 0.5 T: 1.8 T) of two scenarios have been selected in these figures to highlight the effect of the flux density on the temperature of the transformer core under edge burr faults.

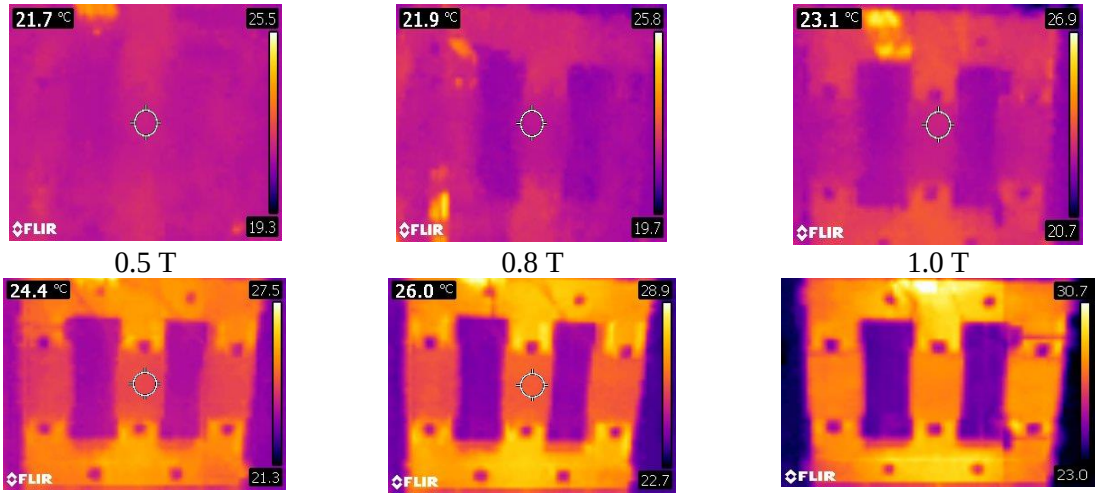

Figure 6-5: Results of scenario 1 faulty operation mode of edge burrs fault at different flux densities.

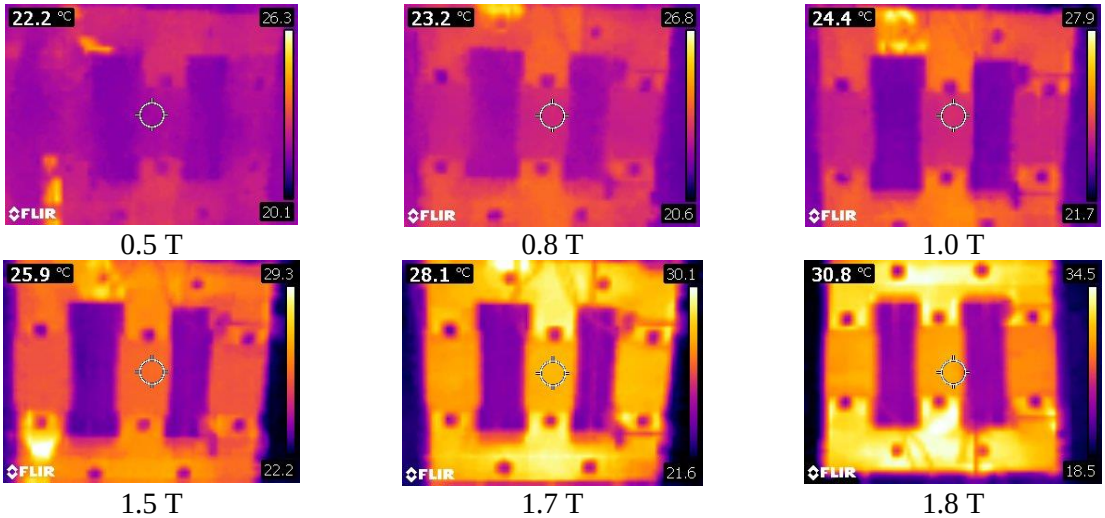

Figure 6-6: Results of scenario 4 faulty operation mode of edge burrs fault at different flux densities.

These figures show that different temperatures recognize the thermal images obtained during edge burr faults compared to those obtained in the healthy operation mode. This means that edge burrs faults considerably affect the transformer core temperature, thus, the performance of the transformer. Indeed, as you can see on the top right corner the temperature increased by 3.8°C from scenario 1 (30.7°C) to scenario 4 (34.5°C) with a flux density of 1.8 T. Meanwhile, with a flux density of 1.7 T, the temperature increased by 1.2°C from scenario 1 (28.9°C) to scenario 4 (30.1°C). This rate of increase becomes more important with the increment of the flux density and the number of affected laminations within the transformer core.

The edge burrs faults increase the temperature inside the transformer. Which, in its round, can increase the transformer current losses. This temperature rise might affect the properties of the insulating oil and/or insulating paper, thus, reducing the performance of the transformer. For this reason, it would be better to examine the effect of such faults in high-capacity transformers.

Overall, the obtained thermal images demonstrated that the edge burrs fault could cause the transformer core temperature to increase, which considerably affects the reliability of the transformer. And Edge burrs affecting the transformer core can increase the transformer core temperature. These later become important with the increase of the flux density and the number of short-circuited laminations.

6.5.3 Lamination insulation faults

As described in Section 6.4, artificial short circuits, as the second type of fault, have been applied between transformer core laminations by removing the insulation covering the laminations. Figure 6-8 shows the captured thermal images for the transformer core. The results correspond to faults between 2, 6, 8, and 12 laminations for 0.5 and 1.8 T flux densities, as indicated in figures 6-8. It should be noted that the impact of the position of the short circuit applied between laminations has been investigated previously using a current signal in chapter 4. The same way and position of the applied faults have been considered in this investigation.

The figure 6-7 shows the maximum and minimum temperature as a function of the number of the affected laminations at flax density of 0.5 and 1.8 T. From this figure, it is clear that the faults' size (number of affected laminations) has an important effect on the temperature within the transformer core.

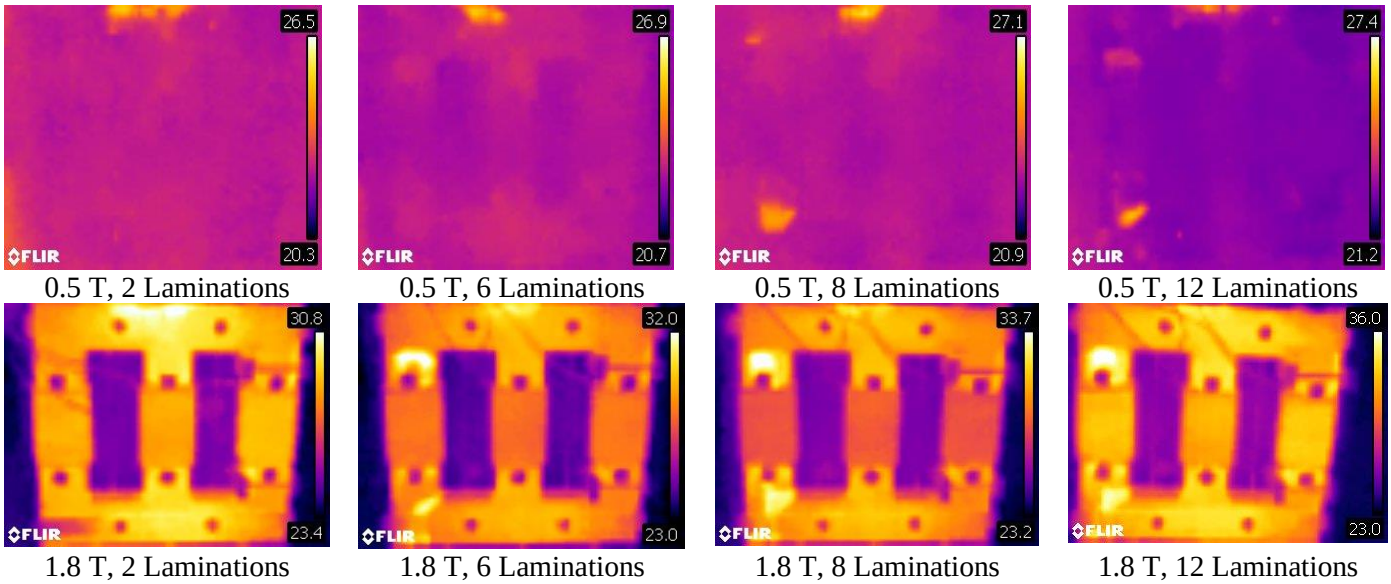

0.5 T, 2 Laminations | 0.5 T, 6 Laminations | 0.5 T, 8 Laminations | 0.5 T, 12 Laminations

1.8 T, 2 Laminations | 1.8 T, 6 Laminations | 1.8 T, 8 Laminations | 1.8 T, 12 Laminations

Figure 6-7: Faulty operation mode results at 0.5 T, 1.8 T

The results show that the temperature due to short circuit laminations is increasing based on the number of shorted laminations, as can be seen in the above figure.. From this figure, it is shown that the increasing temperature caused by the insulation damage fault is related to the number of the laminations in the short circuit as well as to the flux density. It was found for two, six, eight, and twelve shorted laminations that the temperature is extremely high at a flux density of 1.8 T of more than 9 ℃ for those at 0.5 T. For two shorted laminations, the temperature increased by more than 4 ℃ for a flux density of 0.5 T – 1.8 T. And about 6 ℃ of the maximum degree for six and eight shorted laminations at 0.5 T – 1.8 T flux density.

The transformer core temperature caused by the insulation damage fault is related to the number of laminations in the short circuit as well as to the flux density. It was found for two, six, eight and twelve shorted laminations that the transformer core temperature is extremely high at a flux density of 1.8 T, increased with the number of the affected laminations. This significant increase in temperature may lead to an increase in power losses, hence, the transformer efficiency or power failure.

The data from the thermal FLIR C2 camera was saved to the camera's internal memory and then transferred to the PC (Personal Computer) for further processing for thermal image feature extraction.

6.6 Thermal images pre-processing

This section briefly provides the thermal image feature extraction process for detecting and classifying lamination faults in the transformer core. Features have been extracted using the

RGB technique applied to the thermal images. The obtained dataset was treated to reduce the number of features, selecting those most contributing to the overall accuracy. The obtained results are presented and discussed in this section since the full details and the effect of these faults of this work have been studied previously.

6.6.1 Thermal images

Mechanical deformations shear causes burrs on the cut edges, usually followed by the process of punching and cutting the electrical steel. Both faults are the edge burrs and insulation deterioration between laminations, which are the most apparent faults in this type of transformer. These deformations in the core laminations affect the performance of the transformer and electrical machines, causing overheating, which leads to power losses, as experimentally verified in many studies. From the thermal image results, one can obviously distinguish between each operation mode of the transformer by comparing the temperature levels. The temperature increases with both faults of laminations.

Quantifying the thermal images is a common technique to help the process of detection and classification of faults in electrical transformers or other electrical systems. However, it may be visually difficult to detect and classify these faults because of the similarity in the images. For this, the RGB technique has been applied as an image processing technique to the thermal image of the matter.

6.6.2 Proposed RGB technique

After conducting the experiments, more than 40 thermal images were collected, as shown previously. In order to exploit the results and extract the features, the multi-coloured images have been represented by images coded in RGB. Therefore, the original images have been divided into three sets of images. Each set represents a component of the original that corresponds to one of the three colours (R: red, G: green, and B: blue). In other words, every colour of the thermal images will be described in the RGB technique by indicating how much of each of the red, green, and blue is included.

These thermal images are digital imaging systems that are represented by a set of pixels. A pixel is the smallest addressable element in a raster image, so it is the smallest controllable element of each thermal image. The quality of the image increases with the number of pixels as indicated in figure 6-9.

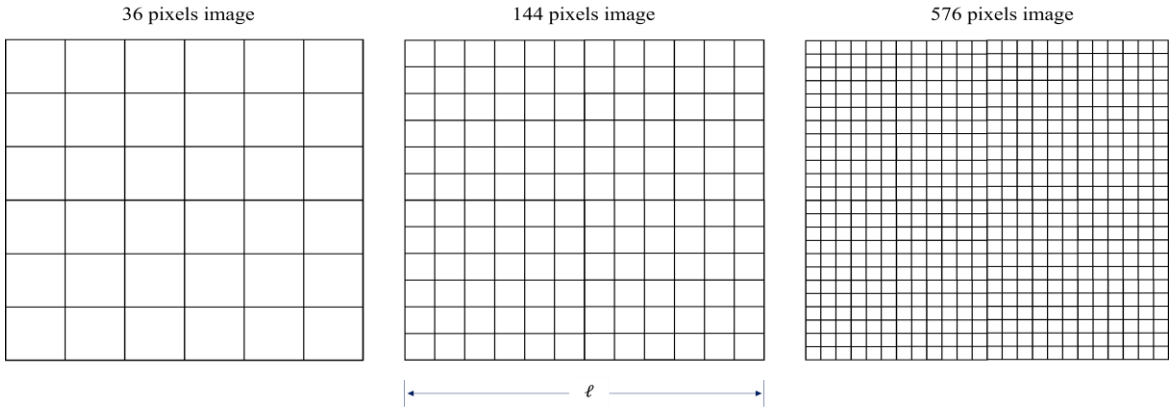

Figure 6-8: Effect of the number of pixels in images

In any given image, every pixel is characterized by a specific colour. It is well known that every colour can be represented by a combination of colours. In this thesis, the RGB system represents all the colors, as indicated in figure 6-10.

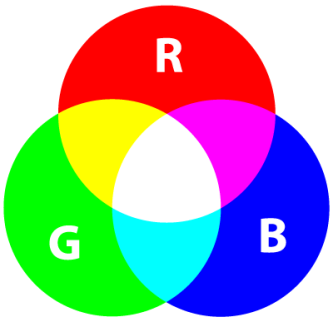

Figure 6-9: combination of colours

This means that each colour should be represented by different quantities of RED, GREEN and BLUE. For instance, we have the following combinations in the next tables:

Table 6-1: The quantities of RED, GREEN, and BLUE

RED	=	1	**x**	RED	+	0	**x**	GREEN	+	0	**x** BLUE
GREEN	=	0	**x**	RED	+	1	**x**	GREEN	+	0	**x** BLUE
BLUE	=	0	**x**	RED	+	0	**x**	GREEN	+	1	**x** BLUE

For white and black, we have, as shown in the next table

Table 6- 2: The quantities of RED, GREEN, and BLUE for white and black

WHITE	=	1	**x**	RED	+	1	**x**	GREEN	+	1	**x** BLUE
BLACK	=	0	**x**	RED	+	0	**x**	GREEN	+	0	**x** BLUE

These three colours represent any other pixel colour; thus, each thermal image is described by three matrices of numbers describing the amount of a given colour in this image. Figure 6-11 shows a typical representation of the process.

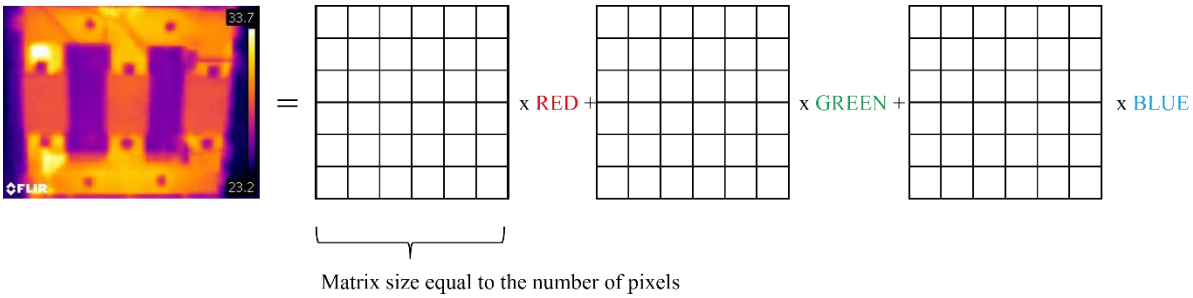

Figure 6-10: A general representation of the images processing

In the proposed model, every thermal image is represented by three independent image planes, one in each of the primary colours: red, green, and blue. A particular colour is done by specifying the amount of each primary component present. In order to identify the faulty conditions, the image is compared with that in a healthy condition. In this case, I compare the variation in the total amount of the faulty colour. Figure 6-12 shows an example of this change between healthy and faulty conditions.

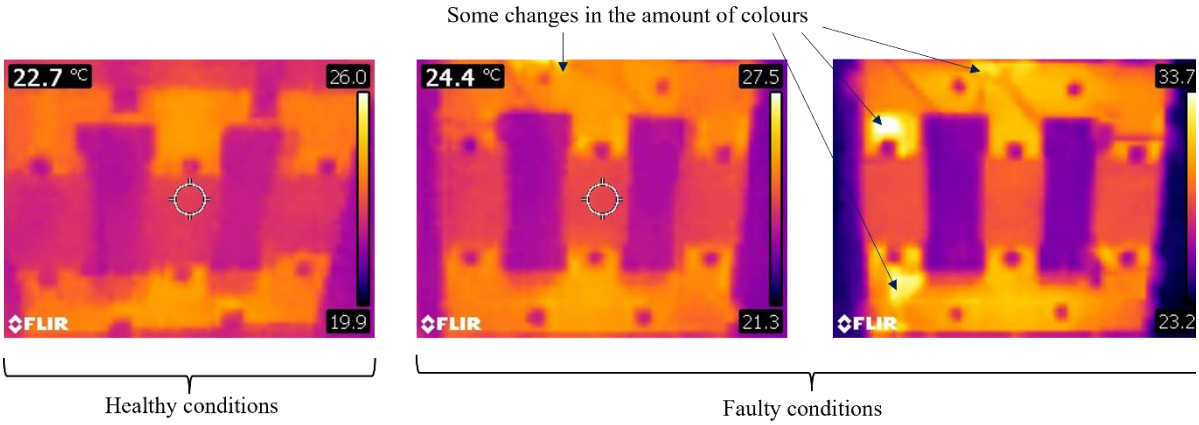

Figure 6-11: Example showing the difference between healthy and faulty conditions

It should be noted that the amount of colour is used as a good feature for fault detection. Any change represents a faulty condition. Moreover, different feature combinations are introduced to classify the faults. The following combinations are considered.

6.6.3 Feature extraction technique

In the first stage, the thermal images were captured without applying any faults - normal conditions (Healthy operating mode). In order to increase the credibility of the database, several flux densities are considered, namely, 0.5, 0.8, 1.0, 1.5, 1.7, and 1.8 T. In the second stage, two types of faults were applied to the transformer core to form the database. A full day was allotted to take the data of each fault scenario separately. This is to leave the transformer core enough

time to cool down. The RGB technique was used for feature extraction by using MATLAB software.

Figure 6-13 shows an example of the RGB technique obtained for 1.8 T flux density for healthy and faulty operation modes.

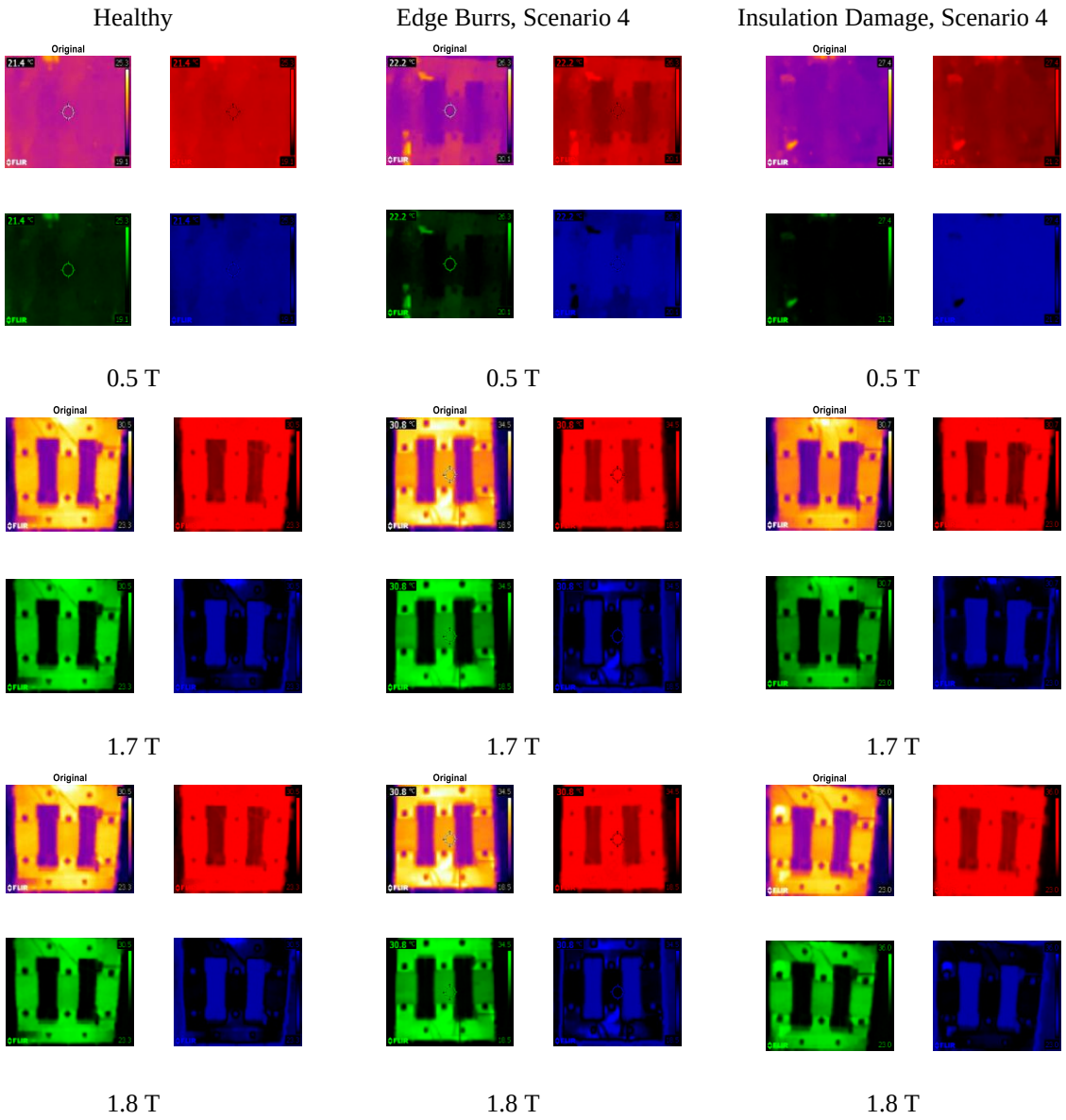

Figure 6-12: The RGB technique obtained result

This figure shows that the healthy operation mode can be distinguished from the faulty condition in the proposed case. And it can be determined that some hot areas are visible in coloured images, especially in green and blue ones. The feature was extracted from the images by RGB technique for the Edge Burrs fault with Healthy mode, and different faulty Scenarios are shown in the following table:

Table 6- 3: The Edge Burrs fault Features

Type	High temperature	Low temperature	R1	R2	R3	R4	R5	R6
Healthy 0.5 T	25.3	19.1	46.0137	89.9712	64.0151	53.9863	10.0288	35.9849
Scenario1 0.5 T	25.5	19.3	46.9059	91.0928	62.0013	53.0941	8.9072	37.9987
Scenario2 0.5 T	25.8	19.7	45.2011	88.7863	66.0125	54.7989	11.2137	33.9875
Scenario3 0.5 T	26	19.8	47.0905	90.8729	62.0367	52.9095	9.1271	37.9633
Scenario4 0.5 T	26.3	20.1	49.0766	92.7073	58.2161	50.9234	7.2927	41.7839

The feature was extracted from the RGB technique for the lamination insulation damage fault with Healthy mode, and a different number of shorted laminations is shown in the following table:

Table 6- 4: The lamination insulation damage fault Features

Type	High temperature	Low temperature	R1	R2	R3	R4	R5	R6
Healthy 0.5 T	25.3	19.2	50.6631	94.5368	54.8002	49.3369	5.4632	45.1998
2Laminations 0.5 T	26.5	20.3	46.1925	90.6234	63.184	53.8075	9.3766	36.816
2Laminations 0.5 T	26.9	20.7	47.9733	92.6712	59.3556	52.0267	7.3288	40.6444
2Laminations 0.5 T	27.1	20.9	47.8445	92.3615	59.794	52.1555	7.6385	40.206
2Laminations 0.5 T	27.4	21.2	54.6003	97.4751	47.9246	45.3997	2.5249	52.0754

"To clarify, I employed different ratios to display the density of each color (from R1 to R6) compared to the total number of pixels, thereby presenting the relative density."

6.6.4 Features selection

The feature selection step minimizes dimensionality by excluding irrelevant features, and feature selection help improve the model performance by focusing only on the important variables. This step is conducted using differential evolution. For instance, the features have been selected based on a graphical representation to distinguish the independent features from the others, which are optimized into representative features. Figure 6-14 shows an example of selected features: (The maximum temperature values, R1, R3, and R5) as a function of the transformer thermal images under 0.5 T flux density for healthy and faulty conditions. Where the maximum temperature values is appear in the top right corner of the thermal image and the R1, R3 and R5 are ratios to display the density of each color.

The next figure, 6-14 shows the faults features and how to be selected. The target feature was marked with a blue circle and other features with an orange star. The feature selection was made by comparing each feature with the others for fault detection.

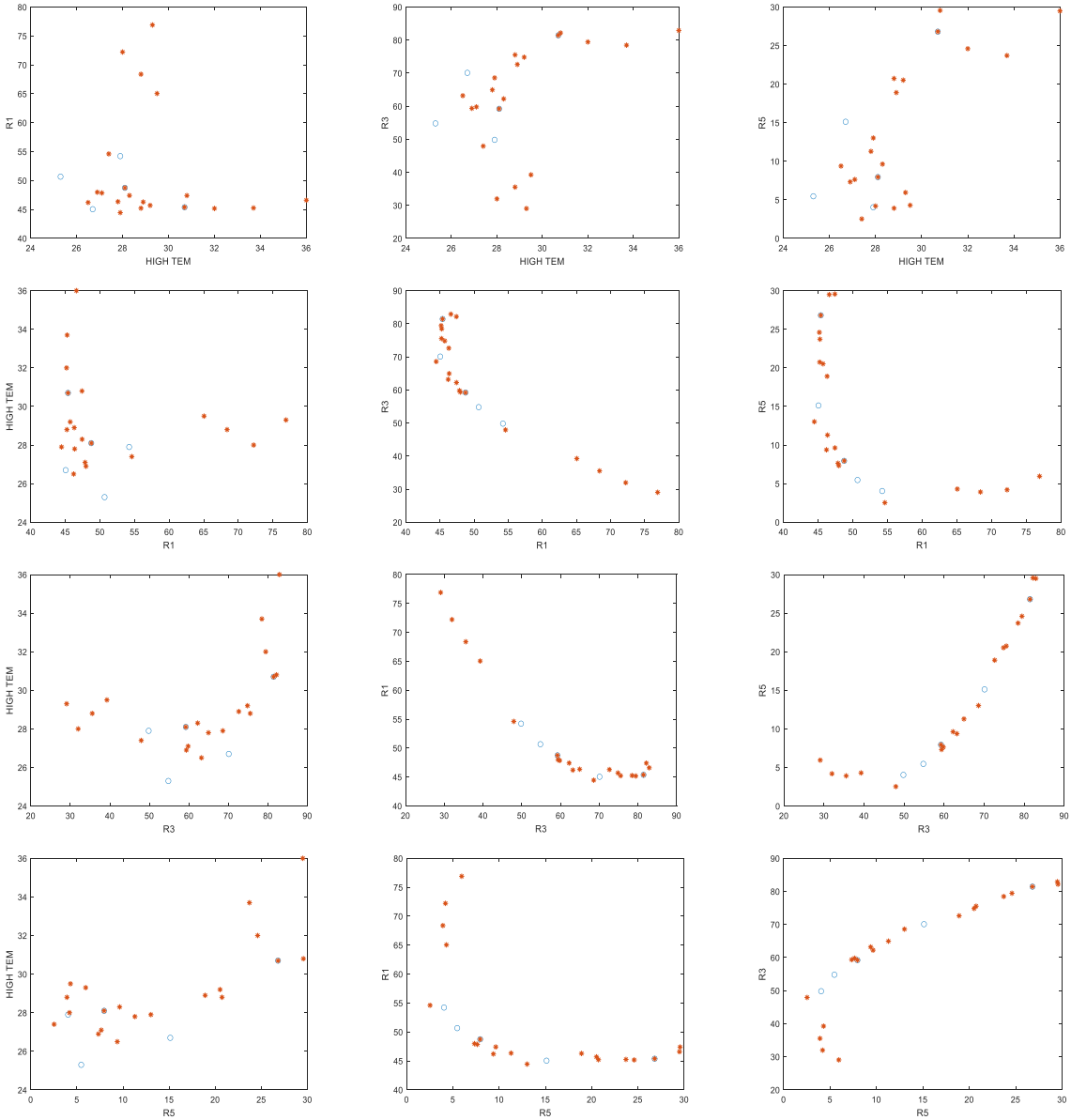

Figure 6-13: a graphical representation for the selected features.

As it was clear in figure 6-14, the features can be detected from each other visually and by using non-linear classification algorithms. However, in figure 6-15, the features are on one path and overlapping, which is difficult to diagnose visually and needs a linear classification algorithm to be detected. The excluded features are (the lower temperature values is appear in the below right corner of the thermal image and the R2, R4 and R6 are ratios to display the density of each colour. The full feature selection is available in appendix 1.

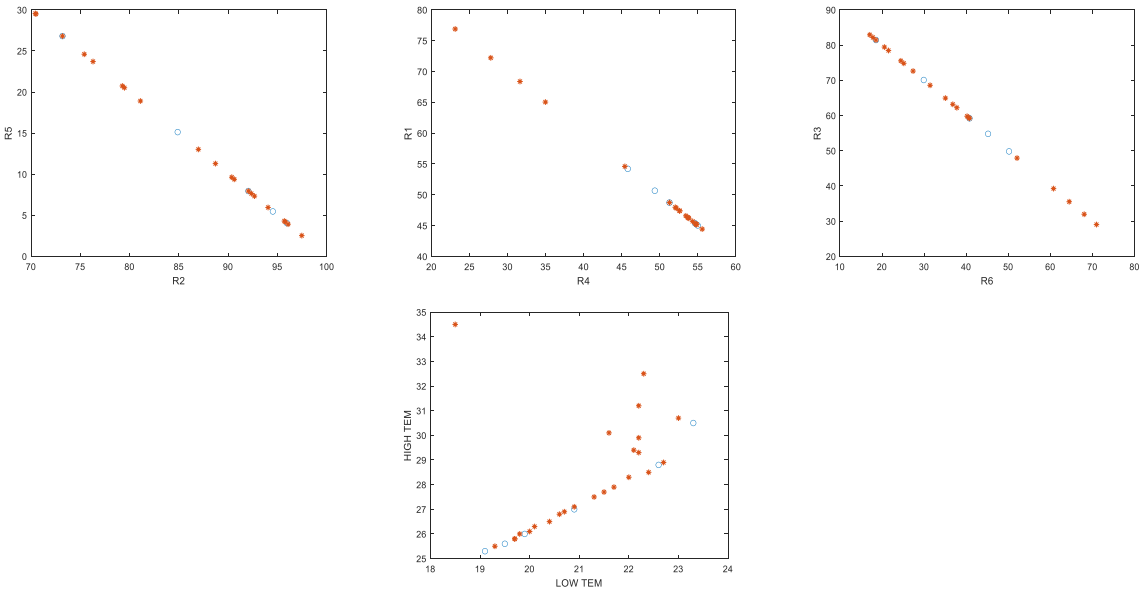

Figure 6-14: a graphical representation for the excluded features.

6.7 Methods of fault detection and classification

This section describes the methods used to detect and classify faults in the transformer core. The database samples used to train and test the classifiers have been presented and discussed. The section also provides the obtained accuracy rate of each classifier for different datasets.

6.7.1 Classification algorithms

For detection and classification, three classifiers have been exploited. These include SVM, KNN, and DT techniques. SVM techniques are usually implemented in classification problems, prediction models, and regression [30]. For the classification problems, the principle of the SVM is to find hyperplanes of separation between two classes *yi* and *yj*. The hyperplanes should be with maximum margin. Which means the classification becomes an optimization problem. The optimization solution is particularly important because hyperplanes represent the decision boundaries that help to distinguish two different classes [31].

The second classifier consists of the KNN algorithm. In this algorithm, the decision of the classifier can be obtained from the vote of the KNN. The vote is based on calculated distances between the sampling points to the nearest neighbours of the total assigned points. Gaussian, triangular, and cosine are some of the typical distances used in this classifier. It should be noted that the KNN technique is easy to implement and apply to any problems, including complex ones such as geographic information, text, images, and sound [32], [33]. Also, it is robust to noise. The introduction of new data does not require the reconstruction of a model. The class is assigned to an object with ease and clarity once the closest neighbours are displayed. The

method performance depends on the distance type, the number of neighbours, and how the neighbours' responses are combined. The results could be of inferior quality if the number of relevant attributes is low relative to the total number of characteristics. The distances on the irrelevant attributes will drown out the proximity on the appropriate attributes. The calculations made in the classification phase can be very time-consuming if the number of data sets is too large.

The third classifier consists of the decision tree (DT) algorithm. This technique obtains a decision following the tree, starting from a root node down to a leaf node [34]. The leaf node comprises the classifier response.

6.7.2 Datasets for training and testing

The dataset for training and testing the model has been managed by considering different scenarios:

1. decomposition of the dataset for training and testing.

-Three types of decomposition of the database have been selected randomly. The decomposition 30-70 means that 30% of the database is reserved for the training process and 70% for testing. The second type of decomposition is 50-50, 50% of the database is used for training and the remaining of 50% of data exploited for testing. The last decomposition is based on 70% for the training phase and 30% for testing.

- The K-Fold cross-validation strategy used to train the dataset for machine learning classifiers

2. managing the detection and classification form for both fault types to be in different scenarios in order to prove the validity of experimental results and the reliability of lamination faults detection and classification by artificial intelligence.

6.8 Results and discussion

6.8.1 Results of fault detection based on thermal images

In this section, both types of faults have been grouped to form a separate class, representing the results of the faulty operation mode. Therefore, a binary classification (healthy and faulty) is formulated where the aim is to detect the presence of faulty conditions. This process is based on the features extracted from the measured current. And the dataset for training and testing was selected randomly. Table 6-6 gives the accuracy rate obtained using three different classifiers see eq (5-1).

Table 6- 5: Accuracy rate for fault detection execution

Scenario	**Accuracy Rate (%)**		
	SVM	KNN	DT
70-30	91.04	98.50	95.52
30-70	90.90	97.90	95.80
50-50	91.34	98.07	94.23

The obtained results show that the proposed classifiers give roughly equivalent results for the three proposed scenarios (data decomposition for training and testing). Overall, the highest obtained result accuracy rate is around 98%, with a maximum of 98.50%, obtained when using 70% of the dataset for the training using the KNN classifier. And the accuracy rate is around 90%, with a maximum of more than 91%, obtained when using 70% of the dataset for the training using the SVM classifier, which is the lowest obtained result. And for the DT classifier the accuracy rate was around 95% with a maximum of 95.80%, obtained when using 30% of the dataset for the training. This indicates that the number and quality of the input vectors have an important impact on the detection results and the classifier. The Confusion matrix of the obtained results is shown in figure 6-16.

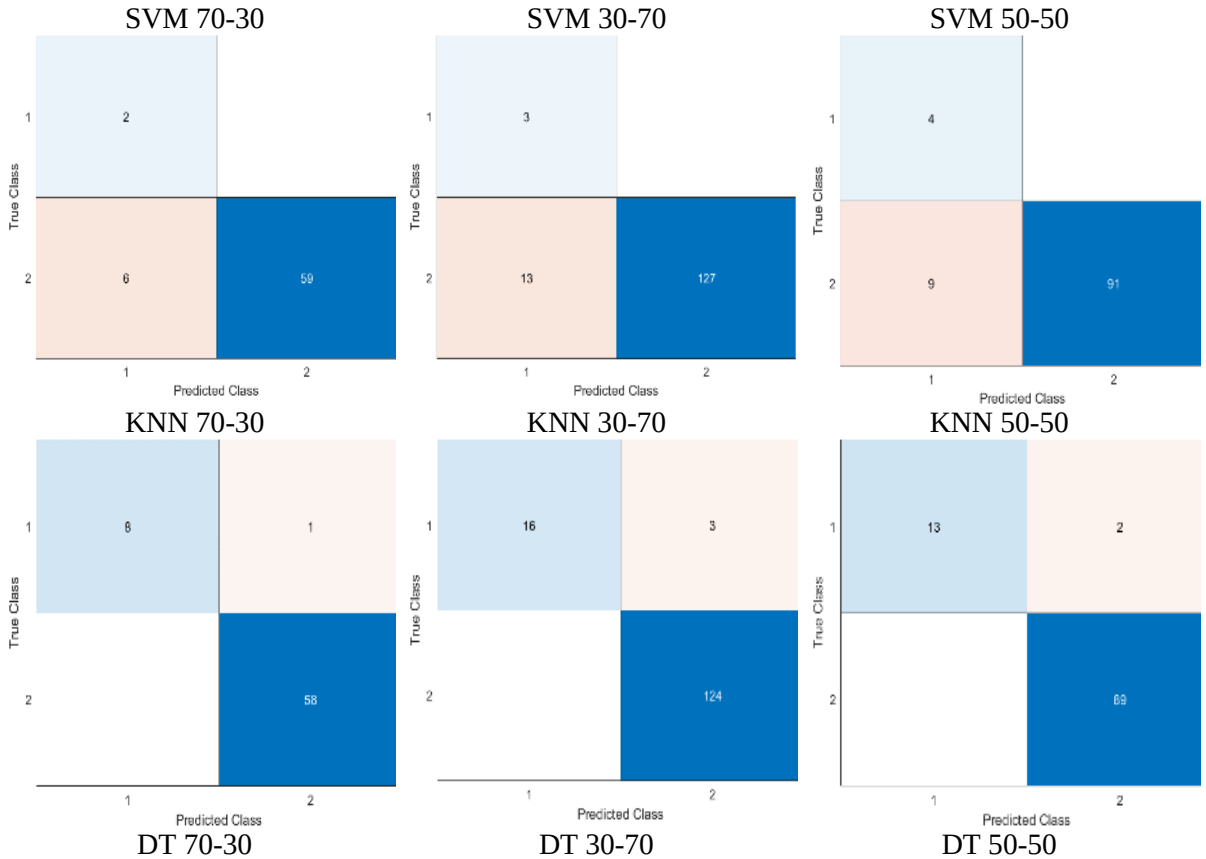

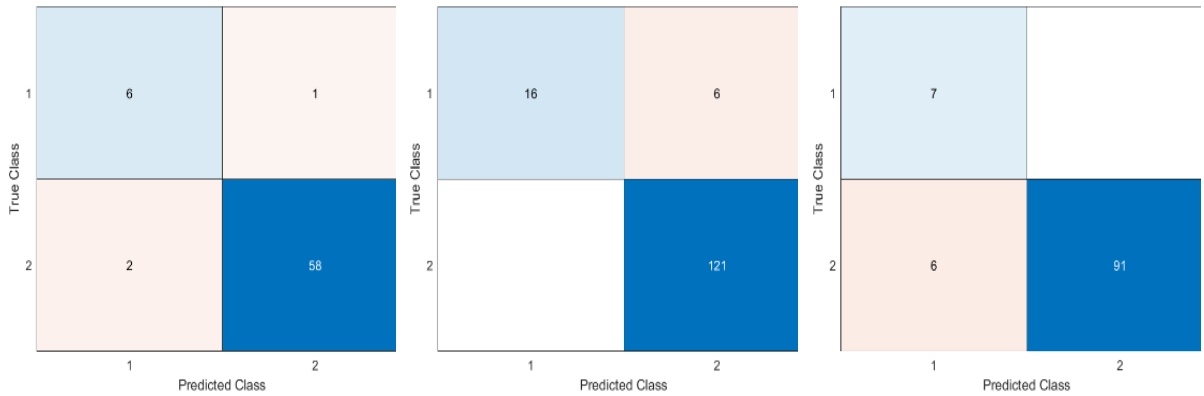

Figure 6-15: Confusion matrix obtained using training/testing scenarios for the three classifiers

In general, the results indicated that fault detection was successful and accurate, especially when using 70% of the dataset for the training. The (KNN) classifier achieved the highest accuracy of detection. And the (DT) classifier achieved slightly lower accuracy. At the same time, the (SVM) classifier achieved the most insufficient accuracy. The findings reassured the lamination faults detection and classification in transformers.

6.8.2 Classification between both types of laminations faults

In this section, based on thermal images, the classification between health conditions and faulty conditions of both fault types in one file has been considered, and the faulty dataset has been separated to form two classes. (The class becomes a three-group classification). Table 6-7 provides the calculated results using the three classifiers and for three scenarios of the training and testing process. The results in this table show the accuracy rate of the three-class, eq (5-1).

Table 6-6: Accuracy rate for fault classification

Scenario	**Accuracy Rate (%)**		
	SVM	KNN	DT
70-30	79.10	97.01	89.55
30-70	76.22	95.80	90.90
50-50	81.73	96.15	91.34

Overall, the results of the KNN classifier show a better accuracy rate than those obtained using the SVM and DT classifiers. Where the KNN accuracy was around 90%, the highest was 97.01% when the dataset for training was 70%, and the lowest was 95.80% when the dataset for training was 30%. And for the DT classifier, the highest accuracy result was 91.34 when the dataset for training was 50%. While for the SVM, the accuracy result was around 80%, with a maximum of 81.73 when the dataset for training is 50%. In general, the results were good for the random selection of the training dataset. And for the three-classes group, the KNN classifier is the best. And from the confusion matrices, one can get a general understanding of the classification process figure 6-17

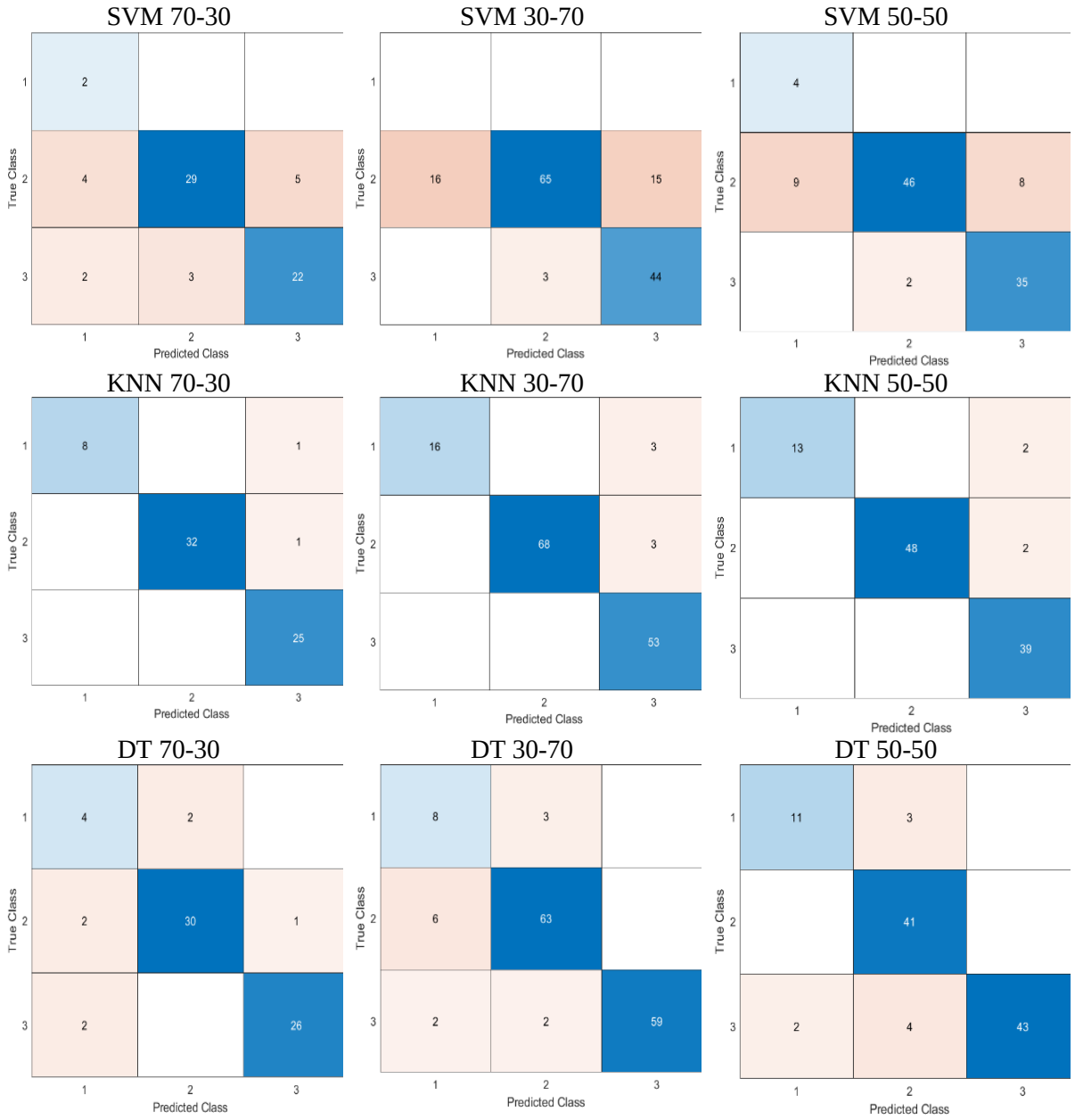

Figure 6-16: Confusion matrix obtained using training/testing scenarios for the three classifiers

In general, the results indicated that the fault classification was successful and somehow accurate, especially when using 50% of the dataset for the training. The (KNN) classifier achieved the highest accuracy of faults classification, and the (DT) classifier achieved slightly lower accuracy, while the (SVM) classifier achieved the lowest accuracy.

6.8.3 Results of fault detection for each fault separately

Based on thermal images, the detection between health and faulty conditions of each type of fault separately has been considered in this part. The classes become a two-group classification for each fault. Table 6-8 provides the calculated results using the three classifiers and for three

scenarios of the training and testing process. The results in this table show the accuracy rate of each class for each fault see eq (5-1).

Table 6-7: Accuracy rate for each class of faults using different classifiers and considering three scenarios

CLASS	TRAINING-TESTING DATA	SVM	KNN	DT
Fault 1	70-30	85.00	100	92.50
	30-70	84.52	100	96,42
	50-50	85.24	100	93.44
Fault 2	70-30	88.23	94.11	85.29
	30-70	84.93	91.78	84.93
	50-50	83.33	90.74	87.03

From this table, one can clearly see that the fault detection results are affected by the type of fault. For instance, the results of the second fault show a better result for all the considered cases and classifiers. The accuracy rate is around 90% with a maximum of more than 94%, obtained when using 70% of the dataset for the training using the KNN classifier and relatively lower accuracy rates when using the SVM classifier, which was 88.23% obtained when using 70% of the dataset for the training. At the same time, An accuracy was 85.29% obtained when using 70% of the dataset for the training with the DT classifier. The lamination's insulation fault can be easily identified from the other conditions. This ascertainment is in accordance with the conclusion made from the experimental results in chapter 5.

In addition, the first fault, which is the Edge Burr fault, provides a good classification result for all the considered cases but not for all classifiers. The KNN classifier gives an over-fitting result, while the other classifiers give good results with an accuracy rate were around 80% with a maximum of more than 92% obtained using the DT classifier when using 70% of the dataset for the training and with maximum of more than 85% using SVM classifier. Overall, it shows relatively lower accuracy rates than the insulation damage fault.

Overall, for the insulation damage fault, the results of the KNN classifier show a better accuracy rate than those obtained using the SVM and DT classifiers. For DT, the accuracy rate is affected by the number of samples used to train the classifier. It is between 84% and 85% when using 70/30 and 30/70 decomposition scenarios, respectively. And more than 94% was obtained when using 70% of the dataset for the training when utilizing a KNN classifier. This classifier obtains an accuracy rate of 90.74% for the case 50/50.

In contrast, the KNN classifier shows the overfitting results for the Edge Burrs fault. And the accuracy rate obtained using the SVM and DT classifiers were relatively close. It was around 80%, with a maximum of 96.42% obtained when using 50% of the dataset for the training with the DT classifier and a maximum of 85% using the SVM classifier when using 70% of the dataset for the training. For better visualization, figure 6-18 shows an example of the confusion matrices obtained using the three algorithms for the three scenarios.

Edge Burrs Fault (Fault 1)

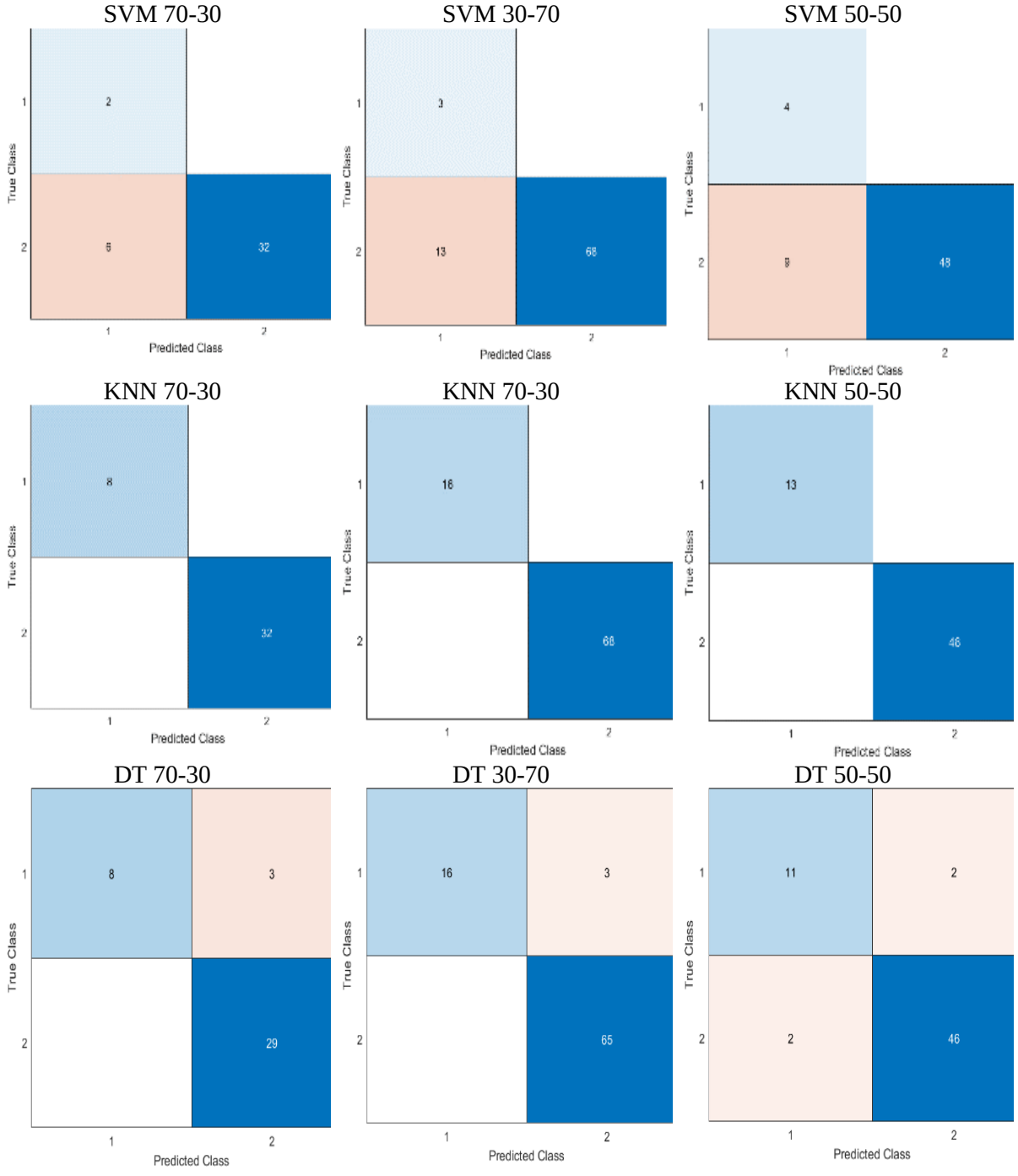

Insulation Damage Fault (Fault 2)

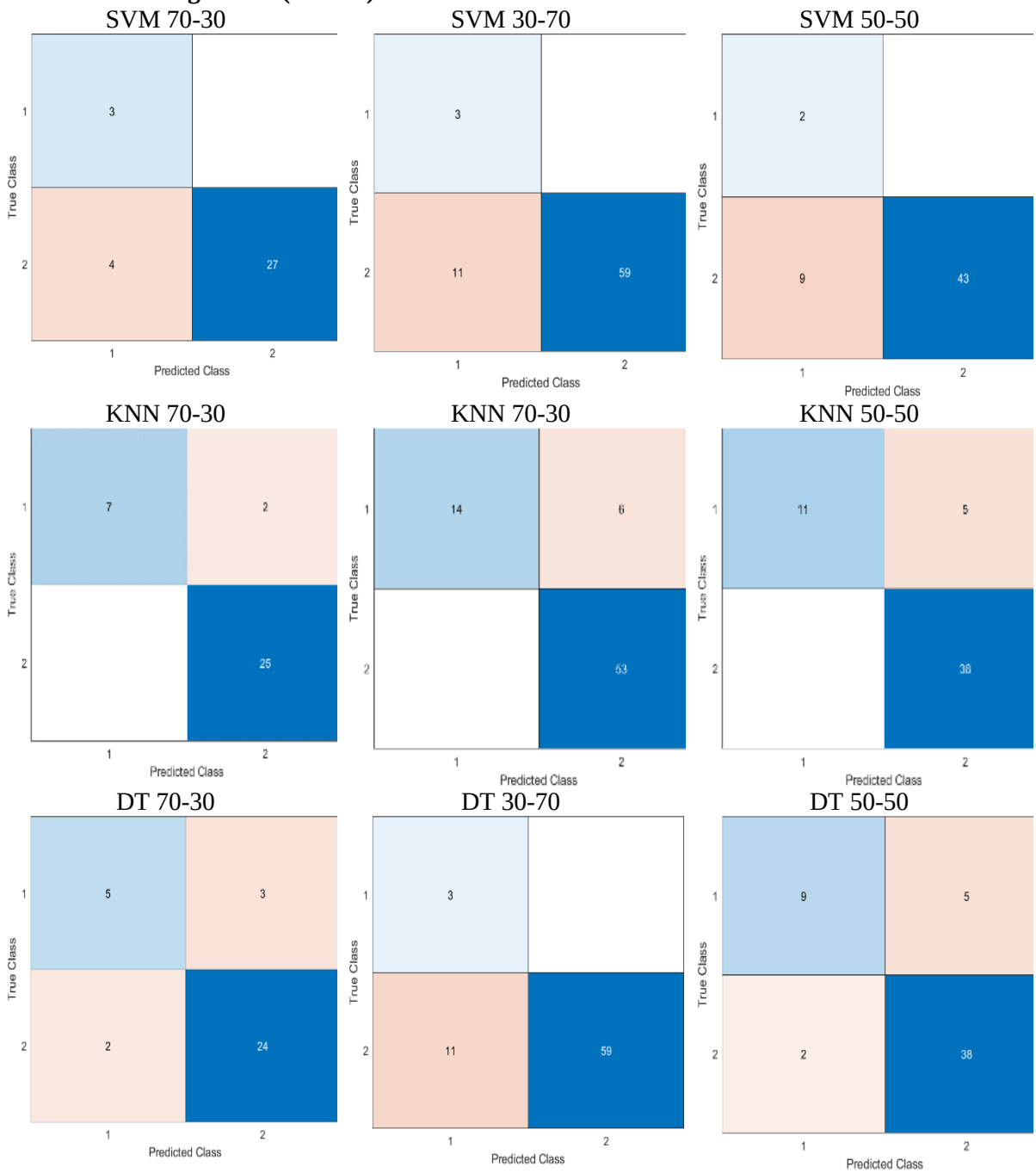

Figure 6-17: Confusion matrix obtained of each class of faults using training/testing scenarios for the three classifiers

In general, the results indicated that the classification was successful, especially for the second fault. These results identified and classified lamination insulation problems in electrical transformers. However, large databases are required to reach higher precision. And more accurate classifications are also required to provide assistance in preventing the electrical system

6.8.4 Fault classification between healthy and different faulty scenarios using a random dataset

In this section, the fault classification results utilising thermal images between healthy and the different scenarios of each fault are based on what was explained in chapter 4. Each fault has a set of scenarios. For example, the insulation damage fault was performed with 2, 6, 8, and 12 laminations with several specified flux density values, which were 0.5, 0.8, 1.0, 1.5, 1.7, and 1.8 T. As well as the Edge Burrs fault was investigated in several scenarios that were also explained in the same mentioned chapter in order to prove and confirm these mentioned target faults and their impact on the performance of the transformer's core. After the satisfactory results obtained from the detection and classification of the two main mentioned faults, the role of detecting the scenarios comes in order to increase the tools and methods of detection of these kinds of faults and to be targeted in the future. The scenarios of each fault have been grouped to form a separate category, with multi-classification scenarios (healthy, and the scenarios of faulty 1, 2, 3, 4.) formulated where the aim is to detect and classify the presence of each scenario.

In general, the insulation damage fault using KNN classifier obtained a good result for different scenarios. However, the other obtained results were unsatisfactory because it was not focused on since it was not the main objective of the research.

With the expected results, a relatively low accuracy rate has been obtained for most of the classifiers because of the low amount of dataset collected for this purpose due to not being focused on since it was not the main objective of the research and due to time limitations.

6.8.4 Edge burrs fault scenarios results

Each type of fault has been grouped to form a separate class, with multi-classification scenarios (healthy and fault scenarios 1, 2, 3, 4). For the results of Edge Burrs fault scenarios, see table 6-9. formulated where the aim is to detect and classify the presence of each scenario. The table provides the calculated results using three different classifiers. For three scenarios of the training and testing process, The results in this table show the accuracy rate of multi classes. As given in eq (5-1):

Table 6-8: The scenarios of Edge Burrs fault

Scenario	**Accuracy Rate (%)**		
	SVM	KNN	DT
70-30	72.50	100	67.50
30-70	67.85	100	58.33
50-50	77.04	100	75.40

The obtained results show that the proposed classifiers do not give roughly equivalent results for the three proposed scenarios (data decomposition for training and testing). Overall, the accuracy rate is around 70%, with a maximum of more than 77%, obtained when using the SVM classifier for the dataset testing the training scenarios using 50% of the dataset for the training. In comparison, 75.40% with the DT classifier used 50% of the dataset for the training, and around 67.50% used 70% of the training. In addition, an overfitting result was obtained using the KNN classifier for different dataset training scenarios. Figure 6-19 shows the confusion matrices obtained using the three algorithms for the three scenarios.

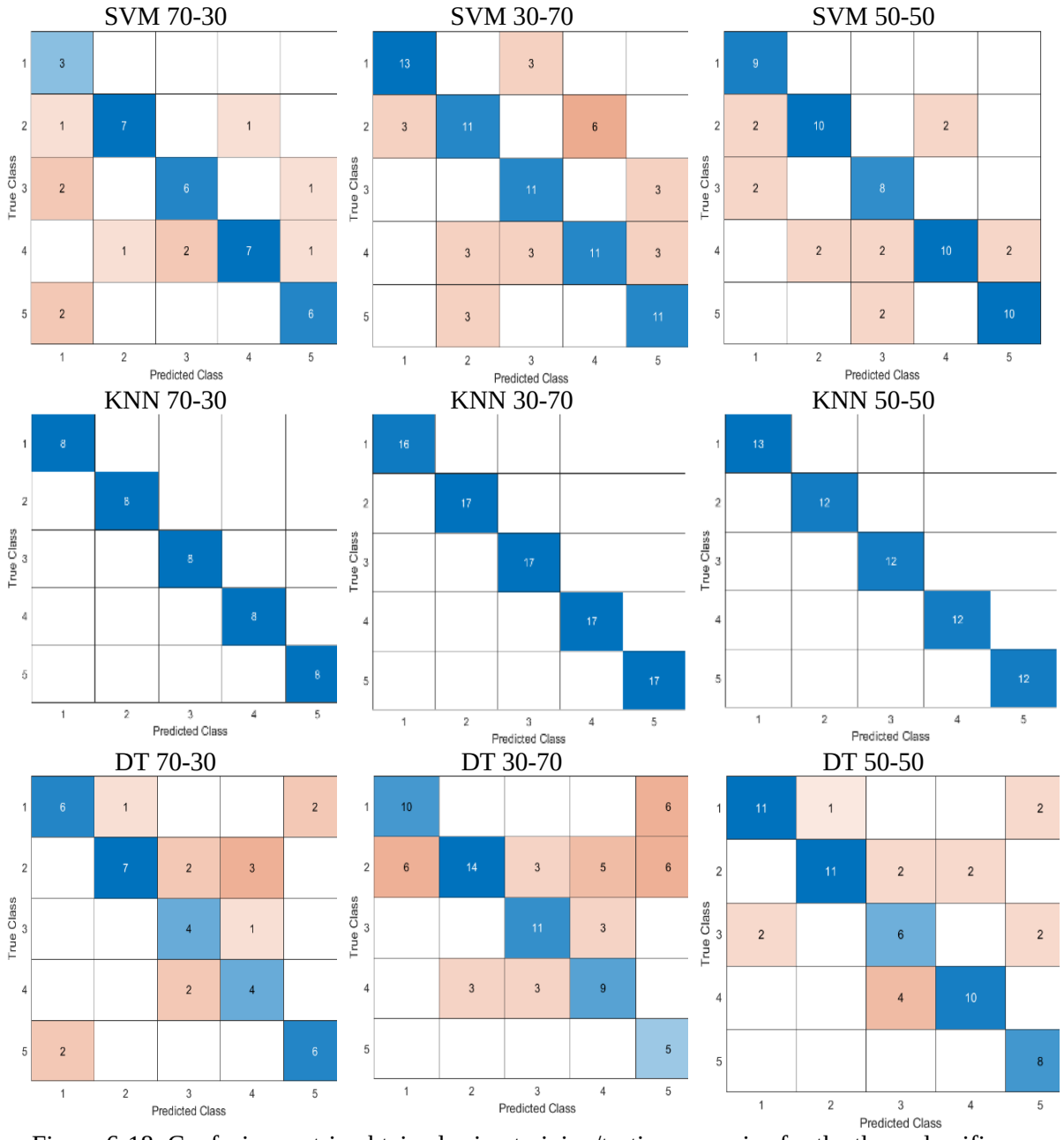

Figure 6-18: Confusion matrix obtained using training/testing scenarios for the three classifiers.

In general, the results indicated that the fault classification was successful for most of the classifiers, especially when using 50% of the dataset for the training. The (SVM) classifier achieved the highest accuracy in faults classification, and the (DT) classifier achieved slightly lower accuracy. In comparison, the (KNN) classifier achieved an over-fitting result. Such findings gave encouragement in the direction of fault detection and classification of lamination faults based on thermal images in an electrical transformer's core. In addition, this leads that the multi scenarios need more focus by increasing the number of images, in data processing (feature extraction) by increasing the number of features, or in classification by choosing appropriate algorithms.

6.8.5 Insulation damage scenarios results

The results in this table show the accuracy rate for multi classes of this fault eq (5-1). The obtained results show that some proposed classifiers gave roughly equivalent results for the three proposed scenarios (data decomposition for training and testing). For the results of insulation damage and fault scenarios, see next table 6-10.

Table 6- 9: The scenarios of insulation damage fault

Scenario	**Accuracy Rate (%)**		
	SVM	KNN	DT
70-30	82.35	94.11	79.41
30-70	63.01	91.78	60.27
50-50	64.81	90.74	81.48

From the table, the accuracy rate is around 80%, with a maximum of more than 82.35%, obtained when using 70% of the dataset for the training with an SVM classifier. While the accuracy was around 90% with the KNN classifiers, with a maximum of 94.11% when using 70% of the dataset for the training, which is the highest result. And the lowest accuracy result obtained was 79.41% using the DT classifier when using 70% of the data or the training but 81.48% when using 50% of the data or the training.

In general, the results indicated that the fault classification was successful and somehow accurate, especially when using 70% of the dataset for the training. The (KNN) classifier achieved the highest accuracy in fault classification. And the (SVM) classifier achieved slightly lower accuracy, whereas the (DT) classifier achieved the lowest accuracy. Figure 6-20 shows the confusion matrices.

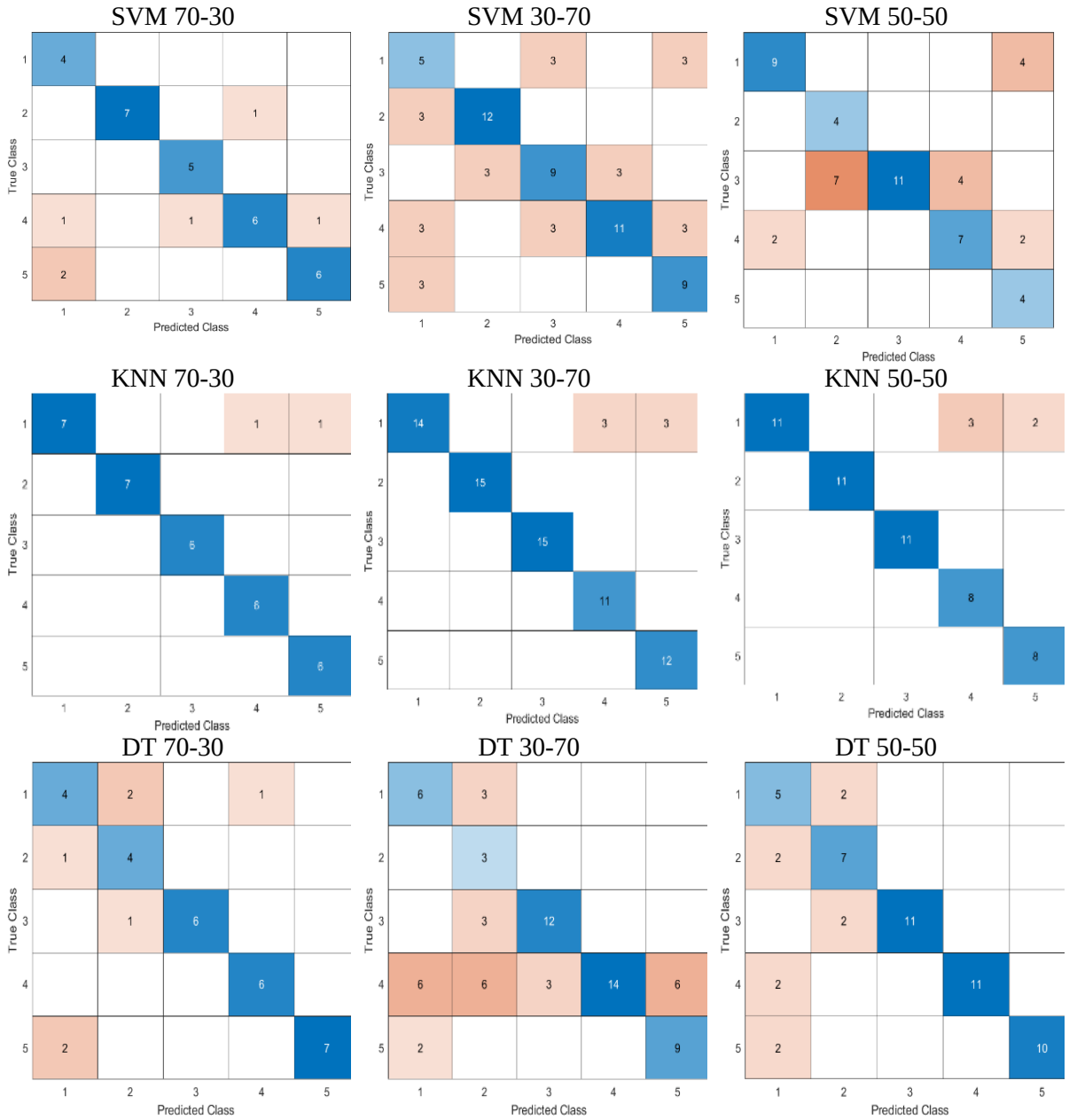

Figure 6-19: Confusion matrix obtained using training/testing scenarios for the three classifiers

In general, the results were satisfactory, especially for the second fault. These results encouraged the use of thermal imaging for fault identification and classification of lamination insulation problems in electrical transformer cores. This indicates that the multi scenarios need more focus, whether it is in laboratory experiments by increasing the number of images, or in data processing (feature extraction) by increasing the number of features and using different feature extraction techniques, or in classification by choosing appropriate algorithms.

6.9 K-fold cross-validation results

6.9.1 Definition of k-fold cross-validation

Cross-validation is a statistical method of evaluating and comparing learning algorithms by dividing data into two segments: one used to learn or train a model and the other used to validate the model. Full details are available in section 5.6.

In this section, the proposed application is assessed based on the experimental data of the thermal image dataset for both faults. In order to verify whether the proposed model, combined with the proposed feature selection techniques to select discriminative features, benefits the fault detection and classification procedure, the acquired dataset with the same extracted features extracted by the RGB technique was used as inputs to the classification algorithms. The selected optimal feature subsets were applied to three machine learning models, KNN, SVM, and DT, for classification into their respective classes. The classifiers are then trained using cross-validation. The training was repeated 3-fold, 5-fold, and 10-fold times with cross-validation techniques to fine-tune the model and ensure consistency in the results. Each classifier's performance was evaluated using its accuracy.

6.9.2 Fault detection using k-fold cross-validation based on thermal images

In this section, both types of faults have been grouped to form one class, representing the results of the faulty operation mode. Therefore, a binary classification (healthy and faulty) is formulated where the aim is to detect the presence of faulty conditions. This process is based on the features extracted from the thermal images. Table 6-11 gives the accuracy rate obtained using three different classifiers, eq (5-1). And the dataset was trained by repeated 3-fold, 5-fold, and 10-fold times with cross-validation techniques.

Table 6- 10: gives the accuracy rate obtained using three different classifiers

Fold Cross-Validation	SVM	KNN	DT
(3-fold) accuracy (%)	92.38	96.19	93.33
(5-fold) accuracy (%)	91.43	98.10	92.38
(10-fold) accuracy (%)	94.89	97.85	95.70

It can be stated that the highest classification accuracy was gained by (KNN) classifier, with an accuracy rate of 97.85% obtained when the model was trained with 10-fold cross-validation for the dataset training by applying the thermal images datasets for fault detection. And it was 96.19% when the model was trained with 3-fold cross-validation. Furthermore, when the DT model was trained with 3-fold cross-validation, the accuracy was 93.33%, and it was further raised to 95.70 % when the model was trained with 10-fold cross-validation using the thermal

images dataset. In addition, the classification accuracy using the SVM classifier was slightly lower, 94.89 % with 10-fold and 92.38% with 3-fold cross-validation for the dataset training. And for a general understanding of the classification process, see the confusion matrices in figure 6-21.

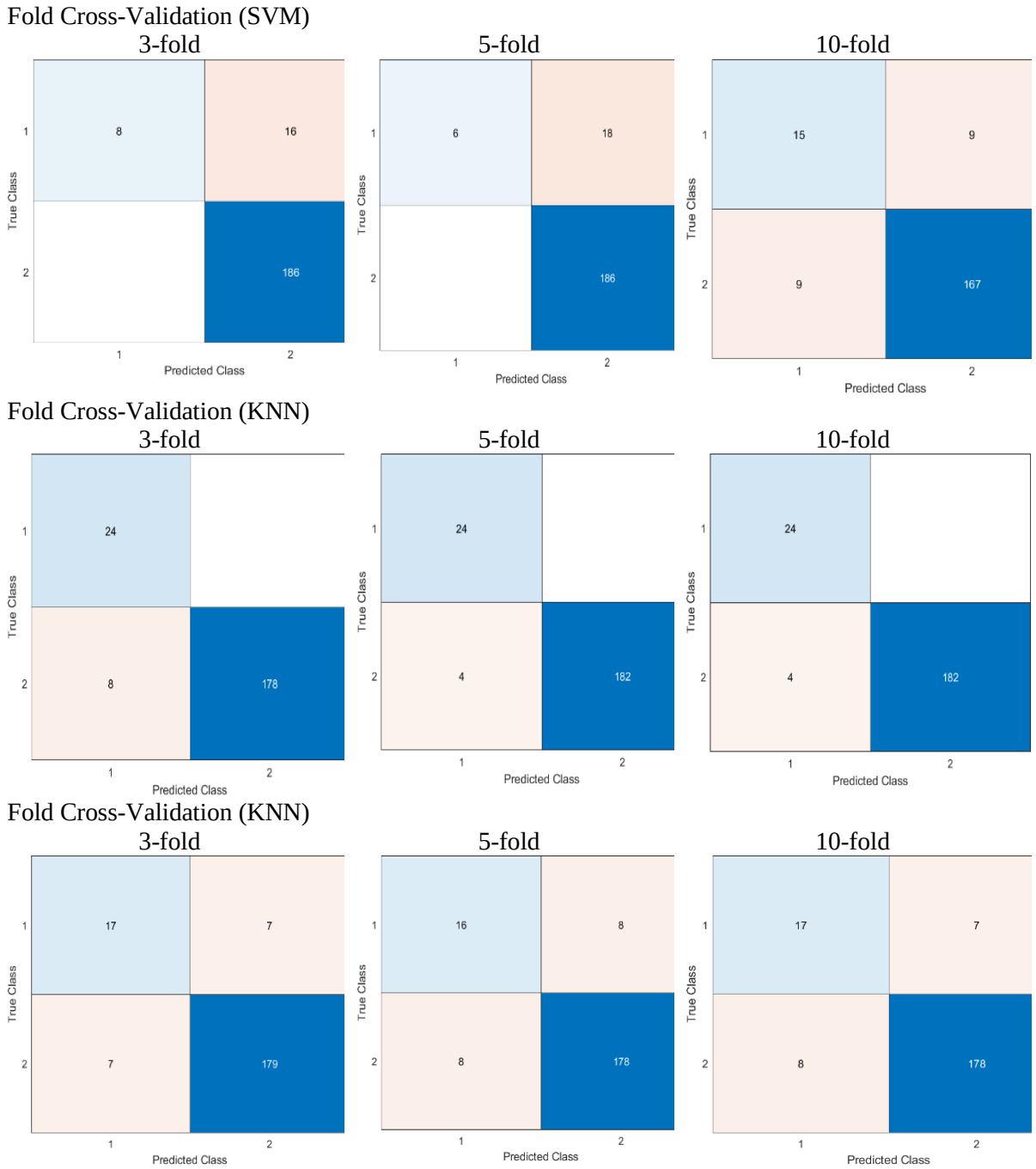

Figure 6-20: Confusion matrix obtained using cross-validation for the three classifiers of fault detection

In general, it can be confirmed that, as stated in Table 6-11, the results indicated that the fault detection was successful and accurate, especially when using 10-fold cross-validation for the

dataset training. The (KNN) classifier achieved the highest accuracy in faults detection, and the (DT) classifier achieved slightly lower accuracy, while the (SVM) classifier achieved the lowest accuracy. In addition, the 10-fold cross-validation of the dataset for the training gives the best results, while the 3-fold cross-validation gives lower results accuracy for the different classifiers. This indicates that artificial intelligence can accurately detect and classify fault detection. These findings supported the use of thermal imaging for fault diagnosis with lamination insulation faults in electrical transformer cores.

6.9.3 Classification for both types of faults using Cross-Validation

In this part, the classification between health conditions and both types of faults has been considered. Both types of faults have been separated to form two classes. The classes become a three-group classification. In table 6-12, the calculation results using the three classifiers, with 3,5, and 10-fold Cross-Validation for three classes of the training process, have been provided. The table results show the three classes' accuracy rates together, eq (5-1).

Table 6- 11: gives the accuracy rate obtained using three different classifiers

Fold Cross-Validation	SVM	KNN	DT
(3-fold) accuracy (%)	82.86	95.24	85.71
(5-fold) accuracy (%)	84.29	96.19	86.67
(10-fold) accuracy (%)	94.57	97.83	95.65

From this table, one can clearly see that the classification results are affected by the value of fold cross-validation. For instance, the results of the 10-fold show a better accuracy for most of the considered classifiers. This means that each fault can be easily identified from the others. In addition, the KNN classifier shows a good result for classification using cross-validation for the dataset training process. Where the accuracy of 97.83 % was obtained with the utilization of 5-fold cross-validation, and 95.24% and 96.19% were obtained with the 3, and 10-fold cross-validation, respectively, the accuracy rate for DT shows a slight decrease. Where an accuracy of 95.65 % obtained with the utilization of 10-fold cross-validation. And 85.71% and 86.67 were obtained with the 5, and 3-fold cross-validation, respectively.

Moreover, the SVM shows relatively lower accuracy rates, especially when the fold value was 3, and 5-fold cross-validation for the dataset training process. The accuracy was 82.86 % and 84.29 %. With 10-fold cross-validation, the accuracy was 94.57%. The overall accuracy rate for each case is presented in table 6-10. And from the confusion matrices one can get a general understanding of the classification process from the confusion matrices to figure 6-22. For example, precision and recall can be defined for each of the classes.

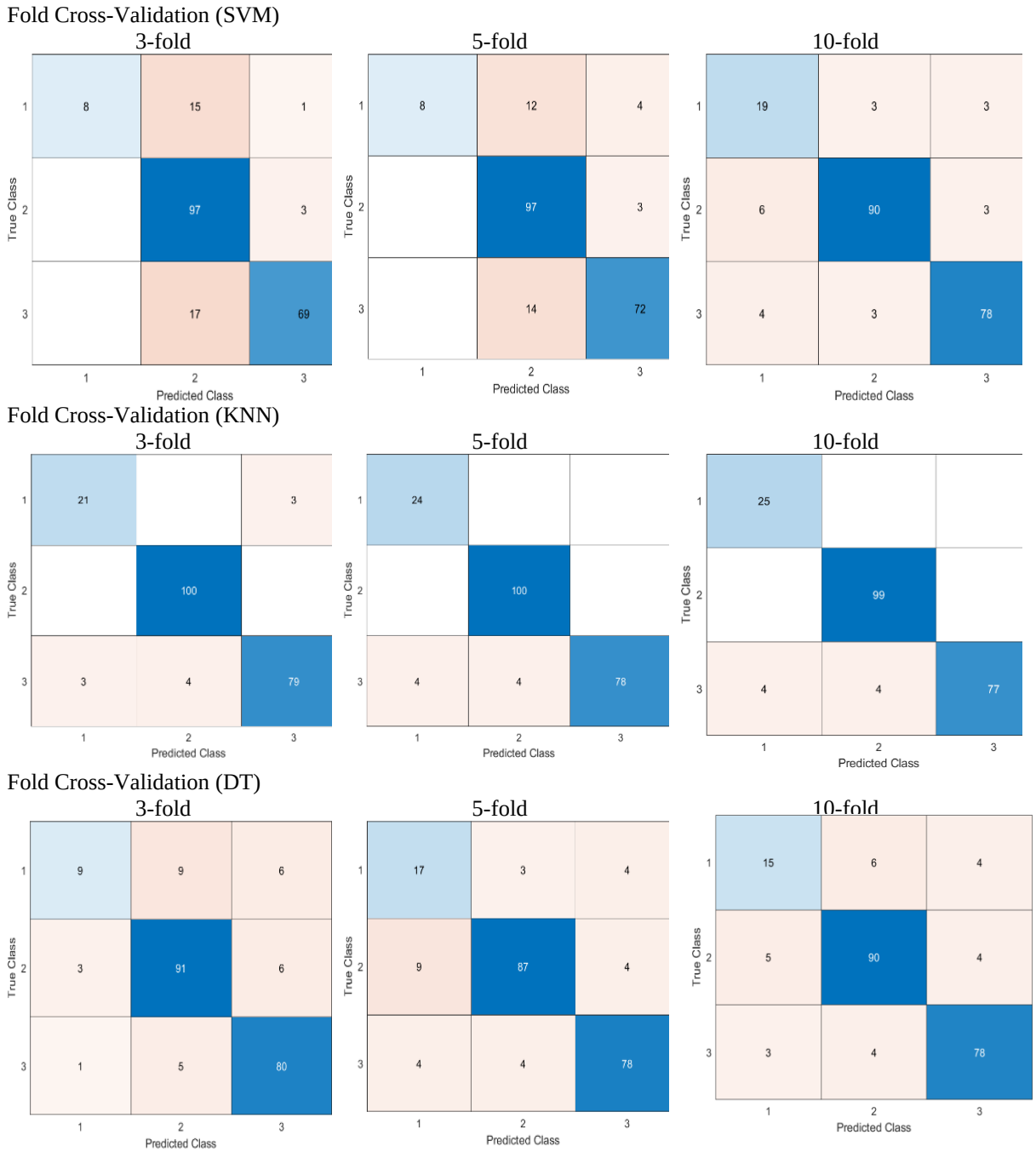

Figure 6-21: Confusion matrix obtained using cross-validation for the three classifiers of fault classification for both types

The laminations fault of the power transformer core can be detected and classified using artificial intelligence based on thermal images. Overall, the accuracy rate of fault classification for both types of faults using Cross-Validation is satisfactory, and the KNN classifier obtained the best result. The overall accuracy of the classification algorithms that were trained with 10-fold cross-validation was the best, indicating that the proposed model is promising for this application.

6.9.4 Detection of each fault separately using Cross-Validation

In this section, the classification between health conditions and each type of fault has been considered separately. Each type of fault has been separated to form one class the classes become a two-group classification. Table 6-13 provides the calculated results using the three classifiers and for three scenarios of the training and testing process. The table results show each class's accuracy rate separately, eq(5-1).

Table 6- 12: accuracy rate for each class of faults using different classifiers and considering three scenarios

Class	Training - Testing Data	Accuracy Rate (%)		
		SVM	KNN	DT
Fault 1	(3-fold) accuracy (%)	87.90	96.77	92.74
	(5-fold) accuracy (%)	87.10	100	94.35
	(10-fold) accuracy (%)	96.00	100	92.93
Fault 2	(3-fold) accuracy (%)	85.05	91.59	84.11
	(5-fold) accuracy (%)	85.98	92.52	85.98
	(10-fold) accuracy (%)	89.41	91.76	90.70

From this table, one can clearly see that the classification results are affected by the type of fault. For instance, the results of the second fault show a better accuracy for all the cases where the obtained accuracy was around 90 %. With a maximum of 91.76 % when using 10-fold cross-validation for the dataset training with the KNN classifier. While the accuracy result for the first fault (Edge Burrs) was obtained overfitting for most of the k-Fold cross-validation with the KNN classifier. For the other classifiers, the accuracy was around 90 % with the SVM classifier for both faults. Though the accuracy obtained with the DT classifier was around 90% for the first fault and around 80 % for the second fault, this means that the second fault (lamination's insulation fault) can be easily identified from the other faults. In addition, edge burrs fault shows a better result for fault detection using the DT classifier than the accuracy rate of the SVM classifier, which shows a slight decrease in its accuracy. Moreover, the second fault shows a better result for fault detection using the KNN classifier than the accuracy rate of the SVM and DT classifiers, where it shows a slight decrease. The overall accuracy rate for each case is presented in table 6-13. And from the confusion matrices, one can get a general understanding of the classification process in figures 6-23 and 6-24.

Edge Burrs Fault (Fault 1).

Fold Cross-Validation (SVM)

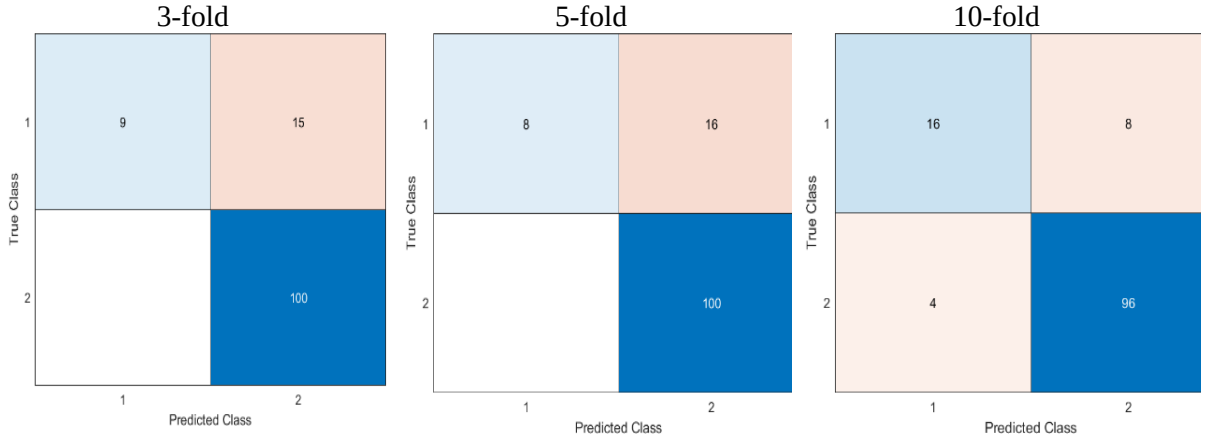

Fold Cross-Validation (KNN)

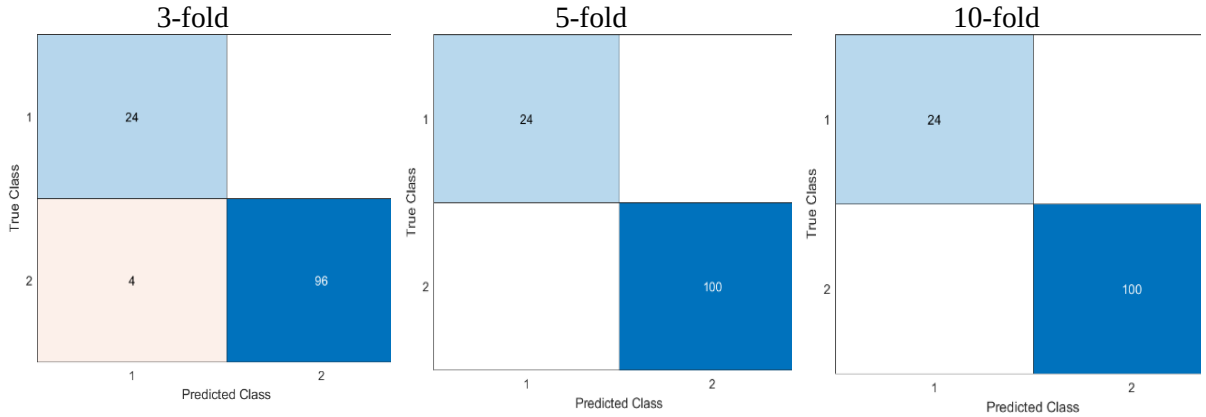

Fold Cross-Validation (DT)

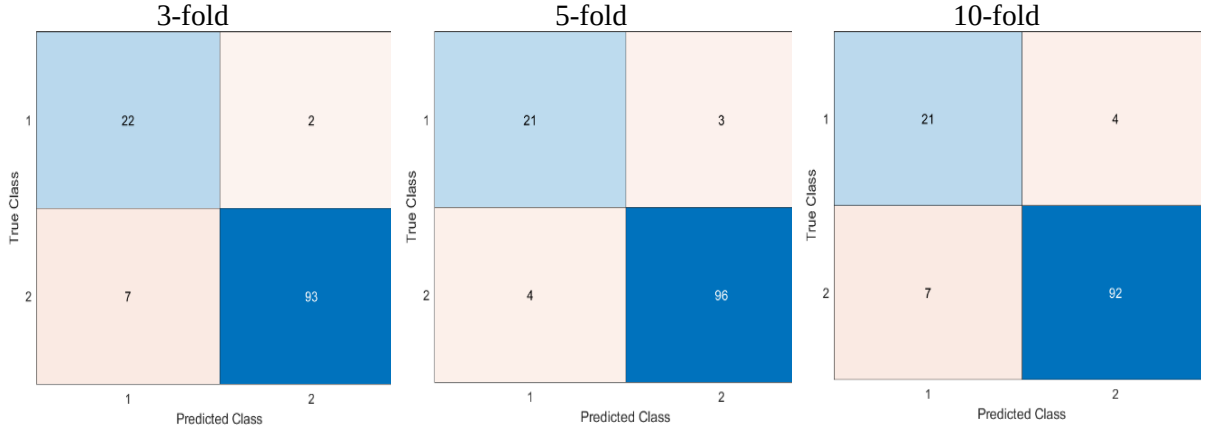

Figure 6- 22: confusion matrix obtained using cross-validation for the three classifiers of fault classification for Edge Burrs fault (Fault 1)

Insulation Damage (Fault 2).

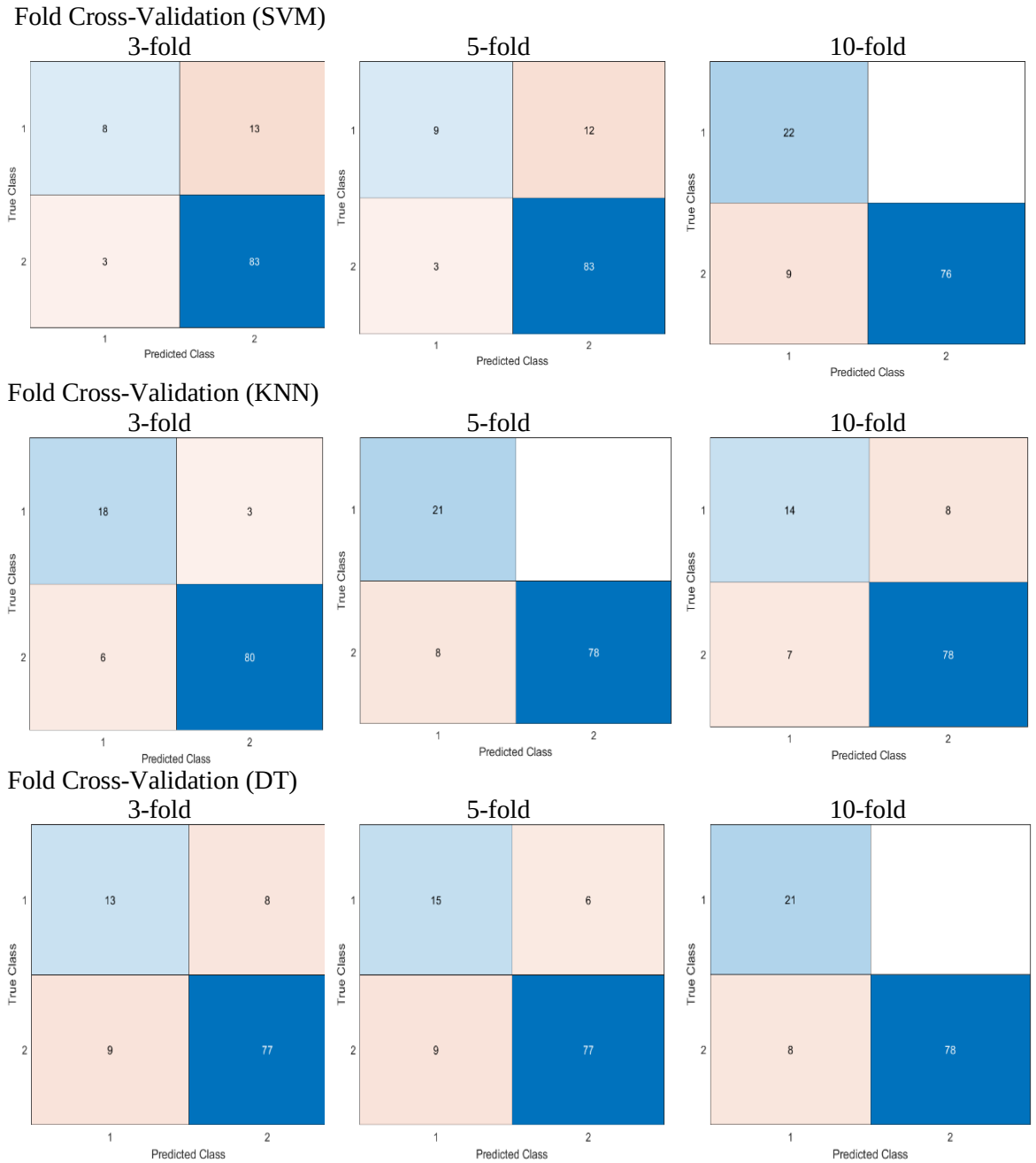

Figure 6-23: Confusion matrix obtained using cross-validation for the three classifiers of fault classification for the insulation damage Fault (Fault 2).

In general, the findings of the detection of each fault separately using Cross-Validation indicate that the proposed fault detection model can be generated using thermal images and has a superior performance based on the accuracy results. The classification algorithms are essential for fault detection and classification in the detection model. The KNN classifier outperformed the DT and SVM classifiers in the second fault, while the DT classifier outperformed the first

fault in most cases in determining the correct class. Additionally, applying a 10-fold cross-validation strategy to train the proposed models could enhance classification accuracy.

6.9.5 Fault classification between healthy and different faulty scenarios using K-Fold Cross-Validation

In this section, the classification accuracy results are presented between healthy and the different faulty scenarios utilising the thermal images of each fault. Each fault has a set of scenarios based on what was explained in chapter 5. For example, the insulation damage fault was performed with 2, 6, 8, and 12 laminations with several specified flux density values, which were 0.5, 0.8, 1.0, 1.5, 1.7, and 1.8 T. Also, the Edge Burrs fault was investigated in several scenarios that were also explained in the same mentioned chapter to prove and confirm these mentioned target faults and their impact on the performance of the transformer's core. After the satisfactory results obtained from the detection and classification of the two main mentioned faults, the role of detecting the scenarios comes to increase the tools and methods of detecting these kinds of faults and to be targeted in the future.

With the expected results, a relatively low accuracy rate has been obtained because of the low amount of dataset collected for this purpose due to not being focused on since it was not the main objective of the research and time limitations.

6.9.6 Edge burrs fault results

Each fault's scenarios have been grouped to form multi classes (healthy and fault scenarios 1, 2, 3, 4) formulated where the aim is to detect and classify the presence of each scenario. For the scenarios results of Edge burrs fault based on thermal images, see table 6-14, the table provides the calculated results using the SVM, KNN, and DT classifiers, and the training was repeated three, five, and ten times with cross-validation techniques to fine-tune the model and ensure consistency in the results for the four scenarios of the fault. The results in this table show the accuracy rate of multi classes, eq (5-1).

Table 6- 13: The Scenarios of Edge Burs faults

Fold Cross-Validation	SVM	KNN	DT
(3-fold) accuracy (%)	58.87	96.77	66.13
(5-fold) accuracy (%)	70.16	100	72.58
(10-fold) accuracy (%)	90.00	100	93.00

From the obtained results, one can see that the proposed classifiers do not give roughly equivalent results for the proposed scenarios (data decomposition for training and testing of the scenarios of edge burrs fault). Overall, the accuracy rate is around 70%, with a maximum of

more than 90.00 %, obtained when using a 10-fold cross-validation dataset for the training with the SVM classifier. On the other side, around 70% was the obtained accuracy using the DT classifier with a maximum of more than 93.00 % when using 10-fold cross-validation of the dataset for the training, which was the highest result. While overfitting was obtained with the KNN classifier when using most of the K-Fold cross-validation of the dataset for the training. The lowest result was obtained by the KNN classifier, while the highest result was obtained when the DT classifier was used with 10-fold cross-validation. Figure 6-25 the confusion matrices.

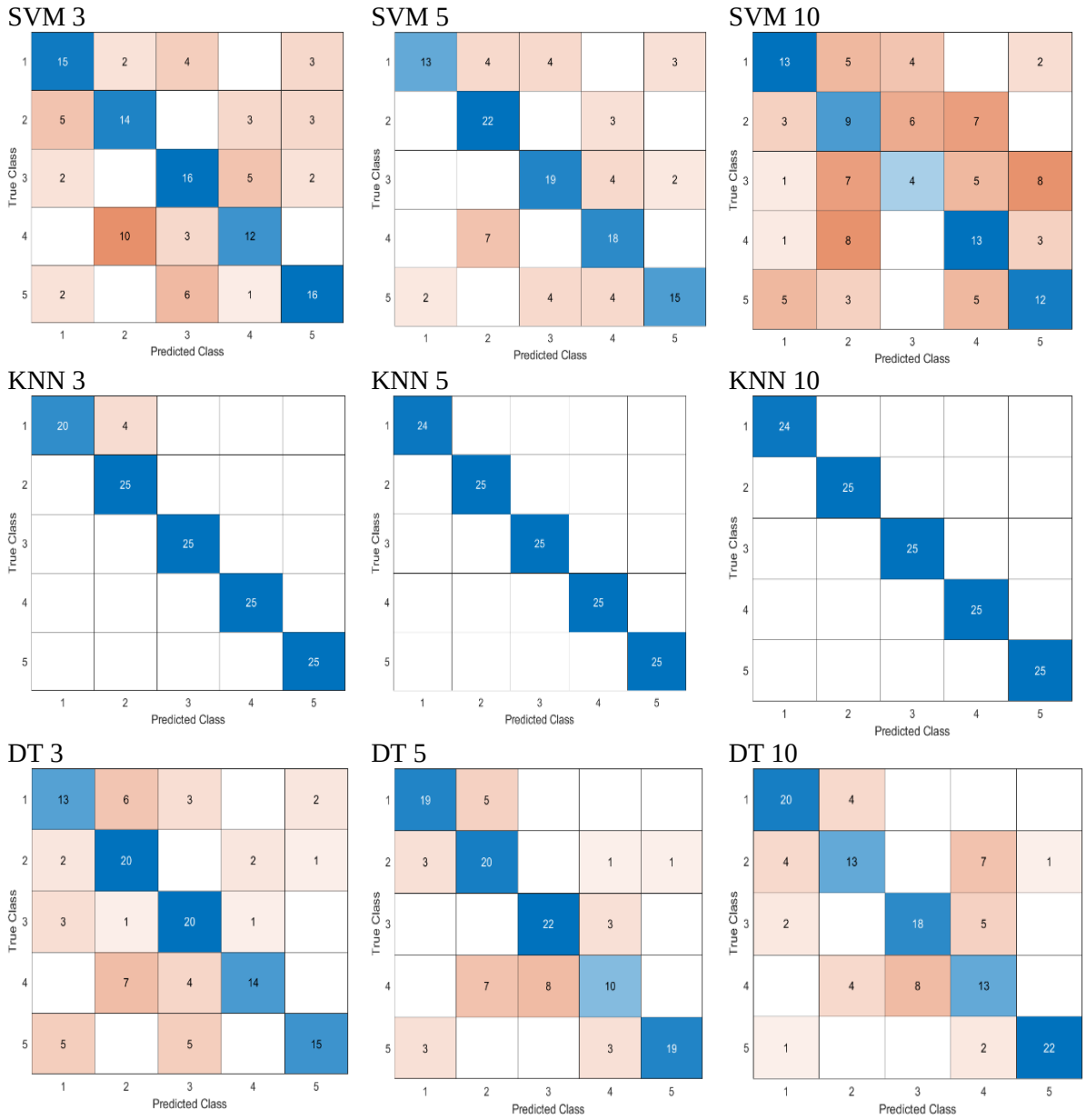

Figure 6-24: Confusion matrix obtained using training/testing scenarios for the three classifiers of the insulation damage Fault

In general, 10-fold cross-validation of the dataset for the training gives the best results while the 3-fold cross-validation gets fewer accuracy results for the different classifiers. When training the model using the K-fold cross-validation strategy, the (DT) achieved the highest classification accuracy. The (SVM) classifier achieved slightly lower accuracy. in comparison, the (KNN) classifier achieved the over-fitting results. This indicates that the multi scenarios of the faulty conditions need more focus, such as collecting more data and extracting more features using different feature extraction techniques.

6.9.6 Insulation damage fault results

For the results of faulty mode scenarios of laminations damage fault based on thermal images. Next, table 6-15 shows this fault's accuracy rate for multi classes, eq (5-1).

Table 6- 14: The scenarios of insulation damage faults

Fold Cross-Validation	SVM	KNN	DT
(3-fold) accuracy (%)	62.62	90.65	68.22
(5-fold) accuracy (%)	66.36	92.52	72.90
(10-fold) accuracy (%)	72.09	90.70	87.21

The obtained results show that some proposed classifiers gave roughly equivalent results for the proposed scenarios. Overall, 92% is the average accuracy rate obtained using the KNN classifier with a maximum of more than 90 %, obtained when using 10-fold cross-validation of the dataset for the training, which was the highest result, and with the SVM classifier around 60% is the accuracy rate was obtained with a maximum of more than 72 % using 10-fold cross-validation which was the lowest results obtained for this fault. On the other side, more than 87 % with the DT classifier when using 10-fold cross-validation of the dataset for the training. And 68% was obtained with 3-fold cross-validation, the lowest obtained result with this classifier. In addition, the confusion matrices in figure 6-26 might helps better comprehend the identification process.

In general, increasing the number of folds in cross-validation increases the accuracy of the models, as more data is used for training and validation. For example, with 10-fold cross-validation, the accuracy is higher compared to 3-fold or 5-fold cross-validation.

In conclusion, the results suggest that KNN is a better performing algorithm compared to SVM and DT, and using a larger number of folds in cross-validation can increase the accuracy of the models.

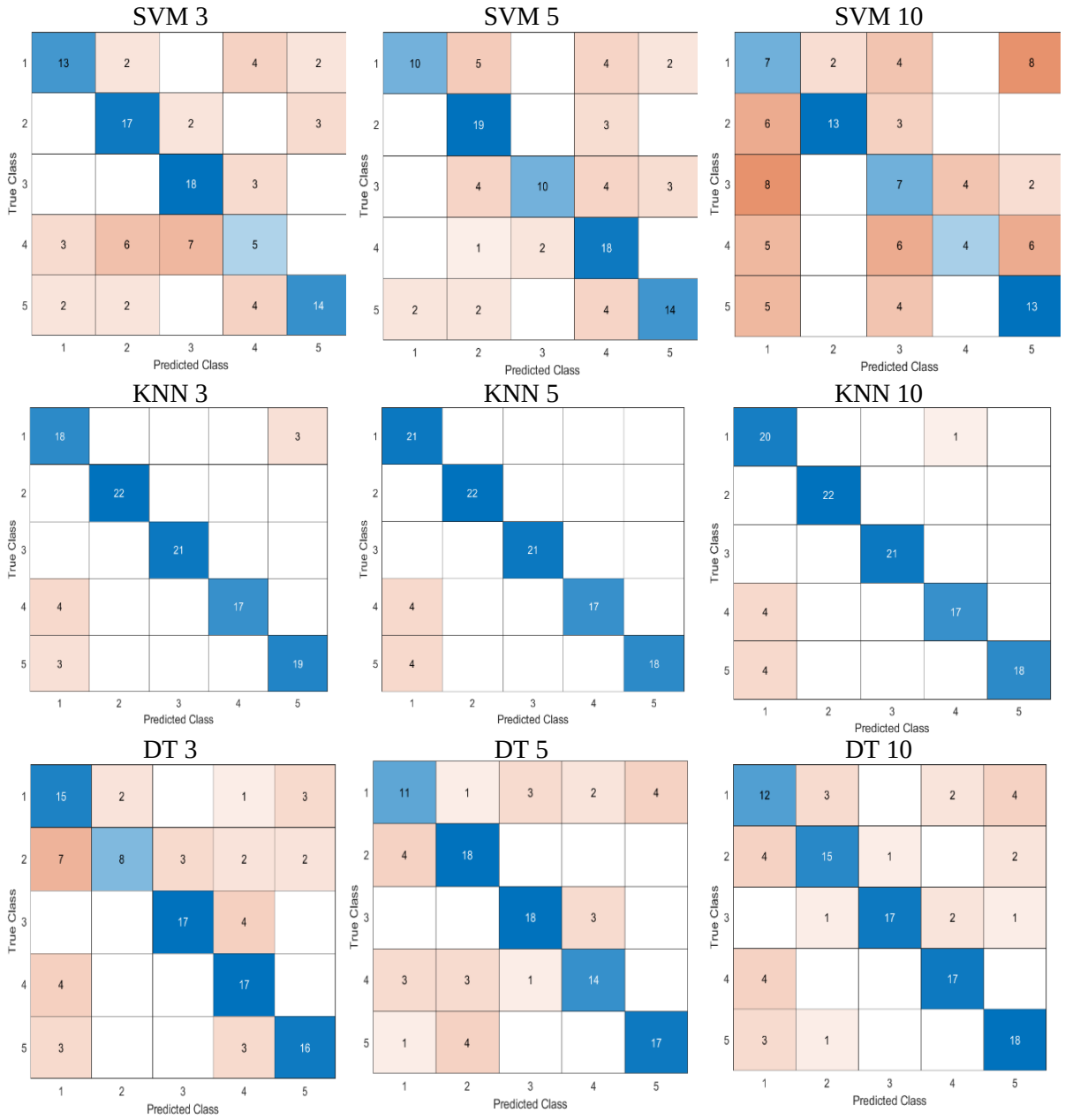

Figure 6-25: Confusion matrix obtained using training/testing scenarios for the three classifiers of the insulation damage Fault

In general, the lamination's insulation fault gives a better result, which means it can be easily identified. And 10-fold cross-validation of the dataset for the training gives the best results, while the 3-fold cross-validation gives fewer results accuracy for the different classifiers. When training the model using 10-fold cross-validation, the KNN achieved the highest classification accuracy, and the DT classifier achieved slightly lower accuracy. In contrast, the SVM classifier achieved the lowest accuracy. This indicates that the multi scenarios of faulty conditions can be accurately detected and classified using artificial intelligence.

6.10 Summary

This chapter presented a study on the detection and classification of lamination faults in the power transformer core. Based on thermal images, the detection and classification of two types of lamination faults (i.e., edge burr and lamination insulation faults) in a three-phase transformer core have been studied. From Chapter 4, experimental results obtained using a 15 kVA transformer were exploited. A new feature extraction technique for thermal images has been presented called the RGB technique, which helps diagnoses faults in the power transformer core and demonstrates its impact. Eight features were extracted, and a graphical representation was made to distinguish the independent features. Four features were selected (the highest temperature value, R1, R3, and R5). Elaborating a total of 222 samples, these features are utilized as input vectors to train and test classification models based on SVM, KNN, and DT algorithms. The dataset for training and testing the model has been managed by considering different scenarios to ensure that the results of the experimental work are accurate and these faults can be identified and classified easily by artificial intelligence. Overall, the obtained results indicated that transformer thermal images are an effective tool for detecting and classifying lamination faults in the transformer core. The following conclusions are also drawn.

1. SVM, KNN, and DT classifiers gave a good accuracy rate of around 98% in the detection purpose where two classes were considered when a random dataset was used and more than 99% when 10-fold cross-validation for the dataset training was used.
2. For the classification, a maximum accuracy rate of 98.50% was obtained using the KNN algorithm. It was 91.34% for SVM and 91.04% for DT classifiers. The classification process was also sensitive to data decomposition, especially for the DT algorithm. And for 10-fold cross-validation for the dataset training, 97 % accuracy has been obtained with the KNN classifier and 86 %, and 84 % obtained with the DT and SVM classifiers, respectively.
3. It was found that the insulation lamination fault presented a good accuracy rate compared to another fault when the KNN classifier was used. Higher precision and recall were obtained for this fault.
4. I Highly recommend Using a new, more advanced thermal camera to get more accurate and clear images
5. For classification between healthy and different faulty scenarios, the obtained results were unsatisfactory because it was not focused on since it was not the main objective of the research.

Such findings indicated that better detection and classification results might be obtained by enlarging the database or using other classification algorithms. It is also suggested to investigate the classification using other features by employing other signal processing techniques.

6.11 Reference

[1] P. Chen, Y. Huang, F. J. Zeng, Y. Jin, X. Zhao, and J. Wang, "Review On Insulation And Reliability Of Dry-type Transformer," *iSPEC 2019 - 2019 IEEE Sustain. Power Energy Conf. Grid Mod. Energy Revolution, Proc.*, pp. 398–402, 2019.

[2] X. Duan, T. Zhao, J. Liu, L. Zhang, and L. Zou, "Analysis of winding vibration characteristics of power transformers based on the finite-element method," *Energies*, vol. 11, no. 9, 2018.

[3] C. Jettanasen and A. Ngaopitakkul, "A novel probabilistic neural network-based algorithm for classifying internal fault in transformer windings," *IEEJ Trans. Electr. Electron. Eng.*, vol. 8, no. 2, pp. 123–131, 2013.

[4] F. Yuan, J. Guo, Z. Xiao, B. Zeng, W. Zhu, and S. Huang, "A transformer fault diagnosis model based on chemical reaction optimization and twin support vector machine," *Energies*, vol. 12, no. 5, 2019.

[5] B. E. Lee, J. W. Park, P. A. Crossley, and Y. C. Kang, "Induced voltages ratio-based algorithm for fault detection, and faulted phase and winding identification of a three-winding power transformer," *Energies*, vol. 7, no. 9, pp. 6031–6049, 2014.

[6] M. Gutten, D. Korenciak, M. Kucera, R. Janura, A. Glowacz, and E. Kantoch, "Frequency and time fault diagnosis methods of power transformers," *Meas. Sci. Rev.*, vol. 18, no. 4, pp. 162–167, 2018.

[7] A. Sedighi, A. Kafiri, M. Shahnazari, M. R. Sehati, and F. Behdad, "Aging Assessment of Distribution Transformers Based on Thermal Imaging," *Proc. - 2019 IEEE Int. Conf. Environ. Electr. Eng. 2019 IEEE Ind. Commer. Power Syst. Eur. EEEIC/I CPS Eur. 2019*, 2019.

[8] A. S. N. Huda and S. Taib, "Application of infrared thermography for predictive/preventive maintenance of thermal defect in electrical equipment," *Appl. Therm. Eng.*, vol. 61, no. 2, pp. 220–227, 2013.

[9] M. Kunicki, A. Cichon, and S. Borucki, "Measurements on partial discharge in on-site operating power transformer: A case study," *IET Gener. Transm. Distrib.*, vol. 12, no. 10, pp. 2487–2495, 2018.

[10] R. Murugan and R. Ramasamy, "Failure analysis of power transformer for effective maintenance planning in electric utilities," *Eng. Fail. Anal.*, vol. 55, pp. 182–192, 2015.

[11] D. A. K. Pham, T. M. T. Pham, H. Borsi, and E. Gockenbach, "A new method for purposes of failure diagnostics and FRA interpretation applicable to power transformers," *IEEE Trans. Dielectr. Electr. Insul.*, vol. 20, no. 6, pp. 2026–2034, 2013.

[12] R. Khalili Senobari, J. Sadeh, and H. Borsi, "Frequency response analysis (FRA) of transformers as a tool for fault detection and location: A review," *Electr. Power Syst. Res.*, vol. 155, pp. 172–183, 2018.

[13] M. Bagheri, A. Zollanvari, and S. Nezhivenko, "Transformer Fault Condition Prognosis Using Vibration Signals over Cloud Environment," *IEEE Access*, vol. 6, pp. 9862–9874, 2018.

[14] V. M. Shiljkut, “REMOTE MONITORING OF POWER TRANSFORMERS THERMAL IMAGE,” no. 045, pp. 12–15, 2012.

[15] S. Bin Lee, G. B. Kliman, M. R. Shah, W. T. Mall, N. K. Nair, and R. M. Lusted, “An advanced technique for detecting inter-laminar stator core faults in large electric machines,” *IEEE Trans. Ind. Appl.*, vol. 41, no. 5, pp. 1185–1193, 2005.

[16] A. Kedous-Lebouc, B. Cornut, J. C. Perrier, P. Manfé, and T. Chevalier, “Punching influence on magnetic properties of the stator teeth of an induction motor,” *J. Magn. Magn. Mater.*, vol. 254–255, pp. 124–126, 2003.

[17] P. Handgruber, A. Stermecki, O. Biro, and G. Ofnery, “Evaluation of interlaminar eddy currents in induction machines,” *IECON Proc. (Industrial Electron. Conf.*, pp. 2792–2797, 2013.

[18] M. Bigdeli, M. Vakilian, and E. Rahimpour, “Transformer winding faults classification based on transfer function analysis by support vector machine,” *IET Electr. Power Appl.*, vol. 6, no. 5, pp. 268–276, 2012.

[19] M. B. Aimoniotis and A. J. Moses, “Evaluation of induced eddy currents in transformer sheets due to edge-burrs, employing computer aided design programs,” *Jt. Int. Power Conf. "Athens Power Tech" Planning, Oper. Control Today’’s Electr. Power Syst. APT 1993 - Proc.*, vol. 2, pp. 847–850, 1993.

[20] R. Mazurek, H. Hamzehbahmani, A. J. Moses, P. I. Anderson, F. J. Anayi, and T. Belgrand, “Effect of artificial burrs on local power loss in a three-phase transformer core,” *IEEE Trans. Magn.*, vol. 48, no. 4, pp. 1653–1656, 2012.

[21] S. V. Ananth and P. Sudhakar, “Performance analysis of a combined cryptographic and steganographic method over thermal images using barcode encoder,” *Indian J. Sci. Technol.*, vol. 9, no. 7, 2016.

[22] Y. Sun *et al.*, “A temperature-based fault pre-warning method for the dry-type transformer in the offshore oil platform,” *Int. J. Electr. Power Energy Syst.*, vol. 123, no. April, 2020.

[23] M. K. Chen, J. M. Chen, and C. Y. Cheng, “Partial discharge detection in 11.4 kV cast resin power transformer,” *IEEE Trans. Dielectr. Electr. Insul.*, vol. 23, no. 4, pp. 2223–2231, 2016.

[24] S. C. Athikessavan, E. Jeyasankar, S. S. Manohar, and S. K. Panda, “Inter-Turn Fault Detection of Dry-Type Transformers Using Core-Leakage Fluxes,” *IEEE Trans. Power Deliv.*, vol. 34, no. 4, pp. 1230–1241, 2019.

[25] E. Gockenbach, P. Werle, and H. Borsi, “Monitoring and diagnostic systems for dry type transformers,” *IEEE Int. Conf. Conduct. Break. Solid Dielectr.*, pp. 291–294, 2001.

[26] C. T. Lee and S. C. Horng, “Abnormality detection of cast-resin transformers using the fuzzy logic clustering decision tree,” *Energies*, vol. 13, no. 10, 2020.

[27] A. K. Al-Musawi, F. Anayi, and M. Packianather, “Three-phase induction motor fault detection based on thermal image segmentation,” *Infrared Phys. Technol.*, vol. 104, no. December 2019, p. 103140, 2020.

[28] M. Bagheri, M. Naderi, and T. Blackburn, “Advanced transformer winding deformation diagnosis: Moving from off-line to on-line,” *IEEE Trans. Dielectr. Electr. Insul.*, vol. 19, no. 6, pp. 1860–1870, 2012.

[29] J. Liu, Z. Zhao, C. Tang, C. Yao, C. Li, and S. Islam, “Classifying Transformer Winding Deformation Fault Types and Degrees Using FRA Based on Support Vector Machine,” *IEEE Access*, vol. 7, pp. 112494–112504, 2019.

[30] A. Mathur and G. M. Foody, "Multiclass and Binary SVM Classification: Implications for Training and Classification Users," in IEEE Geoscience and Remote Sensing Letters, vol. 5, no. 2, pp. 241-245, April 2008, doi: 10.1109/LGRS.2008.915597.

[31] Y. Benmahamed, M. Teguar and A. Boubakeur, "Application of SVM and KNN to Duval Pentagon 1 for transformer oil diagnosis," in IEEE Transactions on Dielectrics and Electrical Insulation, vol. 24, no. 6, pp. 3443-3451, Dec. 2017, doi: 10.1109/TDEI.2017.006841.

[32] J. Jia et al., "Tradeoffs in the Spatial and Spectral Resolution of Airborne Hyperspectral Imaging Systems: A Crop Identification Case Study," in IEEE Transactions on Geoscience and Remote Sensing, vol. 60, pp. 1-18, 2022, Art no. 5510918, doi: 10.1109/TGRS.2021.3096999.

[33] Xiaoyu Luo, ”Efficient English text classification using selected Machine Learning Techniques”, Alexandria Engineering Journal, Volume 60, Issue 3, 2021, Pages 3401-3409.

[34] L. Breiman, J. Friedman, C. J. Stone, and R. A. Olshen, Classification Regression Trees. Boca Raton, FL, USA: CRC Press, 1984.

[35] Eecs.wsu.edu, 2022. [Online]. Available: https://eecs.wsu.edu/~cs445/Lecture_14.pdf. [Accessed: 23- Jun- 2022].

[36] T. Peynot, "Digital Image Processing", Portal.abuad.edu.ng, 2022. [Online]. Available: https://portal.abuad.edu.ng/lecturer/documents/1590138052AMME4710-Chap5-ColourIP.pdf. [Accessed: 23- Jun- 2022].

[37] "Rgb Color Model Cube, HD Png Download , Transparent Png Image - PNGitem", PNGitem.com, 2022. [Online]. Available: https://www.pngitem.com/middle/ThRhwmb_rgb-color-model-cube-hd-png-download/. [Accessed: 23- Jun- 2022].

[38] Refaeilzadeh P., Tang L., Liu H. (2016) Cross-Validation. In: Liu L., Özsu M. (eds) Encyclopedia of Database Systems. Springer, New York, NY. https://doi.org/10.1007/978-1-4899-7993-3_565-2

[39] "K Fold Cross-Validation in Machine Learning? How does K Fold Work?", *MLTut*, 2022. [Online]. Available: https://www.mltut.com/k-fold-cross-validation-in-machine-learning-how-does-k-fold-work/. [Accessed: 21- Jul- 2022].

CHAPTER 7: Optimization Techniques for Classification Purpose

The demand for condition monitoring of power transformers (PT) is on the rise, driven by the need to maintain the reliability and performance of several critical industries. Fault detection in PTs, particularly in the core's lamination, is a crucial area of focus in this regard. This study proposes a hybrid machine learning approach for PT core fault detection, leveraging advances in signal processing and machine learning systems. The methodology uses current signals and thermal images as the key fault parameters for testing. The model was tested on datasets collected from laboratory experiments conducted under both healthy and faulty conditions of PTs with no-load conditions. The data was trained and tested using three widely used machine learning classifiers: Support Vector Machine (SVM), K-Nearest Neighbor (KNN), and Decision Tree (DT). The optimal subset of features was selected to improve the accuracy of the classifiers. While DT achieved the highest accuracy in fault detection, KNN performed slightly lower. SVM, on the other hand, showed the lowest accuracy. To address this, the study combined SVM with Bayesian Optimization Algorithm (BOA) and Particle Swarm Optimization Algorithms (PSO) to develop a hybrid classification model, which showed improvement in accuracy.

7.1 Introduction

As the power grid's capacity continues to expand, power transformers have become the main equipment in the power system. The excellent performance of the power transformer will directly affect the operation of the power grid. Any failure in the power transformer can cause its power to be interrupted. Thus, it is of great significance to detect potential faults in the transformer as soon as possible. Recently, many scholars have been committed to researching their diagnostic methods[1][2]. To achieve stability and safety in power grid operations, an accurate protection scheme is required. A power transformer must be protected by avoiding or reducing damage due to the high cost of maintenance[3]. Regarding their importance in the energy systems, reliable and safe operation of the transformers is of great significance to guarantee a long lifetime [4].

Figure 7-1 shows a flow chart illustrating the major steps of the proposed application as they will be applied to carry out this project. To create a large dataset, the current signal and thermal images are captured using specialized sensors under various operating situations. FFT, CWT, DWT, and RGB are used for each signal collected to retrieve the best features. It is crucial to

determine the right number of discriminative features, as too many features can result in too much noise, whereas too few can lead to a loss of information for the classifier. The computational complexity of classification algorithms is excessive when they use many features unless certain methods for reducing data dimensionality are employed before classification. Thus, in this research, the features have been selected based on a graphical representation to distinguish the independent features from the others, which are optimized into representative features.

In order to detect and classify faults, the feature obtained through the feature selection process is inputted into three classifiers using machine learning. The training and testing were repeated three times to fine-tune the model and ensure consistency in the results.

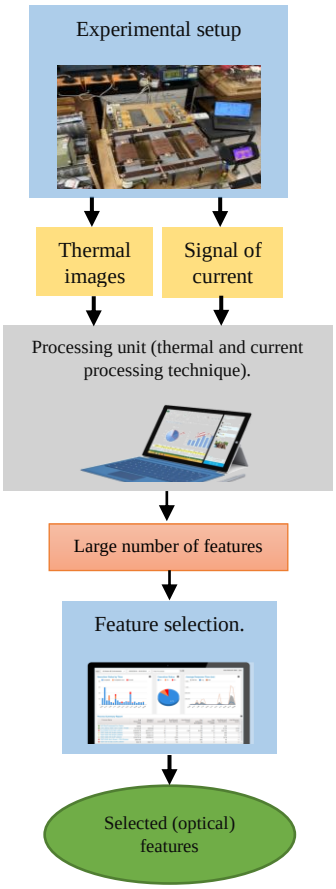

Figure 7- 1: Schematic diagram of the proposed methodology

7.2 Research methodology

This section contains three basic steps: Feature Extraction, Selection Methods, and fault classification process. All of them are explained in detail in previous chapters.

7.2.1 Dataset

The features of current signal for two types of lamination faults (i.e., edge burr and lamination insulation faults) are utilized as input vectors to train and test classification models based on an optimized SVM classifier, elaborating a total of 328 samples of current signals and 222 samples of thermal images. The studied cases for both types of faults based on current signal and thermal images are summarized in table 7-1.

Table 7- 1: Description of the database

Mode	Cases	Description
Normal/healthy	6	6 cases correspond to six selected flux densities
Edge Burr Fault	4x2x6	4 scenarios (S1, S2, S3, and S4) of artificial edge burr fault are applied in 2 and 3 different places within the transformer core. Each fault case (a given scenario in 2 or 3 places) has been examined against 6 cases corresponding to the selected flux densities
Insulation Fault	4x6	4 scenarios of artificial edge burr fault are considered, where each fault has been examined against 6 cases corresponding to the selected flux densities

7.2.2 Bayesian optimization algorithm (BOA):

The optimization of hyperparameters is seen as a black box type of problem. Black box outputs are used for assessing findings from various viable configurations of parameters in order to show how the model performs in generalization. Optimization of hyper-parameters is provided by:

$$X^* = \arg_{X \in U} \max f(X) \qquad (7\text{-}1)$$

where X* is the solution that maximizes the function $f(X)$ over the set of possible values U. The symbol "arg max" represents the argument that maximizes the function. This equation is used to find the input X that results in the maximum value of the function $f(X)$.

Essentially, BOA initially assumes f(X) as the prior distribution before applying later information for continual optimization of the guessing model until this model reflects real distribution[5][6][7][8].

7.2.3 Particle swarm optimization (PSO)

PSO is inspired by the social behaviour of organisms, such as bird flocking and fish schooling, which was first developed by Kennedy and Eberhart [9]. The algorithm seeks to explore the search space by a population of individuals or particles. Each particle represents a single solution with a dynamically adjusted velocity according to its own experience and that of its neighbouring companions. And the population of particles is updated based on each particle's previous best performance and the best particle in the population. This way, PSO combines

local search with a global search to balance exploration and exploitation. Considering a d-dimensional search space, the *i* particle is represented as:

$$\vec{X}_i = (x_{i,1}, xi_{,2},\ldots,x_{i,d}), \quad (7\text{-}2)$$

and its according velocity is represented as:

$$\vec{V}_i = (v_{i,1}, vi_{,2,\ldots,}v_{i,d}). \quad (7\text{-}3)$$

The best previous position of the particle that gives the best fitness value is represented as:

$$\vec{P}_i = (p_{i,1,} pi_{,2},\ldots,p_{i,d}). \quad (7\text{-}4)$$

The best particle among all the particles in the population is represented as:

$$\vec{P}_g = (p_{g,1}, pg_{,2},\ldots,p_{g,d}). \quad (7\text{-}5)$$

Each particle updates its position and velocity in every iteration according to the two best values.

7.2.4 Support vector machine (SVM).

The SVM is another type of classifier commonly used for classification and regression. This algorithm separates datasets into two categories: negative and positive. The proposed dataset is also trained based on statistical learning, which is expressed as a support vector [10]. Based on categorization information, the algorithm constructs the hyperplane. By creating a hyperplane, the positive and negative datasets are spaced optimally. Kernel functions may be used for nonlinear transformations and for SVM when a dataset has separable and non-separable features. Multi-feature mappings make a nonlinearly separable object linearly separable [11]. This has been accomplished using linear kernels, polynomial kernels, and Gaussian radial basis functions (RBF).

7.3 Proposed method

This section describes the proposed (BOA-SVM) and (PSO-SVM) method, which combines parameter optimization with feature selection together, in order to achieve the highest performance. The proposed approach is comprised of two stages. In the first stage, SVM parameter optimization and feature selection are dynamically conducted by implementing the BOA algorithm simultaneously. In the second stage, SVM parameter optimization and feature selection are dynamically conducted by implementing the PSO algorithm simultaneously. The SVM model performs the classification tasks using the optimal parameter pair and feature subset via a random dataset in which three database decomposition types have been selected randomly. The first is a decomposition of 30-70, meaning that 30% of the database is reserved

for the training process and 70% for testing. The second type of decomposition is 50-50, 50% of the database is used for training, and the remaining 50% of data is exploited for testing. The last decomposition is based on 70% for the training phase and 30% for testing.

7.4 Extracted and selected features

7.4.1 Current signals

The FFT and Discrete Wavelet Transform techniques were applied, ten Features were extracted from the transformer currents, and five features were considered: the average value, the magnitude of the fundamental, total harmonic distortion (THD), and the standard deviation (STD). Table 7-2 gives the selected features extracted from the current signal at 0.5 T flux density, representing a relatively low flux density for both faults. The feature selection step minimizes dimensionality by excluding irrelevant features, and feature selection help in improving the model performance by focusing only on the important variables. This step is conducted using differential evolution. For instance, the features have been selected based on a graphical representation to distinguish the independent features among the others, which are optimized into representative features.

Table 7-2: The selected features at 0.5 T flux density

State		Selected Features			
		average (A)	fundamental (A)	THD (%)	STD
H		0.0588	0.049	41.74	0.0383
F1	S1 in 2 Places	0.0611	0.0874	28.88	0.062
	S1 in 3 Places	0.0619	0.08261	27.14	0.062
	S2 in 2 Places	0.059	0.139	16.82	0.0986
	S2 in 3 Places	0.0563	0.1342	20.33	0.0986
	S3 in 2 Places	0.0652	0.0441	57.39	0.0344
	S3 in 3 Places	0.0654	0.0404	56.64	0.0344
	S4 in 2 Places	0.0556	0.1326	19.32	0.0985
	S4 in 3 Places	0.0654	0.1369	22.84	0.0985
F2	2 places	0.0639	0.0862	30.23	0.0653
	6 places	0.0547	0.14	17.63	0.1006
	8 places	0.0623	0.1395	19.91	0.1022
	12 places	0.0586	0.1599	15.34	0.1162
H: healthy- F1: Edge burr fault- F2: insulation fault					

7.4.2 Thermal images

The RGB technique was used for feature extraction by using MATLAB software. Eight features are extracted from the transformer thermal images, and four features have been considered as the following vectors: the high temperature, R_1, R_3, and R_5. Table 7-3 gives the selected features extracted from the thermal images at 0.5 T flux density, representing a relatively low flux density for both faults. The feature selection step is used to minimize dimensionality by

excluding irrelevant features, and Feature selection helps in improving the model performance by focusing only on the important variables. The features have been selected based on a graphical representation to distinguish the independent features among the others.

Table 7- 3: The selected features at 1.7 T flux density

Type	state	High temperature	R_1	R_3	R_5
Healthy	H 0.5 T	25.3	46.0137	64.0151	10.0288
Edge Burrs Fault	S1 0.5 T	25.5	46.9059	62.0013	8.9072
	S2 0.5 T	25.8	45.2011	66.0125	11.2137
	S3 0.5 T	26	47.0905	62.0367	9.1271
	S4 0.5 T	26.3	49.0766	58.2161	7.2927
Insulation faults	2 Laminations	26.5	46.1925	63.184	9.3766
	6 Laminations	26.9	47.9733	59.3556	7.3288
	8 Laminations	27.1	47.8445	59.794	7.6385
	12 Laminations	27.4	54.6003	47.9246	2.5249

7.5 Results and discussion

7.5.1 Results of the BOA-SVM model

Both faults have been grouped to form a separate class, representing the results of the faulty operation mode. And the dataset for training and testing was selected randomly. Therefore, only a binary classification (healthy and faulty) is formulated where the aim is to detect the presence of faulty conditions because the problem becomes a three-group classification. This process is based on the features extracted from the measured current and captured thermal images. Note that the percentage amount for most datasets scenarios is different because they are random. Take the current signals dataset and thermal images data set by using 70% of the dataset for the training of the selected features as an example. The classification accuracies obtained by the BOA-SVM on these two data sets have been improved by 4% and 6%, respectively, as shown in table 7-4.

Table 7-4: accuracy rate for fault detection execution

Scenario	Current Signals		Thermal Images	
	SVM	BOA-SVM	SVM	BOA-SVM
70-30	94.87	98.71	91.04	97.01
30-70	93.88	94.75	90.90	97.90
50-50	94.61	98.46	91.34	98.07

As mentioned before, in these results, I attempted to assess the effectiveness of the SVM classifier without using optimization algorithms. Table 7-4 summarizes the results of the SVM and BOA-SVM for the data sets of the current signals and thermal images with selected features. It can be observed that the classification accuracies achieved by the developed method are much better than those of SVM in all of the data sets. In order to verify the effectiveness of

the proposed method, I show the detailed results using the run iteration thirty times and choose the best result for all of the data sets scenarios. As shown in figure 7-2, the developed BOA-SVM performs significantly better than the SVM classifier in all cases examined. It reveals that the developed method can obtain more appropriate parameters. The better performance of the proposed method can be attributed to all features in the objective function.

Overall, the results of the BOA-SVM model show a better accuracy rate than those obtained using the SVM classifier. For example, the BOA-SVM model accuracy was 98.71% when the dataset for training was 70% which was the highest obtained accuracy for the current signals, instead of the 94.87% obtained with the SVM classifier. And for the thermal images data, the accuracy rate obtained with the BOA-SVM model is 97.01%, instead of the 91.04% obtained with the SVM classifier.

In general, the results indicated that the accuracy rate of the SVM classifier could be improved by incorporating optimization algorithms for hyperparameters to obtain a better accuracy rate and for better visualization. Figure 7-2 shows the results using the run iteration thirty times, and figure 7-3 shows an example of the confusion matrices obtained using the three algorithms for the three scenarios for the BOA-SVM model.

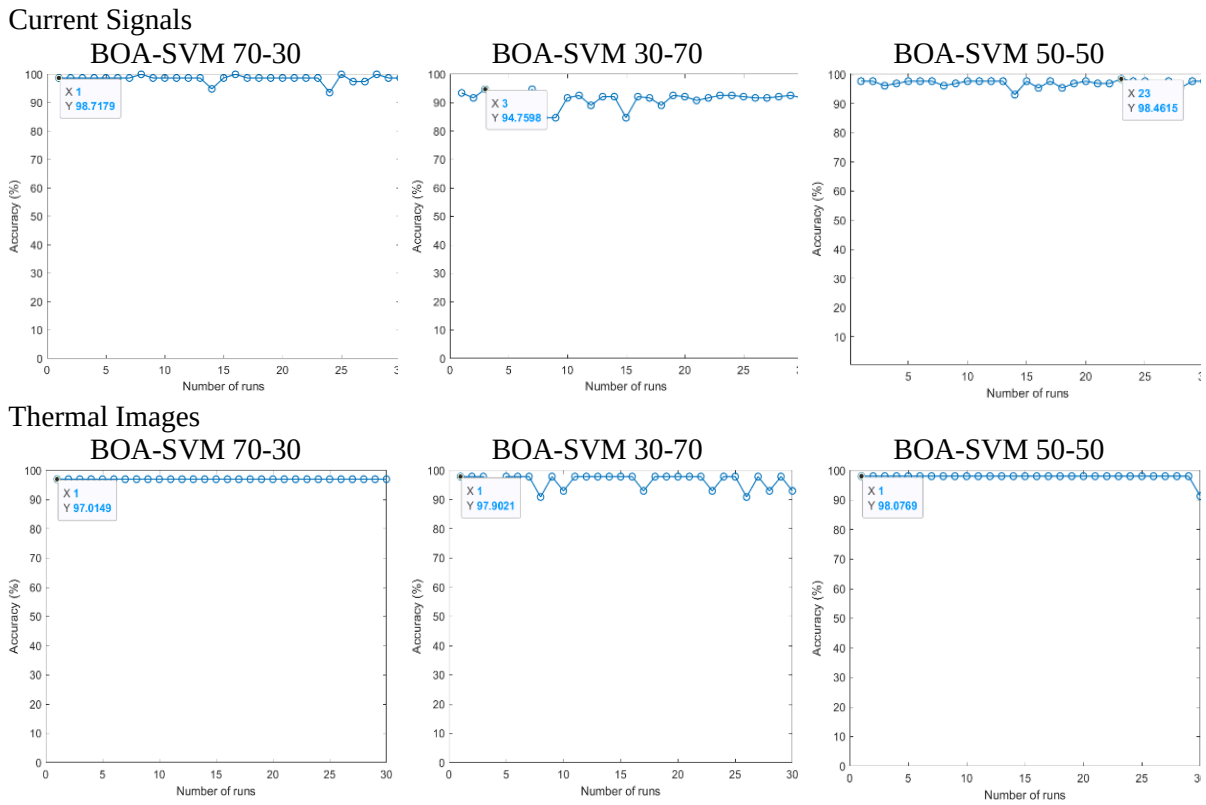

Figure 7- 2: The best results using the run iteration thirty times

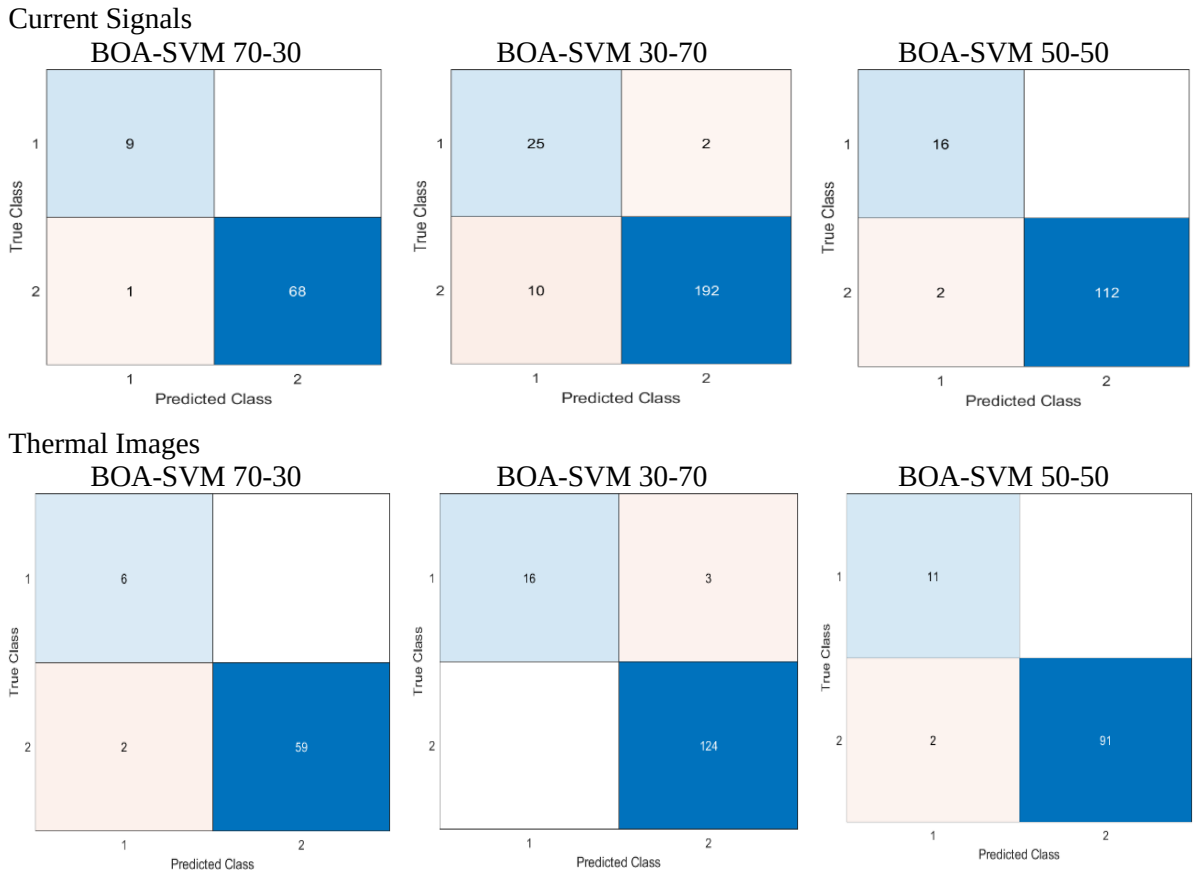

Figure 7-3: Confusion matrix obtained using training/testing scenarios for the (SVM-BOA) of Healthy and both Faults

7.5.2 Results of the PSO-SVM model

In this section, I attempted to investigate whether or not using another optimization algorithm may further improve the classification performance for SVM. Table 7-5 reports the accuracy results for SVM, BOA-SVM, and PSO-SVM for the data sets of the current signals and thermal images with selected features, eq (5-1).

Table 7- 5: The accuracy results for the SVM classifier, BOA-SVM, and PSO-SVM model

Scenarios	**Current Signals**			**Thermal Images**		
	SVM	BOA-SVM	PSO-SVM	SVM	BOA-SVM	PSO-SVM
70-30	94.87	98.71	94.87	91.04	97.01	97.01
30-70	93.88	94.75	91.26	90.90	97.90	97.90
50-50	94.61	98.46	93.07	91.34	98.07	98.07

Compared with the results achieved by BOA-SVM and PSO-SVM. The obtained results by the PSO-SVM have not enhanced the classification accuracy. It can be observed that the classification accuracies for the thermal images achieved the same results for BOA-SVM in all cases. For example, when using 70% of the dataset for the training, the accuracy rate obtained was the same as 97.01% for the BOA-SVM and PSO-SVM model instead of the 91.04%

obtained accuracy rate with the SVM classifier. Moreover, the results obtained by the PSO-SVM for current signals were the same and lowered even than those achieved by the SVM classifier without optimization. For example, when using 70% of the dataset for the training, the accuracy rate obtained was 94.87% with the PSO-SVM model and 94.87% obtained accuracy rate with the SVM classifier, which is the same. When using 50% of the dataset for the training, the accuracy rate obtained was 93.07% with the PSO-SVM model instead of 94.61% obtained accuracy rate with the SVM classifier, which is lower.

In general, compared with the PSO-SVM, the obtained results by BOA-SVM are more appropriate (based on the classification accuracy rates) for the current signals data, while the obtained results by BOA-SVM are the same (based on the classification accuracy rates) for thermal images data. Thus, the developed method of BOA-SVM can find better benefits as compared to PSO-SVM. And for better visualization, figure 7-4 shows the results of the accuracy rate using the run iteration of 200 times.

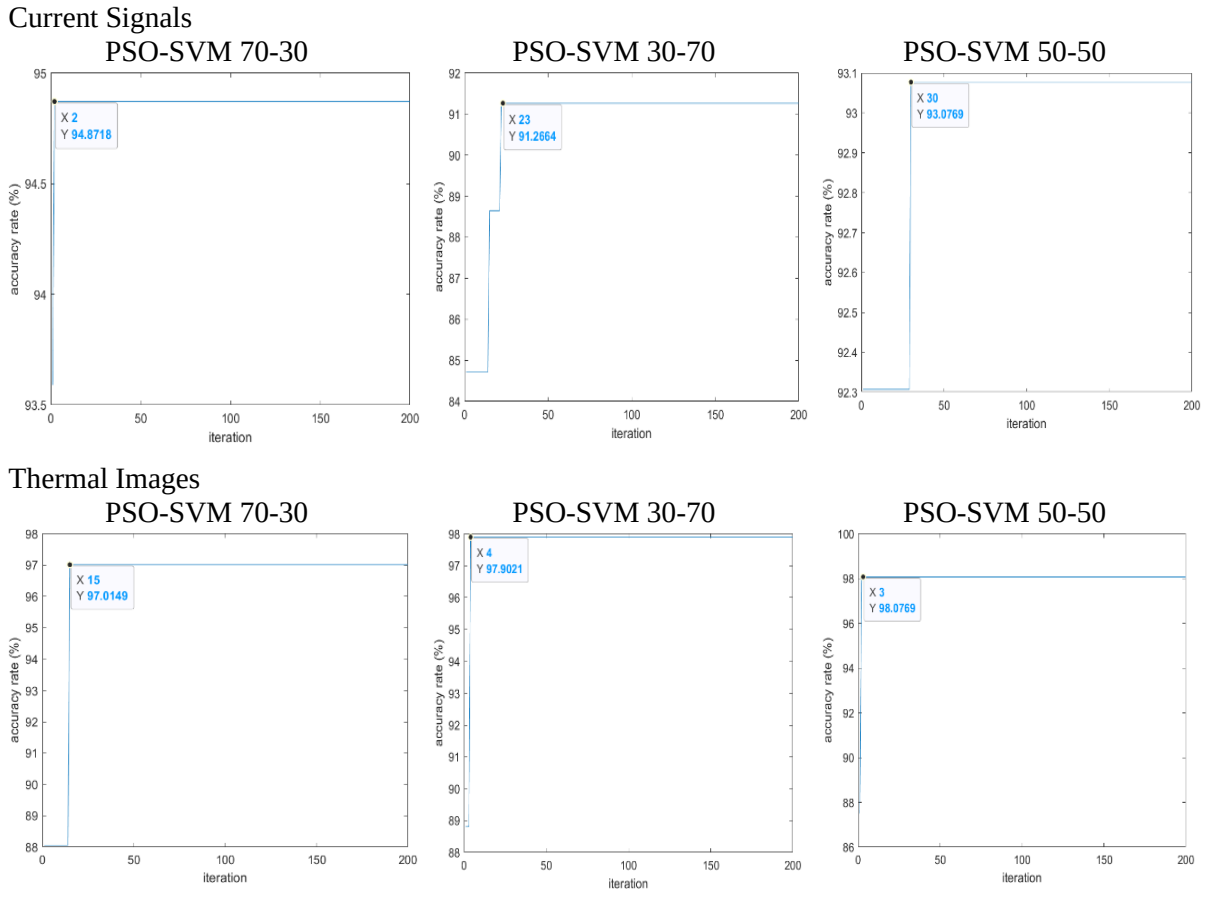

Figure 7- 4: the accuracy rate using the run iteration 200 times

7.6 Summary

As mentioned before, because of the inferior performance acquired by the SVM compared with KNN and DT, as shown in Chapters 5, and 6, the main aim of this work is to increase the efficiency of the proposed method with prediction accuracy.

Both BOA-SVM and PSO-SVM do not generate the same results and prediction accuracy on all of the datasets for current signals. However, they generated the same results and prediction accuracy on all thermal image datasets. The different results of the two methods for the current signals and the approximately identical accuracy of the two methods for the thermal images may be due to the inexact nature of the optimization process and the randomness of the data partitions. And as for the computational time cost, I have computed the running time spent by PSO-SVM and BOA-SVM on all the datasets. Note that the average running time of 200 iterations of PSO-SVM was much less than the average running time of only 30 BOA-SVM. It is worth noting that only one laptop computer was used to act on this work.

In this work, I present BOA-SVM and PSO-SVM based on parameter optimization for SVM. The main contribution of this method lies in the adopted objective function, which aims at maximizing the generalization capability of the SVM classifier. The function simultaneously considers the classification performance of SVM with the iterations. In addition, the proposed methods are implemented in one environment to examine the performance of computational time. Moreover, the developed method is adaptive in nature, attributed to adaptive control parameters. It can also explore a larger search space by introducing the mutation operators that overcome the premature convergence of the other optimization algorithm. In addition, in evaluating lamination fault detection in power transformers, the proposed method can achieve high prediction accuracy and compute efficiently.

Based on empirical analysis, it can be safely concluded that the developed method can serve as a promising alternative tool for parameter optimization and feature selection in SVM. More experiments on larger databases should be done to confirm the overall superiority of the proposed method.

7.7 Reference

[1] A. Akbari, A. Setayeshmehr, H. Borsi, E. Gockenbach, and I. Fofana, "Intelligent agent-based system using dissolved gas analysis to detect incipient faults in power transformers," *IEEE Electr. Insul. Mag.*, vol. 26, no. 6, pp. 27–40, 2010.

[2] X. Yang, W. Chen, A. Li, and C. Yang, "A Hybrid machine-learning method for oil-immersed power transformer fault diagnosis," *IEEJ Trans. Electr. Electron. Eng.*, vol. 15, no. 4, pp. 501–507, 2020.

[3] T. P. Transformers, "New Hybrid Machine Learning Method for Detecting Faults in Three-Phase Power Transformers," 2022.

[4] C. Gu *et al.*, "A Transformer Vibration Signal Separation Method Based on BP Neural Network," *2018 IEEE Int. Power Modul. High Volt. Conf. IPMHVC 2018*, no. 080037, pp. 312–316, 2018.

[5] M. Pelikan, D. Goldberg, and E. Cantu-Paz, "BOA: The Bayesian Optimization Algorithm," *Urbana, Univ. Illinois Urbana-Champaign*, 2005.

[6] J. Snoek, H. Larochelle, and R. P. Adams, "Practical Bayesian optimization of machine learning algorithms," *Adv. Neural Inf. Process. Syst.*, vol. 4, pp. 2951–2959, 2012.

[7] B. Shahriari, K. Swersky, Z. Wang, R. P. Adams, and N. De Freitas, "Taking the human out of the loop: A review of Bayesian optimization," *Proc. IEEE*, vol. 104, no. 1, pp. 148–175, 2016.

[8] F. He, J. Zhou, Z. kai Feng, G. Liu, and Y. Yang, "A hybrid short-term load forecasting model based on variational mode decomposition and long short-term memory networks considering relevant factors with Bayesian optimization algorithm," *Appl. Energy*, vol. 237, no. January, pp. 103–116, 2019.

[9] H. Chen et al., "Towards an optimal support vector machine classifier using a parallel particle swarm optimization strategy", Applied Mathematics and Computation, vol. 239, pp. 180-197, 2014. Available: https://www.sciencedirect.com/science/article/pii/S0096300314005724?via%3Dihub. [Accessed 10 August 2022].

[10] H. Fawzy, E. H. A. Rady, and A. M. A. Fattah, "Comparison between support vector machines and k-nearest neighbor for time series forecasting," *J. Math. Comput. Sci.*, vol. 10, no. 6, pp. 2342–2359, 2020.

[11] J. Seshadrinath, B. Singh, and B. K. Panigrahi, "Investigation of vibration signatures for multiple fault diagnosis in variable frequency drives using complex wavelets," *IEEE Trans. Power Electron.*, vol. 29, no. 2, pp. 936–945, 2014.

CHAPTER 8: Conclusions

8.1 Conclusions

This thesis covered an up-to-date comprehensive review of the core laminations faults and the testing and condition monitoring methods for analysis and detection of faults in power transformers. In addition, the literature review confirmed that artificial intelligence had not yet been applied to diagnose these faults. The thesis has investigated the impact of edge burr faults and the degradation of the lamination insulation on total power loss in a 15 kVA three-phase transformer core through artificial faults. Analytical techniques and experimental work have been utilized to investigate the phenomenon's effect from different aspects based on current signals and thermal images. The equipment that has been used is described in this research to carry out the experimental tests. Description of the specific faults and the data acquisition has also been described.

An experimental methodology was presented to simulate both laminations' faults to investigate the impact on the performance of the power transformer core. Where different scenarios of the faults were applied, and several flux densities were considered, it was found that the edge burrs and insulation degradation can cause flux distortion regarding the recorded current signals, which considerably affects the reliability of the transformer. These effects can increase the transformer currents with the increase of the flux density and the number of short-circuited laminations.

Firstly, for the edge burrs fault, in order to simulate the edge burr fault, a short circuit has been created between laminations of the transformer core. According to the number of sheets in short-circuit (affected area), several scenarios have been selected for this fault. Four scenarios have been considered with different places and affected area size of the transformer core with magnetized in the range of 0.5T to 1.8T. For a completely repeatable and reversible manner to a non-destructive method to detect these defects, a clamping system was designed for the application of the artificial burrs. It was observed that the transformer core was affected, and for a large number of laminations affected by this fault, the overall core losses of the three-phase 15 kVA distribution transformer were doubled.

Secondly, for the Insulation damage fault, removing the insulation on the corresponding laminations to maintain connectivity has been prepared on the two opposing sides of 2, 6, 8, and 12 core laminations at 5 sites on the transformer core. The affected area was around 40

mm2 of the insulation material using rotary equipment, and the considered flux density was 0.5, 1.0, 1.5, 1.7, and 1.8 T. The obtained results show that the insulation degradation is affects the transformer core. The current caused by this fault is related to the number of laminations in the short circuit as well as to the flux density. It was found for two, six, eight, and twelve shorted laminations that the current magnitude is extremely high at a flux density of 1.8 T. In addition, the current magnitude follows a non-linear function with respect to the flux density.

In general, current loss caused by the lamination fault is related to the number of laminations in the short circuit and the area size, as well as to the flux density. It was found that the current magnitude is extremely high at a flux density of 1.8 T, increased with the number of affected laminations. This significant increase in current may lead to an increase in power losses, hence, the transformer efficiency or engendering thermal power transformer failure. And it is worth noting that the faults are produced at different locations in the transformer core.

For the detection and classification of two types of lamination faults (i.e., edge burr and lamination insulation faults) in a three-phase transformer core have been provided by the process of feature extraction and feature selection for the detection and classification of lamination faults in the transformer core. The features have been extracted using signal processing techniques - Fourier Analysis applied to the current signals and RGB technique for thermal images.

Then the features were selected based on a graphical representation to distinguish the independent features among the others, which are optimized into representative features, where four features (Average, Fundamental, Total Harmonic Distortion (THD), and Standard Deviation (STD)) were extracted, elaborating a total of 328 samples for the current signals. For thermal images, four features were selected (the highest temperature value, R_1, R_3, and R_5). Elaborating a total of 222 samples. These features are utilized as input vectors to train and test classification models based on SVM, KNN, and DT algorithms after managing the dataset for training and testing the model by considering different scenarios. 1- decomposition of the dataset for training and testing by random selection 2- the K-Fold cross-validation strategy.

Based on the extracted and selected features, the results confirmed that the transformer lamination's fault can be detected and classified using current signals and thermal images.

For the detection and classification form for both types of lamination faults based on current signals and thermal images, different scenarios have been implemented to prove the validity of experimental results and the reliability of lamination faults detection and classification by artificial intelligence.

a target minimum requirement of 70 % accuracy would ensure that the classifier meets a high level of performance in these scenarios.

Firstly, based on current signals, the different scenarios for detecting and classifying two types of lamination faults (edge burr and lamination insulation faults) in the power transformer core have been provided see table 8-1. The next tables are summarised the obtained results.

Table 8- 1: Obtained accuracy based on current signals using K-Fold cross-validation strategy

The scenarios for the detection and classification		Highest accuracy (%)	Classifier	Lowest accuracy (%)	Classifier
1	Fault Detection for both types of faults has been grouped to form one class (two classes)	99.67	DT	93.81	SVM
2	Fault Classification between health conditions and both types of faults (three classes)	99.67	DT	91.21	SVM
3	Fault Detection of Edge Burrs fault (two classes)	96.08	KNN	83.02	SVM
4	Fault Detection of lamination insulation fault (two classes)	99.55	DT	87.89	SVM
5	Fault Classification between healthy and Edge Burrs fault scenarios (five classes)	66.67	KNN	50.00	DT
6	Fault Classification between healthy and lamination insulation fault scenarios (five classes)	94.85	DT	63.95	SVM

For scenarios 1 and 2, both the highest and lowest accuracy rates are relatively high, with the highest accuracy rates reaching 99.67% and the lowest reaching 91.21%. This suggests that the classifiers are performing well in these scenarios.

For scenarios 3 and 4, the highest accuracy rates are still relatively high (96.08% and 99.55%, respectively), but the lowest accuracy rates are significantly lower (83.02% and 87.89%, respectively).

For scenarios 5 and 6, the highest and lowest accuracy rates are much lower compared to the previous scenarios, with the highest accuracy rates reaching only 66.67% and 94.85%, respectively, and the lowest accuracy rates reaching 50.00% and 63.95%, respectively.

In conclusion, DT performed the best across all scenarios, with the highest accuracy in four out of six scenarios. KNN showed good performance in scenarios 3 and 5, while SVM performed the lowest in all scenarios except for scenario 5, where DT showed the lowest

accuracy. In addition, it was found that the insulation lamination fault presents a good accuracy rate compared to other faults.

Secondly, the different scenarios for detecting and classifying two types of lamination faults (edge burr and lamination insulation faults) in power transformer core based on Thermal images have been provided (see table 8-2.

Table 8-2: Obtained accuracy based on Thermal images using K-Fold cross-validation strategy

The scenarios for the detection and classification		Highest accuracy (%)	Classifier	Lowest accuracy (%)	Classifier
1	Fault Detection for both types of faults has been grouped to form one class (two classes)	99.05	KNN	91.43	SVM
2	Fault Classification between health conditions and both types of faults (three classes)	97.12	KNN	82.86	SVM
3	Fault Detection of Edge Burrs fault (two classes)	96.77	KNN	87.10	SVM
4	Fault Detection of lamination insulation fault (two classes)	94.23	KNN	84.11	DT
5	Fault Classification between healthy and Edge Burrs fault scenarios (five classes)	96.77	KNN	58.87	SVM
6	Fault Classification between healthy and lamination insulation fault scenarios (five classes)	94.44	KNN	62.62	SVM

Again, the results indicated that the fault classification was successful for most scenarios and classifiers. All classifiers gave a good accuracy rate for the detection purpose where two classes were considered. For the classification purpose, the KNN classifier gave the best accuracy, while the SVM classifier gave the lower accuracy.

Due to the (SVM) being less accurate, it was decided to enhance it for fault detection using a random dataset by applying an optimization method based on combining SVM with BOA and PSO optimisation algorithms in developing a hybrid model of classification. This combines parameter optimization with feature selection together in order to achieve the highest performance.

Based on selected features of the current signals and thermal images, the BOA-SVM model can be observed that the classification accuracies achieved by the developed method are much better than those of SVM in all the datasets, and the obtained results by the PSO-SVM have not enhanced the classification accuracy. The classification accuracies for the thermal images have achieved the same results for BOA-SVM in all cases, and for current signals were the same and/or lower even than those results achieved by the SVM classifier.

In general, the obtained results by BOA-SVM are more appropriate than PSO-SVM (based on the classification accuracy rates) for the current signals data, while the obtained results

are the same as PSO-SVM results (based on the classification accuracy rates) for thermal images data.

To conclude, this work has contributed the following:

1- Implementing artificial intelligence to extract and select features of current signals to diagnose two types of lamination faults (edge burr and lamination insulation faults) for a 15 kVA three-phase power transformer. This particular application has utilised three classification algorithms (KNN, SVM, and DT).

2- Using infrared image technology to diagnose the lamination faults based on thermal images with a new feature extraction technique.

3- The SVM classifier has been combined with the GA and PSO optimisation algorithms to increase the fault's diagnosis accuracy.

8.2 The contributions to knowledge

The main contributions of the thesis include the application of artificial intelligence for diagnosing faults in a power transformer, the development of a new method for thermal image feature extraction using the RGB technique, and the improvement of the performance of the SVM algorithm through the application of optimization algorithms.

8.3 Future works

1- large databases are required to reach higher precision and make more accurate classifications to prevent the electrical system by using different sizes of the power transformer core.

2- Using high frequency for data collection because it raises the core temperature for getting a visible thermal image and clear current signals for fault detection and classification.

3- It is also suggested to improve the detection and classification accuracy by adding more features using other feature extraction techniques.

4- For thermal images highly recommend Using a new, more advanced thermal camera to get more accurate and clear images

5- The fault localisation and multi-scenarios of the faulty conditions need more focus, such as collecting more data and scenarios.

Appendix:

Appendix 1: Thermal images and RGB technique

https://docs.google.com/document/d/1OWvmG8N3lZwLBQOprHn1aoUeSuZFi7u/edit?usp=sharing&ouid=112557075303142841699&rtpof=true&sd=true

Appendix 2: FFT technique

https://docs.google.com/document/d/1Z3A4ixIkQk2EQmIoJWjM2OywY1i3dYbw/edit?usp=sharing&ouid=112557075303142841699&rtpof=true&sd=true

Appendix 3: CWT technique

https://docs.google.com/document/d/1wMIs6K7n80D4LYtrPkvKEBIZVyJIQm8/edit?usp=sharing&ouid=112557075303142841699&rtpof=true&sd=true

Appendix 4: DWT technique

https://docs.google.com/document/d/1nB1vjaeXYd3Lcp0cB8i9SJ3ZH_WrmllW/edit?usp=sharing&ouid=112557075303142841699&rtpof=true&sd

Appendix 5: Feature selection

https://docs.google.com/document/d/1bo96Cf0otDpAoYjjQBdpY3nh0O7L26q0/edit?usp=share_link&ouid=112557075303142841699&rtpof=true&sd=true

Appendix 6: Current wave

https://docs.google.com/document/d/14U8Sum8SYg3BC4TtmKEeNBKqwGCquSS/edit?usp=share_link&ouid=112557075303142841699&rtpof=true&sd=true

Appendix 7: The cods

https://drive.google.com/drive/folders/1q8eW3ZSyr_TPfi1Els6W10SuPYd6B_1O?usp=share_link